Evaluation d'images satellitaires à haute résolution spatiale et temporelle pour le suivi de l'utilisation des sols dans les zones agricoles irriguées : application au bassin versant du Berambadi en Inde

Amit Kumar Sharma

UNIVERSITE / SOCIETES
BRETAGNE \ TEMPS
LOIRE / TERRITOIRES

UNIVERSITÉ RENNES 2

THÈSE DE DOCTORAT DE

L'UNIVERSITE RENNES 2
COMUE UNIVERSITÉ BRETAGNE LOIRE

ECOLE DOCTORALE N° 604
Sociétés, Temps, Territoires
Spécialité : Géomatique

Par

Amit Kumar SHARMA

Evaluation d'images satellitaires à haute résolution spatiale et temporelle pour le suivi de l'utilisation des sols dans les zones agricoles irriguées: Application au bassin versant du Berambadi en Inde

Thèse présentée et soutenue à Rennes, le 04 Juin 2019

Unité de recherche : LETG Rennes, UMR 6554 CNRS

Thèse N° :

Rapporteurs avant soutenance :

Agnès Bégué	Directrice de Recherche, CIRAD Montpellier, France.
Pierre-Louis Frison	Maitre de Conférences-HDR, UPEM, Paris France.

Composition du Jury :

Président du Jury:	Eric Pottier	Professeur, Université de Rennes 1, France.
Examinateurs:	M. S. Mohan Kumar	Professeur, Indian Institute of Science, Bangalore, India.
	Julie Betbeder	Chargée de Recherche, CIRAD Montpellier, France.
Directeur de thèse:	Samuel Corgne	Professeur, Université Rennes 2, France.
Co-directeur de thèse:	Laurence Hubert-Moy	Professeur, Université Rennes 2, France.

SHARMA, Amit Kumar. Evaluation d'images satellitaires à haute résolution spatiale et temporelle pour le suivi de l'utilisation des sols dans les zones agricoles irriguées : application au bassin versant du Berambadi en Inde - 2019

Doctor of Philosophy from the

UNIVERSITY OF RENNES 2

COMUE UNIVERSITY BRETAGNE LOIRE

DOCTORAL SCHOOL N° 604
Societies, Time and Territories
Division: Geomatics
By:

Amit Kumar SHARMA

Evaluation of high spatial and temporal resolution satellite images for land use monitoring in irrigated agricultural areas: Application to the Berambadi watershed in India

Thesis presentation and defense will be at Rennes on 04th June 2019
Research Unit: LETG Rennes, UMR 6554 CNRS
Thesis N°:

Reviewers of the thesis:

Agnès Bégué	Research Director, CIRAD Montpellier, France.
Pierre-Louis Frison	Professor Assistant -HDR, UPEM, Paris, France.

Composition of the Jury :

Eric Pottier	Professor, Université de Rennes-1, France.
M. S. Mohan Kumar	Professor, Indian Institute of Science, Bangalore, India.
Julie Betbeder	Chargée de Recherche, CIRAD Montpellier, France.
Thesis director:	Samuel Corgne, Professor, Uni. Rennes-2, France.
Thesis co-director:	Laurence Hubert-Moy, Professor, Uni. Rennes-2, France

Acknowledgments

Evaluation of high spatial and temporal resolution satellite images for land use monitoring in irrigated agricultural areas: Application to the Berambadi watershed in India

Amit Kumar SHARMA

Thesis supervisors: Samuel CORGNE & Laurence HUBERT-MOY

SHARMA, Amit Kumar. Evaluation d'images satellitaires à haute résolution spatiale et temporelle pour le suivi de l'utilisation des sols dans les zones agricoles irriguées : application au bassin versant du Berambadi en Inde - 2019

Acknowledgments

Acknowledgments

I want to express my sincere thanks and gratitude to my research supervisors Prof. Samuel Corgne and Prof. Laurence Hubert-Moy, LETG Rennes, University Rennes 2 for their immense support, excellent guidance and constant motivation at all the stages of my research work. Thank you very much for your time and availability despite your overbooked schedule and responsibilities.

I want to convey my sincere thanks to my thesis steering committee members Prof. M. Sekhar (Civil Engg. IISc/IFCWS-IISc), Dr. Laurent Ruiz (INRA/IFCWS-IISc) and Dr. Sylvain Mangiarotti (CESBIO-Toulouse) for their inspiring encouragement, intellectual input, and support during all stages of my research work. I am always grateful for their kindness, patience, confidence, and support which they had towards me.

I want to thank my Ph.D. defense committee members Prof. Eric Pottier (IETR, Uni. Rennes 1), Prof. M. S. Mohan Kumar (Civil Engg. Dept., IISc-Bangalore, India), Dr. Agnès Bégué (CIRAD-Montpellier), Prof. Pierre-Louis Frison (UPEM-Univ. Paris) and Dr. Julie Betbeder (CIRAD-Montpellier) for accepting the request to evaluate of my thesis. I also would like to thank the jury for their fruitful suggestions to improve my work and their involvement in my thesis defense.

I heartily thank LETG Rennes and IFCWS-IISc for providing me technical support and facilities to perform my thesis work. I want to thank the doctoral school of Uni. of Rennes 2 especially (Joelle Bisson, Valerie Marie Cohier, Suzanne Piel, and Josiane Fernandez), accounts section (Roselyne, Alison, Sebastien, Veronique, and Anne Fourcault), international relational centre (Ewa Mulak-Maerten, Leah and Kelly) and international mobility centre of UBL (Emille, Colette, and Luc) for their kind support and availability to deal with the administrative aspects of the university.

I would also extend my thanks to Dr. Saumya Bhattacharya (ISRO-HQ, Bangalore), Dr. Shiv Mohan (PRL/SAC-ISRO, Ahmedabad), Prof. Nagesh Kumar (Civil Engg.,

IISc), Prof. P. S. Roy (NRSC, ISRO), Dr. Jean Riotte (IRD/IFCWS-IISc), Dr. J. J. Braun (IRD/IFCWS-IISc), Dr. Helene (INRA-Toulouse), Prof. Biswa P. (IITK), Prof. Vinayak K. (IITG), Dr. Rahul Nigam (SAC, ISRO), Dr. Narendra Das (JPL, NASA), Prof. R. R. Navalgund (ISRO-HQ, Bangalore), Prof. Atul Jain (Univ. of Illinois) and Dr. P. S. Thenkabail (USGS) for their support, guidance and motivation at various moments.

I cordially thank my colleagues from France (Jean rene, Veronique, Igor, Xavier, Pauline, Edwige, Alban thomas, Julie betbeder, Julien, Perrine, Fanny, Mael, Mariane, Jean, Audrey, Adeline, Jeanne, Elenore, Chloe, Florent, Renan, Xing Gong, Cyril, Sebastien, Julie Campagna, Gwen, Marion, Gaetan, Clemence, Elodie, Thibaut, Damien carbon, Emilien, Alexandre, Eleanne, Guglielmo, Thomas corpetti, Damien arvor, Thomas houet, Harve quenol) for their kind support.

Many thanks to my well-wishers and friends who have always been inspiring and supportive at all of my difficult times. My heartfelt gratitude to Gaurav, Hemanth, Ajay, Deepak, Sreelakshmi, Shiva, Vinod, Venkatesh, Ravi, Ram, Sat kumar, Sreelash, Rajat, Sounder, Priyesh, Giriraja, Sanjeeva, Marion, Alok, Pawan, Benoit, Jean P. duprey, J. P. bedimo (late) and farmers of the Berambadi watershed.

I am incredibly grateful to my beloved parents and my wife Buvaneshwari Sriramulu, for their unwavering support given to me at all times.

I extend my sincere thanks to DST-CEFIPRA AICHA project (2013-2016), ANR-ATCHA project (2016-2021), UBL student mobility research grant (2017), CNES-TOSCA project (2017-2020), CLS VIGISAT (GIS BreTel) project and STC:ISRO098 project (2010-2013) for providing financial support to pursue my doctoral research and studies.

Amit Kumar Sharma

Acknowledgments

Acknowledgments

List of Symbols, Abbreviations, and Acronyms

AICHA	Adaptation of Irrigated Agriculture to Climate Change
ALI	Advanced Land Imager
AMBHAS	Assimilation of Multi-satellite data at Berambadi watershed for Hydrology And land Surface experiment
ASTER	Advanced Spaceborne Thermal Emission and Reflection Radiometer
ATCHA	Accompanying to Adaptation of Irrigated Agriculture to Climate Change
ATEAM	Advanced Terrestrial Ecosystem Analysis and Modelling
BC	Backscattering Coefficient
BM	Biomass
BreTel	Bretagne Télédétection
CCT	Centre Canadien de Télédétection
CD	Crop Density
CEFIPRA	Le Centre Franco-Indien pour la Promotion de la Recherche Avancée
CH	Crop Height
CLS	Collecte Localisation Satellites
CNES	Centre national d'études spatiales
CNRS	Centre national de la recherche scientifique
CT	Crop Type
DELTA	Dynamic Ecological - Land Tenure Analysis
DoY	Day of Year
EO1	Earth Observation 1
EVI	Enhanced Vegetation Index
FD	Freeman Decomposition
FDVSM	Freeman Durden Volume Scattering Model
GEWEX	Global Energy and Water Balance Experiment
GIS	Geographic Information System
GoPOM	Global Polynomial (ordinary differential equation) Model
GPS	Global Positioning System
GW	Groundwater
HH	Horizontal transmitting and Horizontal receiving polarization
HV	Horizontal transmitting and Vertical receiving polarization

IA	Incidence Angle
IFCPAR	Indo-French Centre for the Promotion of Advanced Research
IFCWS	Indi-French Cell for Water Sciences
IISc	Indian Institute of Science
INRA	Institut national de la recherche agronomique
IRS	Indian Remote Sensing
ISRO	Indian Space Research Organisation
ISTEA	Impression, Strategy, Transmission, Evaluation, and Adjustment
JAXA	Japan Aerospace Exploration Agency
LAI	Leaf Area Index
LETG	Littoral Environnement Télédétection Géomatique
LISS	Linear Imaging Self-Scanning Sensor
LS5	Landsat 5
LS8	Landsat 8
MLC	Maximum Likelihood Classification
MSS	Multispectral Scanner System
MTVI2	Modified Triangular Vegetation Index-Improved
MV	Volumetric Soil Surface Moisture
NAMASTE	Numerical Assessments with Models of Agricultural Systems integrating Techniques and Economics
NASA	National Aeronautics and Space Administration
NDMI	Normalized Difference Moisture Index
NDVI	Normalized Difference Vegetation Index
NIR	Near Infra-Red
NO_3	Nitrate
OA	Overall Accuracy
PA	Producer Accuracy
PD	Polarimetric Decomposition
PDF	Probability Density Function
PolSAR	Polarimetric Synthetic Aperture Radar
PSM	Profile Soil Moisture
RMS	Root Mean Square
RMSE	Root Mean Square Error
RS	Remote Sensing
RS-2	Radarsat-2
RVI	Radar Vegetation Index
S1	Sentinel 1

S2	Sentinel 2
S5T5	Spot5Take5
SAFY	Simple Algorithm For Yield Estimate
SAFYE	Simple Algorithm For Yield and Evapotranspiration estimates
SAR	Synthetic Aperture Radar
SAVI	Soil-adjusted vegetation index
SPOT	Satellite pour l'observation de la Terre
SRTM	Shuttle Radar Topography Mission
SSR	Soil Surface Roughness
STICS	Simulateur mulTIdisciplinaire pour les Cultures Standard
SWAT	Soil & Water Assessment Tool
TDR	Time-Domain Reflectometry
TOSCA	Terre solide, Océan, Surfaces Continentales, Atmosphère
UA	User Accuracy
UBL	l'Université Bretagne Loire
VCI	Vegetation Condition Index
VH	Vertical transmitting and Horizontal receiving polarization
VIC	Variable Infiltration Capacity
VIGISAT	monitoring and protection of the environment by SATellite
VV	Vertical transmitting and Vertical receiving polarization
VWC	Vegetation Water Content
WCM	Water Cloud Model
YD	Yamaguchi Decomposition
YVSM	Yamaguchi Volume Scattering Model

List of Figures

Figure 1 *Organization of the thesis.* 5

Figure 2 *Groundwater abstraction trends in the selected countries.* 20

Figure 3 *The top 10 groundwater abstraction countries and their usage for irrigation purposes (year 2010).* 21

Figure 4 *Irrigation practices in India.* 22

Figure 5 *Cropping seasons in India.* 24

Figure 6 *Climatological seasons in India.* 25

Figure 7 *Electromagnetic spectrum, here Λ represents to the wavelength.* 27

Figure 8 *Earth surface monitoring using optical remote sensing.* 30

Figure 9 *Spectral reflectance curve for the water, soil, and green vegetation using different bands of Landsat satellite.* 31

Figure 10 *The color composites of Landsat reflectance bands (Red, Green, Blue) after LEDAPS atmospheric correction implementation on the top of the atmosphere (left) and surface reflectance (right).* 33

Figure 11 *The atmospheric corrections of Top of Atmosphere (left) and surface reflectance (right) color composites of Landsat-8 reflectance bands (Red, Green, Blue).* 34

Figure 12 *Evolution of microwave satellite.* 41

Figure 13 *Radar image acquisition geometry.* 42

Figure 14 *SAR image geometry in strip-map mode.* 43

Figure 15 *Microwave polarization (Source : CCT)* 44

Figure 16 *Scattering phenomena examples from vegetation.* 47

Figure 17 *Temporal trajectory of a monochromatic plane wave at $z = z0$ (at a fixed abscissa).* 49

Figure 18 *Spatial evolution of the circularly polarised plane wave.* 50

Figure 19 *Schematic sample of a Radar image. (Source : CCT)* 52

Figure 20 *Constructive and destructive interference of the Radar signal.* 53

Figure 21 *Speckle filtering techniques of the SAR images.* 54

Figure 22 *Examples of speckle filters with different window size.* 55

Figure 23 *Example of False Color composite of Radarsat-2 (RS2) with the 3 polarizations (VV,HV,VV) on the Berambadi watershed (in Yellow).* 56

Figure 24 *The electromagnetic wave interaction with a target.* 57

Figure 25 *Example of Grey-scale representation of Span estimation for the image Radarsat-2 QuadPol acquired the 08th June 2013 (Berambadi watershed, India)...* 59

Figure 26 *Example of False Color Composite of Radarsat-2 (RS2) with the 3 components of the Sinclair matrix on the Berambadi watershed (in Yellow).* 60

Figure 27 *Example of False Color Composite of Radarsat-2 (RS2) with the 3 components of the Coherency (T3) matrix on the Berambadi watershed (in Yellow).* 63

Figure 28 *Example of False Color Composite of Radarsat-2 (RS2) with the 3 components of the covariance (C3) matrix on the Berambadi watershed.* 64

Figure 29 *SAR images polarimetric decomposition algorithms.* 65

Figure 30 *Example of False Color Composite of Radarsat-2 (RS2) with the 3 components of the Pauli polarimetric decomposition on the Berambadi watershed.* 67

Figure 31 *Example of False Color Composite of Radarsat-2 (RS2) with the 3 components of the Cloude-Pottier decomposition on the Berambadi watershed.* 68

Figure 32 *H-A-Alpha plane representation.* 69

Figure 33 *Example of False Color Composite of Radarsat-2 (RS2) with the 3 components of the Freeman-Durden (FD) polarimetric decomposition on the Berambadi watershed.* 70

Figure 34 *Image classification methods.* 74

Figure 35 *SVM classifier scheme in linear (a) and non-linear cases.* 75

Figure 36 *Location of the Berambadi watershed.* 80

Figure 37 *Surface soil texture of the Berambadi watershed.* 82

Figure 38 *Annual rainfall in the Gundulupete taluk from the year 1951 till 2016.* 83

Figure 39 *Monthly cumulative rainfall in the Berambadi watershed for the year 2004 till 2018.* 84

Figure 40 *DEM of the Berambadi watershed.* 85

Figure 41 *Crop calendar.* 86

Figure 42 *Turmeric crop (n) growth stages (a to h). After harvesting (i) the mother root (j) and turmeric root (k) it is processed (l) for the transporting (m) to market. ... 88*

Figure 43 *Turmeric crop mixed with other crops like chili (a) and onion (b). 89*

Figure 44 *Banana growth stages (a to d). 90*

Figure 45 *Banana with other crops like beetroot (a), watermelon (b), pumpkin (c) and garlic (d). 90*

Figure 46 *Maize crop growth staged from (a) to (e), harvesting (g) the fruit to sell in the market and remaining stem collection (g) for the fodder of the cows. 91*

Figure 47 *Sunflower crop growth stages from (a) to (e) and harvesting the seeds (f) to sell in the market, the remaining stem is left in the field (g) which will be mixing in the soil during the next cropping season. 92*

Figure 48 *Marigold crop growth stages (a) to (e). 93*

Figure 49 *Sorghum (jowar) crop growth stages (a) to (d). 93*

Figure 50 *Tomato crop growth stages (a) to (f) and fruit harvesting (g). 94*

Figure 51 *Sugarcane growth stages (a) to (c) and harvesting (d). 95*

Figure 52 *Garlic crop images (a) to (e). 96*

Figure 53 *Cabbage crop growth stages (a) to (b). 96*

Figure 54 *Ragi crop growth stages from (a) to (c). 97*

Figure 55 *Solar bean crop growth stages from (a) to (c). 97*

Figure 56 *Country beans crop growth stages from (a) to (d). 98*

Figure 57 *Beetroot crop growth stages from (a) to (d). 99*

Figure 58 *Other crops like Chilli (a), horse gram (b), beans (c), watermelon (d), chickpea (e), pearl millet (f), cotton (g) and pumpkin (h). 101*

Figure 59 *Fallow land variability (from (a) to (z)) in the Berambadi watershed. 102*

Figure 60 *Groundwater is pumping borewell locations in the Berambadi watershed. 103*

Figure 61 *Groundwater pumping and storage in the tank. 104*

Figure 62 *Dug wells which were used for the crop irrigation purposes. 105*

Figure 63 *Dried water tanks (from (a) to (c)) and tank saline soil(d) mixed in the farmland. 106*

Figure 64 *Dried borewells in the watershed. 107*

Figure 65 *Instruments used for the soil (a, b, c, f), crop (e, g) and weather parameters (h) in the watershed.....109*

Figure 66 *Long-term (for the year 2010-18) ground observation monitoring locations. 110*

Figure 67 *Parcel boundary delineation. 112*

Figure 68 *Parcel area histogram. 113*

Figure 69 *Optical satellite images. 114*

Figure 70 *FCC (NIR Red Green) of IRS-LISS-4 satellite image (Date: 28th Jan 2014). ..115*

Figure 71 *Multitemporal FCC of the SAR backscattering from HH HV and VV polarizations.....116*

Figure 72 *Radarsat-2 SAR quad polarization and ultrafine HH- polarization data.....117*

Figure 73 *In-situ measurements and ground observation for crop monitoring (AICHA,ATCHA project and Irriga Detection), in red variables used in the thesis. 119*

Figure 74 *Calibration and validation parcels in the watershed. The X, Y, and Z belong to three regions which represent respectively upper, middle and downstream sections of the watershed..... 125*

Figure 75 *Workflow of the methodology..... 127*

Figure 76 *Accuracy assessment of SVM classified irrigated and non-irrigated croplands. 129*

Figure 77 *A temporal map of irrigated and non-irrigated croplands in Rabi season from 1990 to 2015. .....131*

Figure 78 *Rabi irrigated cropland evolution in the watershed..... 132*

Figure 79 *Spatiotemporal map of Rabi irrigated cropland for the duration 1990 to 2015. ..... 133*

Figure 80 *Temporal map of irrigated croplands in the Summer season from 1991 to 2016. ..... 134*

Figure 81 *Summer irrigated cropland evolution in the watershed..... 136*

Figure 82 *Spatiotemporal map of Summer irrigated area for the duration 1991 to 2016. ..... 137*

Figure 83 *Dual (Rabi and Summer) irrigated cropland evolution in the watershed. .. 139*

Figure 84 *Spatiotemporal map of Dual (Rabi and Summer) irrigated cropland area for the duration 1990 to 2016.* *140*

Figure 85 *Study area and ground observation locations.* *144*

Figure 86 *Daily rainfall of the Berambadi watershed for the Radarsat-2 pass duration* *148*

Figure 87 *Image processing workflow.* *149*

Figure 88 *Spatial distribution of dual-irrigation in the Berambadi watershed in 2013.* *155*

Figure 89 *Spatial distribution of irrigated croplands during kharif cropping season.* *157*

Figure 90 *Spatial distribution of rabi cropping season irrigated croplands. The other croplands are partially groundwater irrigated in the absence of rainfall or grown under only rainfed condition.* *159*

Figure 91 *Multi-satellite images used for the study.* *167*

Figure 92 *Ground observed training (calibration) and validation parcels of annual (summer + kharif + rabi) irrigated (intensive irrigation) and other (partial irrigation in the absence of rainfall, rainfed only and fellow land) croplands for the years 2014, 2015 and 2016.* *169*

Figure 93 *Monthly rainfall during cropping seasons for the year 2014-16.* *171*

Figure 94 *Methodology flow chart.* *172*

Figure 95 *Pre-processed NDVI obtained from various sensors.* *173*

Figure 96 *Linear relation between LS8 OLI NDVI and other corrected NDVI values.* *174*

Figure 97 *The re-constructed temporal NDVI for various crops in the watershed.* *176*

Figure 98 *Seasonal intensive irrigated cropland classification for the year 2014-15.* .. *179*

Figure 99 *Dual and annual irrigated cropland classification for the year 2014-15.* *180*

Figure 100 *Seasonal intensive irrigated cropland classification for the year 2015-16.* . *182*

Figure 101 *Dual and annual irrigated cropland classification for the year 2015-16.* *182*

Figure 102 *Summer irrigated cropland classification for the year 2016.* *184*

Figure 103 *Ground observation locations during kharif and rabi cropping seasons in 2017.* *190*

Figure 104 *Multitemporal composite color of Radarsat-2 UF images (in red : 05th June 2017, in green : 29th June 2017 , in blue : 16th Aug 2017).* *192*

Figure 105 *Major crops (turmeric (a), banana (b), maize (c), sorghum (d), marigold (e), and sunflower (f)) grown in the Berambadi watershed. 193*

Figure 106 *Multitemporal composite color of Radarsat-2 UF images parcel mean values (in red : 05th June 2017, in green : 29th June 2017 , in blue : 16th Aug 2017)..... 194*

Figure 107 *Linear relation between ground observed crop height and the parcel mean HH backscattering coefficient value. 195*

Figure 108 *Relationship between the ground observed crop height (irrespective to the crop type) and parcel mean backscatter value..... 196*

Figure 109 *Crop height and surface heterogeneity representation for samples fields of turmeric, banana, maize, sorghum, marigold, sunflower and backscattering coefficients values 197*

Figure 110 *Ground survey location of turmeric and non-turmeric parcels during kharif and rabi cropping season of the year 2014..... 200*

Figure 111 *Measured LAI growth curves for the monitored turmeric parcels..... 201*

Figure 112 *Image pre-processing workflows for optical and SAR datasets..... 203*

Figure 113 *Estimated LAI RGB color composite of the three dates..... 203*

Figure 114 *Example of the representation of the T33 component issue of Radarsat-2 Quad Pol data at a pixel (a), plot mean (c) and plot standard deviation (c) scales (11th July 2014)..... 205*

Figure 115 *Example of the representation of the Freeman Durden volume scattering intensity of Radarsat-2 Quad Pol data at a pixel (a), plot mean (c) and plot standard deviation (c) scales (11th July 2014)..... 205*

Figure 116 *ANCOVA implementation and SVM classification. 207*

Figure 117 *Turmeric NDVI curve evolution..... 208*

Figure 118 *Satellite NDVI and LAI relation with ground observed LAI..... 208*

Figure 119 *Relation between polarimetric decomposition variables and ground observed LAI relation. where SE_I and T11 represents to the Shannon Entropy (Intensity) and single-bounce diagonal component intensity of the Coherency matrix respectively. 209*

Figure 120 *Methodology to assess the impact of intensive irrigation on groundwater resources..... 214*

Figure 121 *Borewell monitoring location in 2015 and 2016. ..... 214*

***Figure 122** Various interpolation methods implementation on scattered elevation point data. 216*

***Figure 123** Gridded means of groundwater level (GWL in meters) in December 2015. 217*

***Figure 124** Gridded mean value of groundwater level in the summer of the year 2016. ..... 218*

***Figure 125** Gridded percentage of irrigated cropland in rabi 2015. ..... 219*

***Figure 126** Gridded percentage of irrigated cropland in summer 2016. ..... 220*

***Figure 127** Sampled borewell locations and the transect from upstream towards downstream of the watershed. 221*

***Figure 128** Relation between gridded mean groundwater and percentage irrigated area for rabi 2015 (in yellow, the grid cells). 223*

***Figure 129** Relation between gridded mean groundwater and percentage irrigated area for summer 2016 (in yellow, the grid cells). 224*

***Figure 130** Evolution of total number of borewells in the watershed with cumulative annual rainfall and corresponding total irrigated area. 225*

***Figure 131** Groundwater level (GWL) along transect AA' for the Kharif, Rabi and Summer season and the total number of borewells in villages of the experimental watershed in 2015. ..... 226*

List of Tables

Table 1 *List of the high-spatial-resolution (<100m) optical image spectral bands.* 38

Table 2 *List of the optical indices for irrigated cropland monitoring classification.* ... 39

Table 3 *List of all microwave bands.* 40

Table 4 *List of the polarization states.* 45

Table 5 *List of polarizations.* 51

Table 6 *List of the dataset used with Day Of Year (DOY), season and sensor specifications (Thematic Mapper (TM), and Optical Land Imager (OLI)).* 123

Table 7 *Training and validation samples of irrigated and non-irrigated cropland in the Berambadi watershed.* 124

Table 8 *Indices used were: Normalized Difference Vegetation Index (NDVI), Normalized Difference Moisture Index (NDMI), and Enhanced Vegetation Index (EVI).* 126

Table 9 *Rabi season irrigated cropland evolution from 1990 to 2015.* 130

Table 10 *Summer season irrigated cropland evolution from 1991 to 2016.* 135

Table 11 *Dual irrigated cropland evolution from 1990 to 2016.* 138

Table 12 *Characteristics and dates of acquired Radarsat-2 satellite images.* 146

Table 13 *The table presents confusion matrix, user's accuracy, producer's accuracy, overall classification accuracy (OA), and the kappa coefficient for all SVM classified outputs from various polarization indices.* 153

Table 14 *Total irrigated area and classification accuracy for the dual-irrigation practices in the Berambadi watershed. Were a and b are representing respectively irrigated croplands and other (rainfed and fallow) croplands.* 156

Table 15 *Total irrigated area and classification accuracy for the kharif cropping season. Were a and b are representing respectively irrigated croplands and other (rainfed and fallow) croplands.* 158

Table 16 *Total irrigated area and classification accuracy for the rabi cropping season.* 160

Table 17 *Training and validation samples of intensively irrigated cropland and other croplands. 169*

Table 18 *Classification accuracy assessment of intensively irrigated cropland and other croplands for the year 2014-15. Where Irr and Oth represents to the Irrigated and other cropland respectively. 178*

Table 19 *Classification accuracy assessment of intensively irrigated cropland and other croplands for the year 2015-16. Where Irr and Oth represents to the Irrigated and other cropland respectively. 181*

Table 20 *Classification accuracy assessment of intensively irrigated cropland and other croplands for the year 2016. ..... 183*

Table 21 *Validation of the proposed study. 185*

Table 22 *Characteristics and dates of the acquired Radarsat-2 UF satellite images.... 191*

Table 23 *Optical and SAR satellite images. 202*

Table 24 *Estimation of the kappa coefficient. 210*

Table of contents

Acknowledgments vii

List of Symbols, Abbreviations, and Acronyms xi

List of Figures xv

List of Tables xxiii

Table of contents xxv

Introduction Générale (Français) 1

General introduction (English) 7

CHAPTER 1 : Irrigated area monitoring in India 13

1.1 Introduction 13

1.2 Green revolution and irrigation evolution in India 19

1.3 Remote sensing application for irrigated cropland monitoring 25

1.3.1 Optical remote sensing 28

1.3.2 Radar remote sensing 39

1.3.3 Image classification algorithms 73

CHAPTER 2: Study area and Dataset 79

2.1 Introduction 79

2.2 Berambadi watershed characterization 81

2.2.1 Cropping seasons 85

2.2.2 The diversity of farming practices 87

2.2.3 Irrigation practices 103

2.3 Ground observations and in-situ measurements 107

2.3.1 Ground observation parcels identification 110

2.3.2 Parcel digitization in the Berambadi watershed 111

2.4 Remote sensing dataset 113

2.4.1 Multispectral optical images 114

2.4.2 Synthetic Aperture Radar (SAR) images 115

2.5 Crop monitoring 118

CHAPTER 3: Historical evolution of irrigated cropland identification 121

3.1 Introduction 121

3.2 Dataset used in the study 122

3.2.1 Remote sensing data used for the study 122

3.2.2 Ground observation 123

3.3 Results and discussion 128

3.3.1 Irrigated and non-irrigated cropland classifications 128

3.3.2 Irrigated and non-irrigated cropland analysis during Rabi season (post-monsoon) 129

3.3.3 Irrigated and non-irrigated cropland analysis during the summer season 133

3.3.4 Dual season (Rabi and Summer) irrigated and non-irrigated cropland analysis 137

CHAPTER 4: Irrigated cropland identification ____ *143*

4.1 Evaluation of Radarsat-2 quad-pol SAR time series images for monitoring groundwater irrigation ____ **143**

4.1.1 Ground observation ____ 144
4.1.2 Satellite images used for the study ____ 145
4.1.3 Ground observations ____ 146
4.1.4 Image processing ____ 149
4.1.5 Results ____ 151
4.1.6 Discussion ____ 160
4.1.7 Conclusion ____ 162

4.2 Seasonal intensive groundwater irrigated cropland identification using NDVI time-series images ____ **165**

4.2.1 Dataset used for the study ____ 165
4.2.2 Methodology ____ 171
4.2.3 Results and discussion ____ 177

CHAPTER 5: Crop type monitoring and characterization ____ *189*

5.1 Sensitivity analysis of multitemporal Radarsat-2 (UF) images with crop growth ____ **189**

5.1.1 Ground observation locations ____ 190
5.1.2 Materials and methods ____ 191
5.1.3 Results and discussion ____ 194

5.2 Turmeric monitoring using Radarsat-2 (QuadPol) and Landsat-8 time series images 199

5.2.1 Introduction ____ 199
5.2.2 Ground observation and dataset ____ 200
5.2.3 Methodology ____ 202
5.2.4 Results and discussion ____ 207

CHAPTER 6: Assessing impact of intensive irrigation on groundwater resources ____ *213*

6.1 Introduction ____ **213**

6.2 Material and methods ____ **213**

6.3 Results and discussion ____ **221**

6.3.1 Relation between irrigated cropland and groundwater level. ____ 222
6.3.2 Relation of borewell evolution and intensive irrigation ____ 224

CHAPTER 7: Conclusion and Perspectives ____ *229*

References ____ *235*

List of publications ____ *273*

***Table** of contents*

Introduction Générale (Français)

Evaluation d'images satellitaires à haute résolution spatiale et temporelle pour le suivi de l'utilisation des sols dans les zones agricoles irriguées : Application au bassin versant du Berambadi en Inde

Dans le contexte du changement global, la gestion de la ressource en eau douce à des fins agricoles représente un défi majeur pour la sécurité alimentaire à l'échelle mondiale (Endo et al., 2017; Kummu et al., 2016; Salmon et al., 2015). À l'heure actuelle, la population mondiale est d'environ 7,5 milliards d'habitants et devrait atteindre 8,5 milliards d'habitants d'ici 2025 (Bonilla-Moheno et al., 2013; Dash, 2012; Gun et al., 2011; Knauer et al., 2017; Taylor, 2014). Pour nourrir la population mondiale en 2012, environ 324 millions d'hectares (Mha) dans le monde ont été aménagés pour l'irrigation et environ 275 Mha de terres ont été effectivement irriguées (FAO). Près de 20% de terres cultivées irriguées fournissent 40% de la production alimentaire mondiale en utilisant 70% de l'eau douce mondiale pour l'irrigation (Ambika et al., 2016; Salmon et al., 2015; A K Sharma et al., 2018).

L'agriculture est la principale source d'emploi en Inde et une partie importante de la population indienne en dépend pour sa subsistance (Ambika et al., 2016; Krishna Kumar et al., 2004; Roy et al., 2015b). Cependant, la production agricole est fortement influencée par les événements climatiques extrêmes, les changements à long terme des précipitations et de la température de l'air, le contexte économique, politique et social, , etc. (Ambika et al., 2016; Krishna Kumar et al., 2004). La surexploitation des ressources en eaux souterraines, l'augmentation de la température en hiver, les précipitations irrégulières pendant la saison des moussons et l'absence de stratégies d'adaptation efficaces auront des impacts plus ou moins importants sur la productivité des cultures (Ambika et al., 2016; Mondal et al., 2015; Rodell et al., 2009).

En Inde, le parcellaire agricole est caractérisé par ailleurs par une grande variabilité des pratiques agricoles, plusieurs saisons culturales sur une année civile sont possibles associés à des pratiques d'irrigatione très hétérogènes (Bhavani et al., 2017; Jain et al., 2013; Mondal et al., 2014; Roy et al., 2015b; Siebert and Zhao, 2014; Wilken et al., 2017).

Les territoires agricoles en Inde sont généralement caractérisés par des paysages fragmentés par un petit parcellaire agricole et de très fortes variabilités spatiotemporelles dans les pratiques agricoles. Ainsi, près de 94% des exploitants

agricoles possèdent des exploitations inférieures à 4 ha (Ambika et al., 2016; Narayanamoorthy, 2011) et la taille des parcelles agricoles est généralement inférieure à 1 ha (Robert et al., 2017b; A K Sharma et al., 2018). L'identification des cultures irriguées, leur suivi et caractérisation représentent encore un enjeu majeur d'un point de vue scientifique mais également d'un point de vue économique et sociétal (Bhaduri et al., 2012; Dheeravath et al., 2010; Gandhi and Namboodiri, 2009; Gumma et al., 2000; Mondal et al., 2016; Narayanamoorthy, 2011; Robert et al., 2018; Shah, 2007; Thenkabail et al., 2009b, 2008, 2009a; Wilken et al., 2017).

L'irrigation dans les territoires agricoles peut être définie comme une pratique agricole spécifique qui consiste à apporter artificiellement de l'eau douce à une culture afin de palier un déficit hydrique et permettre un développement optimal de la plante (Bégué et al., 2018; F. S. Nakayama, 1991; Siebert et al., 2005; Spalding and Exner, 1993). Cette pratique agricole, réalisée à partir de différents dispositifs (forages, canaux d'irrigation et pompes) et matériels (dispersion, goutte à goutte et gravitaire) offre une assurance de production et de revenu primordiale pour de nombreux exploitants agricoles (Biswas and Tortajada, 2009; Fishman et al., 2015; Siebert et al., 2005; Tal, 2016). L'usage de l'irrigation est dépendante de nombreux facteurs tels que la phénologie des cultures, le climat, ou la disponibilité de la ressource en eau (Barik et al., 2016; Fishman, 2018; Gumma et al., 2011; Pavelic et al., 2012; Zwart et al., 2010).

D'un point de vue temporel, l'irrigation est une pratique très ponctuelle (de quelques heures à plusieurs jours), et d'un point de vue spatial, elle est généralement appliquée à une échelle parcellaire (Kussul et al., 2016; Sitokonstantinou et al., 2018). Son identification (localisation spatiale) et sa caractérisation (type de culture, suivi phénologique...) par télédétection représentent donc encore des challenges scientifiques majeurs (Atzberger, 2013; Bargiel, 2017; Canisius et al., 2018; Liu et al., 2013; Mangiarotti et al., 2018; Palchowdhuri et al., 2018). L'identification des surfaces agricoles irriguées et la caractérisation de ces surfaces nécessitent en effet une haute répétitivité temporelle combinée à une haute résolution spatiale, des méthodes de classifications intégrant l'information multi-temporelle et multi-source, des cartographies à fine échelle, etc. (Betbeder et al., 2014b; Campos-Taberner et al., 2017, 2016a; Claverie et al., 2012; Dusseux et al., 2015; El Hajj et al., 2009; Liu et al., 2014; Thomas et al., 2008; Vrieling et al., 2017; Zheng et al., 2016).

La télédétection spatiale représente un outil d'observation privilégié pour le suivi et la caractérisation des cultures à différentes échelles spatiales et temporelles (Turner et al., 2007). La télédétection optique, la plus fréquemment utilisée, présente cependant des limites liée à la présence de nuages. Dans les régions tropicales comme l'Inde,

caractérisées par une couverture nuageuse importante durant la saison des pluies, de nombreuses études combinent l'imagerie optique avec l'imagerie radar qui s'affranchit des conditions atmosphériques et d'illumination (Bégué et al., 2018; Corgne et al., 2016a; Qi et al., 2017). L'usage combiné de l'imagerie optique et radar permet ainsi d'acquérir des séries temporelles d'images, ce qui représente un enjeu majeur pour le suivi des cultures caractérisées par une forte variabilité spatiale et temporelle liée aux rotations culturales, aux pratiques agricoles telles que l'irrigation, aux facteurs sociaux, économiques, climatiques (Betbeder et al., 2015a; Fieuzal and Baup, 2016; Sharma et al., 2016).

L'objectif principal de cette thèse vise à identifier et caractériser les surfaces irriguées sur un bassin versant agricole en utilisant des séries temporelles d'images satellites optiques et radar à haute résolution spatiale. Le bassin versant expérimental du Berambadi qui fait partie de l'Observatoire Environnemental "Bassins versants Expérimentaux Tropicaux" (BVET) géré par le LMI CEFIRSE (Laboratoire Mixte International Cellule Franco-Indienne de Recherche en Science de l'Eau) de l'Institut des Sciences de Bangalore (Inde). Sur ce bassin versant expérimental, trois objectifs spécifiques ont été identifiés : le premier consiste à faire un état des lieux de l'évolution de l'agriculture irriguée à échelle fine sur les 30 dernières années ; le second objectif vise à identifier et caractériser les cultures irriguées sur plusieurs cycles culturaux et à une échelle intra-annuelle ; le troisième objectif consiste à étudier l'impact de l'irrigation sur les aquifères souterrains du bassin versant.

Pour atteindre ces objectifs, quatre points et questions de recherche associées ont été identifiées sue le bassin versant expérimental du Berambadi en Inde :

(i) Le premier point vise à quantifier l'évolution de l'agriculture irriguée sur une échelle fine au cours des trois dernières décennies.

Question de recherche : Comment effectuer le suivi des terres irriguées à l'aide de données de télédétection ?

(ii) Le deuxième point vise à identifier et à caractériser les cultures irriguées sur plusieurs cycles de culture et à une échelle intra-annuelle.

Question de recherche : Quelle est la contribution des images optiques et SAR pour caractériser les cultures irriguées à une échelle intra-annuelle ?

(iii) Le troisième point vise à suivre les cultures à l'aide d'images optiques et de séries temporelles SAR.

Question de recherche : Quelle est la contribution des images satellites optiques et SAR pour suivre la croissance des cultures ?

(iv) Le quatrième point vise à étudier l'impact de l'irrigation sur les aquifères souterrains du bassin versant.

Question de recherche : Existe-t-il une relation entre les pratiques d'irrigation intensive et les ressources en eaux souterraines ?

La thèse est ainsi principalement divisée en six chapitres (Figure 1). Le premier chapitre présente un état de l'art sur l'identification et la caractérisation des cultures irriguées par télédétection. Les différentes pratiques d'irrigation et de gestion de l'eau à des fins agricoles sont d'abord analysées. Les images satellitaires optiques et radar utilisées pour la caractérisation des cultures ainsi que les principales méthodes de classification d'images sont ensuite exposées.

Le chapitre deux décrit dans un premier temps l'espace d'étude et les données utilisées en détaillant les mesures *in-situ* et les enquêtes menées sur le bassin versant expérimental du Berambadi. Dans un deuxième temps, ce chapitre aborde la gestion des bases de données recueillies sur le terrain et le prétraitement radiométriques et géométriques appliqués aux images optiques et radar.

Le troisième chapitre présente une estimation de l'évolution historique des cultures irriguées entre 1990 et 2016 sur deux saisons culturales (rabi et été) à l'aide d'une série temporelle d'images satellitaires optiques. L'histoire de l'irrigation saisonnière et de la double irrigation s'est développée dans le passé.

Le chapitre quatre est focalisé sur l'identification des surfaces irriguées et non irriguées sur une période récente (2014-2016) à partir de séries temporelles d'images radar et optiques. Ce chapitre est scindé en deux parties : la première décrit la méthodologie développée pour discriminer les terres cultivées irriguées des terres non irriguées en utilisant des séries temporelles d'images polarimétrique Radarsat-2 ; dans la seconde partie, des séries chronologiques de NDVI estimées à partir de séries temporelles d'images optiques sont évaluées.

Le chapitre cinq est focalisé sur les potentialités des images radar et optiques pour la caractérisation des cultures irriguées. Ce chapitre est divisé en deux parties : la première évalue le potentiel des images Radarsat-2 (mode UltraFin) pour l'estimation de la hauteur des cultures. La deuxième partie porte sur l'utilisation conjointe de variables polarimétriques et de variables optiques pour la cartographie du curcuma.

Le chapitre six présente une analyse sur les relations entre l'évolution de l''irrigation intensive et le niveau des eaux souterraines sur le bassin versant de Berambadi. L'étude a été réalisée à l'échelle du km² pour deux saisons culturales : le Rabi et l'été.

Cette thèse a été réalisée dans le cadre de trois programmes de recherche : le programme CEFIPRA (Projet « AICHA, 2012-2016) » et l'ANR ATCHA (2017 -2021) coordonnés par L. Ruiz (INRA) et M. Sekhar (IISc), ainsi que le programme TOSCA du CNES (Projet « Irriga-détection », 2017 -2018) coordonné par S. Corgne (Université Rennes 2). L'objectif principal des projets AICHA et ATCHA est de combiner un modèle intégré et une approche participative pour accompagner les agriculteurs dans l'adaptation de leurs systèmes face au changement climatique. Grâce à une approche interdisciplinaire, impliquant hydrologues, géochimistes, pédologues, agronomes, géographes, économistes et sociologues et avec la participation de partenaires indiens, scientifiques et acteurs du développement agricole, ces projets visent à démontrer la pertinence des modèles intégrés pour partager les connaissances entre chercheurs et acteurs et pour co-construire et évaluer des scénarios de développement durable. Le projet « Irriga-détection » est focalisé sur l'évaluation de séries temporelles d'images satellites optiques et radar à haute résolution spatiale pour identifier et caractériser des cultures irriguées.

Les attendus de ce travail de thèse visent d'une part, à évaluer les potentialités des images de télédétection optique et radar pour l'identification et la caractérisation des cultures irriguées à une échelle spatiale fine et d'autre part, à étudier les relations entre l'évolution de l'irrigation sur le bassin versant expérimental du Beramabadi et le niveau des aquifères souterrains.

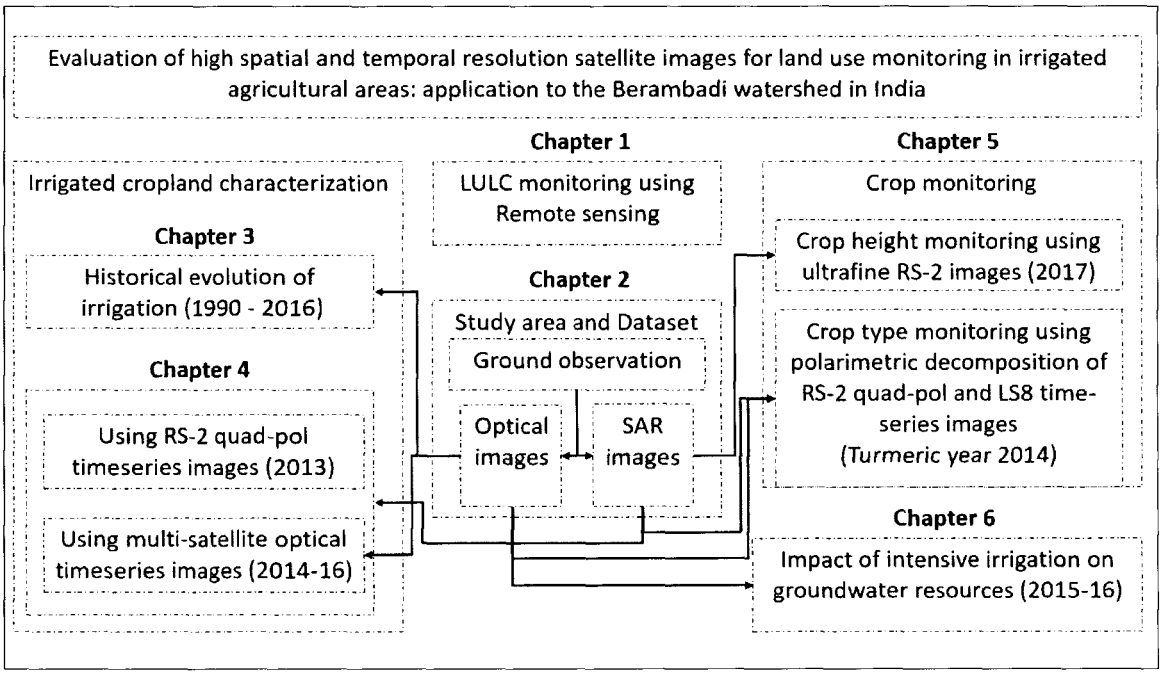

Figure 1 Organization of the thesis.

General introduction (English)

In the context of global change, the management of freshwater resources for agricultural purposes represents a major challenge for the global food security (Endo et al., 2017; Kummu et al., 2016; Salmon et al., 2015). Currently, the world's population is approximately 7.5 billion and is expected to reach 8.5 billion by 2025 (Bonilla-Moheno et al., 2013; Dash, 2012; Gun et al., 2011; Knauer et al., 2017; Taylor, 2014). To feed the world's population in the year 2012, about 324 million hectares (Mha) worldwide land was developed for irrigation, and about 275 Mha of land was originally irrigated (FAO). Nearly 20% of irrigated cropland provides 40% of global food production using 70% of the world's fresh water for irrigation purposes (Ambika et al., 2016; Salmon et al., 2015; A K Sharma et al., 2018).

The agricultural sector is the main source of employment in India, and a significant portion of the Indian population mainly depends on it for their livelihood (Ambika et al., 2016; Krishna Kumar et al., 2004; Roy et al., 2015b). However, agricultural production is strongly influenced by climatic variabilities like long-term changes in precipitation and air temperature, episodic extreme events, the economic, political and social context, etc. (Ambika et al., 2016; Krishna Kumar et al., 2004). The irregular rainfall during the monsoon season and lack of effective adaptation strategies will have directly significant impacts on crop productivity (Ambika et al., 2016; Mondal et al., 2015; Rodell et al., 2009).

In India, the agricultural parcel is characterized by a great variability of agricultural practices, several crop seasons over a calendar year are possibly associated with very heterogeneous irrigation practices (Bhavani et al., 2017; Jain et al., 2013; Mondal et al., 2014; Roy et al., 2015b; Siebert and Zhao, 2014; Wilken et al., 2017). India is characterized by very small agricultural farm size, about 94% of farmers own farms with area less than 4 ha (Ambika et al., 2016; Narayanamoorthy, 2011) with parcels size generally less than 1 ha (Robert et al., 2017b; A K Sharma et al., 2018) which increases the vulnerability of farmers to climate change. The agricultural territories in India are thus generally characterized by landscapes fragmented with small agricultural field and very strong spatiotemporal variability. Identification, monitoring and characterization of irrigated crops still represent a major scientific challenge and an important stake for an economic and a societal point of view (Bhaduri et al., 2012; Dheeravath et al., 2010; Gandhi and Namboodiri, 2009; Gumma et al., 2000; Mondal

et al., 2016; Narayanamoorthy, 2011; Robert et al., 2018; Shah, 2007; Thenkabail et al., 2009a, 2008, 2009b; Wilken et al., 2017).

Irrigation is a specific agricultural practice, which involves bringing artificially fresh water to a crop to overcome a water deficit and allow optimal plant development (Bégué et al., 2018; F. S. Nakayama, 1991; Siebert et al., 2005; Spalding and Exner, 1993). This agricultural practice, carried out from different devices (boreholes, irrigation canals, and pumps) and equipment (dispersion, drip, and gravity) offers an insurance of production and income paramount for many farmers (Biswas and Tortajada, 2009; Fishman et al., 2015; Siebert et al., 2005; Tal, 2016). The use of irrigation is dependent on many factors such as crop phenology, climate condition, availability of water resources, irrigation availability, etc. (Barik et al., 2016; Fishman, 2018; Gumma et al., 2011; Pavelic et al., 2012; Zwart et al., 2010).

From a temporal point of view, irrigation is a very punctual practice (from a few hours to several days), and from a spatial point of view, it is generally applied on a parcel scale (Kussul et al., 2016; Sitokonstantinou et al., 2018). Irrigated areas identification (spatial location) and its characterization (type of culture, phenological monitoring, etc.) by remote sensing therefore still represent major scientific challenges (Atzberger, 2013; Bargiel, 2017; Canisius et al., 2018; Liu et al., 2013; Mangiarotti et al., 2018; Palchowdhuri et al., 2018). The identification of irrigated agricultural areas and the characterization of these surfaces require a high temporal repetitiveness combined with high spatial resolution and classification methods which permits multi-temporal and multi-source information combination (Betbeder et al., 2014b; Campos-Taberner et al., 2017, 2016a; Claverie et al., 2012; Dusseux et al., 2015; El Hajj et al., 2009; Liu et al., 2014; Thomas et al., 2008; Vrieling et al., 2017; Zheng et al., 2016).

Spatial remote sensing represents a privileged observation tool for the monitoring and the characterization of crops at different spatial and temporal scales (Turner et al., 2007). Optical remote sensing, which is the most frequently used, is nevertheless very quickly confronted with observation limits linked to the presence of clouds (A K Sharma et al., 2018; Sharma et al., 2016; Thenkabail et al., 2009b; Velpuri et al., 2009). In tropical regions such as India, with significant cloud cover during the rainy seasons, many studies combine optical imaging and radar imagery, which eliminates the conditions of illumination and atmospheric conditions (Bégué et al., 2018; Corgne et al., 2016a; Qi et al., 2017). The combind use of optical and radar imaging thus allows a greater image acquisition repeatability, which represents a major challenge for the monitoring of crops characterized in particular by a strong spatial and temporal

variability linked to crop rotations, agricultural practices, social, economic and climatic factors (Betbeder et al., 2015a; Fieuzal and Baup, 2016; Sharma et al., 2016).

The main objective of this thesis is to identify and characterize irrigated areas in an intensive agricultural watershed using time-series of high spatial resolution optical and radar satellite images. The experimental Berambadi watershed which is part of the Environmental Observatory "Tropical Experimental Watersheds" (BVET) managed by the LMI CEFIRSE (Mixed International Laboratory Cell Franco-Indian Research in Water Science) of the Indian Institute of Science (IISc) Bangalore (India). In this experimental watershed, three specific objectives have been identified: the first is to take stock of the evolution of irrigated agriculture on a fine-scale over the last 30 years; The second objective is to identify and characterize irrigated crops over several crop cycles at an intra-annual scale; and The third objective is to study the impact of irrigation on the underground aquifers of the watershed.

To fulfill the thesis objectives four specific sections and research questions have been identified in the Berambadi experimental watershed.

(i) The first objective is to quantify the evolution of irrigated agriculture on a fine-scale over the last three decades.

Research question: How to quantify and evaluate the history of irrigation using remote sensing products?

(ii) The second objective is to identify and characterize irrigated crops over several cropping cycles and at an intra-annual scale.

Research question: What is the contribution of multi-sensor images from optical and SAR platforms to characterized the seasonal irrigated croplands?

(iii) The third objective is to monitor crops using optical and SAR time-series images.

Research question: What is the contribution of multiple satellite images from optical and SAR platforms to monitor crops?

(iv) The fourth objective is to study the impact of irrigation on underground aquifers in the watershed.

Research question: Is there a relation between intensive irrigation practices and groundwater resources?

The thesis is mainly divided into six chapters (Figure 1),

The first chapter presents state of the art on the identification and characterization of irrigated crops by remote sensing. The different irrigation and water management practices based on these are analyzed. The satellite and radar images used for the characterization of cultures as well as the classification methods of the images are then.

Chapter two first describes the experimental watershed and the data used, detailing the *in-situ* measurements and surveys conducted on the experimental Berambadi watershed. In a second step, this chapter deals with the management of databases collected in the field with the pretreatment of satellite products such as radiometric and geometric pretentions applied to optical and radar images.

The third chapter presents the historical evolution of irrigated crops between 1990 and 2016 over two cropping seasons (rabi and summer) using multi-temporal optical satellite imagery. The history of seasonal irrigation and dual irrigation has been generated which explains the expansion of irrigation practices in the watershed over three decades.

Chapter four focuses on identifying the classification of irrigated and non-irrigated areas in recent years (2014-2016) on the study catchment area from polarimetric and optical radar images. This chapter is divided into two parts; the first part describes the methodology for identifying irrigated croplands using time series of quad radar images of Radarsat-2. The second part uses a time series of NDVI estimated from optical images for the identification of irrigated crops.

Chapter five analyzes the potential of radar and optical images for the characterization of irrigated crops. This chapter is divided into two parts. The first part evaluates the potential of Radarsat-2 images (UltraFine mode) for estimating crop height. The second part deals with the combined use of optical indices and polarimetric variables for turmeric crop mapping.

Chapter six presents an analysis on relations between irrigation evolution and groundwater levels on the Berambadi watershed. The study was carried out at the scale of a km^2 for two cropping seasons: rabi and summer.

This thesis was carried out within the framework of three research programs: the CEFIPRA program (« AICHA » project, 2012-2016) and ANR (« ATCHA » project, 2017-2021) coordinated by L. Ruiz (INRA) and M. Sekhar (IISc), as well as the CNES-TOSCA (« Irriga-detection » project, 2017-2018) coordinated by S. Corgne (University of Rennes 2). The main objective of the AICHA and ATCHA projects is to combine an

integrated model and a participatory approach to support farmers in adapting their systems to climate change. Through an interdisciplinary approach, involving hydrologists, geochemists, soil scientists, agronomists, geographers, economists, and sociologists and with the participation of Indian partners, scientists and agricultural development actors, these projects aim to demonstrate the relevance of integrated models for sharing knowledge between researchers and the farmers to co-construct and evaluate sustainable development scenarios. The "Irriga-detection" project focuses on time series evaluation of high spatial resolution optical and radar satellite images to identify and characterize irrigated crops.

The expected results of this thesis work are on the one hand, an evaluation of remote sensing SAR and optical data for the identification and characterization of irrigated crops and on the other hand, the analysis of relations between irrigation practices and groundwater levels on the Beramabadi experimental watershed.

CHAPTER 1 : Irrigated area monitoring in India

Summary

This chapter introduces a literature review on the concepts of irrigation evolution in the Indian subcontinent and in-depth synthesis of various irrigated cropland studies. Global groundwater resources abstraction for irrigation purposes is highlighted and discussed. The "green revolution" advantage and disadvantages have been addressed in respect of farming practices in India. The various irrigation practices and cropping/climatological seasons in India are discussed. The synthesis on remote sensing technology for the earth observation studies is presented with a focus to the support from optical and SAR remote sensing satellite products.

1.1 Introduction

Earth's total stored freshwater volume is approximately 8-10 million km^3 (Margat, 2008), which is more than 2000 times of the current withdrawal (surface and groundwater combined) (Gun, 2012) but it is not spatially distributed. Hence, it is required to monitor crop water requirement and crop management practices for better understanding the impact of intensive irrigation practices to changing environmental conditions (Bégué et al., 2018; Jain et al., 2015; Ramachandiran and Pazhanivelan, 2016). Large-scale water abstraction for the various human needs is increasing tremendous pressure on global water resources (Maryam Salehi et al., 2017). Three-fourth global freshwater abstraction is used for irrigation purposes to fulfill 40 % of the total global food requirements (Maryam Salehi et al., 2017; Salmon et al., 2015). Increasing water demand for irrigation purposes is likely to increase the pressure on the river ecosystem (Agarwal et al., 2000; Maryam Salehi et al., 2017). Global demands for food, feed, and fuel of the world's growing population is increasing with unprecedented rates, and the pressure on agriculture sector is increasing (Gibbs et al., 2010). According to local challenges, sustainable agriculture practices are being

performed by the farmers globally. Global environmental changes can be a track with earth observation studies. The major global land cover conversion was noticed across the tropics from forest land to agricultural land during the period year 1980-2000 (Lambin and Meyfroidt, 2011). Land surface observation and monitoring are becoming a key indicator for a better understanding of the global change, and it plays a significant role in the ecosystem processes and climate dynamics (Goldewijk et al., 2017; Roy et al., 2015b; Thenkabail et al., 2011). Land-use change impact on the surface albedo, evapotranspiration (ET), greenhouse gases (GHGs) sources and sinks, climatic system properties, and may rise radiative forcing which further can impact on climate locally or globally (Katharine et al., 2014). According to the United Nation (UN) Food and Agriculture Organization (FAO) agricultural statistics database (FAOSTAT), the total global cropland is about 15.3 million km^2 with a global cropland harvesting of 77% per year (Stefan Siebert et al., 2010). Despite all kind of land use and land cover classification uncertainties, it is a need with the priority of historical land use reconstruction for climate dynamics modeling, and land use planning (Goldewijk et al., 2017; Thenkabail et al., 2011). According to local challenges, sustainable agriculture practices are being performed by the farmers globally. The increasing global population is required the crop production needs to be double 2050 under various water management policy scenarios (Maryam Salehi et al., 2017).

India is the largest groundwater user in the world, with one-fourth global freshwater consumption (Bhaduri et al., 2012). India becomes dominant agriculture country with about 60% of Indian land used for the crop cultivation (Roy et al., 2015b). Out of the total agricultural land, 50% is cropland, 6.8% is fallow land (category of agricultural land which is not cultivated at present), and 2.4% is a plantation. Indian land use and land cover (LULC) changes have been manifested regarding agriculture land expansion from the forested land reduction. India is one of the best examples of significant change in land use and land cover over past few decades with high variability of LULC categories (Dheeravath et al., 2010; Roy et al., 2015b, 2015a). The Directorate/Bureau of Economics and Statistics (DES/BES) was responsible in India to monitor and maintain the conventional national scale records of LULC changes (Roy et al., 2015b). Several studies were conducted to monitor Indian LULC change in

the last decade at various scales like agro-climatic zones, biogeographic regions, metrological sub-divisions, bioclimatic zones, and at watershed scales (Dheeravath et al., 2010; Roy et al., 2015b; Skakun et al., 2017; Thenkabail et al., 2009b).

Agricultural practices can be majorly divided into six categories according to the farming practices (FAO, 2016; Government of India, 2015; Roy and Shah, 2002; Wales, 2002; Wood et al., 2014):

(i) Subsistence farming: All farming practices which are performed by the farmers for their family consumption comes under subsistence farming. Mainly these farmers are with small and fragmented landholdings. They use simple and primitive cultivation techniques (Schneibel et al., 2017).

(ii) Commercial farming: Farming practices which are cultivation to sell in the market to earn money comes in this category. These farmers are using modern farming techniques like intensive irrigation, chemical fertilizers, insecticides, pesticides and high yield seeds (high yielding variety (HYV) or genetically modified seeds) (Brown et al., 2013).

(iii) Extensive farming: The production (crop yield) of crop per unit land is separating the intensive and extensive cropping practices. Extensive farming is mainly performing by USA, Canada, and Europe. These farming practices are utilizing a large patch of land for the cultivation, and the total production can be high, but per unit yield usually less (Knauer et al., 2017).

(iv) Intensive farming: These farming practices are focused on maximum production per unit of land. Due to the limited farming land availability, some parts of the world (like in Japan and Kerala) perform intensive farming practices (Shah et al., 2006).

(v) Plantation farming: Tea, coffee, rubber, banana, and spices (like cardamom, cinnamon, black pepper, etc.) are examples of plantation crops. These cropping practices are purely for sale in the nation or international market.

(vi) Mixed farming: Farmers with mixed crop cultivation are economically better than others as they perform both raising crops and rearing animals (for livestock) simultaneously (Biazin and Sterk, 2013).

Irrigation practices and its emergence

The irrigation is an artificial application of controlled water supply to grow crops and to maintain landscapes as per crop/land-water requirement (Dheeravath et al., 2010; Ozdogan and Gutman, 2008; Rodda and Ubertini, 2004). In around 4500 BC, irrigation was used in the alluvial plans of Indus valley civilization as a mean of water manipulation (Rodda and Ubertini, 2004). In the Indus valley, civilization, sophisticated irrigation, and water storage systems like reservoirs and canal were constructed in around 2600 BCE (Rodda and Ubertini, 2004). In the present era, there are several modes of irrigation used by the farmers like surface irrigation, micro-irrigation (ex. drip irrigation), sprinkler irrigation (ex. center pivot irrigation, lateral move irrigation, lawn sprinkler irrigation, and hose-end sprinkler irrigation) and sub-irrigation techniques. The irrigated areas can be majorly divided into two categories, fully irrigated areas and partial irrigated areas, irrespective to the surface and groundwater deliveries. The agricultural land comes using 60 percent or more water supply to cultivate crops during the entire crop life span known as fully irrigated croplands. The partial irrigated areas or supplementary irrigated areas receives artificial water supply between 30 to 60 percentage during the crop life span.

The main sources of irrigation are borewells, tanks, canals, perennial canal, multipurpose river valley, etc. (Dhiman, 2012a). Agriculture is the largest water-use sector, with 70% water withdrawn from the surface and groundwater resources (Shiklomanov, 2000; Siebert et al., 2005). Groundwater is the world's largest freshwater resource, and it is critically important for agriculture and global food security (Aeschbach-hertig and Gleeson, 2012; Famiglietti, 2014; S Siebert et al., 2010). In the year 1973, the total area equipped for the irrigation was 196.1 million ha, which has increased to 325.1 million ha in the year 2013 (FAO 2016). Food security needs to produce more crops, then the requirement to feed the growing population (Beddington et al., 2012; Jin et al., 2018; Kumar et al., 2012). The world population has increased threefold after the year 1950, and the total global agricultural land has increased by approximately 50% (Goldewijk et al., 2017). The fast-growing population

pressure on food security brought new techniques to grow intensive cropping. This new technique includes various crop management and water management practices with the intensive use of different inorganic and organic fertilizers (Khan and Hanjra, 2009; Liang et al., 2016; Spalding and Exner, 1993).

The intensive irrigation regions in the world are North India (Ganges and Indus river basins), Pakistan (Indus river basin), China (Hai He, Huang He, and Yangtze river basins), California (Mississippi-Missouri river basin), Egypt and Sudan (Nile river basin) (Biswas and Tortajada, 2009; Llamas and Martínez-Santos, 2005; Siebert, 2005). Global groundwater overexploitation was driven by population growth, industrial requirement, economic development, agricultural activities for food security, etc. (Bank, 2010; Gun, 2012; Peck, 2007; Wada et al., 2010). In the year 2013, approximately 38.4% of the total area equipped for irrigation was facilitated by groundwater irrigation (FAO 2016). A large amount of freshwater is fulfilling the crop water requirement for irrigation purposes but, another side it is causing water scarcity in around the world (Melton et al., 2012; Sekhar M et al., 2011; Shah et al., 2009; Shiklomanov, 2000). This overexploitation causes the groundwater depletion in the large groundwater systems in both semi-arid and humid regions of the world (Sekhar et al., 2016; Singh and Singh, 2002; Wada et al., 2010). Irrigation is required in the arid regions for the crop production, but in the semi-arid and humid regions, irrigation is for increasing crop yields (Atzberger, 2013; Jain et al., 2016; Salmon et al., 2015).

Farmers in India were encouraged with various revolutions in the past like the "green revolution" (improved crop yield, water for irrigation, fertilizer application, etc.), the "white revolution" (increasing quantity and quality of the milk), the "blue revolution" (motivating pisciculture), the "yellow revolution" (oil seeds crops) and the "pink revolution" (livestock for meat production) (Feola et al., 2015; Gumma et al., 2016; Robert et al., 2018; Roy et al., 2007; Thenkabail, 2010; Wales, 2002). Still, farmers are facing a couple of challenges (Wales, 2002) like:

(i) Crop production: the growing trend of population and stability in food production is continuously increasing gap between demand and production. The increasing gap is becoming a challenge for agricultural

scientists, planners, and policymakers (Battude et al., 2017; Jain et al., 2016; Salmon et al., 2015).

(ii) High investment: Good quality seeds (HYV (high yield variety)), fertilizers, insecticides, pesticides, farm labor, irrigation systems, machinery, etc. are a basic need for sustainable growth and high crop yield. Unfortunately, these inputs are out of reach to a small and marginal landholding farmer due to their economic conditions (Kumar et al., 2012; Roy and Shah, 2002).

(iii) Soil contamination and exhaustion: Chemical fertilizers, pesticides, and insecticides are assisting farmers in increasing crop yield. These inputs are also polluting soil, freshwater resources, and crop products. Soil exhaustion is happening by cultivating the same crop multiple time as soil loses its nutrients (Assadian et al., 1998).

(iv) Freshwater for irrigation: Intensive irrigation using surface water and groundwater may help to feed huge population of the world, but it impacts drastically on the available freshwater resources. After the green revolution, the several irrigation techniques were implemented by the farmers and resultant the surface water is getting disappear, and groundwater is depleting day by day (Fishman et al., 2015; Llamas and Martínez-Santos, 2005).

(v) Climatic undulation: Global climatic change is impacting directly on food security. Undulating in rainy days, unpredictable rainfall intensity, increasing atmospheric temperature, increasing sea level, and increasing intense cyclones are results of changing climate conditions. These climate changes are adversely affecting crop production around the world (Lipper et al., 2018; Mall et al., 2006).

(vi) Globalization: With the growing world's population, the urbanization is increasing, and agricultural land is squeezing. These symptoms of globalization are adversely impacting on the agriculture sector. The main factor of the globalization is climatic change, freshwater unavailability for irrigation and reducing profits from the crop production (Lambin and Meyfroidt, 2011).

(vii) Mechanization: Agriculture crop production is directly dependent on mechanization. Sufficient power supply for sustainable agricultural practices with an application of new environment-friendly farming techniques enables farmers to produce crops efficiently using less power (FAO, 2006).

(viii) Agricultural marketing: It is required the proper handling, planning, organizing, and directing of agricultural products to satisfy farmer, producer, and the consumer. Storage, warehousing, and cold store are required to hold and preserve goods from the production until consumption. Huge quantity of agricultural products around the world is getting waste due to mismanagement of agricultural marketing. Planning production (growing and harvesting), packing and packaging, transport, storage, agro- and food processing, distribution, advertising, and the sale can mutually use to secure agriculture marketing (Alex, Duncan; Stephen, 1993; Robert et al., 2018).

1.2 Green revolution and irrigation evolution in India

Agricultural revolutions in India were aimed for technology transfer to improve and increase crop productivity. The green revolution is the fifth agricultural revolution in the world. The green revolution is aimed to adopt new technologies and methods of crop cultivation includes mechanization. The development of high-yield varieties of cereal grains, expansion of the irrigation infrastructure, distribution of hybridized seeds, modernization farming management techniques, synthetic fertilizers and pesticides to the farmers were main approaches of the Green revolution (Pellegrini and Fernández, 2018; Thenkabail, 2010). It includes high-yield varieties (HYVs) of cereals like a draft, wheat, and rice production with chemical fertilizers, agro-chemicals, and with controlled water-supply or irrigation practices. Indian agricultural sector after the green revolution has expended with a variety of irrigation modes, fertilizers, and high yield crop varieties (Ambika et al., 2016). The Ford Foundation and the Rockefeller Foundation were wholly involved in the green

revolution. During 1961 India Green revolution brought remarkable changes in the Indian agricultural sector after the 1970's and groundwater became the backbone of the green revolution in India (Narayanamoorthy, 2011; Roy et al., 2007).

Figure 2 shows that between the year 1940 to 1980, the United States of America (USA) was the world leader for groundwater abstraction and then after India overtake the USA (Margat and Gun, 2013). India has noticed a sudden jump in the total groundwater abstraction between 1960 and 1970, and this was the time when the "Green Revolution" became matured in India. After the year 1980, India leads in the World for groundwater abstraction, and in the year 2010, the total groundwater abstraction of India was 251 km³ (Margat and Gun, 2013). The Government of India provided free electricity to farmers in many states to promote the green revolution (Barik et al., 2016; Shah et al., 2009).

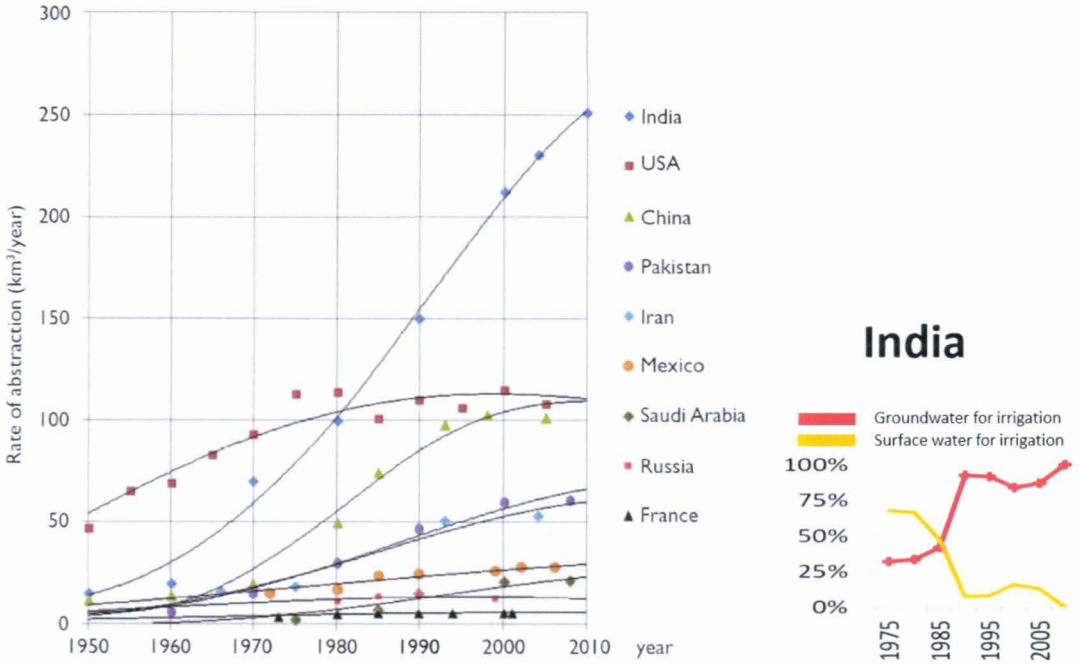

Figure 2 Groundwater abstraction trends in the selected countries.
Source: (Margat and Gun, 2013) *and Karnataka annual season crop report, Doddaballapur taluk (2015).*

After the green revolution (the 1970s) in India, the surface water used for irrigation has decreased, and groundwater usage was increased, as shown in figure 2 (Govt. of

Karnataka, 2015). And between the year 1980 and 1990, the vast change is noticed with majority replaced of surface water irrigation to the groundwater irrigation (Figure 2).

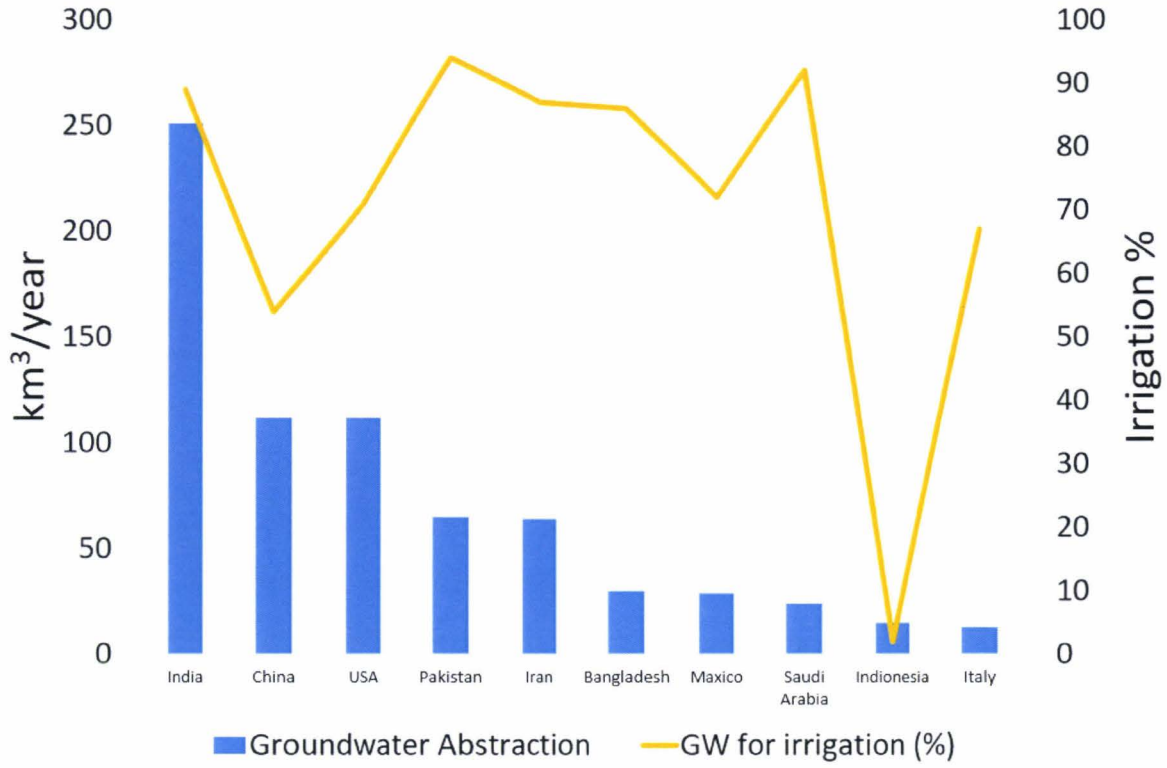

Figure 3 The top 10 groundwater abstraction countries and their usage for irrigation purposes (year 2010).
Source: (Margat and Gun, 2013).

In the year 2010, maximum groundwater abstraction in the World and its use for the irrigation is noticed in India, as shown in figure 3 (Margat and Gun, 2013). About 89% of the total pumped groundwater in India is used for irrigation purposes in the year 2010 (Margat and Gun, 2013). The impact of enormous groundwater pumping for various purposes disconnected the river baseflow and many places in India the surface flow got disappeared (Bhanja et al., 2019; Taylor, 2014). Total Indian river catchment is about 252.8 million ha (Mha), and out of the total, about 186,900 ha is having of surface water resources (FAO). In India, 47.7% of the total agricultural cropland were reliably irrigated in the year 2013-14 (S Siebert et al., 2010). Indian rivers are originating from four main mountain ranges, known as Himalaya and Karakoram ranges, Aravali range, Sahyadri or the Western Ghats, Vindhya and Satpura ranges.

Indian irrigation practices can be broadly divided into two categories:

- groundwater irrigation
- surface water irrigation.

The total irrigated cropland using groundwater and surface water were respectively 63.7% and 36.3%. The groundwater irrigation is mainly using open wells and borewells. Surface water irrigation uses canals water, tank/reservoir water, etc. The Indira Gandhi canal is the longest irrigation canal in India, the length of this canal is about 650 km. This canal assists farmers of north-west India to perform irrigation activity and supplies drinking water to the various villages.

Crop and water management practices are varying with the regional and local weather condition and farmers economic situation (Biswas and Tortajada, 2009; Roy and Shah, 2002; Shah, 2007). Surface or flood irrigation is suitable for the cropland with a slope less than 8% (Llamas and Martínez-Santos, 2005; Shahriar Pervez et al., 2014) and land with a slope greater than 20% are not suitable for the agriculture purposes (Ambika et al., 2016). Due to financial support and subsidize schemes from the government of India in present years, farmers were motivated to use drip irrigation for all possible irrigated crops like turmeric, ginger, banana, sugarcane, etc. This initiative reduces the evaporation of the water concerning the traditional method of surface irrigation. As shown in figure 4, there are three main modes of irrigation practices used by the farmers in India:

(i) drip irrigation,
(ii) sprinkler irrigation, and
(iii) surface or flood irrigation.

Drip Irrigation | Sprinkler Irrigation | Surface Irrigation

Figure 4 *Irrigation practices in India.*

The Directorate of Economics and Statistics (DES) of Government of India accounts for the 162 major and 221 medium irrigation projects (Thenkabail et al., 2009b). As per DES, irrigation by groundwater, a small reservoir, and tank are part of minor irrigation. However, it is noticed in the present scenario that the minor irrigation occupies more area than the major irrigated land, with about 200 km^3 water per year (Gumma et al., 2011). As per Ministry of Water Resources (MoWR), the total irrigated cropland area for the year 2001-02 was 84 Mha (Dheeravath et al., 2010; Dhiman, 2012b; Thenkabail et al., 2009b). Out of the total irrigated area, 52 Mha belongs to the minor irrigation (11 Mha is groundwater & tanks, and 9Mha is small reservoirs irrigated cropland), and 31 Mha are significant irrigated land (MoWR). According to DES the net irrigated area has been increased by approximately 30Mha between the year 1950 and year 2002 (Ambika et al., 2016; Gumma et al., 2011; Thenkabail et al., 2005). In the year 2000-01, approximately 18.5 million groundwater units were existing which includes, 9.62 million dug wells, 8.35 million shallow tube wells, and 5.3 million deep tube wells (Gandhi and Namboodiri, 2009). The main crops in India can be divided into four main categories: foodgrains (Rice, Wheat, Maize, Pulses, and millets); cash crops (Cotton, Jute, Sugarcane, Tobacco, and oilseeds); plantation crops (Tea, Coffee, Coconut and Rubber) and horticulture crops (Fruits and vegetables).

In India, the cropping seasons are categorized according to the National Food Security Mission (https://nfsm.gov.in/nfmis/rpt/calenderreport.aspx). As shown in figure 5, there are three major cropping seasons in India known as kharif (spring or monsoon) cropping season, rabi (autumn or post-monsoon) cropping season and the summer (some places known as zaid) cropping season (E. D. Spratt, 1978; Thenkabail et al., 2008). The cropping season duration differs in various part of India depends on regional weather condition (Ambika et al., 2016; Douglas et al., 2009; Paul et al., 2016; Vittal et al., 2016).

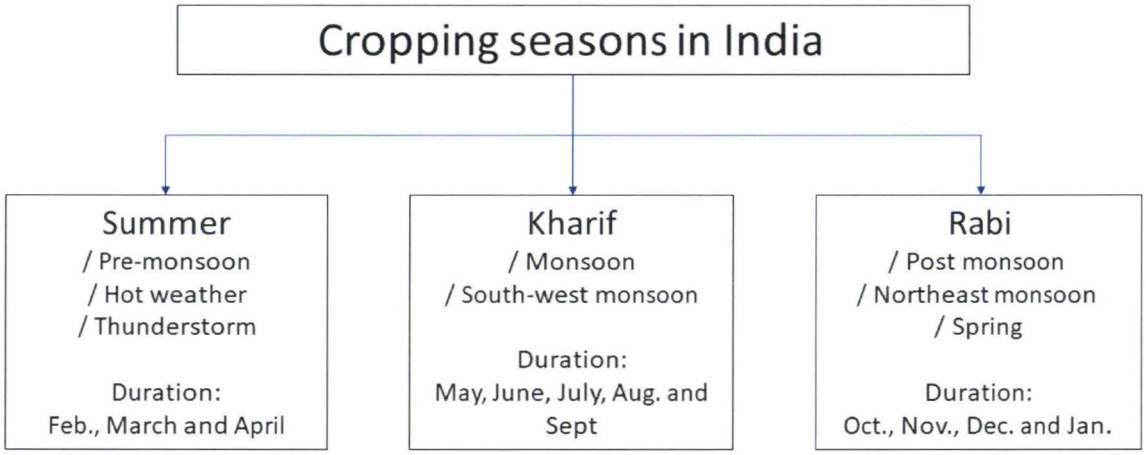

Figure 5 *Cropping seasons in India.*

The kharif cropping season is from month June till September with high variety of crops like Rice, Cotton, Maize, Rice (Paddy), Sorghum, Groundnut, Pearl millet / Bajra, Pulses (Arhar / Tur), Soya bean, Cotton, Finger millet (Ragi), Turmeric, Sugarcane, Bitter gourd, Green gram, Sesame, Black gram, Cowpea (chavala), etc.

Rabi cropping season is also having a high variety of crop types like Cereals (Rice, Wheat, Oat, Barley, Maize), Seeds (Mustard, Alfalfa, Cumin, Coriander, Fenugreek, Isabgol, Groundnut, linseed), Vegetables (Carrot, Chickpea/Gram, Onion, Tomato, Potato) and Banana, Sugarcane, etc. (E. D. Spratt, 1978; Government of India, 2015; Heller et al., 2012).

Summer cropping season mainly focused on vegetable and the fruits with only irrigation facilitated farmlands. However, Sugarcane and banana are annual crops with twelve-month crop growth duration. Mainly three types of cropping practices are under the practice in India, as per the weather and farmers economic condition. These three farming practices are fully irrigated cropping, partial irrigation, and non-irrigation (Bégué et al., 2018; Jain et al., 2013).

The Indian weather condition has a vast heterogeneity with various geographic scales and topography. Based on the native vegetation, temperature, precipitation, and their seasonality in India, the Koppen-Geiger climate classification system can be subdivided into six major climatic subtypes. These major climatic are ranging from

the arid desert in the western region, glaciers and alpine tundras in the northern region, and the humid tropical regions with rainforests in the southwest region and in the Lakshadweep islands (https://en.wikipedia.org/wiki/Climate_of_India). Furthermore the twelve broad Koppen climate classes of India are tropical rainforest, tropical monsoon, tropical savanna (wet and dry), cold desert, hot semi-arid, cold semi-arid, Mediterranean dry (hot summer), subtropical humid (summer, dry winter), subtropical highland (dry winter), subtropical humid (summer, no dry), continental hot summer, continental warm summer, continental dry winter, continental subarctic (dry winter). Indian Meteorological Department (IMD) categorized four climatological seasons known as winter season also known as cold weather season (January and February), summer season is also known as pre-monsoon or hot weather season (March to May), summer monsoon season or south-west monsoon season (June to September), and post-monsoon season or north-east monsoon season (October to December) in India (Jha and Bharti, n.d.) (Figure 6).

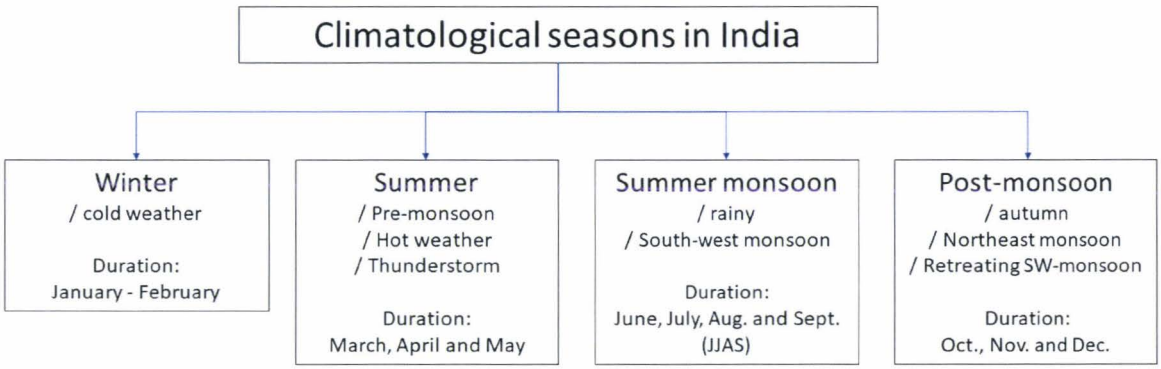

Figure 6 *Climatological seasons in India.*

1.3 Remote sensing application for irrigated cropland monitoring

Remote sensing is the science and art of obtaining the information about an object, area, or phenomenon through the analysis of data acquired by a device that is not in contact with the object, area, or phenomenon under investigation (Lillesand and

Kiefer et al., 1987). The remote sensing system characteristics include the energy source, atmosphere, energy-matter interactions at the earth surface, sensor, and data processing unit with transmission for multiple data users. An ideal remote sensing system includes a uniform energy source, a non-interfering atmosphere, a series of unique energy-matter interactions at the earth surface, a super sensor (sensitive to all wavelengths), and a real-time data processing system with transmission facility to the multiple data users.

Remote sensing is the best available solution to monitor earth surface with high spatiotemporal resolution (Dominique et al., 2016; Esch et al., 2018; Li et al., 2017; Nayak et al., 2010). Satellite remote sensing and areal remote sensing are mainly used by the researchers to monitor land use and land cover practices. Monitoring earth surface at spatial and temporal scales is a required input to bridge various disciplines like ecology, geography, sociology, economics, mathematics, geology, physics, urban studies, etc. (Fletcher et al., 2018; Turner et al., 2007). Remote sensing uses light, which is an electromagnetic wave vector. Broadly the electromagnetic (EM) wavelength (Figure 7) for the earth observation can be divided into three parts known as optical (visible-NIR), thermal IR, and microwave (Gitelson et al., 2002; Lee and Pottier, 2009; Pettry and Powell, 1975; Tucker, 1979; USGS and U.S. Geological Survery, 2016). The earth observation studies are using high spatial and temporal resolution bandwidths of visible-NIR spectrum (Chandrasekar et al., 2010; Liu et al., 2016; Roy et al., 2016; Thenkabail et al., 2005) and microwave spectrum (Chen et al., 2016; Idol et al., 2016; Kenduiywo et al., 2017; Liesenberg and Gloaguen, 2012; Xie et al., 2017) were mainly used by the researchers.

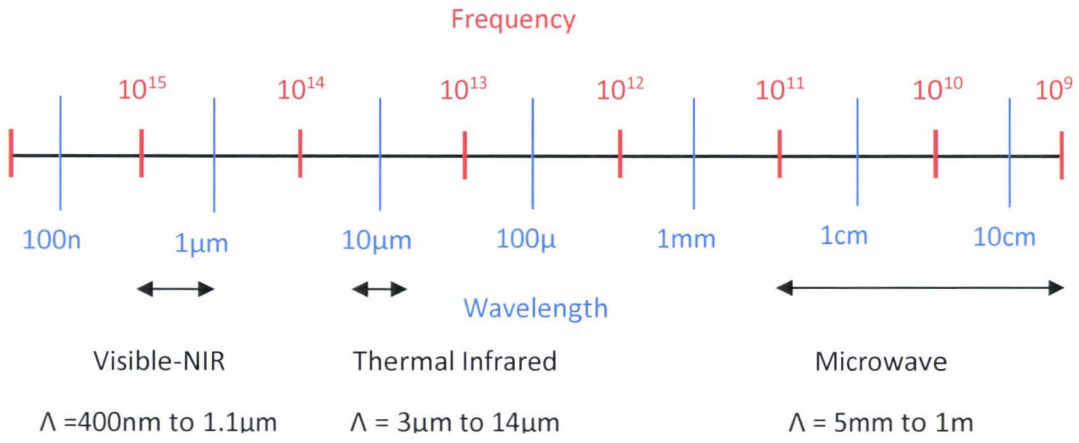

Figure 7 Electromagnetic spectrum, here Λ represents to the wavelength.

Monitoring earth surface at spatial and temporal scales is a required input to bridge various disciplines like ecology, geography, sociology, economics, mathematics, geology, physics, urban studies, etc. (Fletcher et al., 2018; Turner et al., 2007). Inputs from the remote sensing play a key role in tackling global issues like food security, climate change, weather forecasting, and better resource management at different spatial and temporal scales. Remote sensing potentials for the earth observation are:

(i) capability to provide temporal information of various land-use practices and land cover features at the regional and global scale;

(ii) assistance to monitor crop, and soil temporal characteristics to provide decision support for precision farming at watershed or basin scales;

(iii) estimation of the greenhouse gases (GHG) emissions like net CO_2, etc.;

(iv) estimation of the rainfall, evapotranspiration (ET), and other climatic variables.

Numerous challenges can be noticed to monitor agricultural croplands with remote sensing data in India. The three main challenges were noticed to monitor agricultural croplands from space were:

(i) the small size of the crop fields (Jain et al., 2013; Mangiarotti et al., 2018; White and Roy, 2015). Farmers use to divide their farmlands into small-small parcels as per their water and crop management resources.

Monitoring small size crop field is one of the main challenges for precise land use, and land cover classification, the majority of crop fields or parcels are inferior to 1 ha. High spatial-temporal resolution remote sensed images with ground observation could be used for machine learning algorithms for cropland monitoring.

(ii) cloud cover during the main two cropping seasons is the most significant obstruction for optical remote sensing (Gao et al., 2018; Hosseini and McNairn, 2017; Khandelwal et al., 2017; Minh et al., 2017). This gap can be filled either by using multiple optical satellites (Kussul et al., 2016) or with combination of radar and optical images (Betbeder et al., 2016b; Hong et al., 2014; Shao and Zhang, 2016) or by using only radar images (Niu et al., 2016).

(iii) parcel scale ground observation during the entire cropping season is required to understand the farming practices (Wood et al., 2014) and farmers' strategy (Chalise and Naranpanawa, 2016; Shah et al., 2006; Singh et al., 2011). A portion of this precise ground observation can further feed to the machine learning or deep learning algorithms for accurate land use classification (Chen et al., 2018; Maggiori et al., 2017; Palchowdhuri et al., 2018). The results can be further validated using the remaining ground observation information by estimating user accuracy, producer accuracy, overall classification accuracy, and kappa coefficient (Cheema and Bastiaanssen, 2010).

1.3.1 Optical remote sensing

Optical remote sensing is delivering its service non-stop from the 1970s and upgrading the technology and methods dramatically with a wide range of imaging scales with a potential interest and importance of the researchers, land managers and planners (Rogan and Chen, 2004). The spatial resolution is now available from sub-centimeter to 1 km with a daily revisit capability. In the present era, most utilized optical satellites for land use and land cover monitoring are Landsat-8, Sentinel-2, SPOT-5,6, Pleiades, and Worldview-2. A considerable number of coarse-resolution satellites images also

available free of cost for the national or world land use and land cover (LULC) research purposes (Houghton and Nassikas, 2017; Salmon et al., 2015; Szogs et al., 2017). LULC monitoring at watershed scale or catchment scale research purposes can procure free high-resolution satellite images (Bégué et al., 2018; Campos-Taberner et al., 2016b; Hazaymeh and K. Hassan, 2016; Jawak et al., 2015; Lobell and Asner, 2003; Navarro et al., 2016). Some other missions with high spatial resolution datasets also used for the LULC monitoring studies like spot 6,7 and IRS-P6 (Gumma et al., 2014; Pandya et al., 2012; Stibig et al., 2007).

1.3.1.1 Basics of optical remote sensing

Remote sensing systems used for image acquisition are mainly characterized by the wavelength or range of wavelength. The remote sensing data acquisition process is comprised of mainly five elements namely: energy source, propagation through the atmosphere, energy interactions with the earth's surface features, airborne or space-borne sensor to record the reflected energy, and generation of digital data or images using sensor data. In the optical remote sensing systems are recording reflected energy generated by the natural resource from the earth surface objects limited to the visible, near-infrared and mid-infrared wavelength ranges. The primary wavelength ranges send for the earth observation in the optical section range was between 0.4µm to 12µm.

Basic diagram of the satellite remote sensing process for earth surface observation is shown in figure 8. The emitted natural energy from the sun is traveling through the atmosphere and interacting with the earth surface objects. After interacting with earth surface objects like natural or anthropogenic the reflected waves in the form of energy is recording by the spaceborne or airborne sensors. The reflected energy from various earth surface objects depends on the absorption, reflection, refraction, and transmission property of the object.

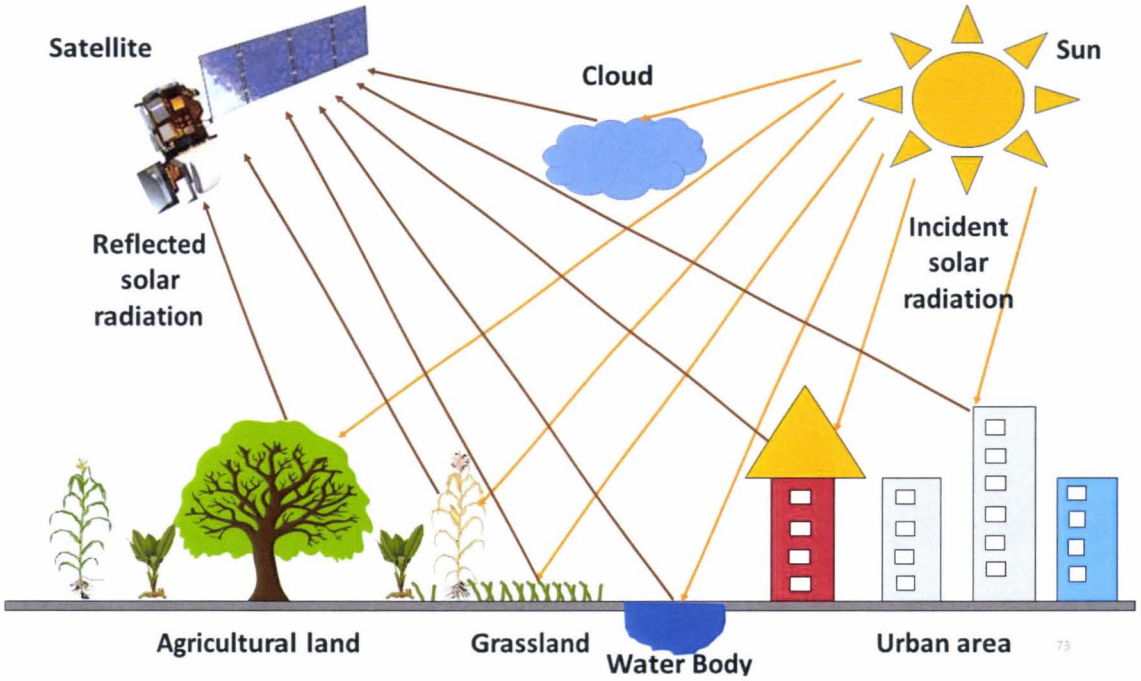

Figure 8 Earth surface monitoring using optical remote sensing.

Four fundamental energy interactions are occurring during the electromagnetic wave interacting with earth surface feature. These four fractions of incident electromagnetic energy (E_I) are reflected energy (E_R), absorbed energy (E_A), refracted energy (E_r), and/or transmitted energy (E_T). As per the principle of conservation of energy, we can state the basic interrelation between these four energy fractions as presented in equation 1 (Lillesand et al., 2015).

$$E_I(\lambda) = E_R(\lambda) + E_A(\lambda) + E_r(\lambda) + E_T(\lambda) \qquad \text{Equation 1}$$

Where all energy fractions being a function of wavelength λ.

The spectral reflectance (ρ_λ) of an earth surface object received by remote sensing sensor is equal to the ratio of energy reflected from the object and incident energy to the object. The total spectral reflectance in percentage is presented in equation 2.

$$\rho_\lambda = \frac{E_R(\lambda)}{E_I(\lambda)} \times 100 \qquad \text{Equation 2}$$

Spectral reflectance graph of an earth surface object as a function of wavelength is known as the spectral reflectance curve. The spectral reflectance curve gives through information about the spectral properties of an object. Spectral reflectance curve also

plays an important role in the selection of specific wavelength to the corresponding earth surface object.

Figure 9 presents the reflectance curves for three land surface features : water, green vegetation, and bare soil. This reflectance curve was created using various spectral band images of the Landsat satellite image covering visible, near-infrared and mid-infrared spectral regions. It is seen in figure 9 that the water reflects about 13% or less in the blue-green ranges, and a smaller reflection can be noticed in the red region. In the near-infrared and mid-infrared regions, no reflectance (or 100% absorption) of the water can be noticed. High reflectance of dry soil in the mid-infrared region and less reflectance of green vegetation comparatively represents that the mid-infrared in owing to moisture content. Green vegetation reflectance curve shows considerably more constant with high reflectance in the near-infrared region (from 0.7µm to 1.3µm). This near-infrared region wavelength is dominated by the plant cell structure, while the visible range is highly sensitive to the plant pigment (Richards and Jia, 2006).

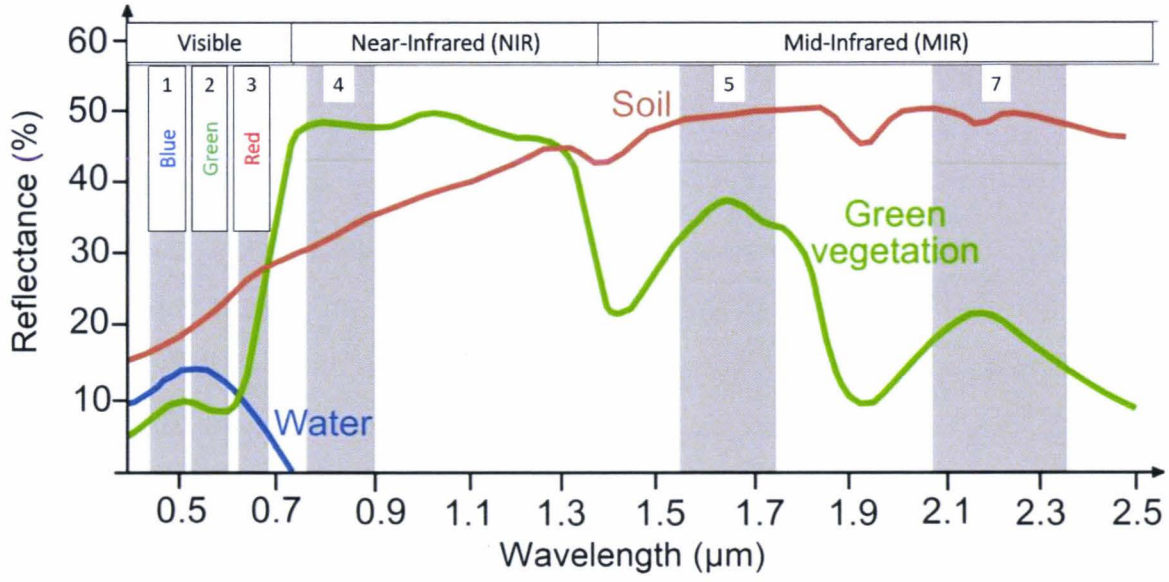

Figure 9 Spectral reflectance curve for the water, soil, and green vegetation using different bands of Landsat satellite.
Source: (Richards and Jia, 2006; Zarcheshm, 2018)

1.3.1.2 Optical image pre-processing

Image pre-processing referred to the image restoration and rectification to correct sensor's/platform's radiometric and geometric distortions. The main cause of these errors is image geometry, atmospheric conditions, sensor's noise/response and variations in the optical satellite images illumination images (Huete et al., 1994; Thenkabail et al., 2011; Turner et al., 1999). The image pre-processing includes atmospheric/ radiometric correction-optical and geometric correction. All kind of distortions is varying with the image, sensor, satellite, and image acquisition condition. The radiometric distortions can be mainly divided into two categories: sensor related and others. Sensor related radiometric distortion causes due to three errors: a detector to detector photo response non-uniformity (PRNU), detector failure or degradation and defocusing or motion blur. The other radiometric distortions include stagger effect, atmospheric effects, noise due to electronic circuits or photon noise, transmission losses and data compression or decompression (Kuan et al., 1985). The image radiometric distortions can be correct adaptive photon noise removal, dynamic range adjustment (DRA) enhancement, de-convolution approaches, image degradation and restoration (Krishna-ISRO, 2018). The surface reflectance and atmospheric correction can be performed using atmospheric corrections as the Second Simulation of a Satellite Signal in the Solar Spectrum (6S) radiative transfer model (U.S. Geological Survery, 2016; Vermote et al., 1997). Landsat Ecosystem Disturbance Adaptive Processing System (LEDAPS) is also a highly standardized and stable automatic surface reflectance modeler, which can ensure comparability of reflectance from sensors of Landsat satellites (Dutrieux et al., 2016; Jeffrey G. Masek et al., 2006; U.S. Geological Survery, 2016; Zhu, 2017). Due to the cloud cover and sensor malfunctioning, the temporal resolution cannot maintain the same (Dutrieux et al., 2016). Several atmospheric radiative transfer models are available to perform correction of the propagation of radiation through a medium which is affected by the absorption, emission and scattering processes. The widely used atmospheric radiative transfer models are 6S (Second Simulation of a Satellite Signal in the Solar Spectrum), MODTRAN (MODerate resolution atmospheric TRANsmission) and DART (Discrete

anisotropic radiative transfer) (Huete et al., 1992; Rosas et al., 2017; Vermote et al., 1997).

The raw spectral bands may have increased uncertainties, inherited from the surface reflectance source data, and in the area of atmospheric correction is affected by the adverse climatic conditions, includes:

i. Hyper-arid or snow cover regions,
ii. Low sun angle conditions,
iii. Coastal regions with land area smaller size relative to the adjacent water.
iv. Area with extensive cloud contaminations.

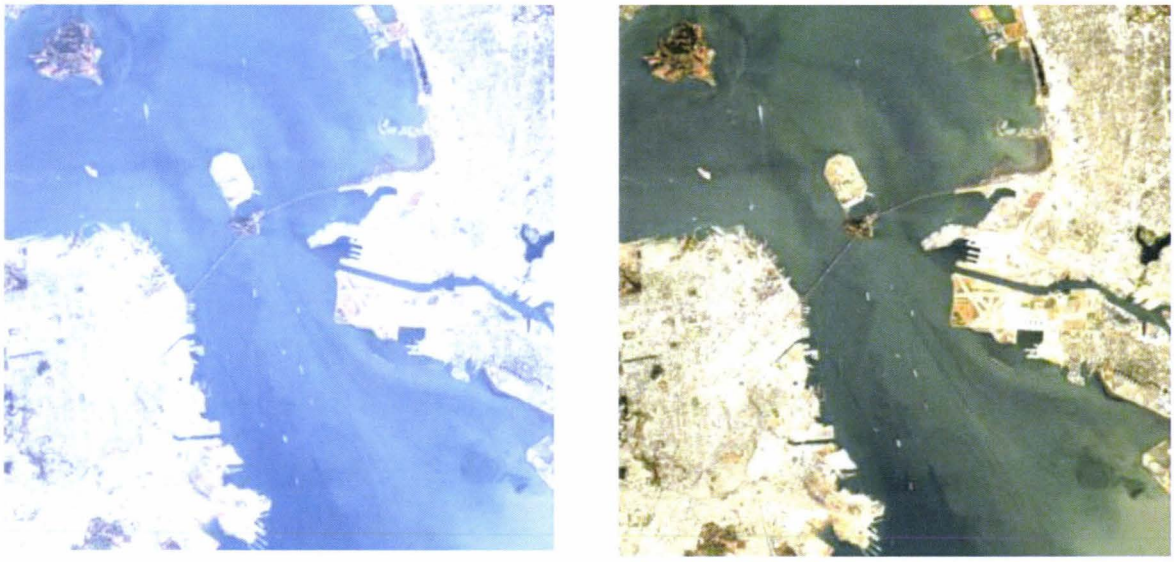

Figure 10 The color composites of Landsat reflectance bands (Red, Green, Blue) after LEDAPS atmospheric correction implementation on the top of the atmosphere (left) and surface reflectance (right).
Source: (USGS and U.S. Geological Survery, 2016), *date: 07th July 1999.*

The water vapor, ozone, geopotential height, aerosol optical thickness, and the digital elevation are input with Landsat data to Second Simulation of a Satellite Signal in the Solar Spectrum (6S) radiative transfer models. The 6S models generated Top of Atmosphere (TOA) Reflectance, Surface Reflectance, Brightness Temperature, and masks for clouds, cloud shadows, adjacent clouds, land, and water. Figure 10 and 11 are the example of implementation of LEDAPS atmospheric correction model and 6S radiative transfer models to generated top of atmosphere and surface reflectance composites.

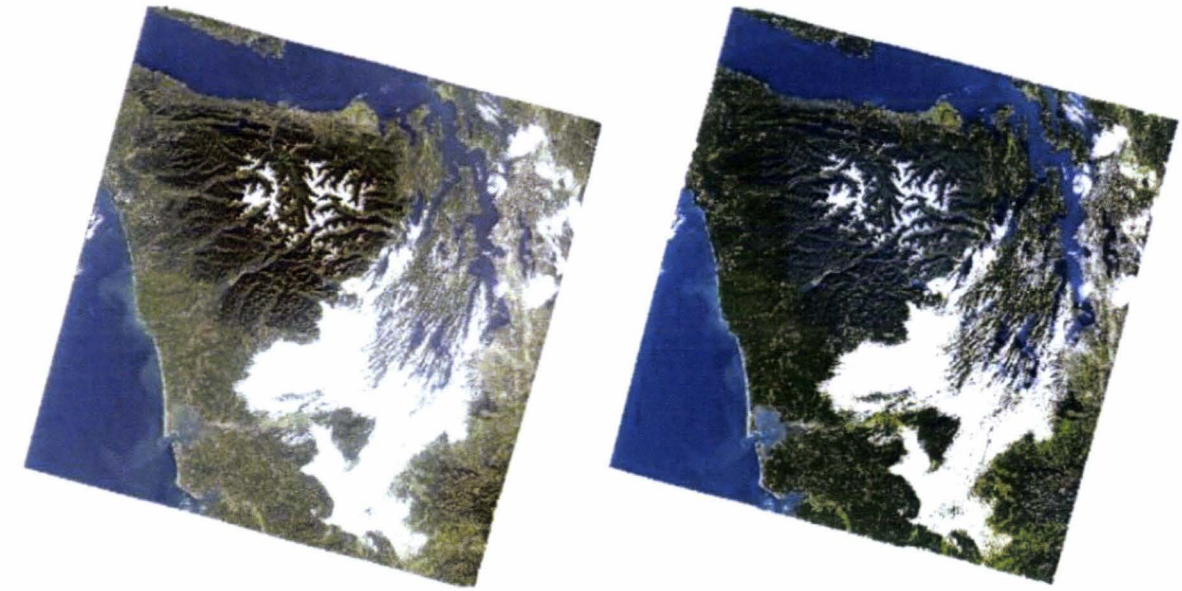

Figure 11 The atmospheric corrections of Top of Atmosphere (left) and surface reflectance (right) color composites of Landsat-8 reflectance bands (Red, Green, Blue). *Source:* (USGS and U.S. Geological Survery, 2016), *date: 14th Oct 2013.*

Geometric distortions are causing due to four main causes: scene, sensor, platform, map projection, and datum transformation. The geometric corrections can be performed by image transformation (systematic or ground control point-based) and by resampling methods (nearest neighbor, bilinear or bicubic). The scene related to geometric distortion is causing due to earth rotation, earth curvature, and terrain effects. The sensor-related geometric distortion is causing due to scan non-linearities, non-uniform sampling rate, panoramic view due to tilt, and sensor mounting angles (and alignments). The raw satellite images need to pre-process before using them for land use and land cover image classification (Thenkabail et al., 2011; Zhu, 2017).

1.3.1.3 Evaluation of optical data for irrigated areas monitoring

Irrigated area monitoring using optical remote sensing was done by several studies using advanced tools (Velpuri et al., 2009). High spatial resolution and coarse spatial resolution satellite datasets such as NASA, Indian Remote Sensing Linear Imaging self Scanning Sensor, and European Space Agency missions for the irrigated area monitoring studies (Gumma et al., 2014; Saadi et al., 2015; Thenkabail et al., 2009b). The total global annual irrigated area (AIA) and area available for irrigation (TAAI) was estimated by the (Thenkabail et al., 2008) using multi-satellite time-series NDVI

datasets and auxillary secondary data inculeds ground observations. The time-series multi-satellite were estimated using six combinations of various sensors: Advanced Very High Resolution Radiometer (AVHRR) 3-band and Normalized Difference Vegetation Index (NDVI) 10-km monthly time-series for the year 1997- 1999, Système pour l'Observation de la Terre Vegetation (SPOT-VGT) NDVI 1-km monthly time series for the year 1999, East Anglia University Climate Research Unit (CRU) rainfall data at 50-km gridded monthly time series for the year 1961-2000, Global 30 Arc-Second Elevation Data Set (GTOPO30) 1-km digital elevation data of the world, Japanese Earth Resources Satellite-1 Synthetic Aperture Radar (JERS-1 SAR) data for the rain forests during two cropping seasons for the year 1996, and University of Maryland Global Tree Cover 1-km data for the year 1992-93. A 159 layers single mega-file data-cube (MFDC) of the world was composed by re-sampling different data types into a common 1-kilometer spatial resolution. The MFDC was segmented based on the elevation, temperature, and precipitation zones followed with image classification. The quantitative spectral matching techniques (SMT) method was adopted to group class spectra derived from unsupervised classification and match the same with ideal or target spectra. Resultant, the annual irrigated area and area available for irrigation were estimated.

For the last millennium total global AIA estimated was 467 Mha (million hectares) and the TAAI was 399 Mha (Thenkabail et al., 2008). The irrigated area distribution for various continents and countries were highly skewed. Asia, Europe, North America, South America, Africa, Austrila were accounted annualized irrigated area respectively 79%, 7%, 7%, 4%, 2%, and 1%. China and India noticed to be the two leading irrigated countries with AIA respectively 152 Mha and 132 Mha, together China and India accounting 62% of global AIA. Whereas the TAAi for the China and India is estimated respectively 112 Mha and 101 Mha. The GIAM classification accuracy was estimated from 79% to 91% with the errors of omission and the errors of commission not exceeding 21% and 23% respectively.

Satellite Pour l'Observation de la Terre vegetation (SPOT-VGT) NDVI time-series for the three years used for irrigated cropland monitoring by the Velpuri et al., 2009. Xiong et al. used Google Earth Engine (GEE) to estimate irrigated cropland extent map

with 30m spatial resolution NDVI time series generated using Sentinel-2 and Landsat-8 images (Xiong et al., 2017). Moderate Resolution Imaging Spectroradiometer's (MODIS), Terra mission and Landsat satellite products are well known for land use and land cover studies (Biggs et al., 2006; Dheeravath et al., 2010; Teluguntla et al., 2017; Thenkabail et al., 2009b; Zheng et al., 2015). However, the available high temporal frequency satellite products (MODIS) are of coarse (250 m or more) to medium (Landsat (30 m)) spatial resolution. In a country like India where small (less than 1 ha) agricultural fields are dominant, Very High Spatial Resolution (VHSR) remotely sensed images are required to identify the irrigated crops (Gumma et al., 2011; Thenkabail et al., 2009a; Velpuri et al., 2009). At the same time, extensive ground data is required for the calibration and validation of classification outputs. It is evident from the literature that several studies focused on identifying irrigated cropland areas (Ambika et al., 2016; Ozdogan et al., 2010; Thenkabail et al., 2009a; Zheng et al., 2015). For precise irrigated classification, outputs need either time series (Gumma et al., 2000; Zheng et al., 2015) for the complete cropping duration or in case of non-availability of time-series satellite images, a single satellite image during the peak of cropping season (Ozdogan et al., 2010, 2006) is required. A robust methodology capable of quantifying irrigated cropland with high accuracy at field scale from the satellite images remains a challenge.

The literature of irrigated area monitoring can be divided into four main sections according to the various spatial scales of the study: local, regional, continental and the global scales (Ozdogan et al., 2010). The local scale studies for irrigated cropland study used method of mapping like photo interpretation, image arithmetic, image classification, segmentation, image fusion, etc. implemented on the sensors like Landsat TM/ETM+, SPOT, LISS, Advanced Very High Resolution Radiometer (ASTER), The Advanced Wide Field Sensor (AWiFS), China-Brazil Earth Resources Satellite (CBERS), Sentinel-2 Multispectral Imager (MSI), and Thailand Earth Observation System (THEOS) (Ferrant et al., 2017; Heller et al., 2012; Thiruvengadachari, 1981). The regional scale irrigated cropland monitoring was performed using methods like time-series analysis, supervised/unsupervised classification, and masking with sensors like Landsat TM/ETM+, MODIS, MERIS,

AVHRR, and SPOT-VGT (Alexandridis et al., 2008; Biggs et al., 2006; Thenkabail et al., 2005; Xiao et al., 2006). The continental scale irrigated cropland mapping were performed using time-series analysis with ancillary datasets and data fusion methods on Landsat TM/ETM+, MODIS, MERIS, AVHRR, and SPOT-VGT sensors (Biggs et al., 2006; Meier et al., 2018; Ozdogan and Gutman, 2008; Shah et al., 2006; Thenkabail et al., 2009b). The global irrigated cropland was performed using unsupervised clustering, machine learning algorithms applied to the time-series datasets, and also used other ancillary data like statistical and ground observations implemented on MODIS, MERIS, AVHRR, and SPOT-VGT sensors (Loveland et al., 2000; Thenkabail et al., 2009a, 2006).

Image spatial resolution plays a vital role to estimate irrigated areas, the role of spatial resolution is exposed by (Velpuri et al., 2009). He estimated the total irrigated area in the Krishna River basin in India using four satellite sensor images of different spatial resolution. He used AVHRR (1100 m), MODIS (500 m), MODIS (250 m), and Landsat (30 m) images for the study and noticed a significant irrigated area difference respectively 86%, 93%, and 95% with respect to the Landsat (30 m) derived irrigated area (9.36million hectares). This study concludes the irrigated area estimation is with high calssification accuracy with high spatial resolution (Landsat data 84%) compares to the coarse spatial resolution images (MODIS 500 m (77 %), MODIS 250 m (79 %), and AVHRR 1100 m (63 %) and it was noticed that the coarse spatial resolution outcomes are underestimating the total irrigated area (Velpuri et al., 2009).

Optical satellites used for the irrigated area monitoring are having various spectral bands, which can be defined with their wavelength. A list of high spatial resolution (inferior to 30 m spatial resolution) optical satellites payloads are presented with their spectral band and wavelengths in table 1. The multispectral high spatial resolution optical sensors generally having spectral bands in the visible range (blue, green and red), infrared range (near-infrared), and short (SWIR) or medium infrared (MIR) ranges. These spectral bands are assisting to study various earth surface features like surface water, land use, land cover, and identification & characterization of croplands. The intra-annual and intra-seasonal time-series optical images were used for the

evaluation for irrigated cropland monitoring and crop type classification (Betbeder et al., 2015b; Dusseux, 2014).

Table 1 List of the high-spatial-resolution (<100m) optical image spectral bands.

Spectral band	Wavelength (µm)	Satellite used
Ultra-blue (coastal/ aerosol)	0.435 - 0.451	LS8, EO1-ALI, S2
Blue	0.452 - 0.512	LS4-5, LS7, LS8, EO1, S2
Green	0.533 - 0.590	LS1-3, LS4-5, LS7, LS8, EO1, SPOT5-7, IRS-LISS3, IRS-LISS4, S2
Red	0.636 - 0.673	LS1-3, LS4-5, LS7, LS8, EO1, SPOT5-7, IRS-LISS3, IRS-LISS4, S2
NIR	0.851 - 0.879	LS1-3, LS4-5, LS7, LS8, EO1, SPOT5-7, IRS-LISS3, IRS-LISS4, S2
Shortwave Infrared (SWIR) 1	1.566 - 1.651	LS4-5, LS7, LS8, EO1, SPOT5-7, IRS-LISS3, S2
Thermal	10.40-12.50	LS4-5, LS7
Shortwave Infrared (SWIR) 2	2.107 - 2.294	LS4-5, LS7, LS8, EO1, S2
Panchromatic	0.503 - 0.676	LS7, LS8, EO1, SPOT5-7
Cirrus	1.363 - 1.384	LS8, S2
Thermal Infrared (TIRS) 1	10.60 - 11.19	LS8
Thermal Infrared (TIRS) 2	11.50 - 12.51	LS8

Irrigated cropland monitoring using optical remote sensing satellite sensors generally use spectral bands indices. The common optical spectral indices used for irrigated cropland monitoring is presented in the Table 2. The normalized difference vegetation index (NDVI), ratio vegetation index (RVI), soil-adjusted vegetation index (SAVI), enhance vegetation index (EVI), MTVI2 (modified triangular vegetation index 2), VCI (vegetation condition index), GEMI (Global Environmental Monitoring Index) and LAI (leaf area index) are commonly used irrigated cropland monitoring indices. The

normalized difference moisture index (NDMI) is widely used for soil moisture, wetland, and waterbody monitoring.

Table 2 List of the optical indices for irrigated cropland monitoring classification.

Index	Equation	Reference
NDVI	$\frac{NIR - R}{NIR + R}$	(Huete et al., 1992)
RVI	$\frac{R}{NIR}$	(Ridao et al., 1998)
SAVI	$\frac{NIR - R}{NIR + R + 0.5} * 1.5$	(Huete, 1988)
EVI	$\frac{NIR - R}{NIR + 6 * R - 7.5 * B + 1}$	(Liu et al., 2012)
MTVI2	$\frac{1.5(1.2(NIR - G) - 2.5(R - G))}{\sqrt{((2 * NIR + 1)^2 - (6 * NIR - 5 * \sqrt{R}) - 0.5)}}$	(Haboudane et al., 2004)
VCI	$\frac{NDVI_{present\ month} - NDVI_{min}}{NDVI_{max} + NDVI_{min}} * 100$	(Kogan, 1995; Quiring and Ganesh, 2010)
NDMI	$\frac{NIR - SWIR}{NIR + SWIR}$	(Jin and Sader, 2005)
GEMI	$\frac{eta * (1 - 0.25 * eta) - (Red - 0.125)}{(1 - Red)}$ where $eta = \frac{[(2*NIR^2 - Red^2) + 1.5*NIR + 0.5*Red]}{(NIR + Red + 0.5)}$	(Pinty and Verstraete, 1992)

1.3.2 Radar remote sensing

Cloud cover represents the biggest obstacle for monitoring land use with optical remote sensing (Ma, 2013). Active radar satellite offer cloud penetration capacity (longer wavelength, Table 2) and day/night sensing capability which brought microwave remote sensing in focus for land use and land cover monitoring (Capodici et al., 2017; Corgne et al., 2016b; Pottier et al., 2012).Tropical countries like India have eight-month cloud cover, for the land use and land cover studies microwave remote sensing represents a interesting ancillary to the optical remote sensing. Different types of microwave remote sensing exist as radar/altimeter/scatterometer (active or by generating energy pulses) or radiometers (passive or using natural energy) (Lee and Pottier, 2009; Mulder et al., 2011). A wide range of microwave bands (respected to

their wavelengths) is used according to the application (Brisco et al., 2015; Dorigo et al., 2012; Mulla, 2013; Omar et al., 2017; Prasad, 2009). A list of various microwave bands are presented in table 2 with their corresponding frequency and wavelengths, it was observed that the longer wavelengths are sensitive to the crop monitoring and shorter wavelengths are for moisture (Baghdadi et al., 2012; Betbeder et al., 2014a; Chen and Huang, 1996; Oh et al., 1992; Parrens et al., 2017; Pottier et al., 2012). Due to C-band wavelength is approximately 5 cm it is noticed that C-band SAR images were used widely for the crop, soil surface and moisture monitoring (Baghdadi et al., 2012; Erten et al., 2016; Wang et al., 2018; Zribi et al., 2013).

Table 3 List of all microwave bands.

Band	Frequency (GHz)	Wavelength (cm)
P	0.225 – 0.39	133 – 76.90
L	0.39 – 1.55	76.90 – 19.30
S	1.55 – 4.20	19.30 – 7.10
C	4.20 – 5.75	4.10 – 5.20
X	5.75 – 10.90	5.20 – 2.70
Ku	10.90 – 22.00	2.70 – 1.36
K	24.05 – 24.25	1.24
Ka	33.4 – 36.0	0.89 – 0.83

Seasat was the first onboard satellite equipped with SAR sensor launched in the year 1978. It was operated in L-band SAR with HH polarization. In the 80s, the emergence of polarimetry and radar interferometry techniques development can be seen in figure 12. The European Space Agency (ESA) launched its first civilian Earth Observation Satellite (ERS) in the year 1991. The ERS-1 was equipped with a Ku band (13.8 GHz) SAR sensor with VV polarization configuration. In 1992 Japanese space agency Japan Aerospace Exploration Agency (JAXA) has launched Japanese Earth Resources Satellite "FUYO-1" (JERS-1) with L-band SAR and HH polarization configuration. The Radarsat-1 satellite was launched by the Canadian Space Agency (CSA) with C-band (5.3GHz) and HH polarization configuration. Spaceborne Imaging Radar (SIR) was the first full polarimetric or quad-polarization satellite (HH, HV, VV, and VH polarization) with C-band frequency was launched by the National Aeronautics and

Space Administration (NASA) in 1994. Followed with the SIR-C ENVISAT (2002) and ALOS (2006) was launched by the ESA and JAXA, respectively. Radarsat-2 satellite was launched by the CSA in the year 2007 to provide high spatial (~10 m) and temporal resolution (24 days revisit) with C-band and quad-polarization configuration. In the year 2010 German TerraSAR-X satellite was launched with very high spatial (~ 1.5 m in "spotlight mode") and temporal resolution (revisit capacity of 11 days). The TerraSAR-X was configured with the X-band (6.65 GHz) and quad-polarizations. Indian Space Research Organisation (ISRO) has launched Radar Imaging SATillite (RISAT-1) in the year 2012 with C-band (5.35 GHz) frequency configuration. The Sentinel-1 C-band SAR satellite was launched in the year 2014 by ESA under Copernicus program satellite constellation with free data available for the public research purposes.

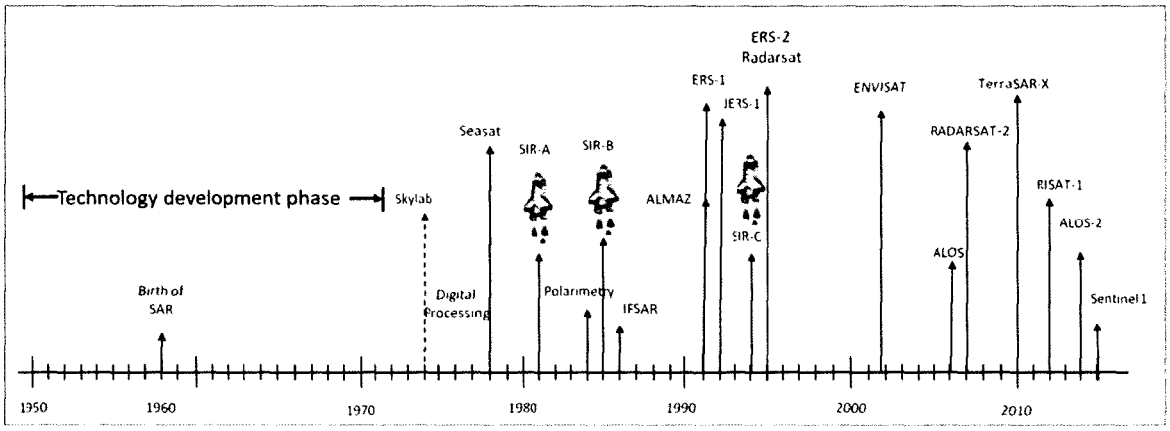

Figure 12 Evolution of microwave satellite.
Source: (Betbeder, 2015)

1.3.2.1 SAR Geometric configuration and spatial resolution

The radar signal acquisition geometry of a SAR sensor influences the image characteristics in the radar imaging. The image distortions can occur due to the lateral geometry in the radar images. Figure 13 demonstrates the inversion of image procured by the ground antenna is required due to the transmitted information by the sensor-equipped in the satellite is represents the inversion pixel, but the viewing direction remains the same. As satellite moves along to the azimuth, the radar antenna transmits pulses to the earth surface, and the backscattered pulses are recorded by the

sensor receiver. The pixel size of radar image corresponds to the time lag between the transmission and receiving pulses by the sensor, and the spatial resolution represents the discrimination of two objects from each other (Betbeder, 2015; Lee and Pottier, 2009).

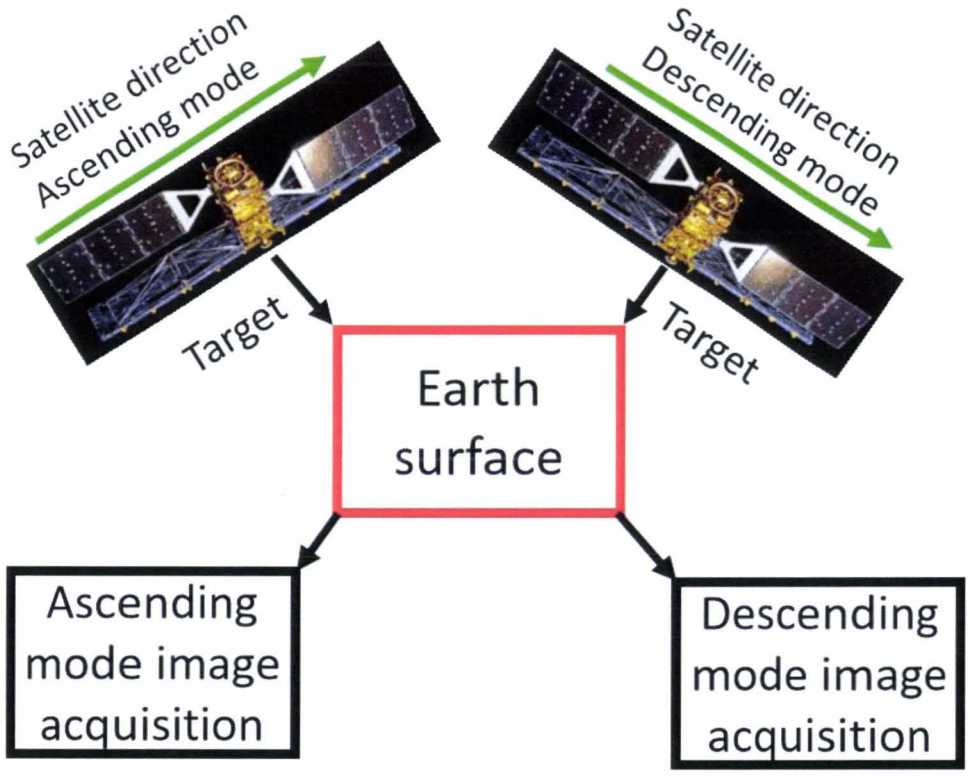

Figure 13 Radar image acquisition geometry.

The spatial resolution of an image refers to the number of pixels utilized to construct a digital image. Spatial resolution is becoming the most important criteria for SAR images with an ability of the imaging radar for separation of two closely spaced scatters. Very short pulse durations are necessary to construct high spatial resolution in range. Generation of short pulses with high energy is required to obtain a sufficient signal-to-noise (SNR) ratio, which enables detection of the reflected signals. The total number of columns in the SAR image is reciprocal to the sampling frequency of backscattered wave acquisition. As presented in figure 14 the first column in SAR image corresponds to the earth surface object closest to the sensor (proximal range or near range), and the last pixel corresponds to the furthest surface object (digital range and far range). Due to the near and far range, incidence angle varies for the first and pixel of the same image.

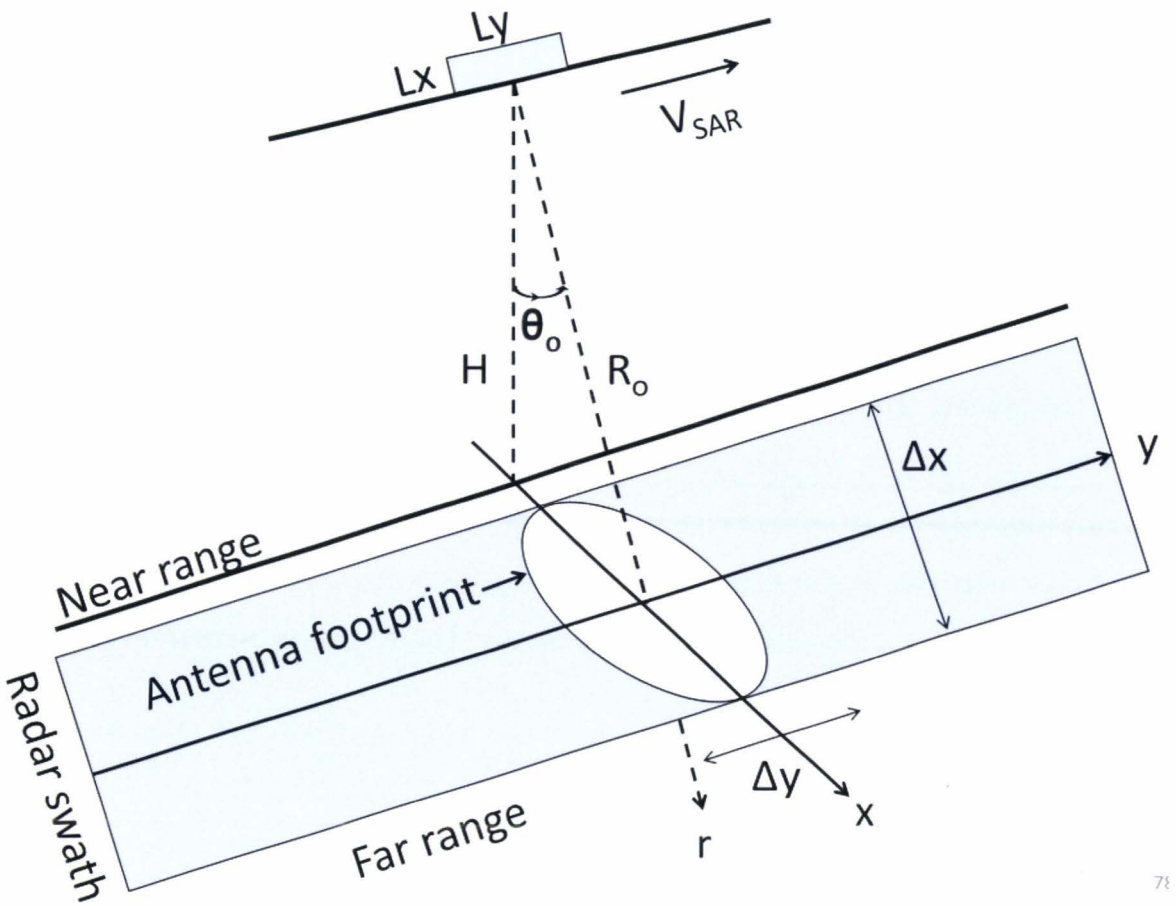

Figure 14 SAR image geometry in strip-map mode.

Where θo, Ro, H, V_{SAR}, Δx, Δy, r, x, y, and radar swath are respectively angle of incidence, distance between the radar and the antenna footprint centre, height of the SAR imaging system situated, velocity of the satellite, range swath, azimuth swath, slant range or radar line of sight, ground range or area covered by the antenna, azimuth or antenna footprint (perpendicular to the flight direction) total area scanned by the antenna beam, and Ly & Lx are the physical dimensions of the antenna.

The side-looking radar (SLR) couldn't illuminate the scene at nadir due to it is getting confused between the right and left parts of the image. The resolution in the distance is then projected depends on the ground distance according to the local slope and incidence angle. The ground distance from the slant distance and sensor altitude from the earth surface can be further calculated using trigonometric functions (Figure 14). The pixel size in linear direction (or azimuth direction) depends on the length of the emitted wave, size of the antenna, and the ground-radar distance.

1.3.2.2 Polarization basics

Polarization represents the orientation of the electromagnetic field of the concern wavelength. Radio Detection and Ranging (RADAR) generally distinguish two types or chaps of polarization: vertical (V) and horizontal (H). Horizontal and vertical polarizations were widely used for various land use and land cover monitoring due to their less complexity in the wave propagation (McNairn et al., 2009; Ulaby, 1975; Wiseman et al., 2014). The orientation of the transmitted wave pulse electric field vector with respect to the horizontal direction is referred to as microwave polarization. As shown in figure 15, the beam is called "H" polarised if the electric field vector oscillates in the parallel to the horizontal direction. And the beam is called "V" polarised if the electric field vector oscillates in the direction perpendicular to the horizontal direction.

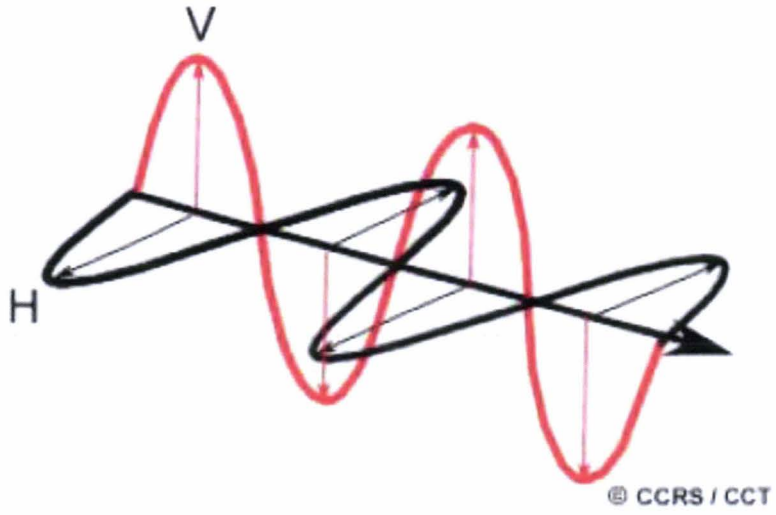

Figure 15 Microwave polarization (Source : CCT)

The "H" or "V" polarised beam, after interacting to the earth surface object the polarization state may be altered (Liew Soo Chin, 2001). Due to earth surface interaction, the backscattered microwave energy usually has a combination of two polarization states. Hence, depending on the polarization states of the transmitted and received signals. As shown in Table 4, four possible polarization combinations known as *HH*, *HV*, *VH*, and *VV* can be possible. The *HH* and *HV* polarizations are

referred to as *like-polarised* or *co-polarised* signals, while *HV* and *VH* polarizations are referred to as *cross-polarised.* Partially polarized and partially depolarized backscattering is occurring when many objects will respond to the polarized incident radiation by reflecting signals. In this case, the power of the polarized component divided by the total reflected power is the degree of polarization. A list of various polarization states with unitary jones vector, Stokes vector, orientation, ellipticity, and polarization ratio is presented in table 4 (Gherboudj et al., 2011; Kumar et al., 2017; Lee and Pottier, 2009; Signal and Giordano, 2016; Singh et al., 2014). The main polarization states are horizontal, vertical, linear±45°, left/right circular, etc.

Table 4 List of the polarization states.

Polarization states	**Unitary Jones vector** $(\hat{\mu}(\vec{x},\vec{y}))$	**Stokes vector** (g_E)	**Orientation** $(\emptyset)$	**Ellipticity** (τ)	**Polarization ratio** $(\rho(\vec{x},\vec{y}))$
Horizontal (H)	$\begin{bmatrix}1\\0\end{bmatrix}$	$\begin{bmatrix}1\\1\\0\\0\end{bmatrix}$	0	0	0
Vertical (V)	$\begin{bmatrix}1\\0\end{bmatrix}$	$\begin{bmatrix}1\\-1\\0\\0\end{bmatrix}$	$\frac{\pi}{2}$	0	$\propto$
Linear +45°	$\frac{1}{\sqrt{2}}\begin{bmatrix}1\\1\end{bmatrix}$	$\begin{bmatrix}1\\0\\1\\0\end{bmatrix}$	$\frac{\pi}{4}$	0	1
Linear -45°	$\frac{1}{\sqrt{2}}\begin{bmatrix}-1\\1\end{bmatrix}$	$\begin{bmatrix}1\\0\\-1\\0\end{bmatrix}$	$\frac{3\pi}{4}$	0	-1
Left circular	$\frac{1}{\sqrt{2}}\begin{bmatrix}1\\j\end{bmatrix}$	$\begin{bmatrix}1\\0\\0\\1\end{bmatrix}$	-	$\frac{\pi}{4}$	j
Right circular	$\frac{1}{\sqrt{2}}\begin{bmatrix}1\\-j\end{bmatrix}$	$\begin{bmatrix}1\\0\\0\\-1\end{bmatrix}$	-	$-\frac{\pi}{4}$	-j

1.3.2.3 Radar equation and image interpretation

The RADAR equation is comprised of received power (P_r), transmit power (P_t), gains of the transmitting and receiving antenna (G^2), the wavelength of Radar (λ), effective section of the Radar (σ), and the distance between the transmission and receiving radar objects (R^4). The effective section of the Radar is depended on the coefficient of reflection of the target. The basic Radar equation can be written as equation number 3 and 4.

$$P_r = \frac{P_t G^2 \lambda^2}{(4\pi)^3 R^4} \sigma \qquad \text{Equation 3}$$

When the Radar waves are interacting with earth surface objects, the Radar equation can be written as:

$$P_r = \frac{\lambda^2}{(4\pi)^3} \int \frac{P_t G^2 \lambda^2}{(4\pi)^3 R^4} \sigma \, A_e \qquad \text{Equation 4}$$

where A_e represents the earth surface where Radar waves are interacting.

The backscattering coefficients can be calculated by $10log_{10}$ of the energy ratio. And the energy ration can be calculated with the ratio of received energy to reflected energy (transmitted energy). Physical scattering from various earth surface features are providing indirect information of the object. For example, vegetation canopy interact with radar signal as a group of volume scatters composed discrete plant components like leaves, stems, stalks, limbs, etc. Radar waves which can penetrate plant canopy have surface scattering with the soil surface. Volume scattering with plant canopy is high when the radar signals approximate the mean size of plant components and the strong backscattering from the vegetation can be noticed. Short wavelength radar signals (λ=2 cm to 6 cm) are ideal for monitoring crop canopies like corn, soybeans, wheat, etc. and tree leaves. The longer wavelengths with λ=10 cm to 30 cm are ideal for the tree trunk and limbs monitoring (Lillesand et al., 2015).

As shown in the figure 16, mainly three types of scattering phenomena are occurring between signal and surface known as surface scattering or single bounce, odd scattering or dihedral scattering or double-bounce and volume scattering (Lee and Pottier, 2009). The surface scattering (Bragg surface), double-bounce scattering (dihedral) and volume (dipole) scattering (diffusion) can interpret precisely

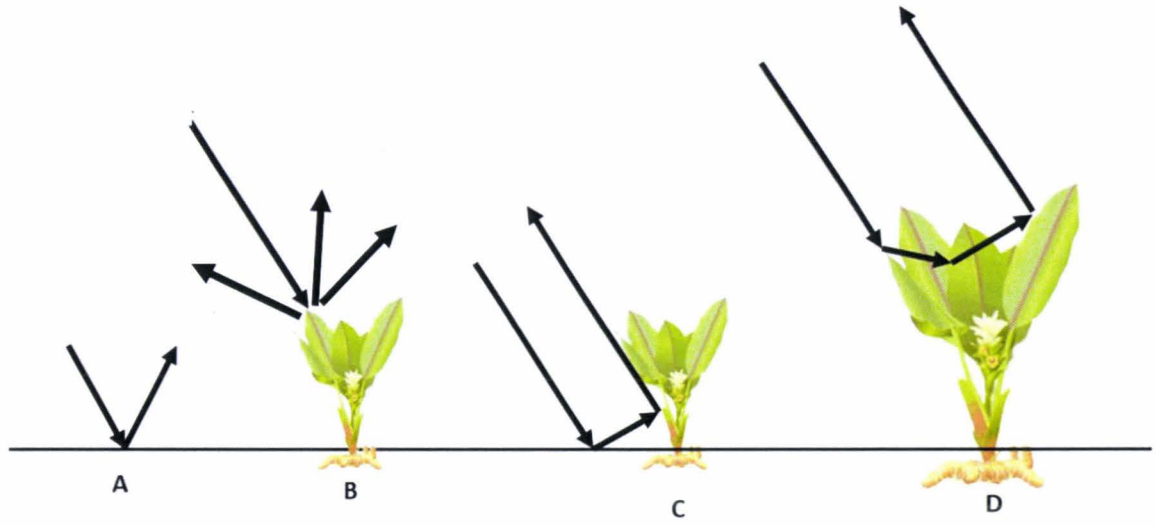

respectively homogenous land use features or objects, complex structures, and random scattering objects (Lee and Pottier, 2009).

Figure 16 Scattering phenomena examples from vegetation.
Where (A) is correpsond to specular scattering, (B) a diffuse scattering, (C) a double-bounce scattering and (D) a volume scattering.

Smooth surfaces like water or flat ground, are backscattering the radar beams in the opposite direction in a specular scattering. Rough surfaces are comparatively scattering the incident energy in multiple directions, and most of the incident energy is getting scattered. In rough surfaces, high backscattering energy to the receiver can be noticed in the same polarization as the transmitted pulse. The maximum scattering phenomenon or volume scattering can be noticed in agricultural croplands and forest vegetation. For soil surface roughness, it is generally described with the root-mean-square (RMS), height (s), correlation length (L), and Gaussian or exponential distributed autocorrelation functions (ρ) of the soil surface height (Martinez-Agirre et al., 2017; Ulaby et al., 1979).

In addition to that, radar signal interpretation will highly depend of soil moisture conditions (Reddy, 2008). Soil moisture represents a critical variable, and plays a vital role in linking the global terrestrial water, energy, and carbon cycles (Karthikeyan et al., 2017). The surface soil moisture (~5 cm) is highly variable and important for the sustainability for the agricultural crop growth (Salgado et al., 2001). Retrieving Surface Soil Moisture (SSM) is still a challenge the remote sensing community as the SSM is highly sensitive to the surface roughness, vegetation canopy, and soil texture (Rondeaux et al., 1996). Soil moisture quantitatively describes the amount of water present in the pore spaces of unsaturated soils. The soil moisture can be express in term of volumetric units ($\frac{m^3_{water}}{m^3_{soil}}$), depth units ($\frac{mm_{water}}{mm_{soil}}$), mass units ($\frac{kg_{water}}{m^2_{soil}}$), and relative soil moisture ($\frac{SM_{actual}}{SM_{saturation}}$). Several physically-based models, empirical, semi-empirical, regression and machine learning models have been developed to monitor SSM (F. Del Frate et al., 2003; Karthikeyan et al., 2017). *In-situ* measurements are the most important input for all these models for high accuracy.

Generally, radar signals are more sensitive to the surface soil moisture at low frequencies, and low incidence angles (Ulaby et al., 1983) and the radar signals with high incidence angle are more sensitive to the soil surface roughness (Zribi et al., 2019).

1.3.2.4 Polarymetry Basics

The electromagnetic waves have intrinsic vector nature. Wave polarization concept is necessary to understand the complete description of wave propagation and wave scattering phenomenon. Polarimetry is the science which measures and interprets the polarization properties of an object's backscattering pattern. An electromagnetic wave is composed of electric and magnetic field vectors varying in time and space in a plane which is perpendicular to the direction of wave propagation. In free space plane, electric and magnetic fields propagate at the speed of light ($3*10^8$ m/sec). The wave propagation is orthogonal according to Maxwell's equations. Due to this reason, the behavior of electromagnetic wave can observed electric field vector as a function of time and space. The representation of this electric vector function can be present as:

$$\vec{E}(z,t) = \begin{bmatrix} E_{0x}\cos(\omega t - kz + \delta_x) \\ E_{0y}\cos(\omega t - kz + \delta_y) \\ 0 \end{bmatrix}$$

With...

Normally, the spatial evolution of a monochromatic wave in a space plane follows a helical trajectory along the $\hat{z}$ axis. The three-dimensional helical curves are difficult to present and to perform practical experiment. Due to the complexity to present and analyze the three-dimensional helical trajectories. Generally, it is preferable the characterization of a wave in time domain at a fixed position (Lee and Pottier, 2009). The temporal behavior within the equi-phase plane has been studied. This is orthogonal to the direction of wave propagation and at a fixed location along the $\hat{z}$ axis. With time the wave propagates through equi-phase plane and describes the characteristic elliptical locus. Figure 17 shows the temporal trajectory of a monochromatic plane wave at a fixed position also known as polarization ellipse, which describes the wave polarization.

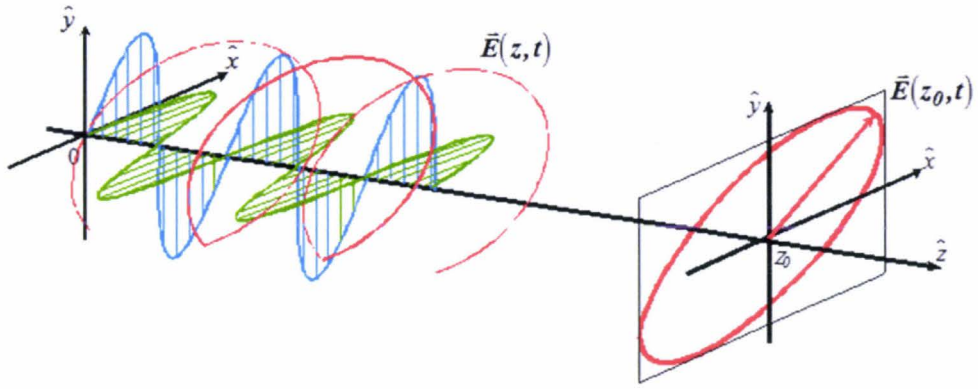

Figure 17 Temporal trajectory of a monochromatic plane wave at $z = z_0$ (at a fixed abscissa).
Source: (Lee and Pottier, 2009)

At a fixed time, t = t_0 , electric field of the propagating electromagnetic wave is composed of two orthogonal sinusoidal waves. In general, these sinusoidal waves have different amplitudes and phases at origin. Figure 18 shows the temporal evolution of a circularly polarised plane wave.

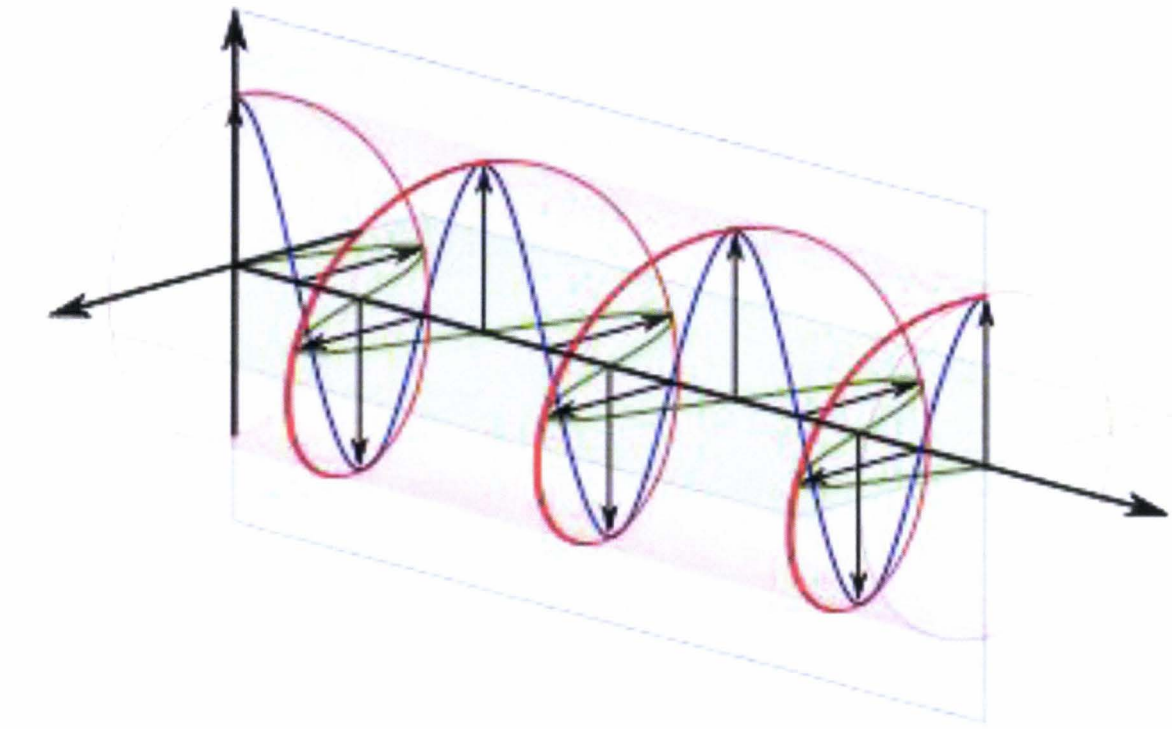

Figure 18 Spatial evolution of the circularly polarised plane wave.

1.3.2.5 SAR image processing

- **Calibration**

SAR image is a 2D array of pixels which is formed by the columns and rows (Lee and Pottier, 2009). Each pixel is providing a complex number associated with the reflectivity of all scatterers, and these complex numbers are containing the amplitude and phase information of the scatterers. The polarimetric SAR data is consist of four polarimetric backscattering polarisations (HH, HV, VH, and VV). These polarimetric backscattering polarisations are interacting differently with earth surface features. These backscattering's are a function of various parameters like:

(i) wave frequency (*f*),
(ii) wave polarization,
(iii) imaging configuration (incident angle and scattering direction),
(iv) object geometric structure, and
(v) object dielectric properties.

The SAR image calibration can be implemented on complex (real and imaginary parts) radiometric and geometric components (Luscombe, 2009). As a SAR is an imaging measurement instrument, and for all measurement instruments, it is required to calibrate the values measured (Erlangung, 2016). The SAR image primary measurement quantities are:

(i) amplitude;

(ii) phase;

(iii) location.

The pre-processing algorithms can be implemented to remove noise from the SAR polarization images. Results can be achieved according to the objective of image procurement (like crop biophysical properties, surface soil moisture, flood monitoring, soil surface roughness studies, forest studies, urban studies, etc.). For backscaterring coefficients analysis, we need to apply equation 5 to convert images from linear to decibel (dB).

$$\sigma°(dB) = 10.log10(\sigma°linear) \qquad \text{Equation 5}$$

$$\text{Where, } \sigma°\text{linear(dB)} = (Ks.DN^2 - NEBN).\sin(\theta) \qquad \text{Equation 6}$$

Ks is a calibration constant, DN is the digital number of a pixel (amplitude), NEBN is noise equivalent beta naught (sensor noise), and θ is incidence the angle of the radar signal.

Table 5 List of polarizations.

Polarization	Description	Reference
$\sigma°$hh	Horizontal transmission and horizontal receiving	(Oh et al., 1992; Ulaby, 1975)
$\sigma°$hv	Horizontal transmission and vertical receiving	
$\sigma°$vv	vertical transmission and vertical receiving	
$\sigma°$vh	Vertical transmission and horizontal receiving	

- **Speckle reduction**

Speckle is granular noise which is inherent to SAR images and generally degrades the backscattering signal/image quality. Speckle noise, in the conventional radar, results from the random fluctuations in backscattering signals. Due to each resolution cell is associated with an extended target which contains several scattering centers. These cells elementary returns by positive or negative interference can cause light or dark image brightness, which is also called "salt and pepper" appearance. Figure 19 illustrates speckle in the homogenous earth surface region with full constructive interference (brightest), full destructive interference (darkest) and varying degrees of interferences (at various greyscales).

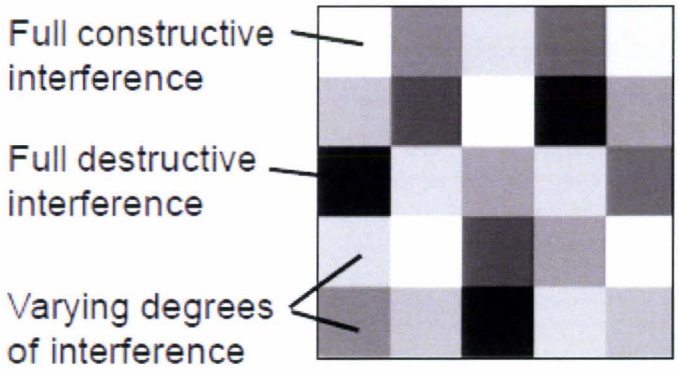

Figure 19 Schematic sample of a Radar image. (Source : CCT)

The constructive and destructive interferences are occurring due to the phase intervals between the backscattering signals. The intensity of the resulting combined signal will be amplified by constructive interference if the returning waves are in phase with one another. The destructive interference is causing due to the returning waves from within a pixel are at completely opposite phases, and they tend to reduce each other's intensity in the combined signal. The speckles are causing in the radar signal due to the constructive and destructive interference produce a random pattern of brighter and darker pixels in radar images. Figure 20 presents the difference between constructive and destructive interference formation from backscattering signals.

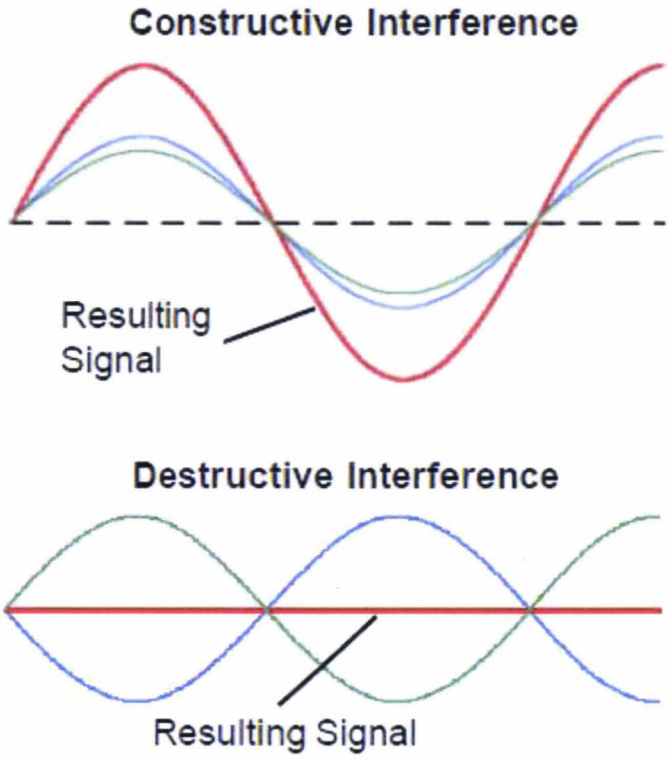

Figure 20 Constructive and destructive interference of the Radar signal.

The image analysis and interpretation processes are getting affected due to speckles in the SAR images. Speckle can be considered as noise in image processing, and we can identify them by comparing each pixel in an image with its neighbor pixels. The pixel of an image is assumed to contain noise if the difference between a given pixel value and its surrounding pixels values exceeded an analyst specific threshold. Main cause of the speckles in SAR images is the coherent interface of reflected waves scattered from the various elementary objects (Goodman, 1976; Lee and Pottier, 2009). The noise of a pixel can be reduced by replacing that pixel value with the average of its neighbor values. Usually, 3*3, 5*5 or 7*7 moving neighbors or windows of the pixel is used in such processes. Polarimetric SAR speckle noise can be reduced by implementing various polarimetric filtering methods presented in figure 21, known as Boxcar, Median, Lee, Refined Lee, Lee Sigma, Frost, Local statistics, Refined local statistics, Geometrical, Morphological, Maximizing a posteriori probability, IDAN (Intensity-Driven Adaptive-Neighbourhood), etc.

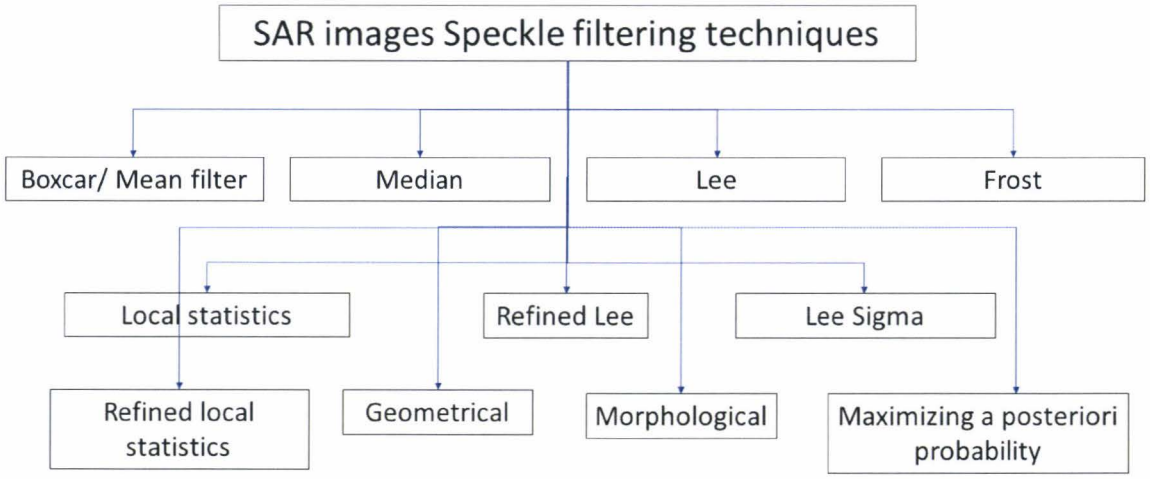

Figure 21 Speckle filtering techniques of the SAR images.

The Boxcar filter is incoherent averaging of covariance/coherency matrices with fixed window size (Lee et al., 1994). Over homogenous land use and land cover areas like agricultural land Boxcar filter shows the best filtering performance comparison to other filters to polarimetric SAR images (Pichierri and Hajnsek, 2017). Boxcar has some drawbacks as sharp edges and point scatters. Refined lee filter is a minimum mean square error (MMSE) filter, and it was developed based on the multiplicative model (Lee et al., 2015). Speckle noise near strong edges remains challenges for the refined lee filter. IDAN is a conventional filtering method with pixels selection from homogeneous areas inside a fixed window size (Cao et al., 2011). Lee sigma filter estimates Gaussian noise distribution and filters the central pixel for a defined window (Lee, 1983; Lee et al., 2015). In the improved sigma, filter has come out with the drawback of sigma lee that it the mean of pixels within two sigma range is always underestimated due to maybe noise distribution is not symmetric (Lee et al., 2009). Frost filtering technique commonly used to correct multiplicative noise by smoothing radar images (Frost et al., 2012; Singh et al., 2014).

The main objective of speckle filtering is to reduce noise in uniform regions using some type of averaging. The process is performing with preserving brightness variation that occurs at boundaries between regions of different overall brightness. Figure 22 shows some example of speckle filter noise removal outcomes using various window size. Filters are reducing the noise but not eliminating the speckle noise.

According to the application and to improve image quality number of filters may be required to use to reduce speckle to an acceptable level. Variation in pixel value after and before noise reduction with the loss of spatial resolution needs to be determined for the images and interpretation objectives.

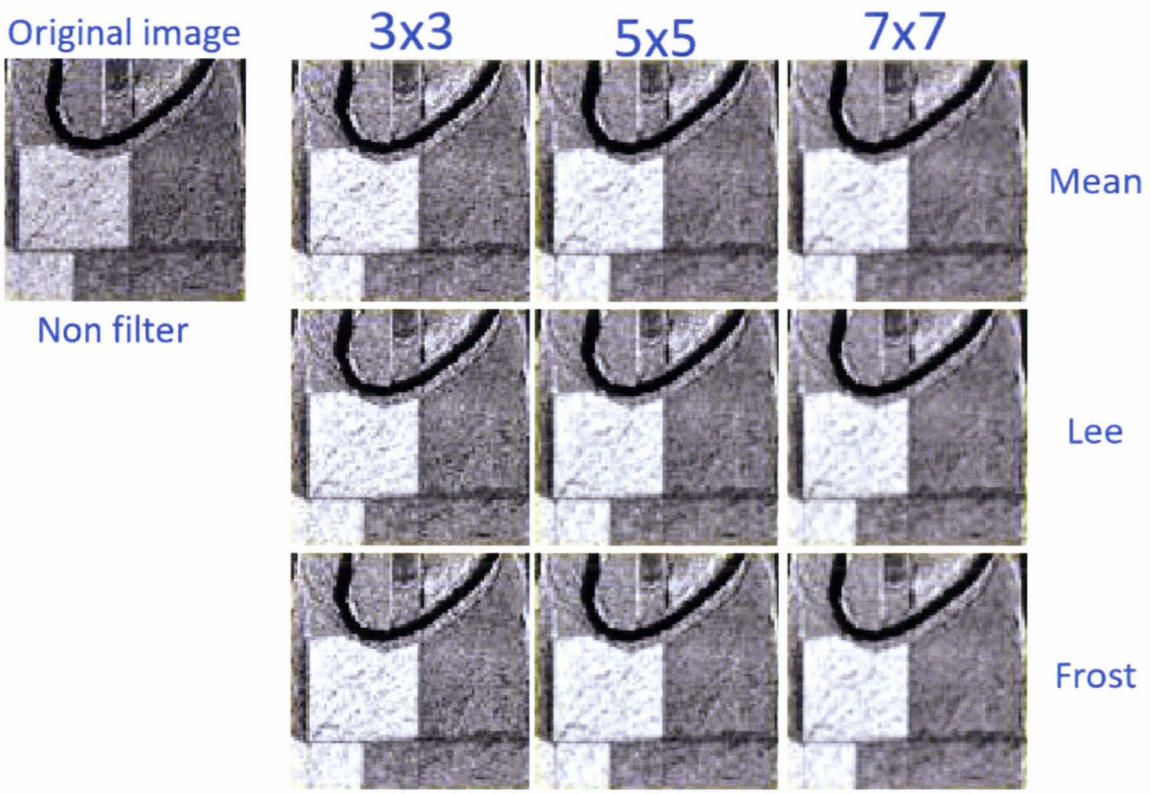

Figure 22 Examples of speckle filters with different window size.
Source: CCT.

- **Visualisation and interpretation**

The RGB color composite can be constructed to visualize SAR backscattering signals from earth surface features as for optical images. A False Color Composite (FCC) can be created considering HH, HV and VV polariation's with respectively red, green and blue bands of color.

In this part, to illustrate the different steps of processing, we used a Radarsat-2 (C-band) image in polarimetric mode acquired the 8 June 2013 on the study area in India (Berambadi watershed).

Figure 23 is representing the construction of FCC using SAR backscattering's polarizations. In the composite color of SAR backscattering polarizations reserve forest (west) is highly sensitive the green color or HV polarisation. It is representing the cross-polarization is more sensitive to forest land monitoring. The purple color is representing in most of the agricultural fallow lands, which is representing the red color (HH polarization) and blue color (VV polarization) are more sensitive to the fallow lands. The waterbody (in black) is having least backscattering with the cross-polarization (HV pol), which can also help to distinguish water body for other land surface features.

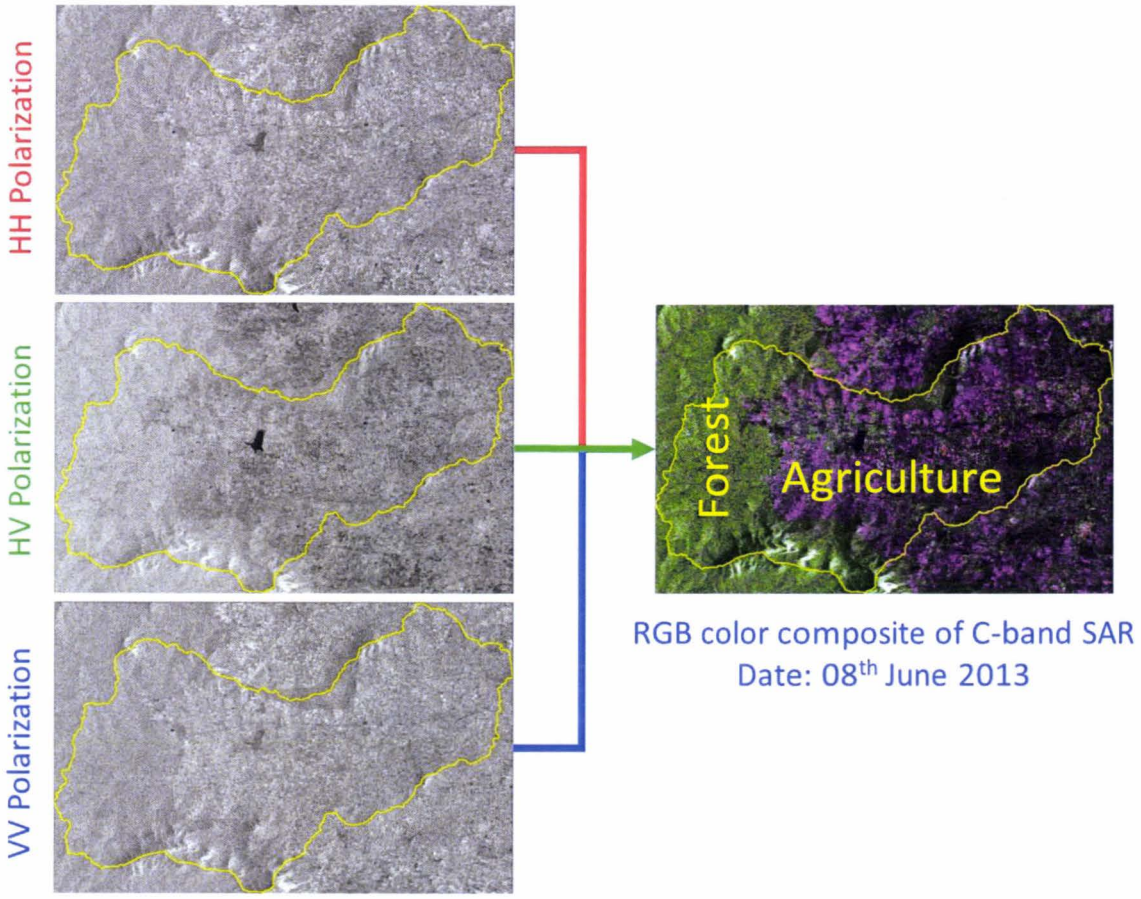

Figure 23 Example of False Color composite of Radarsat-2 (RS2) with the 3 polarizations (VV,HV,VV) on the Berambadi watershed (in Yellow).

- **Scaterring Matrix elements extraction**

The electromagnetic wave propagation takes particular time and space to teach a target, and its backscattering from the target after its interaction is presented in figure 24. Radar equation can derive from describing the electromagnetic wave interaction with a given target or object. The radar equation can establish a relation between the power that the targets intercepts from the incident electromagnetic wave and the reradiated power by the same target in the form of scattered wave.

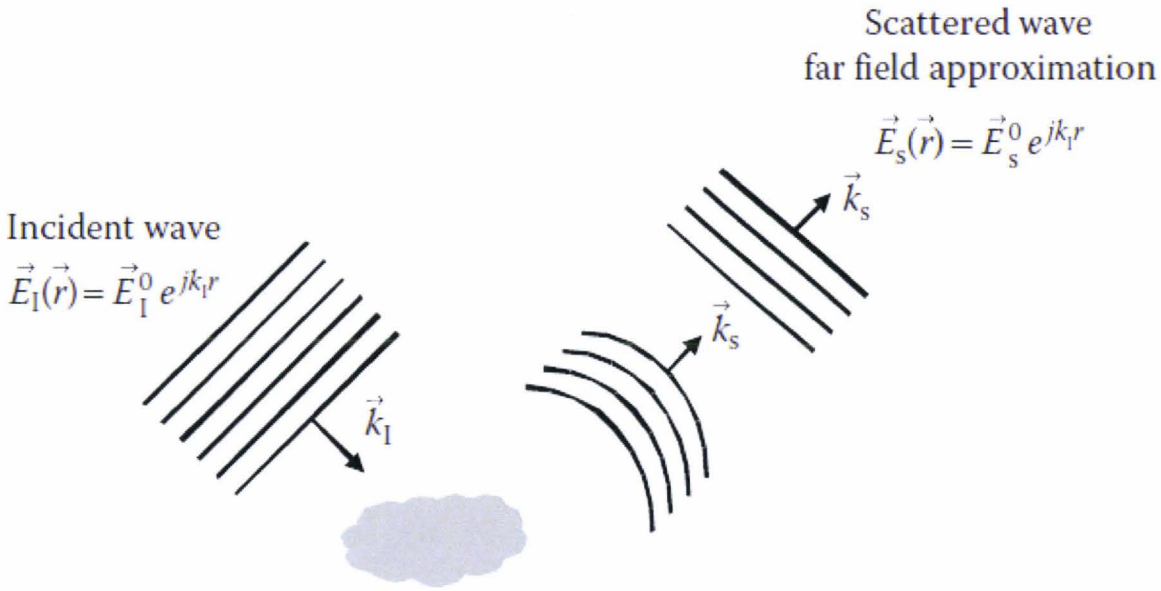

Figure 24 The electromagnetic wave interaction with a target.
Source: (Lee and Pottier, 2009)

The governing radar equation to describe the interaction of the electromagnetic wave with a target can be express as equation 7.

$$P_R = \frac{P_T G_T(\theta,\Phi)}{4\pi r_T^2} \sigma \frac{A_{ER}(\theta,\Phi)}{4\pi r_R^2} \qquad \text{Equation 7}$$

where P_R represents the total power detected by the receiving system, P_T is transmitted power, G_T is the transmitting antenna gain, A_{ER} is the effective aperture of the receiving antenna, r_R is the distance between the target and receiving system, θ is the azimuth angle, and Φ is the elevation angle.

Radar cross-section area σ determines effects of the target of interest on balance of powers established by the following radar equation number 8.

$$\sigma = 4\pi r^2 \frac{|\overrightarrow{E_S}|^2}{|\overrightarrow{E_I}|^2} \qquad \text{Equation 8}$$

Here the radar cross-section of a target is a function of large number of parameters which may not be possible to consider individually. These parameters can be broadly divided into two sets; the first set of these parameters are connecter with the imaging system are:

i. Wave frequency f,
ii. Wave polarization, and
iii. Imaging configuration: incident (θ_I, ϕ_I) and scattering (θ_S, ϕ_S) directions.

The second set of parameters are comparatively related to the target itself:

i. The geometrical structure of the object or target, and
ii. Dielectric properties of the object or target.

The scattering matrix elements can be related to the radar cross-section of a given target as follow equation number 9.

$$\sigma_{qp} = 4\pi |S_{qp}|^2 \qquad \text{Equation 9}$$

It follows that in the Horizontal-Vertical basis or in the Cartesian basis, the 2*2 complex backscattering S matrix can be expressed as the equation 10 (Lee and Pottier, 2009).

$$S_{(\hat{x},\hat{y})} = \begin{bmatrix} S_{XX} & S_{XY} \\ S_{YX} & S_{YY} \end{bmatrix} = S_{(\widehat{u_H},\widehat{u_V})} = \begin{bmatrix} S_{HH} & S_{HV} \\ S_{VH} & S_{VV} \end{bmatrix} \qquad \text{Equation 10}$$

The S matrix elements S_{HH} and S_{VV} are producing power return in the co-polarized channels and the elements S_{HV} and S_{VH} are producing the power return in the cross-polarized channels. The reciprocity theorem (in case of reciprocal propagation medium) can be applid to the backscattering matrix. And the backscattering matrix

can be symmetric if the role of transmitting and receiving antennas are interchanged and can be write as $S_{HV} = S_{VH}$ (Lee and Pottier, 2009).

The total scatter power of the polarimetric radar system is called Span. The span of a polarimetric radar system can be express as the equation 11.

$$\text{Span} = T_r(S\,S^{*T}) = |S_{11}|^2 + |S_{12}|^2 + |S_{21}|^2 + |S_{22}|^2 \qquad \text{Equation 11}$$

where $T_r(A)$ represents of a matrix A. As per the reciprocal theorem, in the monostatic case (backscattering direction) the Span can be express as the equation 12 and can be represented in picture format as figure 25.

$$\text{Span} = T_r(S\,S^{*T}) = |S_{11}|^2 + 2|S_{12}|^2 + |S_{22}|^2 \qquad \text{Equation 12}$$

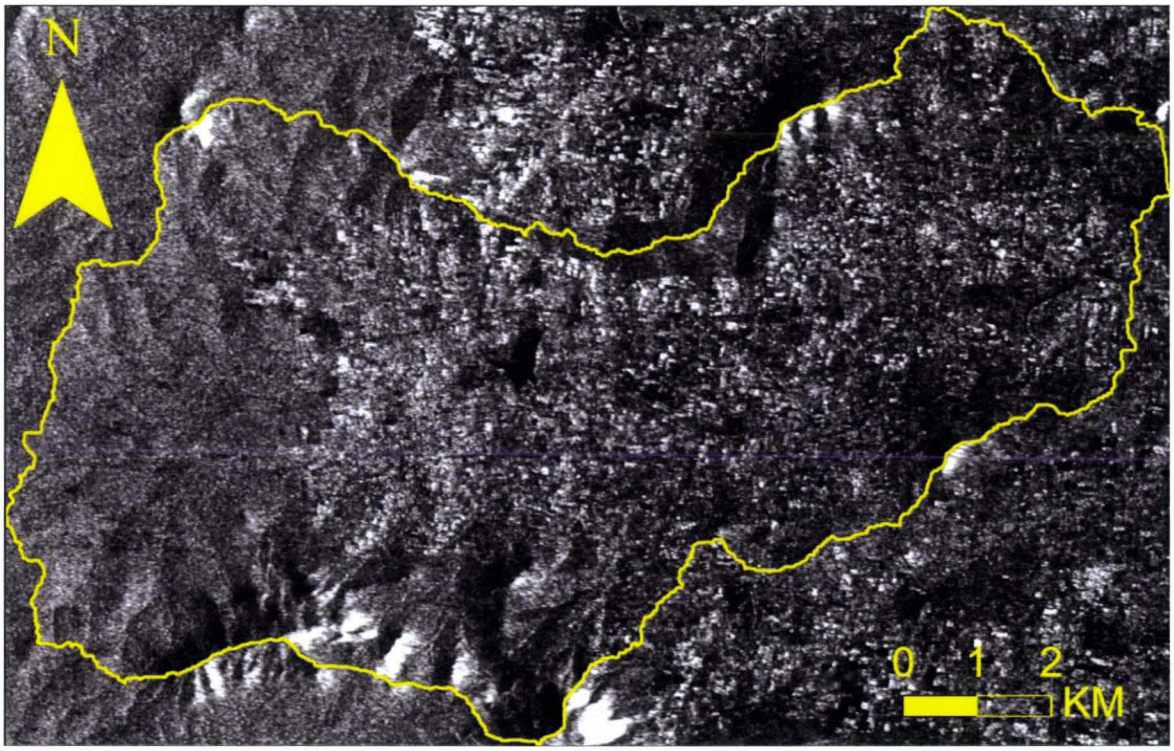

Figure 25 Example of Grey-scale representation of Span estimation for the image Radarsat-2 QuadPol acquired the 08th June 2013 (Berambadi watershed, India).

The monostatic case (backscattering direction) os a given target can be characterized by five parameters: three amplitudes and two relative phases. In the monostatic case, the backscattering matrix S can be express either in the "backscattering alignment" (BSA) or "forward scatter alignment" (FSA) convention, this is called the Sinclair S

matrix (Lee and Pottier, 2009). The BSA or FSA convention of *S* backscattering matrix can be express as equation 13.

$$S_{BSA} = \begin{bmatrix} -1 & 0 \\ 0 & 1 \end{bmatrix} S_{FSA} \qquad \text{Equation 13}$$

The classical 2x2 coherent Sinclair matrix S (Figure 26) can be represent by the vector V(·), as follow equation number 14 (Lee and Pottier, 2009).

$$S = \begin{bmatrix} S_{XX} & S_{XY} \\ S_{YX} & S_{YY} \end{bmatrix} = \underline{k} = V(S) = \frac{1}{2} T_r(S\Psi) \qquad \text{Equation 14}$$

where Ψ is a complete set of 2x2 complex basis matrix. The matrix components are constructed as an orthogonal set under the Hermitian inner product.

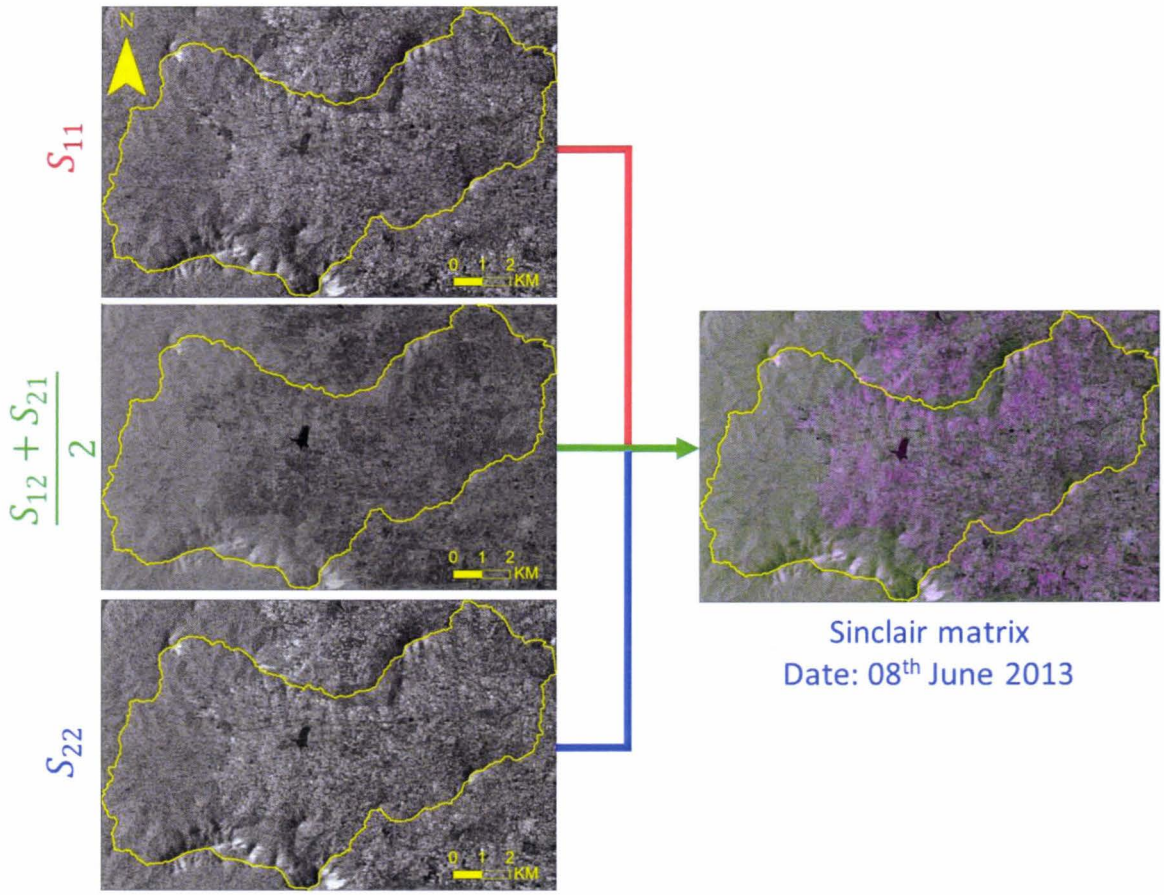

Figure 26 Example of False Color Composite of Radarsat-2 (RS2) with the 3 components of the Sinclair matrix on the Berambadi watershed (in Yellow).

- **Polarimetric coherency or covariance matrices**

The concept "distributed target" arise due to all radar targets are not stationary or fixed; they are generally situated in a dynamically changing environment. These dynamically changing environments are subject to spatial and temporal variations. Such scatterers are called as partial scatterers or distributed targets; these scatterers are analogous to the partially polarized waves. Even though the environment is dynamically changing, we need to make assumptions concerning stationary, homogenous, and ergodicity. It is required to study this property more precisely by introducing the concept of space and time-varying stochastic processes. The target or the environment can be described by the second-order moments of the fluctuations. These moments of the fluctuations can be extracted from the polarimetric coherency or covariance matrices.

In the bistatic scattering case, the 4x4 polarimetric Pauli coherency T_4 matrix and the 4x4 polarimetric Lexicographic covariance C_4 matrix can be generated from the outer product of the associated target vector with its conjugate transpose (Lee and Pottier, 2009; Niu and Ban, 2013). The Pauli coherency T_4 matrix and Lexicographic covariance C_4 mathe trix can be write as the equation 15 and 16 respectively.

$$T_4 = \langle k \cdot k^{*T} \rangle \qquad \text{Equation 15}$$

$$C_4 = \langle \Omega \cdot \Omega^{*T} \rangle \qquad \text{Equation 16}$$

Where the $\langle ... \rangle$ indicates the temporal or spatial ensemble averaging with assuming homogeneity of the random medium.

The 4x4 polarimetric Pauli coherency T_4 matrix (equation 15) can be rewritten and express as equation 17,

$$T_4 = \left\langle \begin{bmatrix} |k_1|^2 & k_1 k_2^* & k_1 k_3^* & k_1 k_4^* \\ k_2 k_1^* & |k_2|^2 & k_2 k_3^* & k_2 k_4^* \\ k_3 k_1^* & k_3 k_2^* & |k_3|^2 & k_3 k_4^* \\ k_4 k_1^* & k_4 k_2^* & k_4 k_3^* & |k_4|^2 \end{bmatrix} \right\rangle \qquad \text{Equation 17}$$

where the matrix components can be eloborate as: k_1= S_{hh}+ S_{vv}, k_2= (S_{hh} - S_{vv}), k_3= (S_{hv} + S_{vh}), k_4= (S_{hv} - S_{vh}).

The 4x4 Lexicographic covariance C_4 the matrix can be rewrite and present as the equation number 18.

$$C_4 = \left\langle \begin{bmatrix} |\Omega_1|^2 & \Omega_1\Omega_2^* & \Omega_1\Omega_3^* & \Omega_1\Omega_4^* \\ \Omega_2\Omega_1^* & |\Omega_2|^2 & \Omega_2\Omega_3^* & \Omega_2\Omega_4^* \\ \Omega_3\Omega_1^* & \Omega_3\Omega_2^* & |\Omega_3|^2 & \Omega_3\Omega_4^* \\ \Omega_4\Omega_1^* & \Omega_4\Omega_2^* & \Omega_4\Omega_3^* & |\Omega_4|^2 \end{bmatrix} \right\rangle \qquad \text{Equation 18}$$

where the matrix components can be elaborate as Ω_1= S_{hh}, Ω_2= S_{hv}, Ω_3= S_{vh}, Ω_4= S_{vv}.

During construction of the polarimetric coherency T_4 matrix and polarimetric covariance C_4 matrix, it needs to note that both matrices are Hermitian positive semidefinite matrices. These matrices satisfy the equation 19, and they contain non-negative eigenvalues and orthogonal eigenvectors.

$$T_r(T_4) = T_r(C_4) = Span \qquad \text{Equation 19}$$

In monostatic backscattering, the reciprocity contains Sinclair scattering matrix in symmetrical form ($S_{HV} = S_{VH}$). Thus the four-dimensional polarimetric Pauli coherency T_4 matrix and the polarimetric Lexicographic covariance C_4 matrix can reduce to the three-dimensional matrices. The three-dimensional polarimetric coherency T_3 matrix and the covariance C_3 the matrix can be rewritten as equation 20 and 22 respectively.

$$\begin{bmatrix} \langle|Shh + Svv|^2\rangle & \langle Shh + Svv\rangle\langle(Shh - Svv)^*\rangle & 2\langle(Shh + Svv)Shv^*\rangle \\ \langle Shh - Svv\rangle\langle(Shh + Svv)^*\rangle & \langle|Shh - Svv|^2\rangle & 2\langle(Shh - Svv)Shv^*\rangle \\ 2\langle Shv(Shh + Svv)^*\rangle & 2\langle Shv(Shh - Svv)^*\rangle & 4\langle|Shv|^2\rangle \end{bmatrix}$$

Equation 20

Figure 27 presents the RGB color combination of various diagonal components of coherency matrix T3.

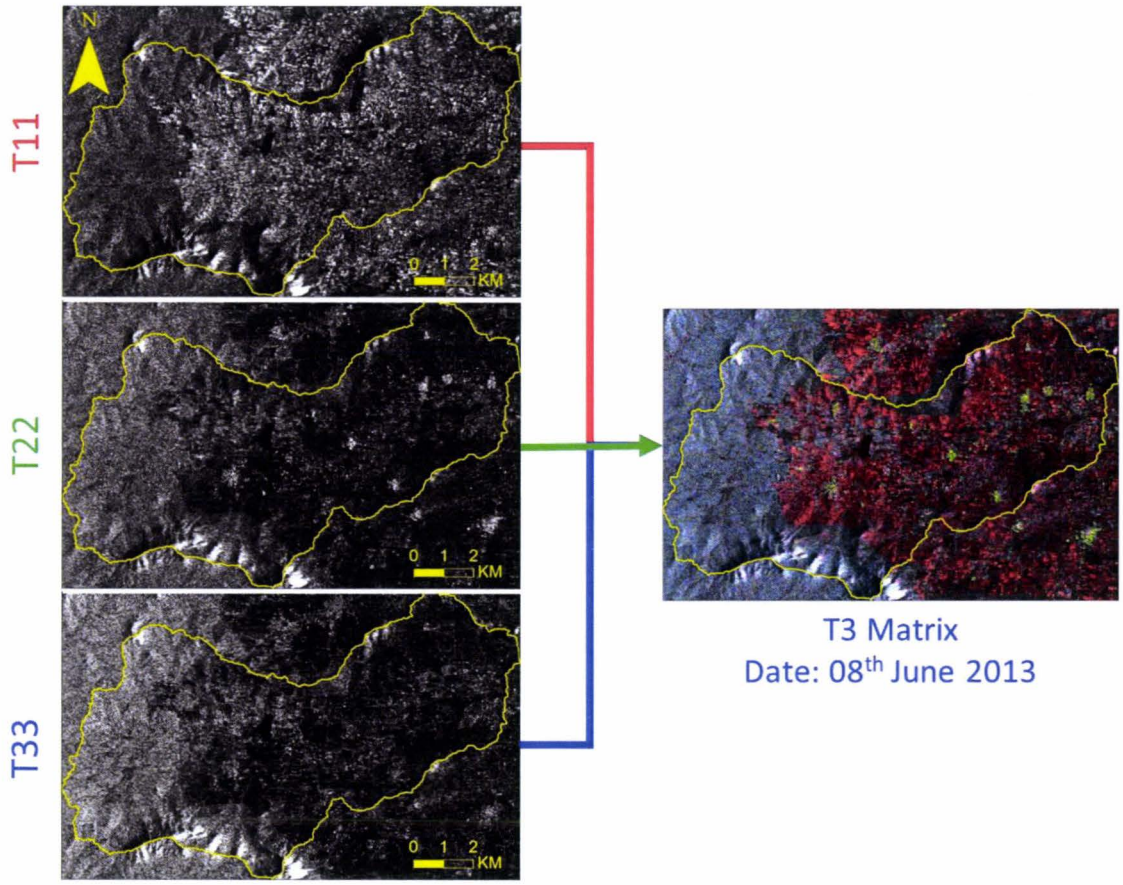

Figure 27 Example of False Color Composite of Radarsat-2 (RS2) with the 3 components of the Coherency (T3) matrix on the Berambadi watershed (in Yellow).

The polarimetric coherency T_3 matrix can also be rewritten as equation 21.

$$T_3 = \begin{bmatrix} 2\langle A_0 \rangle & \langle C \rangle - j\langle D \rangle & \langle H \rangle - j\langle G \rangle \\ \langle C \rangle + j\langle D \rangle & \langle B_0 \rangle + \langle B \rangle & \langle E \rangle + j\langle F \rangle \\ \langle H \rangle - j\langle G \rangle & \langle E \rangle - j\langle F \rangle & \langle B_0 \rangle - \langle B \rangle \end{bmatrix} \quad \text{Equation 21}$$

Coherency matrix $\langle [T_3] \rangle$ is a set of nine independent parameters like A_0 (total scattered power from the targets regular, smooth and convex depolarizing components), Bo (total scattered power from the targets irregular, rough and non-convex depolarizing components), Ao+Bo (total scattered power), Bo+B (total symmetric depolarized power), Bo-B (total non-symmetric depolarized power), C&D (local and global shape depolarization components of symmetric targets), E&F (local and global twisting depolarization components due to non-symmetries), G&H (local and global coupling between symmetric and non-symmetric terms).

The three-dimensional polarimetric covariance C_3 matrix can be express as equation 22 and presented as figure 28. It presents the various diagonal components of the covariance three-dimensional matrix.

$$C_3 = \begin{bmatrix} |S_{11}|^2 & \sqrt{2}S_{11}S_{12}^- & S_{11}S_{22}^* \\ \sqrt{2}S_{12}S_{11}^- & 2|S_{12}|^2 & \sqrt{2}S_{12}S_{22}^- \\ S_{22}S_{11}^* & \sqrt{2}S_{22}S_{12}^- & |S_{22}|^2 \end{bmatrix} \qquad \text{Equation 22}$$

Where, $S_{11} = S_{hh}$, $S_{12} = S_{hv}$, $S_{21} = S_{vh}$, $S_{22} = S_{vv}$.

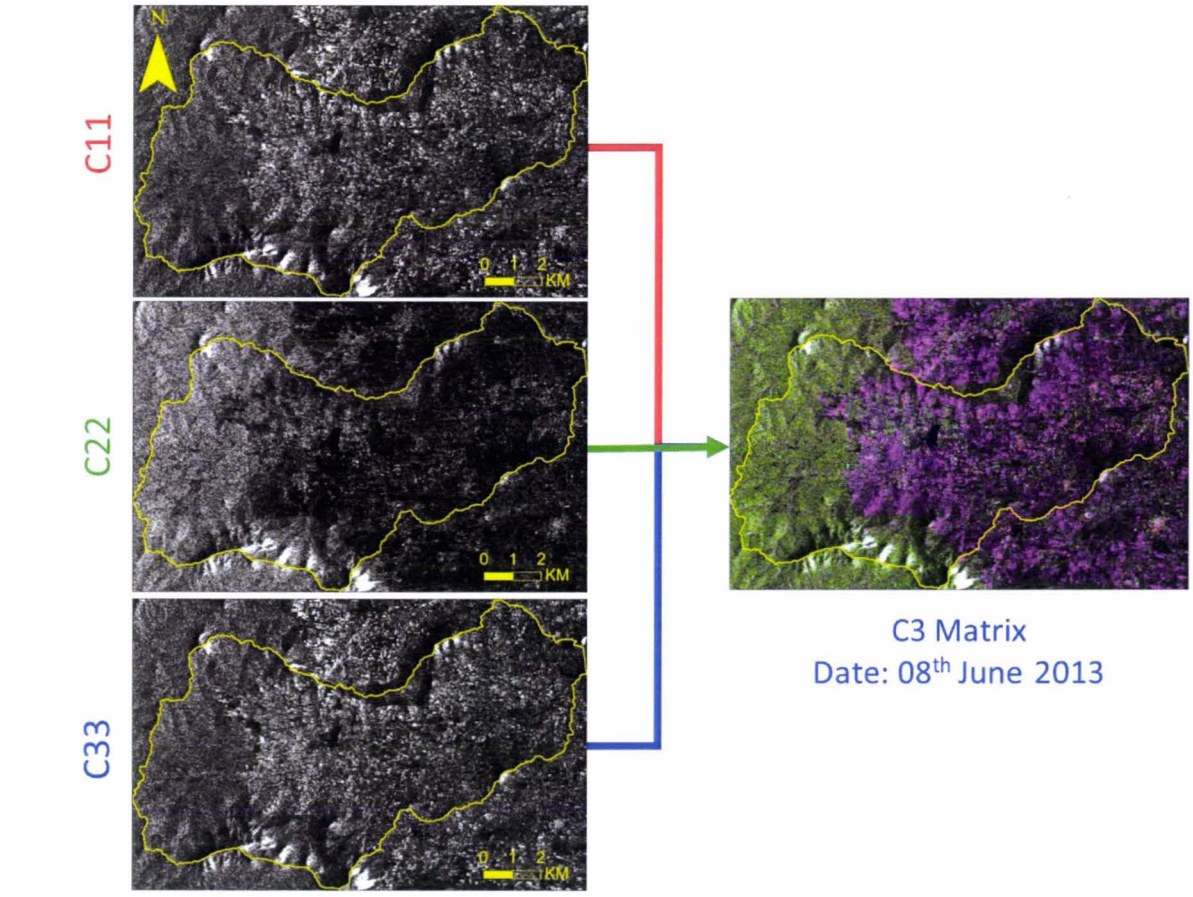

Figure 28 Example of False Color Composite of Radarsat-2 (RS2) with the 3 components of the covariance (C3) matrix on the Berambadi watershed.

- **Polarimetric decompositions**

The polarimetric decomposition can be divided mainly into two categories: coherent decomposition or pure scatterers and in-coherent decomposition or distributed scatterers (Figure 29) (Lopez-Martinez and Poitter, 2015). The objective of the coherent decompositions is to express the measured scattering matrix by the radar.

In-coherent decomposition, as its clear from the name, when the in-coherency is there in the transmission or receiving signal, this kind of decompositions were used for the image classification.

The commonly used coherent decompositions are Pauli decomposition, Krogager decomposition, and Cameron decomposition. On the contrary, to handle speckle noise present in the images can characterize statistically using in-coherent decompositions. The in-coherent decompositions can be further divided into three categories like model-based freeman decompositions, phenomenological huynen decomposition, and the eigenvector-eigenvalue based decomposition. Polarimetric decomposition algorithms like Cloude, Yamaguchi, VenZyl, Generalized Freeman-Durden, Freeman-Durden Sinclaire, and Pauli provides information from the surface, double-bounce and volume scattering. Polarimetric decomposition algorithms like Cloude, Yamaguchi, VenZyl, Generalized Freeman-Durden, Freeman-Durden Sinclaire, and Pauli provides information from the surface, double-bounce and volume scattering.

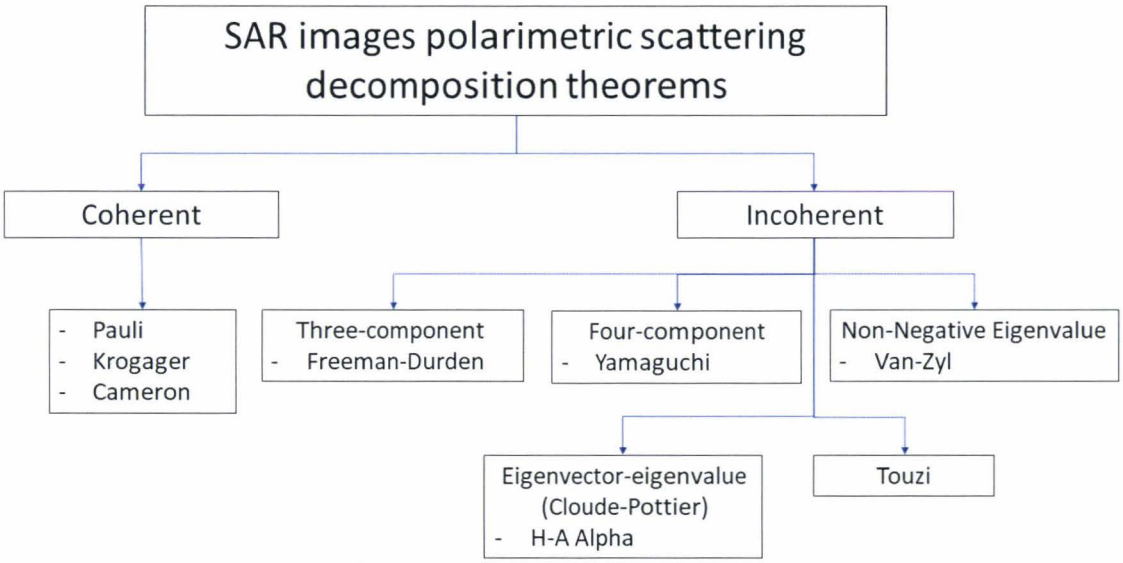

Figure 29 SAR images polarimetric decomposition algorithms.

The Pauli, Krogager and Cameron polarimetric decompositions are coherent polarimetric decompositions. Freeman-Durden (three-component), Yamaguchi (four-component), Van-Zyl (non-negative eigenvalue), Cloude-Pottier or H-A-α

(eigenvector-eigenvalue) and Touzi polarimetric decompositions are categorized as an incoherent polarimetric decomposition algorithm (Lee and Pottier, 2009; Lopez-Martinez and Poitter, 2015). Scattering matrices allows the characterization of a scattering object for a given frequency and geometry. These matrices provide information at a particular combination of transmitting and receiving polarization states (Lee and Pottier, 2009). The polarimetric SAR images are becoming complex due to the complexity of scattering processes and the high variability of scattering objects (Lopez-Martinez and Poitter, 2015). Polarimetric decomposition algorithms are using these coherency and covariance matrices as input to provide a solution for land use and land cover interpretation.

Pauli decomposition presents the scattering S matrix in the form of the complex sum of the Pauli matrices. Here an elementary scattering mechanism is associated with each basis matrix. The Pauly decomposition with scattering components can be express as equation 23.

$$[S] = \begin{bmatrix} Shh & Shv \\ Shv & Svv \end{bmatrix} = \frac{a}{\sqrt{2}}\begin{bmatrix} 1 & 0 \\ 0 & 1 \end{bmatrix} + \frac{b}{\sqrt{2}}\begin{bmatrix} 1 & 0 \\ 0 & -1 \end{bmatrix} + \frac{c}{\sqrt{2}}\begin{bmatrix} 0 & 1 \\ 1 & 0 \end{bmatrix} + \frac{d}{\sqrt{2}}\begin{bmatrix} 1 & -j \\ j & 1 \end{bmatrix} \quad \text{Equation 23}$$

where a, b, c, and d all are complex components as presented in equation 24, 25, 26, and 27, respectively.

$$a = \frac{S_{HH}+S_{VV}}{\sqrt{2}} \quad \text{Equation 24}$$

$$b = \frac{S_{HH}-S_{VV}}{\sqrt{2}} \quad \text{Equation 25}$$

$$c = \frac{S_{HV}+S_{VH}}{\sqrt{2}} \quad \text{Equation 26}$$

$$d = j\frac{S_{HV}-S_{VH}}{\sqrt{2}} \quad \text{Equation 27}$$

Pauli decomposition application to the deterministic targets can consider the coherent composition of four scattering mechanisms (Lee and Pottier, 2009):

i. scattering from the plane surface (single or odd-bounce scattering)
ii. scattering from the diplane (double or even-bounce scattering)
iii. scattering from the volume-surface (random scattering or oriented target scattering)

iv. all antisymmetric components of the scattering S matrix.

The Pauli polarimetric decomposition RGB color composite representation was shown in figure 30.

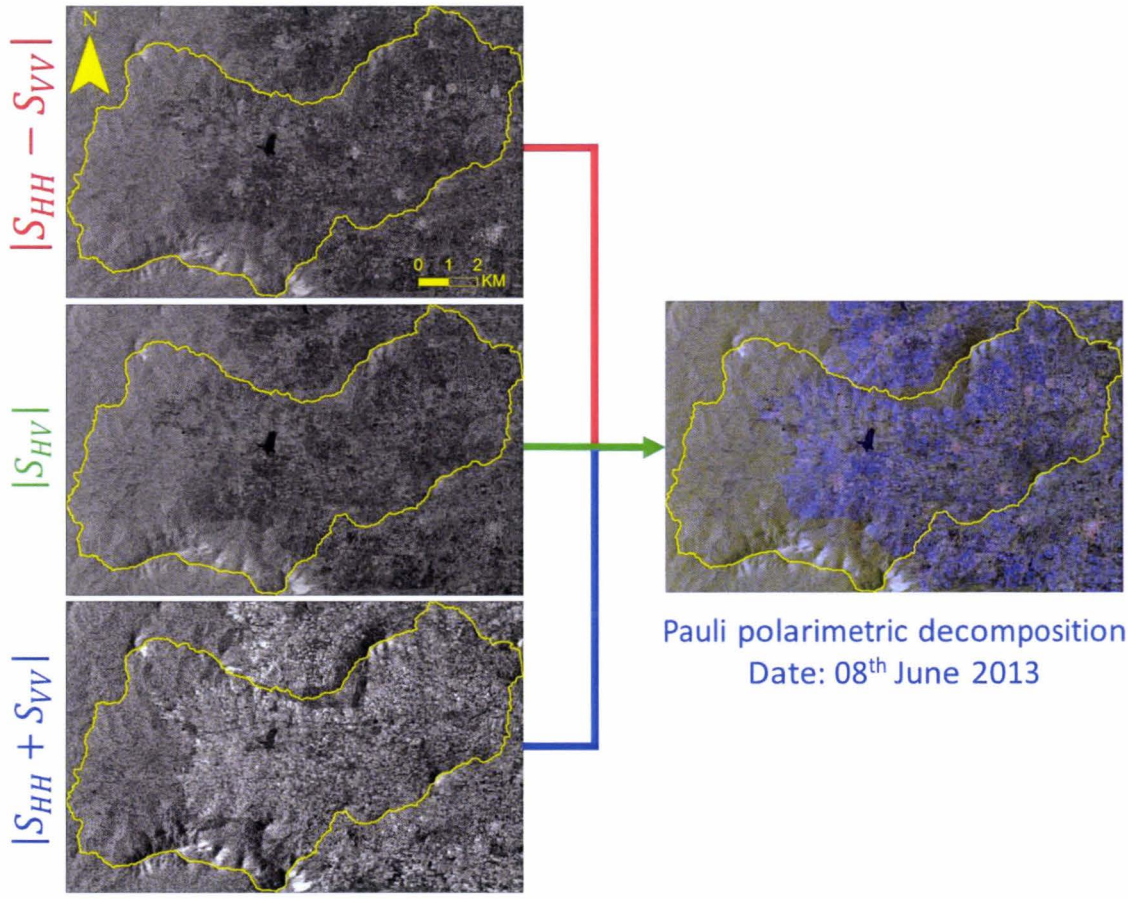

Figure 30 Example of False Color Composite of Radarsat-2 (RS2) with the 3 components of the Pauli polarimetric decomposition on the Berambadi watershed.

The Entropy (H), Anisotropy (A) and Alpha angle (α) polarimetric descriptor is an incoherent decomposition. In the year 1997, S. R. Cloude and E. Pottier proposed an innovative method for extracting average parameters from the experimental datasets using a smoothing algorithm based on the second-order statistics (Cloude et al., 1997). This method is not relying on any assumption of a particular underlying statistical distribution. So, this model is free from the physical constraints imposed by such statistical multivariate models. An eigenvector analysis of the three-dimensional (3x3) polarimetric coherency matrix is used due to it is providing a basis invariant description of the scatterer with specific decomposition types of scattering processes

(the eigenvectors) and their relative's magnitudes (the eigenvalues). The eigenvalues used to construct the entropy polarimetric descriptor with values ranging from 0<H<1 (Dore, 2014). The entropy polarimetric descriptor provides information about the randomness of scattering mechanisms associated with the T3 coherency matrix. All components of the H-A-alpha polarimetric decomposition is presented in figure 32. The RGB color composite in figure 31 used entropy, anisotropy and alpha-angle as red, green and blue color respectively.

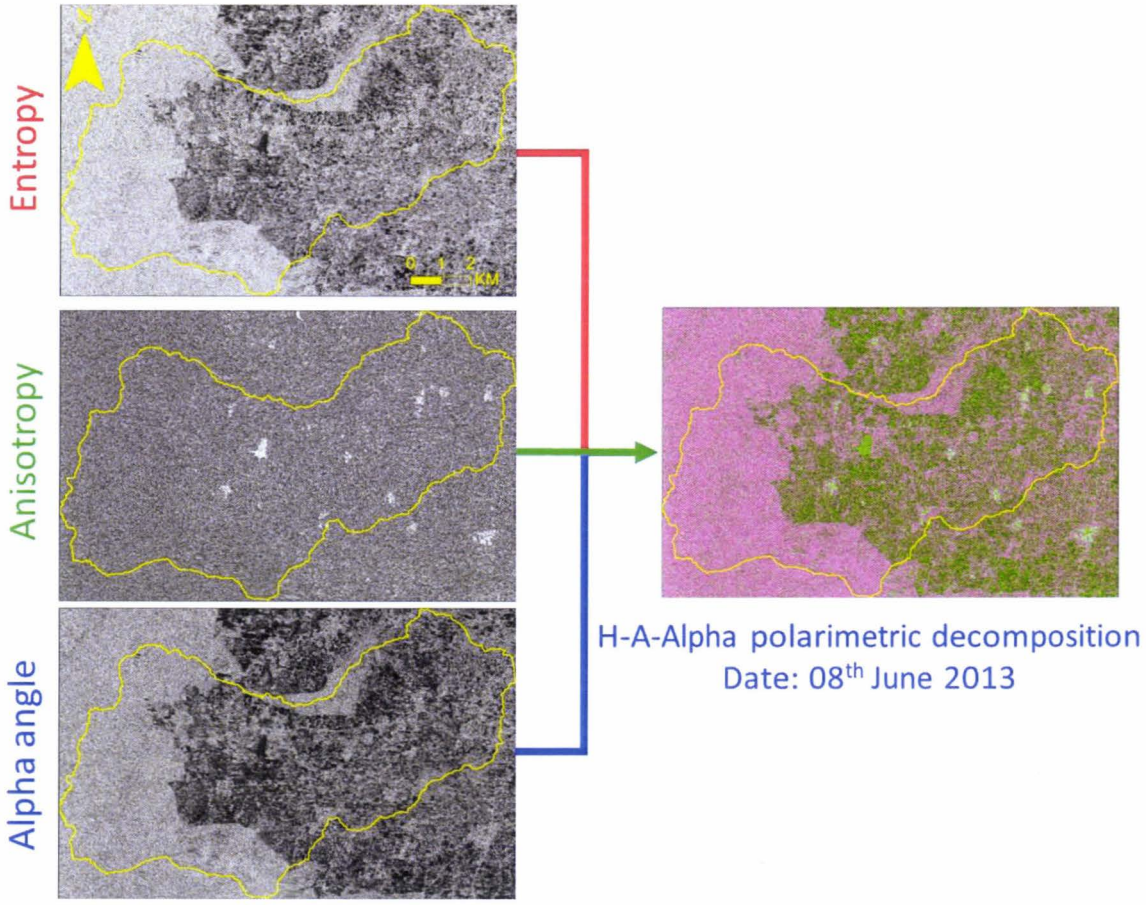

Figure 31 Example of False Color Composite of Radarsat-2 (RS2) with the 3 components of the Cloude-Pottier decomposition on the Berambadi watershed.

In the year 1997, Cloude and Pottier have proposed an unsupervised classification scheme based on two-dimensional H/α plane with all random scattering mechanisms representation (Lee and Pottier, 2009). The basis of this idea was to represent entropy scattering mechanisms of the inherent revisability from various earth surface features. The alpha angle – entropy relation can be used to identify the underlying average scattering mechanisms. The H/α plane (Figure 32) is sub-divided into nine basic zones

according to various earth surface features with respect to the different scattering behavior.

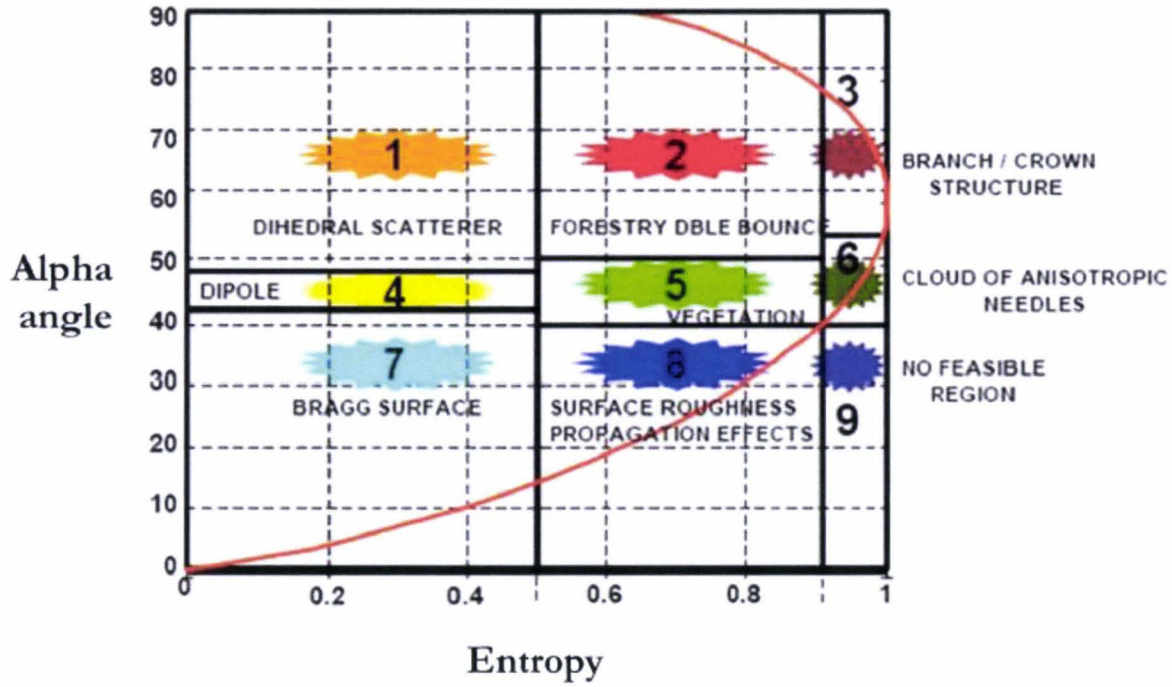

Figure 32 H-A-Alpha plane representation.

Source:(Lee and Pottier, 2009)

In the H/α plane, the boundary values are set on basic scattering mechanisms properties (corresponds to the H and α) of the earth surface features. Even though some degree of arbitrariness can be found, which are not dependent on a particular dataset. The successful implementation of H/A/α polarimetric decomposition for the earth surface monitoring is widely used for the research activities. The *Shannon Entropy* has been introduced by J. Morio in the year 2007 as a sum of two components: intensity (SE_I) and polarimetry (SE_P) (Morio, 2007; Réfrégier and Morio, 2006). The *Shannon Entropy* can be express as equation 28.

$$SE = log(\pi^3 e^3 |T_3|) = SE_I + SE_P \qquad \text{Equation 28}$$

where SE_I is the intensity contribution, which depends on the total backscattered power and SE_P is the polarimetric contribution which depends on the Barakat degree of polarization (pT). The SE_I and SE_P terms can be express as equations 29 and 30 respectively.

$$SE_I = 3log\left(\frac{\pi elT}{3}\right) = 3log\left(\frac{\pi eTr(T_3)}{3}\right) \quad \text{Equation 29}$$

$$SE_P = \log(1 - p_T^2) = log\left(27\frac{|T_3|}{Tr(T_3)^3}\right) \quad \text{Equation 30}$$

The Freeman-Durden polarimetric decomposition is a method to fit a physically-based three-component scattering mechanism model in the polarimetric SAR observations without utilizing any ground observations (Dore, 2014; Lee et al., 2006). The *Freeman-Durden* polarimetric decomposition mechanisms of are based on canopy scatterer from a cloud of randomly oriented dipoles, even-or double-bounce scatter from a pair of orthogonal surfaces with a different dielectric constants, and Bragg scatters from a moderately rough surface. Figure 33 represents RGB color composite of various scattering mechanisms of Freeman-Durden polarimetric decomposition.

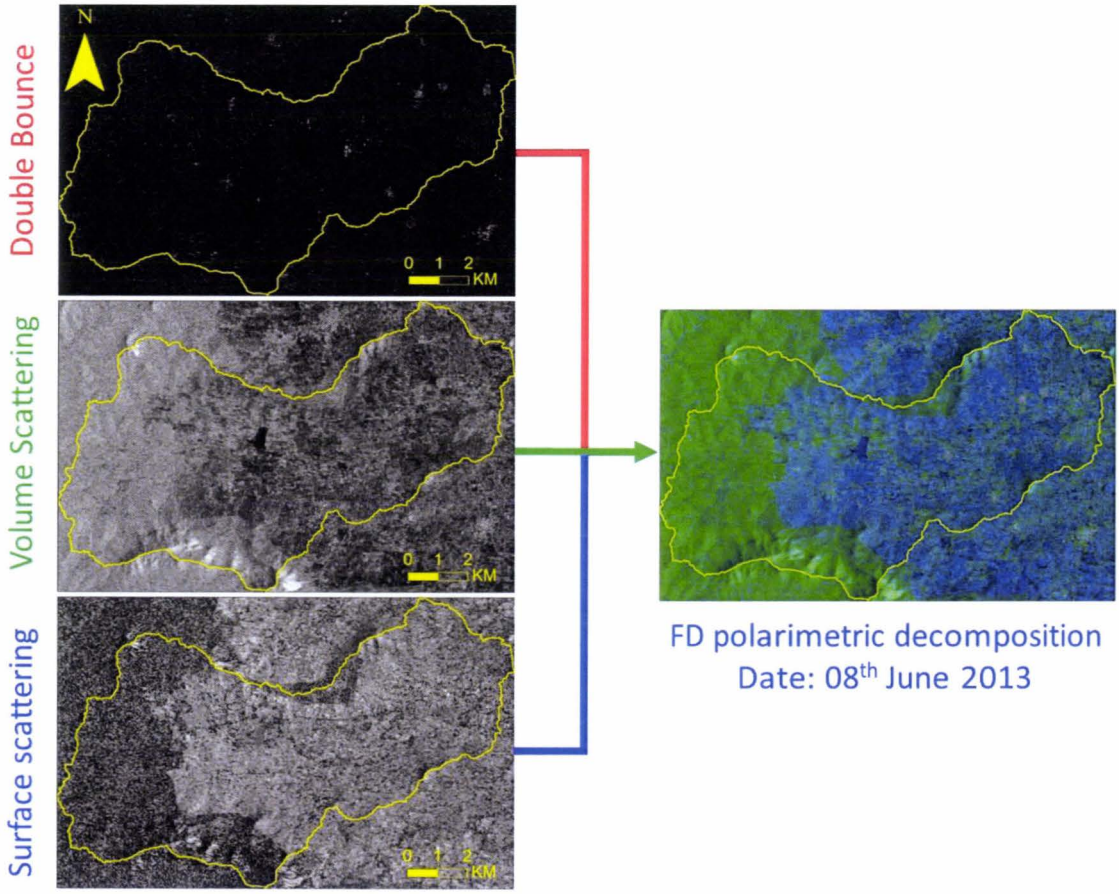

Figure 33 Example of False Color Composite of Radarsat-2 (RS2) with the 3 components of the Freeman-Durden (FD) polarimetric decomposition on the Berambadi watershed.

The freeman decomposition models the covariance matrix $\langle[C_3]\rangle$ consists volumetric scattering (canopy scatterer can be modeled as a random dipole), double-bounce scattering (modeled by the dihedral corner reflector) and surface or single-bounce scattering (modeled by the first-order Bragg surface scatterer).

1.3.2.6 Evaluation of SAR data for irrigated areas monitoring

Optical remote sensing capacities are limited to regions like south of India with high level of cloud cover while SAR remote sensing is not affected by atmospheric conditions (Inoue et al., 2014). Furthermore, SAR data are highly sensitive to the soil dielectric constant which increases with water content (Chen et al., 1995) that makes it very relevant to irrigated cropland monitoring during entire cropping seasons.

Several studies have successfully conducted for irrigated cropland monitoring like paddy rice fields monitoring using multi-temporal SAR datasets (Kumar et al., 2016; Yuzugullu et al., 2015; Y. Zhang et al., 2017). However, paddy rice fields are a special case since they are inundated, which makes to distinguish SAR backscattering signals for rice and non-rice fields. Few studies used SAR datasets for irrigated cropland monitoring at high spatial resolution in except paddy fields multiple cropping practices watersheds (El Hajj et al., 2014; Gao et al., 2018). SAR data is affected by the soil moisture and vegetation growth so the irrigation events can be identified by the SAR signals as it is changing the soil moisture in agricultural fields and it helps to the cultures flourish (Gao et al., 2013). Gao et al. used C-band SAR time-series images form Sentinel-1 satellite platform with VH and VV polarizations over Spain agricultural watershed. They have estimated agricultural parcels scale mean backscatter polarization intensities for the irrigated crops, irrigated trees, ad non-irrigated fields. The Support Vector Machine (SVM) and Random Forest (RF) machine learning algorithms were used to perform supervised classification and it was noticed that the 81.08% and 82.2 percent classification accuracy were estimated respectively for both algorithms. (Ferrant et al., 2017) used time-series of sentinel-1 dual polarization with

Sentinel-2 optical dataset to monitor groundwater irrigated croplands in southern Indian watershed. They monitored irrigated cropland for the two cropping seasons (*Rabi* and *Kharif*) with the error of 3.5% and 5% respectively. Hoang et al. used dual-pol and quad-pol Radarsat-2 SAR multi-temporal images to monitor Rice crop in Cau river basin in Vietnam (Hoang et al., 2016). They find SVM classification more accurate and reliable than the thresholding techniques for the study. Hajj et al. monitored soil moisture over irrigated grassland using X-band SAR data over southeast France. Study used inversion technique based on multi-layer perceptron neural networks (NNs) to invert Water Cloud Model (WCM) for soil moisture estimation with a root mean square error (RSME) between 3.6 vol.% to 6.1 vol.% (El Hajj et al., 2016). Saheli et al. used Radarsat-2 H/A/Alpha polarimetric decomposition to monitor agricultural crops and forested areas in Germany (Salehi et al., 2017). Betbeder et al. used TerraSAR-X dual-pol time-series images for wetland vegetation monitoring in northwest region of France (Betbeder et al., 2015b). It was noticed from this study that the Shannon entropy polarimetric decomposition classification using SVM algorithm can classify wetland vegetations with high classification accuracies. Hajj et al. used TerraSAR-X and COSMOS-SkyMed X-band SAR time-series images for irrigated grassland monitoring in France watershed (El Hajj et al., 2014). The study shows the potential of X-band SAR for irrigated grassland monitoring due to high penetration depth of the X-band.

Irrigated cropland monitoring using SAR needs knowledge of agricultural and hydrological sciences. Since the irrigation is time dynamic activity during the entire cropping season, multi-temporal or time-series of SAR datasets are required for the precise irrigation studies. Irrigated cropland monitoring study can assist with polarimetric decomposition algorithms (Maryam Salehi et al., 2017), polarization indices (El Hajj et al., 2016), physical models (Baghdadi and Zribi, 2016), semi-empirical models (Baghdadi et al., 2017a), empirical models (Filion et al., 2016), and vegetation contribution models (Gherboudj et al., 2011). The IEM model was first introduced by the Fung et al. in 1992. Integral Equation Model (IEM) is a dominant physical model to simulate the backscatter coefficient as a function of dielectric constant, sensor parameters, radar frequency, SAR polarization, incidence angle, RMS

height, correlation length and autocorrelation function (Chen et al., 1995; Steele-Dunne et al., 2017; Zribi et al., 2013). Semi-empirical models are simplified mode of physical models by addressing issues pertaining to the roughness conditions. These models are having conceptual background of physical models with simulations or experimental studies, that helps simplification of the model (Karthikeyan et al., 2017). The most common widely applied in the literature semi-empirical models are proposed by Oh et al. (1992) and Dubois et al. (1995). The empirical models are confined to local-scale studies due to lack of physical basis. To calibrate the empirical models, good quality in-situ observations of soil and agricultural practices is required. Most of the studies with high accuracy conducted using physical, semi-empirical and empirical approaches are valid under bare soil conditions. The effect of vegetation to the SAR backscattering signals can also incorporate in these models to monitor precise irrigated croplands. Attema and Ulaby (1978) introduced Water-Cloud Model (WCM) to tackle the effect of vegetation and soil. The WCM is also a semi-empirical model by nature as the model parameters are site-dependent and need to calibrate (Hosseini and McNairn, 2017). The polarization indices and polarimetric decompositions can provide the soil and crop variable to various models for precise irrigated cropland monitoring.

1.3.3 Image classification algorithms

Land use and land cover classification can be performed with airborne and spaceborne spatiotemporal images. Satellite image classification majorly divided into two parts: unsupervised and supervised classification (Hoekman et al., 2011; Ma et al., 2017; Thakkar et al., 2014). Supervised classification methodologies required precise ground observation during the satellite pass date and time (Abbas et al., 2013; Palchowdhuri et al., 2018; J. Zhang et al., 2017). In case if the ground observation is not precise to calibrate remotely sensed images, the unsupervised classification using pixel clustering algorithms can be used, and the validation can be obtained by comparing other studies or government statistics (Alrababah and Alhamad, 2006; C. Liu et al., 2018; Thakkar et al., 2014). Figure 34 presents various image classification techniques (Chen et al., 2017; Lück and van Niekerk, 2016; Teluguntla et al., 2017).

Commonly used supervised image classification algorithms are support vector machine, neural networks, maximum likelihood classification, discriminant analysis, and random forest classification (Figure 34). Supervised regression algorithms are linear regression, GLM (generalized linear model), SVR (support vector regression), GPR (Gaussian process regression), ensemble methods and neural network. Unsupervised classification algorithms are based on clustering using the pixel value. The main unsupervised classification or clustering algorithms are a k-mean, k-method, hierarchical, Gaussian mixture, hidden-Markov model, EM-cluster, etc. (Du et al., 2012; Ma et al., 2017). Artificial intelligence (AI) algorithm are most common, and machine learning (ML) is part of it, which can be further subcategorized as deep learning and data science. Chaos (Mangiarotti et al., 2018), object-based classification, semi-supervised classification algorithms also can be implemented for precise land use and land cover classification (Ma et al., 2017).

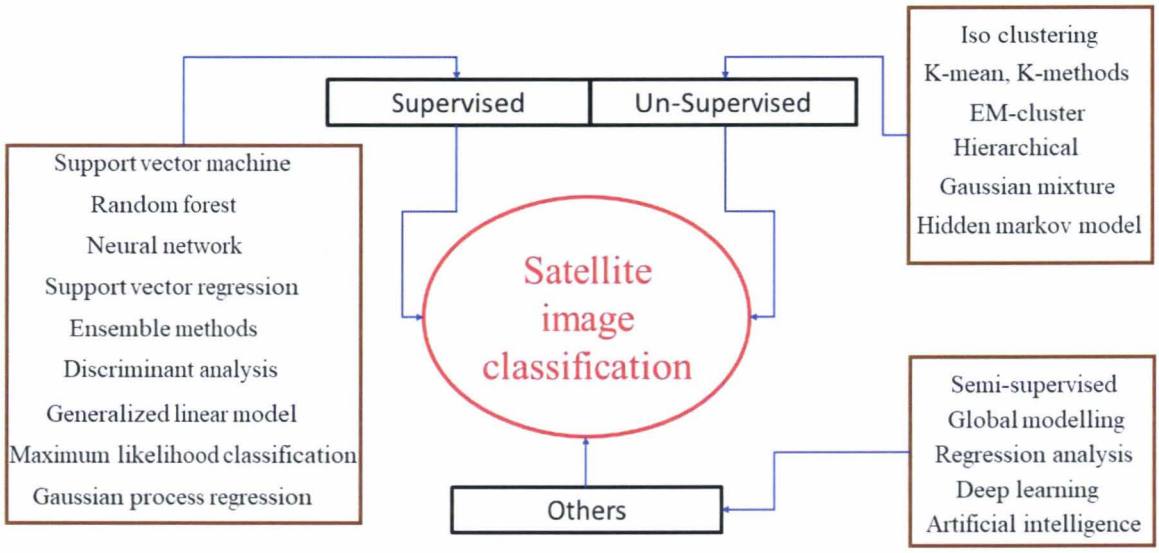

Figure 34 Image classification methods.

Support vector machine (SVM) was formerly known as binary classifiers with an algorithm adapted to reduce the multiclass problems (Foody and Mathur, 2004). It was developed in the late 1970s, but SVM became more famous for remotely sensed

image processing in last decade due to algorithm's flexibility and higher classification accuracy outputs (Mountrakis et al., 2011; Pal and Mather, 2005; Zheng et al., 2015). An SVM is a supervised non-parametric discriminative statistical learning classifier (Li et al., 2007). SVM classifier performs supervised classification, in which it discriminates training samples with multidimensional hyperplanes in the feature space (Mavroforakis and Theodoridis, 2006). SVM is a set of supervised learning methods widely used for the classification, regression and outlier detection (Guzmán et al., 2018; Pedregosa et al., 2011). Figure 35 is an example of the linear and non-linear hyperplanes generated by the SVM classifier (Lardeux et al., 2009).

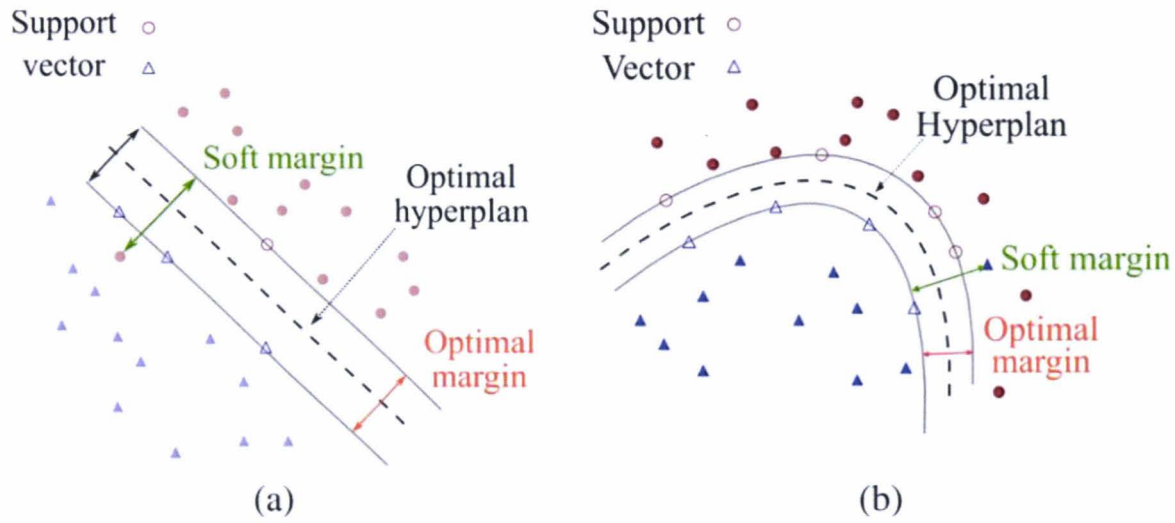

Figure 35 SVM classifier scheme in linear (a) and non-linear cases.
source: (Lardeux et al., 2009).

SVM is well known for the optimal separating hyperplane between various classes with the help of training cases. The training samples falling within the boundaries are the most critical for discrimination, SVM accurately illustrate these samples and prioritize them from the other classifiers. With comparison to other classifiers like neural networks, decision tree, and discriminant analysis, SVM performs better in the case of small training sets too (Betbeder et al., 2014a; Foody and Mathur, 2004). The samples lie at the edge of the class distribution in feature space, SVM uses them as training samples, while maximizing the likelihood classifier uses class means and covariance of training samples as an input (Foody and Mathur, 2004; Zheng et al., 2015). It fits for the remote sensing applications to perform precise land use and crop classifications

(Löw et al., 2013). The Guidici et al. (Guidici and Clark, 2017) study presented relative study to classify land cover classification using two machine learning classifiers (RF and SVM) and one deep learning classifier (Convolution Neural Network) and it was noticed that that SVM and CNN classifiers are performing reasonably higher with kappa classification accuracy 88%. With this review, we decided to choose the SVM algorithm for our land use classifications. Quality of classification are validated by estimating overall accuracy, confusion matrix (kappa coefficient), user's accuracy (inversely related to commission error), producer's accuracy (inversely related to omission error), and bias (bias = user' accuracy - producer's accuracy) (Foody, 2002; Schultz et al., 2016). The kappa coefficient can be obtained using confusion matrix by estimating overall classification accuracy to validate the classification outputs (Gumma et al., 2016; Peña-Arancibia et al., 2014; Qiu et al., 2018).

Conclusion of the chapter

In this first chapter, we presented the "Green Revolution" in India and its contribution to irrigation problematics. In particulary, we discussed on the groundwater depletion in the past decades and its relation with irrigation agricultural practices. We further discussed on remote sensing theory and its applications as it represents a very interesting tool for monitoring irrigated areas. The role of optical and SAR remote sensing for irrigated cropland monitoring is in-depth, reviewed and discussed. Optical and SAR indices estimation and their application for irrigated areas monitoring are presented as they can provide interesting inputs for the physical, empirical and semi-empirical models for precise irrigated cropland monitoring.

CHAPTER 2: Study area and Dataset

Summary

This chapter gives detailed information about the experimental watershed, performed ground observations for the agricultural cropland monitoring, and the satellite datasets used for the thesis research work. The detailed synthesis of various crops cultivation and satellite data treatment is presented in the chapter.

2.1 Introduction

Berambadi watershed is a part of the Kabini river basin, which is a major tributary of the Cauvery river located in southern peninsular India (Sekhar et al., 2016) (Figure 36). Kabini river basin (Area ~ 8,000 km^2) is also identified as a Critical Zone Observatory (CZO) (Feng et al., 2017; Sekhar et al., 2016; Seyfried et al., 2018). Berambadi watershed is monitored by the Indo-French cell for water sciences (IFCWS-IISc) since the year 2002 under various national and international research projects (Ruiz and Sekhar, 2016; Sekhar et al., 2016; Sekhar and Ruiz, 2010).

The Berambadi watershed is established under project AMBHAS (Assimilation of Multi-Satellite at Berambadi watershed for Hydrology and land Surface experiments) (A.K. Sharma et al., 2018; Tomer et al., 2015) as a calibration (CAL) and validation (VAL) site of various satellite missions like Radarsat-2, Soil Moisture and Ocean Salinity (SMOS) and Radar Imaging SATellite (RISAT-1). Berambadi watershed was established by IFCWS-IISc laboratory to perform various hydro-bio-geo-chemical studies (Ruiz et al., 2016; Sekhar et al., 2016; Sriramulu et al., 2017b), socio-ecological studies (Robert et al., 2018, 2017b), and land surface studies (Eswar et al., 2016; Sharma et al., 2016; Tomer et al., 2015). The Berambadi experimental watershed is located in the Gundlupet taluk, Chamrajanagra district of Karnataka state in south India.

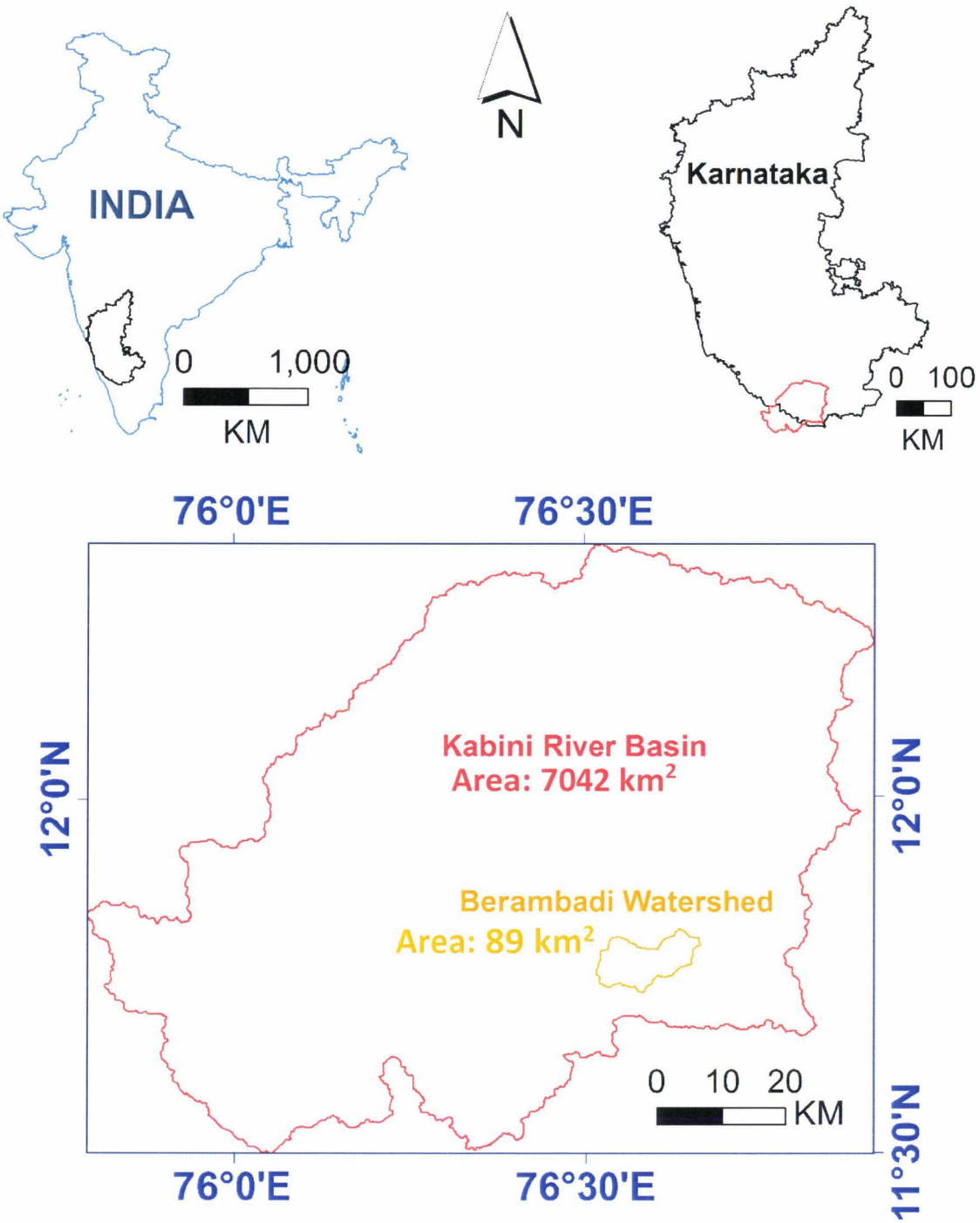

Figure 36 Location of the Berambadi watershed.

The thin layer between the top of the canopy and bottom of the groundwater aquifer involving rock, soil, water, air and living organisms where all complex interactions are happening is responsible for the natural habitat and availability of life-sustaining resources (NRC report 2001, (Sekhar et al., 2016). This thin layer is known as Earth

Critical Zone. The Berambadi watershed is established as a pilot study of the Kabini CZO. The CZO's main objectives are to monitor water-soil-life interactions and impact of climate change and LULC changes and their impacts on hydrological and biological fluxes (Banwart et al., 2013; Sekhar et al., 2016; Seyfried et al., 2018).

2.2 Berambadi watershed characterization

Berambadi watershed is characterized as an agricultural watershed with intensive groundwater irrigation. The total area of the Berambadi watershed is 89 km^2. The 58% land of the watershed is characterized as an agricultural cropland, and approximately 20% of the agricultural croplands are characterized as an intensive groundwater irrigated cropland. The Berambadi watershed is an excellent example of a complex agrosystem with high variability in the form of land-use dynamics and land-use practices. Major land use and land cover categories in the watershed are agricultural cropland (approximately 52%), reserved forest (about 32%) and others like settlement, waterbody, wasteland, road network, etc. (about 16%) (A K Sharma et al., 2018). The North-west and southern part of the Berambadi watershed is surrounded by the Bandipur reserve forest. Berambadi watershed is an agricultural watershed with high variability of land-use practices. Majority of farmers are rainfed cultivation crops (during monsoon and post-monsoon cropping seasons) in the watershed and groundwater is the only source of irrigation in the Berambadi watershed.

The Berambadi watershed is focused to monitor groundwater level, groundwater quality, soil hydraulic properties, rainfall distribution, crop types, land-use practices, surface soil moisture, root zone soil moisture, farmers decision for crop production and adaptation of farming practices for climate-changing conditions (Ruiz et al., 2016; Ruiz and Sekhar, 2016; Sekhar and Ruiz, 2010). To increase the water holding capacity of farmland farmers use to transport rich clay soil from the downstream or ponds and use to mix in their farmlands (Sriramulu et al., 2017a), which may increase the farm salinity too (Kizza, 2016).

National Bureau of Soil Survey and Land Use Planning (NBSS-LUP) has classified the soil map of the Berambadi watershed. Soil texture in the Berambadi watershed can be categorized into six main soil texture categories (Figure 37) like clay (17%), clay loam (7.6%), sandy loam (13.4%), gravelly loamy sand (9%), loamy sand (3.3%), and sandy clay loam (50.2%) (Anuraga et al., 2006). Clay soils are existing in the valleys of the watershed, and they are considered as a fertile with high water holding capacity soils (Ferrant et al., 2016; Grisso et al., 2009).

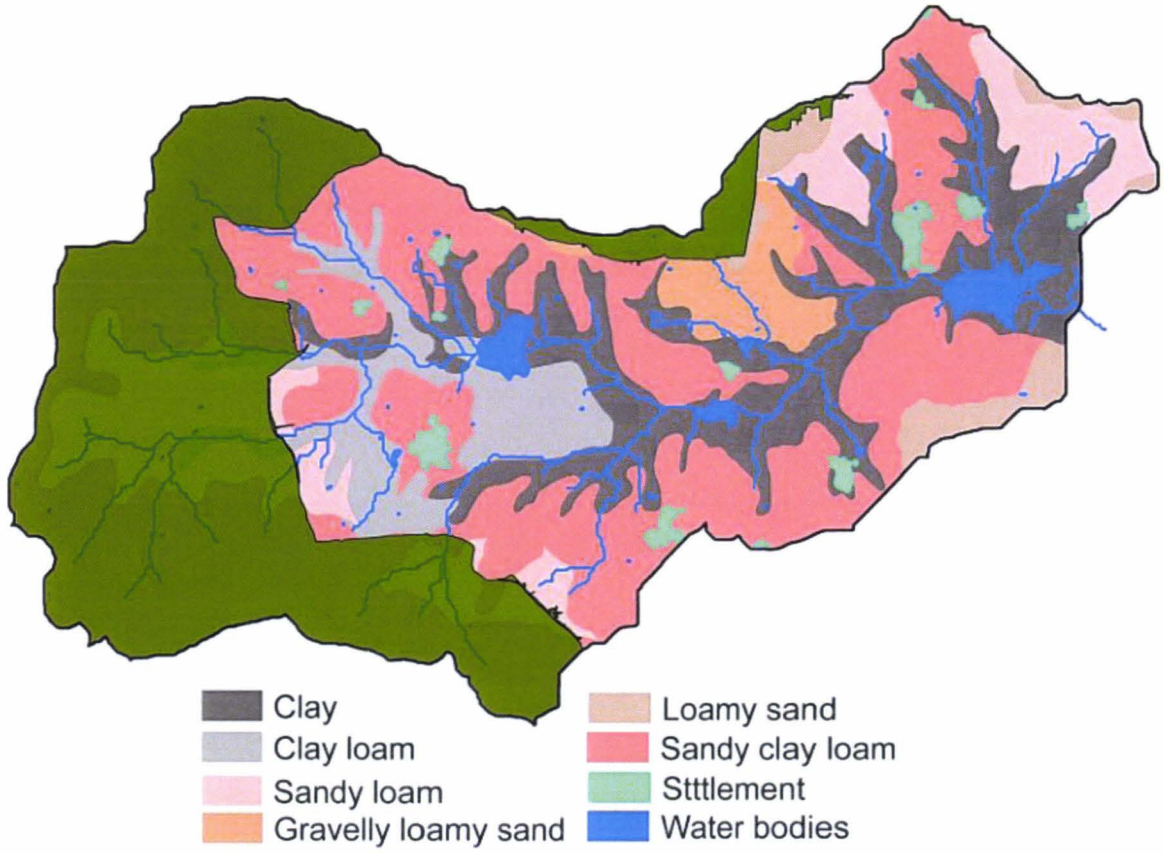

Figure 37 Surface soil texture of the Berambadi watershed.

Indian Meteorological Department (IMD) has characterized four meteorological seasons in India, winter (January and February), pre-monsoon (March to May), south-west monsoon (June to September) and post-monsoon (October to December). According to the local weather condition farmers are planning to cultivate the crops. As presented in figure 38, the study site mainly cultivated three crops (kharif, rabi, and summer) in a year. The long-term (annual) cumulative rainfall

(kharif+rabi+summer) in the study region from the year 1951 till 2016 daily rainfall data (Figure 38) has been collected from the Gundulupete taluk weather station (maintained by the Karnataka State Natural Disaster Monitoring Centre (KSNDMC)).

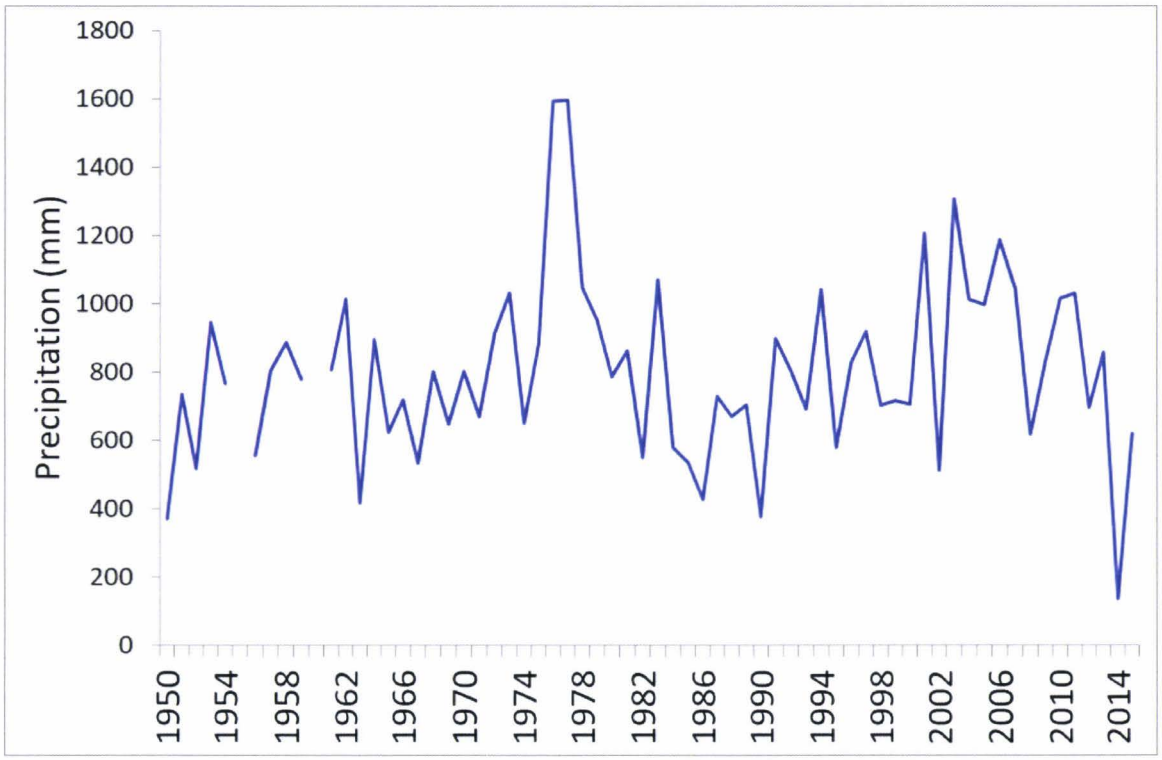

Figure 38 Annual rainfall in the Gundulupete taluk from the year 1951 till 2016.

Annual precipitation for the cropping year 2015 = Precipitation (kharif 2015 + rabi 2015-16 + summer 2016). The Berambadi watershed is characterized as a semi-arid climate zone with an annual rainfall of approximately 800 mm (Javeed et al., 2009). The annual potential evapotranspiration (PET) in the watershed is about 1100 mm (Eswar et al., 2016; Tomer et al., 2015). The higher annual PET of approximately 300 mm in the watershed is due to intensive groundwater irrigation practices (A K Sharma et al., 2018). The monthly cumulative rainfall (precipitation) in the watershed (Muddur weather station) is presented in Figure 39 from the year 2004 till the year 2018 with some data gap in the year 2008-09 and 2012. The south-west monsoon is dominant in the Berambadi watershed with cumulative seasonal rainfall of approximately 550 mm.

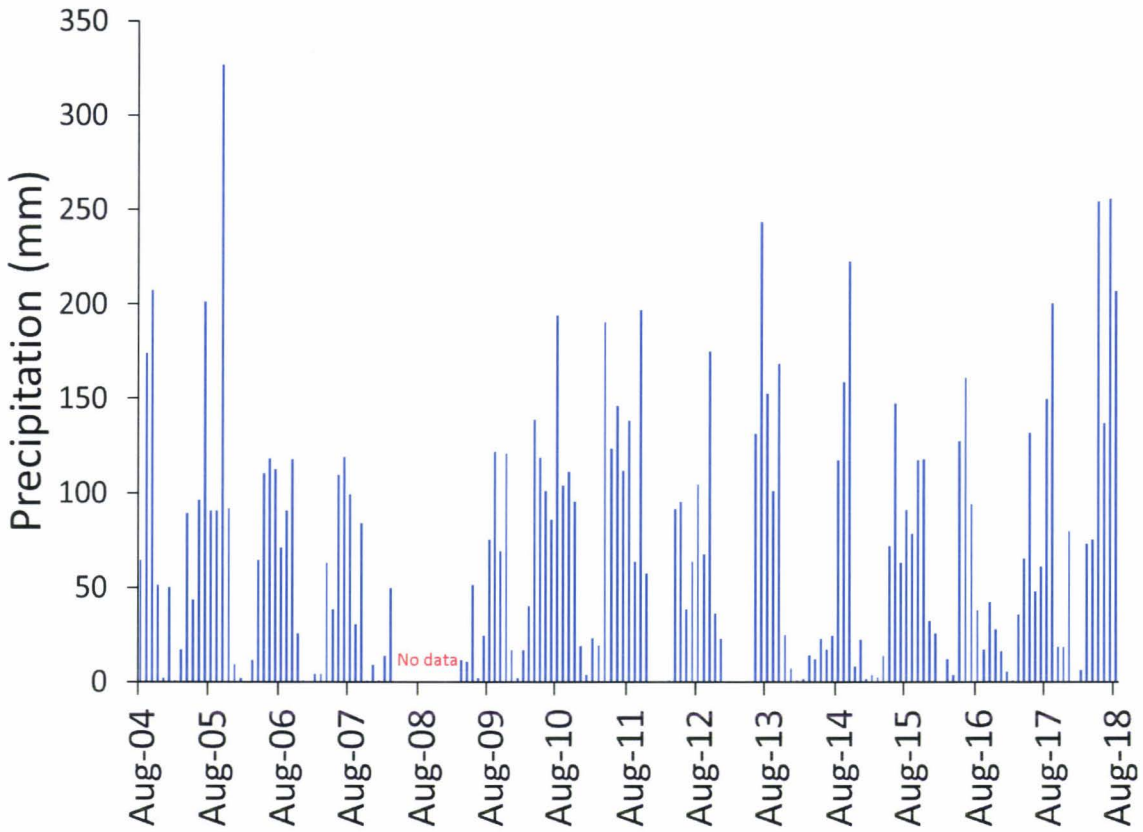

Figure 39 Monthly cumulative rainfall in the Berambadi watershed for the year 2004 till 2018.

Shuttle Radar Topographic Mission (SRTM) 1 arc-second product (Y. Liu et al., 2018; Xiong et al., 2017) with 30 m spatial resolution Digital Elevation Model (DEM) is used with Soil Water Assessment Tool (SWAT) model (Di Luzio et al., 2002) to delineate the watershed boundary and drainage network (Figure 40). The highest and lowest altitude in the Berambadi watershed is respectively 1369 m and 807 m. The main drainage of the watershed is connecting reserve forest in the west and the outlet of the watershed in the east.

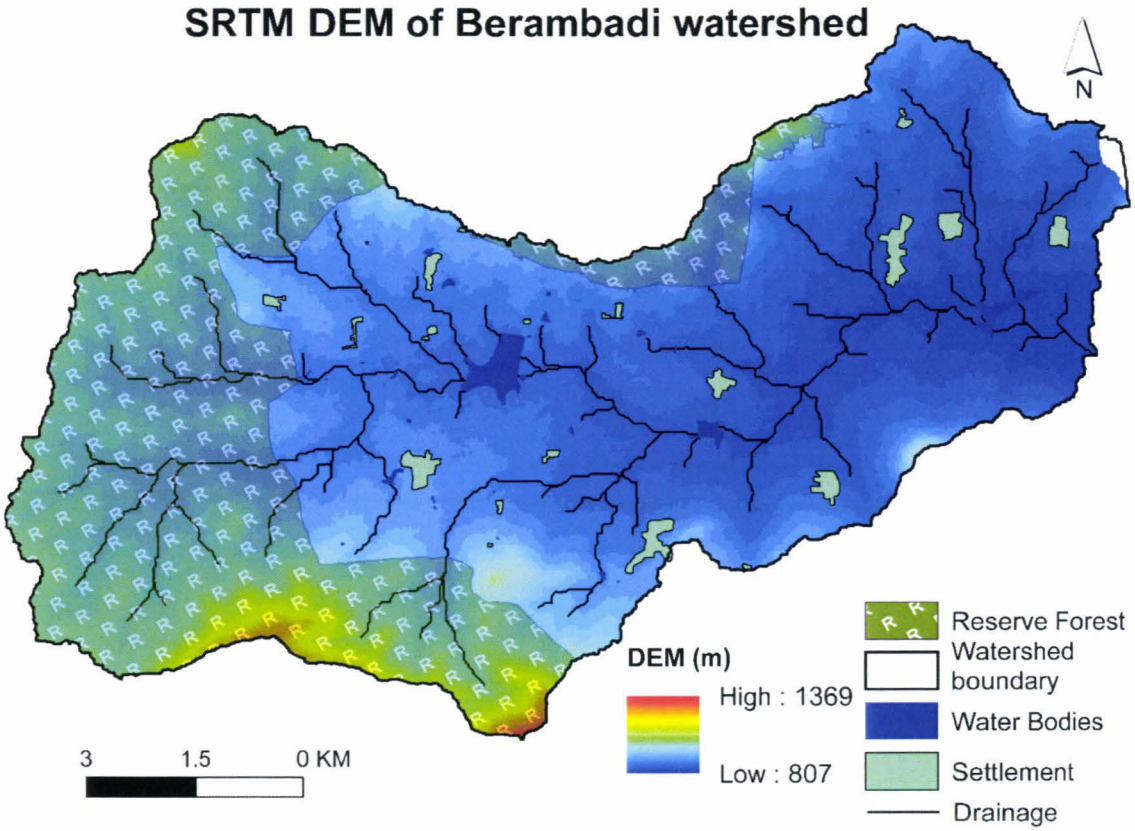

Figure 40 DEM of the Berambadi watershed.

2.2.1 Cropping seasons

Crop production in the Berambadi watershed primarily depends on the monsoon rainfall. Farmers adopted local climatic conditions and growing various crops according to the local cropping seasons (Robert et al., 2017b). Mainly, the Berambadi watershed is characterized into three cropping seasons known as summer, kharif, and rabi (Figure 41). Kharif cropping season follows the main monsoon duration, and it was noticed by the ground survey that the during kharif season approximately 95% of farmers are cultivating their farmlands. The crops in this season are divided into two main categories rainfed and irrigated. The major rainfed crops of this season are maize, country beans, sunflower, marigold, sorghum, finger millet and, groundnut. Main irrigated crops of kharif season are chili, onion, beetroot, solar beans, tomato, turmeric, ginger, sugarcane, and banana. In case of insufficient rainfall or shift in rainy days', farmers use to partial irrigate their croplands. Even though it depends on the

groundwater facility availability with farms. Sometimes farmers use to borrow or purchase water from the neighborhood farmlands to protect their crops.

	Summer Season	Kharif Season (monsoon)	Rabi Season (post-monsoon)
	15th Jan to 15th May	**15th May to 15th Sept**	**15th Sept to 15th Jan**
Non-irrigated crops		Maize Country beans Sunflower Marigold Sorghum Finger millet Groundnut	Maize Country beans Chickpea Groundnut Horse gram Gram Cotton
Irrigated crops	Watermelon Beetroot Cabbage Tomato	Chilli Beetroot Solar beans Tomato	Solar beans Garlic Cabbage Beetroot
		Turmeric (8 to 9 months)	
	Sugarcane (12 months)		
	Banana (12 months)		

Figure 41 Crop calendar.

Rabi cropping season begins in September with some extended crops like turmeric, banana, sugarcane and, ginger. During rabi season, mainly irrigated and non-irrigated crops are cultivating. Due to less rainy days, the total area for non-irrigated cropland is lesser than kharif cropping season. The main non-irrigated crops of this season are maize, country beans, chickpea, groundnut, horse gram, gram, and cotton. Due to recharge after monsoon cropping season (in normal monsoon year farmers are not pumping the groundwater and this duration the groundwater is getting recharge (A K Sharma et al., 2018)), farmers with borewell facility are cultivating irrigated crops like solar beans, garlic, cabbage, beetroot, turmeric (continues from the kharif season), sugarcane and banana. Summer cropping season does not have fixed rainy days, so it completely depends on the groundwater irrigation. The main crops of this season are vegetables, watermelon, beetroot, cabbage, tomato, sugarcane, and banana. Due to non-availability of rainfall, the PET in summer season is higher than the kharif and rabi (Eswar et al., 2016; Sekhar et al., 2016).

2.2.2 The diversity of farming practices

Multiple crops with various cropping management practices make the system complex to study using remote sensing techniques. It is important to understand the various crop growth stages and the farm management practices in the Berambadi watershed by field surveys. A total more approximately 30 crop varieties are cultivating in the watershed. Some crops are seasonal, some are dual season and some crops span is annual.

Turmeric (Figure 42(n)) is one of the major crops being cultivated in the watershed, which is used as a spice worldwide. Turmeric crop is considered as a cash crop, and growth duration of the turmeric crop is eight months (15^{th} May to 15^{th} Jan). Turmeric is starting with kharif cropping season and continuing to the rabi season irrigation of approximately 15 days interval. Figure 42 has shown various stages (from seeding (a) until harvesting (i)). Once the turmeric leaves are fully dried, it is an indication that turmeric roots can be harvested. After harvesting the turmeric roots, it is further divided into two parts mother root and turmeric roots. Farmers are collecting storing these mother roots to seed next year. After harvesting the turmeric roots, it needs to do a process before selling it in the market. As shown in the image (l) of Figure 42, farmers are making a pit, boiling turmeric roots, and then letting them dry. After this process, turmeric roots are becoming hard, and it can preserve for a longer duration.

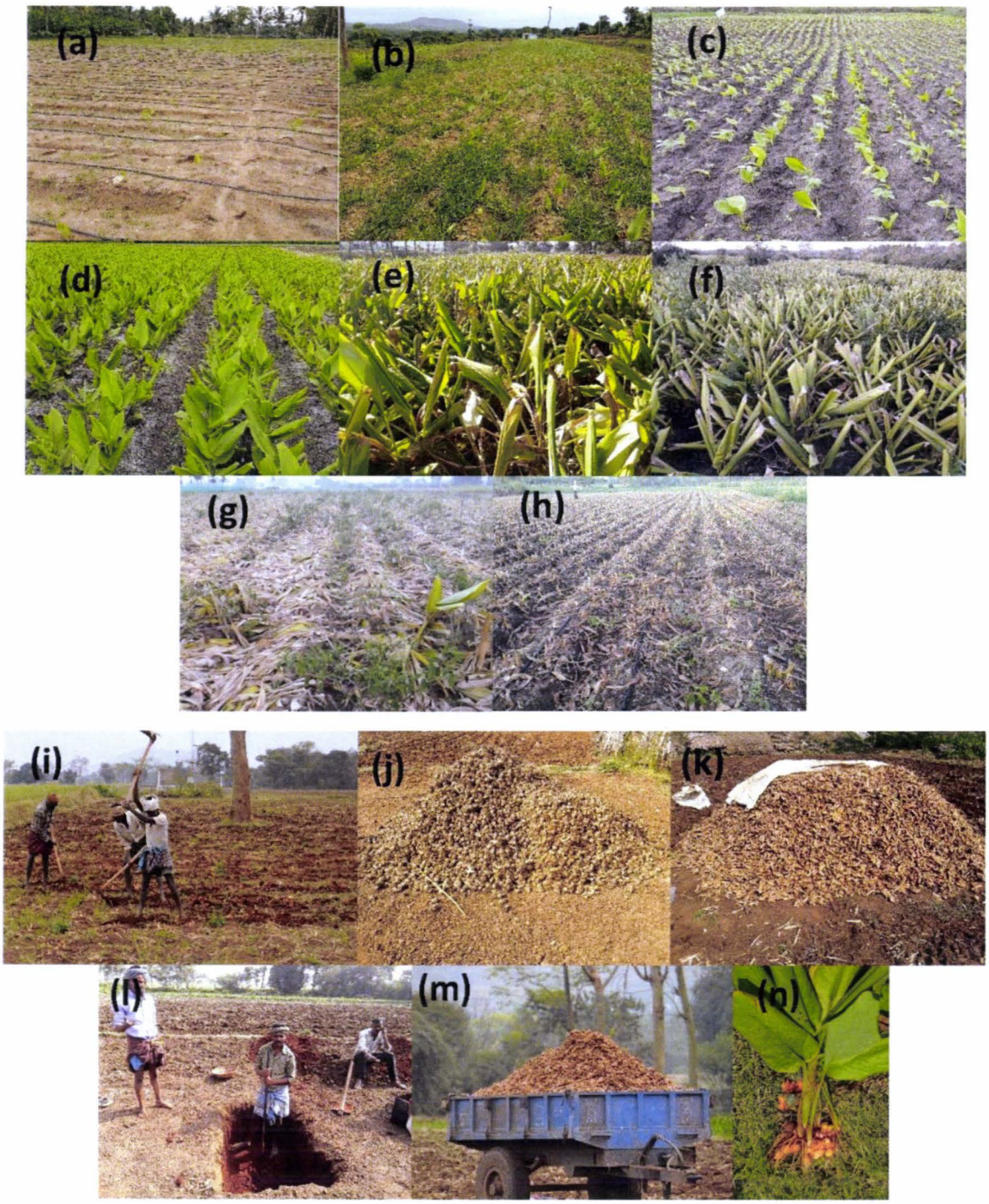

Figure 42 *Turmeric crop (n) growth stages (a to h).* After harvesting (i) the mother root (j) and turmeric root (k) it is processed (l) for the transporting (m) to market.

Turmeric crop needs high surface soil moisture or intensive irrigation during crop growth. Total cultivation duration of the turmeric crop is eight months. Due to long-duration crop, farmers prefer to seed short duration (2-3 months) crop with as shown

in Figure 43. Usually, onion and beetroot use to grow with turmeric so that farmers can get financial support after three-months by selling beetroot or onion. Some farmers prefer to grow chili to grow with turmeric as chili is also of the eight-month crop with several harvesting stages. Turmeric crop is cultivated using all three kinds of irrigation practices known as drip, flood, and sprinkler, as per farmers' financial condition.

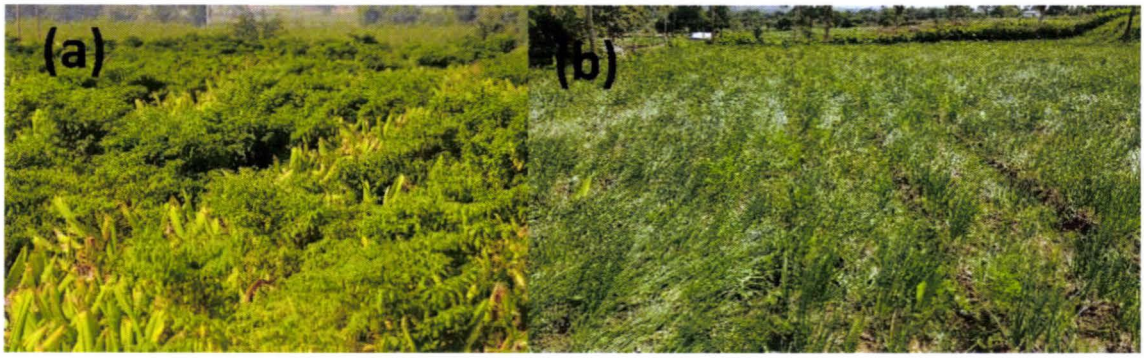

Figure 43 Turmeric crop mixed with other crops like chili (a) and onion (b).

Banana is a twelve-month duration irrigated crop (Figure 44). Normally banana is seeding in the rabi cropping season, and it is harvesting in the next year same cropping season. After monsoon season the groundwater usually became shallow and during rabi seasons sunny days are more compared to the kharif season. Banana is required intensive irrigation facility with three days' interval in starting for first three months. To avoid the crop loss due to groundwater uncertainty, farmers are using sprinkler irrigation while seeding for the first three months and then switching to the drip irrigation for remaining crop duration.

Figure 44 Banana growth stages (a to d).

Due to banana is a twelve-month crop, farmers prefer to cultivate three-month short duration crops with it like watermelon, beetroot, garlic, and pumpkin. The multi-cropping (Figure 45) supports farmers financially and help to utilize initial intensive irrigation.

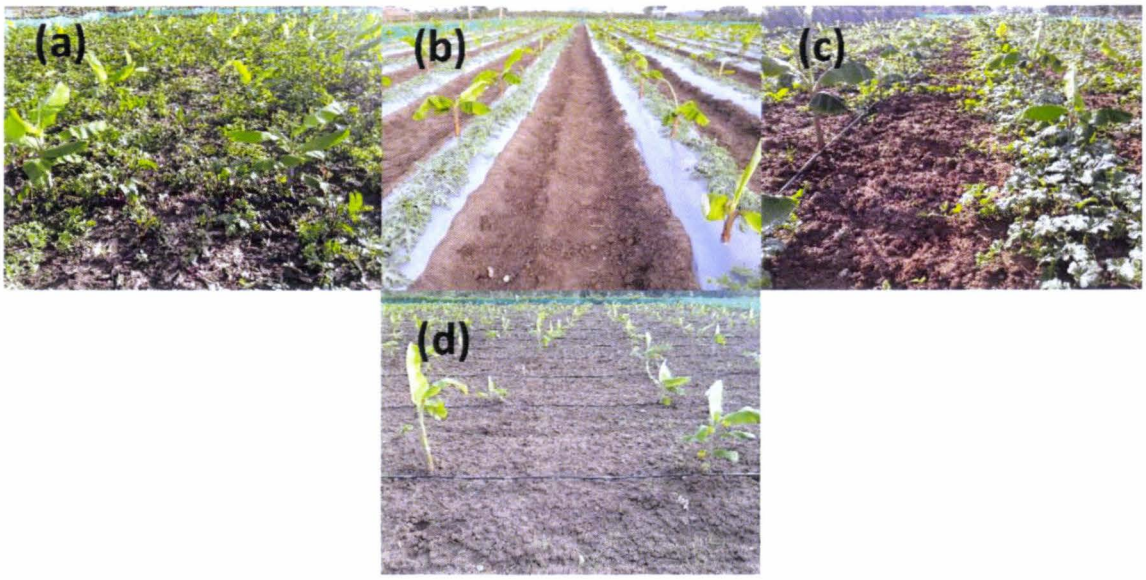

Figure 45 Banana with other crops like beetroot (a), watermelon (b), pumpkin (c) and garlic (d).

Maize is one of the six major crops in the watershed during both kharif and rabi cropping seasons. Majority of farmers are cultivating maize without irrigation, few farmers during less rainy days are utilizing partial irrigation for the maize crop. The maize grain is using for the human's food, and the remaining part of the plant is using as fodder for the livestock. Figure 46 shows various growth stages of the maize crop.

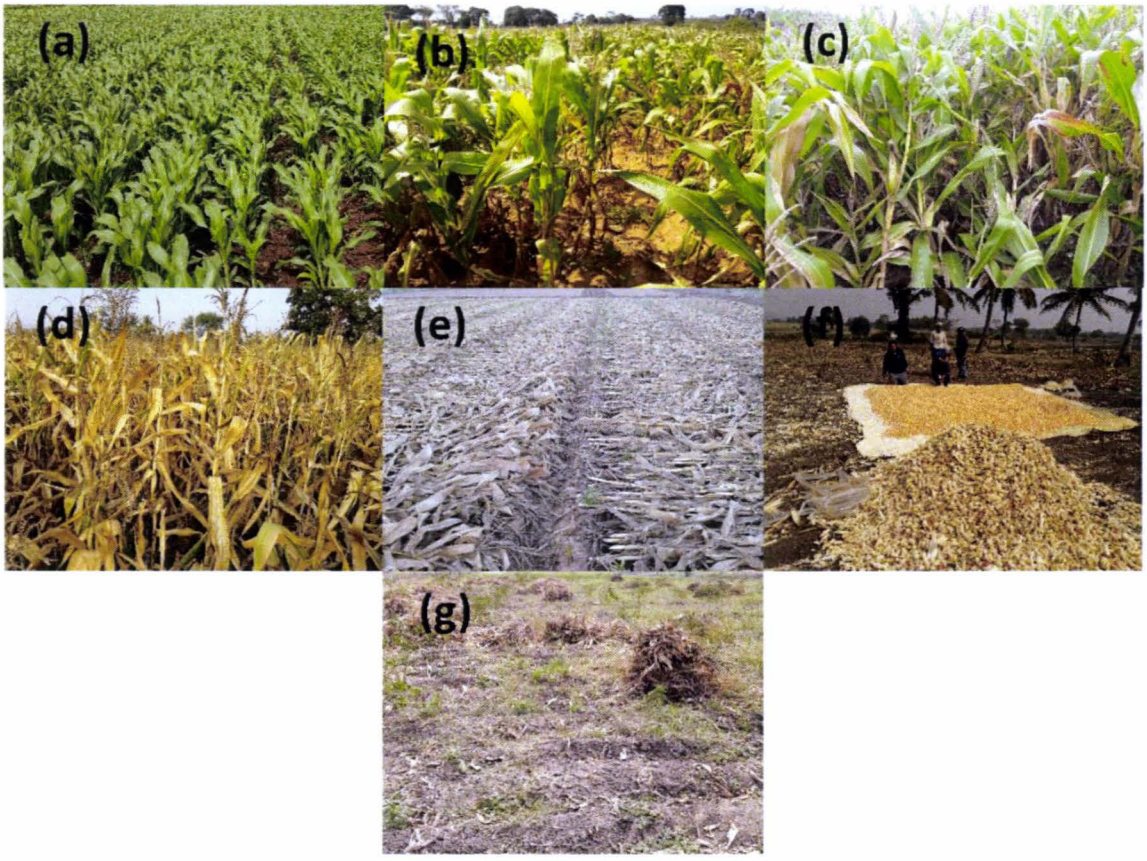

Figure 46 *Maize crop growth staged from (a) to (e), harvesting (g)* the fruit to sell in the market and remaining stem collection (g) for the fodder of the cows.

Sunflower is also one of the six major crops cultivating in the watershed during the kharif cropping season. Figure 47 shows various growth stages of the sunflower crop. It is growing only during kharif season spatially distributing in the watershed. The sunflower grains are using to extract its oil for cooking purposes. After harvesting

sunflower buds, farmers are leaving the stem in the farmland and mixing with soil during the next cultivation.

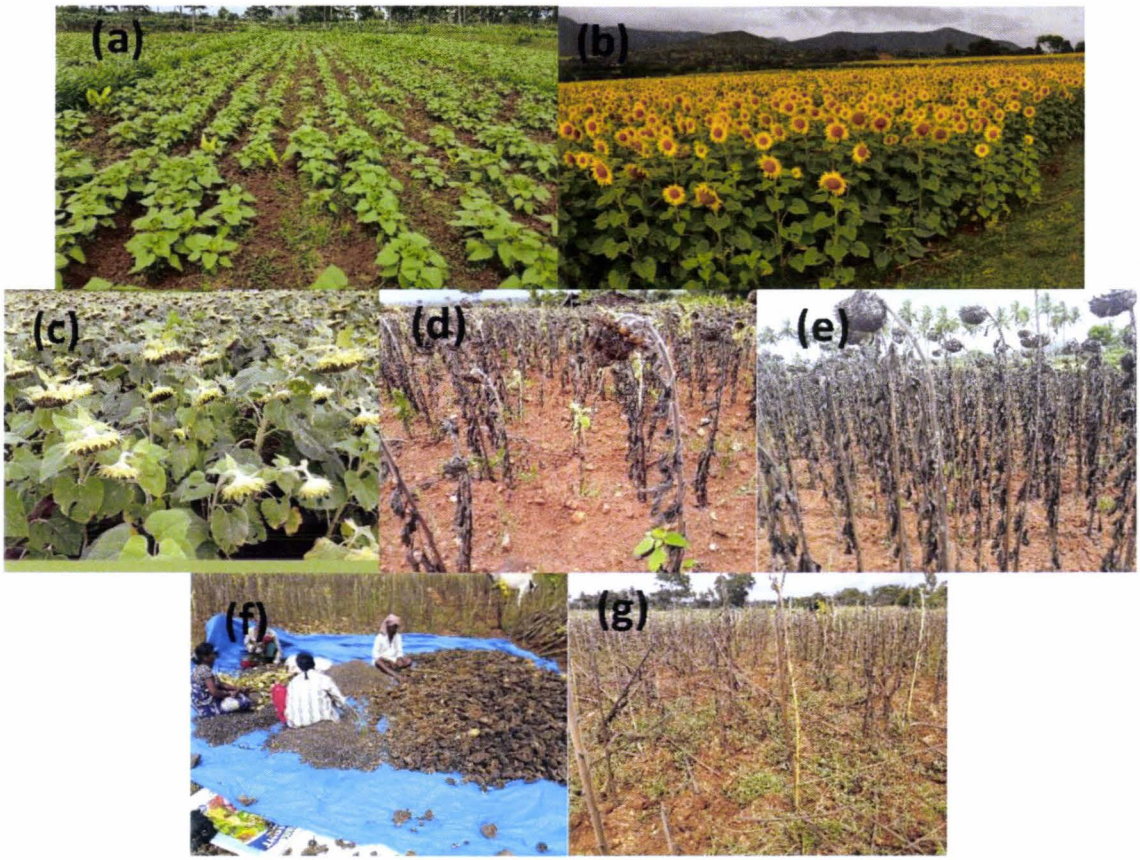

Figure 47 *Sunflower crop growth stages from (a) to (e) and harvesting the seeds (f)* to sell in the market, the remaining stem is left in the field (g) which will be mixing in the soil during the next cropping season.

Marigold is also a vastly growing crop in the watershed during the kharif cropping season. Figure 48 presented various stages of the marigold crop. Marigold is first cultivating in the nursery and, after two weeks it is shifting to the farmlands. It is a rainfed crop, but sometimes farmers are utilizing partial irrigation during cultivating in the nursery before transferring in the farmlands. Marigold is harvesting multiple time during crop growth for perfume purpose and decoration purposes. After three months of the cultivation, farmers are harvesting big flowers only, and like this, they are proceeding every week. After all harvestings, farmers are letting the dried stems in the farmlands and mixing with soil during the next cultivation.

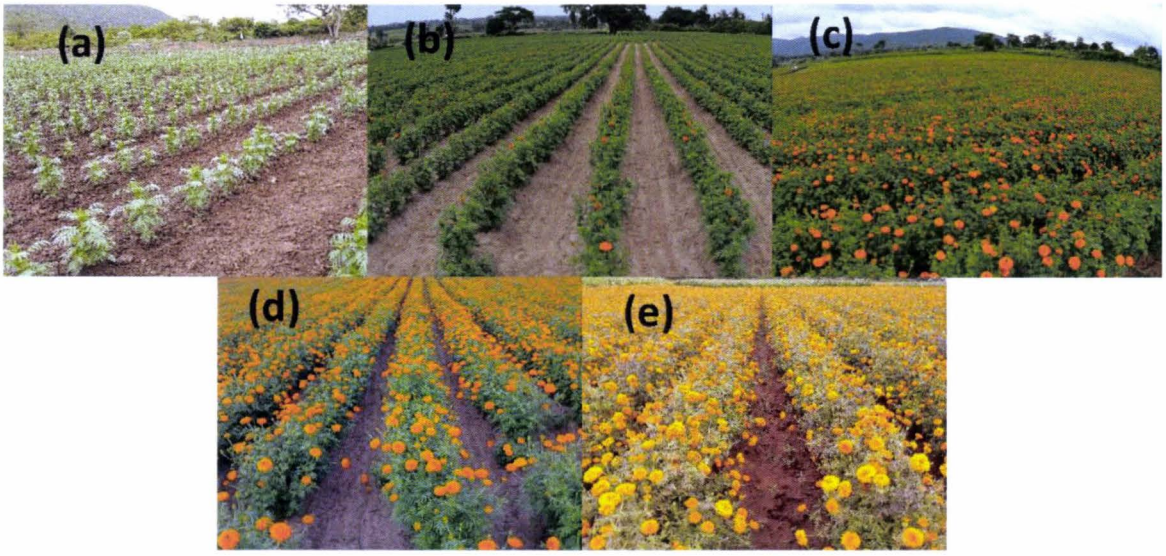

Figure 48 Marigold crop growth stages (a) to (e).

Sorghum is also a vastly growing crop in the watershed during the kharif cropping season. Sorghum is also known as Jowar crop. Figure 49 presents various growth stages of the sorghum crop. It is a purely rainfed crop and needed less farmer's assistance. The powder of sorghum grains is used to prepare bread in various parts of India, and the stem of the plant is using as fodder for the livestock.

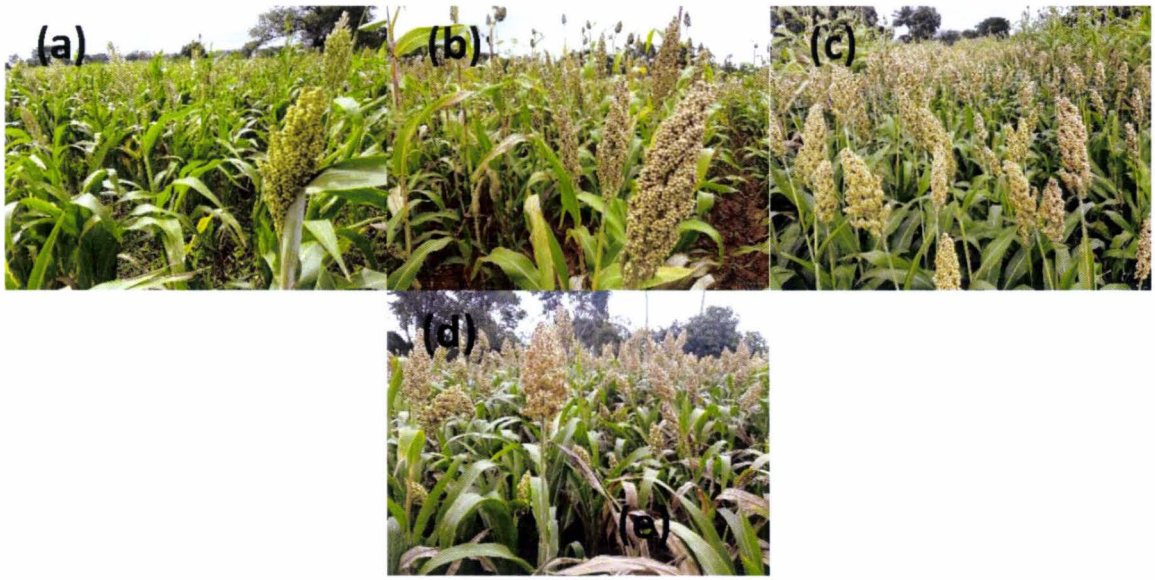

Figure 49 Sorghum (jowar) crop growth stages (a) to (d).

Tomato is considered as a cash crop with several harvestings. It is a purely irrigated crop of four-five months' duration. First, the tomato is planting in the nursery and then shifting to the farmlands (Figure 50(a)). It is required to take care during complete growth stages as the plant is fragile. Tomato is usually growing in the rabi season, but some farmers are cultivating in the kharif and summer seasons also. During rabi season sunny days are more than kharif and the groundwater use to be shallow after getting a recharge by the monsoon. So, the farmers with groundwater facility and preferring to grow tomato usually cultivating in the rabi season. Due to the price of vegetables are comparatively high in the summer season, farmers with groundwater facility prefer to cultivate vegetables in the summer season too. Figure 50 presents various growth stages of tomato crop and, an image (g) show the harvesting stage. After finishing of all harvesting, the dried stems use to mix with the soil during next cultivation.

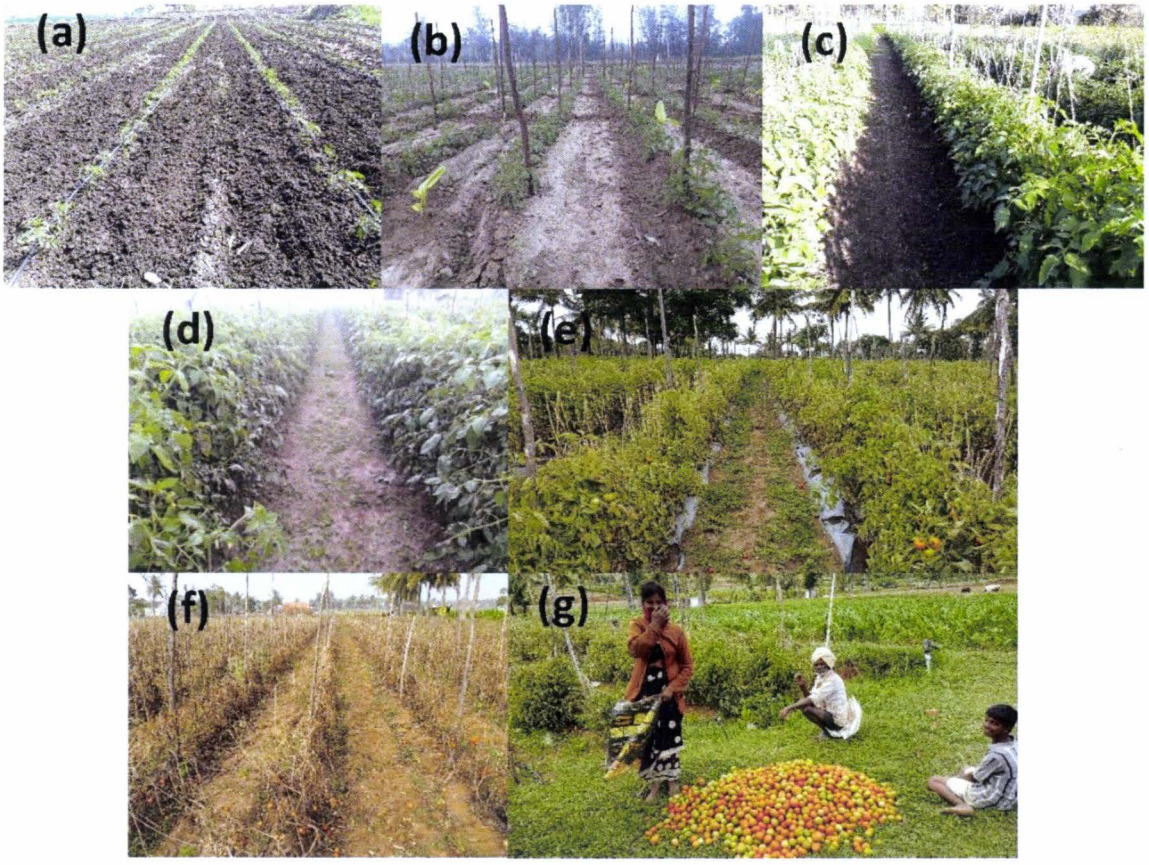

Figure 50 Tomato crop growth stages (a) to (f) and fruit harvesting (g).

Farmers with good irrigation facility only plan to grow sugarcane, as it is twelve-month duration crop. Majority of farmers in the watershed sugarcane starts with sprinkler or flood irrigation and then after two-three months they are switching to the drip irrigation. Figure 51 shows the cultivation stages of the sugarcane crop. Farmers are cultivating and harvesting the sugarcane manually only. After harvesting the sugarcanes either farmers are making jaggary locally, or they are selling it to the sugar mills for sugar preparation.

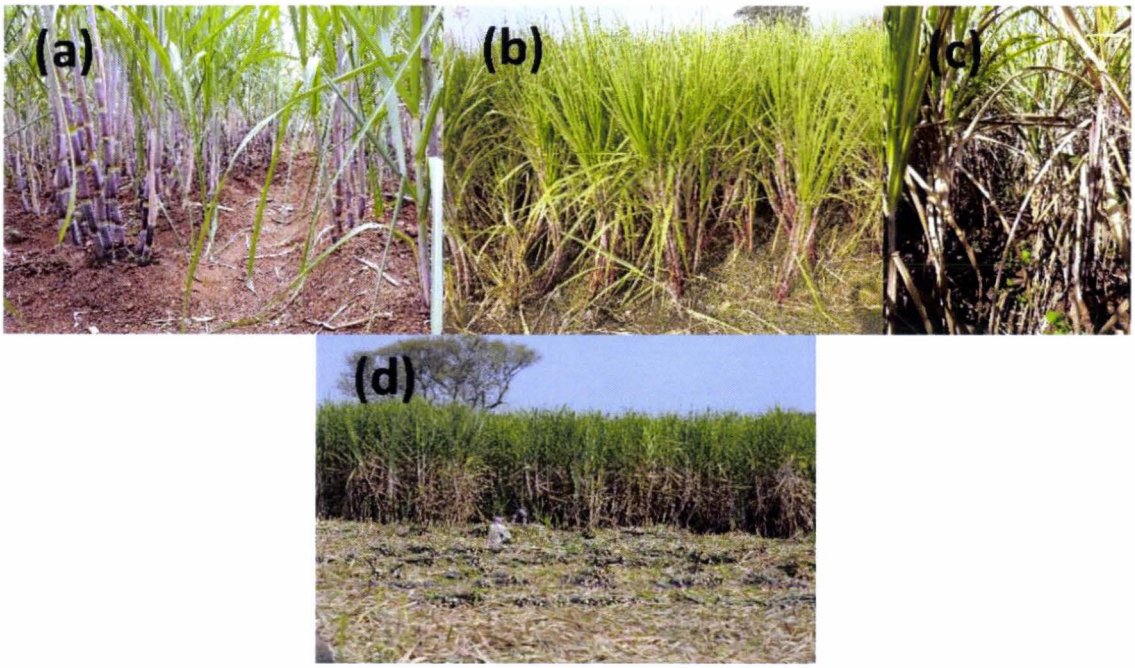

Figure 51 Sugarcane growth stages (a) to (c) and harvesting (d).

Garlic is also one of the cash crops grown in the Berambadi watershed. The crop growth duration is about three months with intensive irrigation using drip or sprinkler irrigation. Normally garlic is cultivated in rabi, but some farmers are growing in the kharif season also. The crop density of garlic is approximately 42 plants per m^2. Figure 52 shows various cultivation stages of the garlic crop.

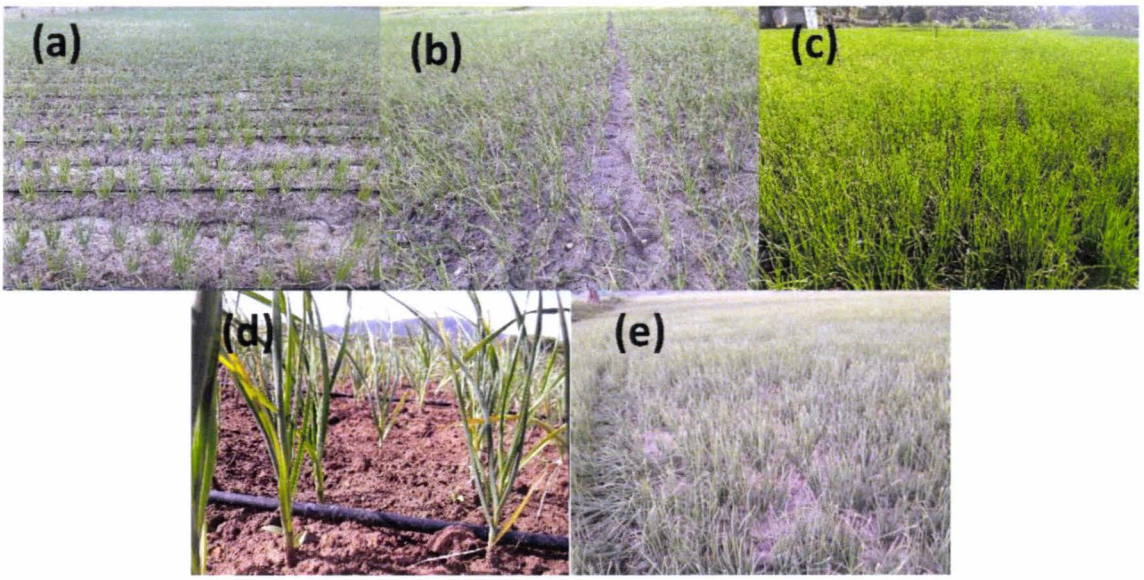

Figure 52 Garlic crop images (a) to (e).

Cabbage is an irrigated crop can be found all three cropping seasons in the Berambadi watershed. Majorly cabbage is grown in rabi and summer cropping seasons. It is a four-month duration crop need intensive irrigation facility. The cabbage crop density is six units per m^2; farmers are starting cabbage in the nursery and then shifting it to the farmlands. Figure 53 shows images of cabbage crop cultivation in the Berambadi watershed.

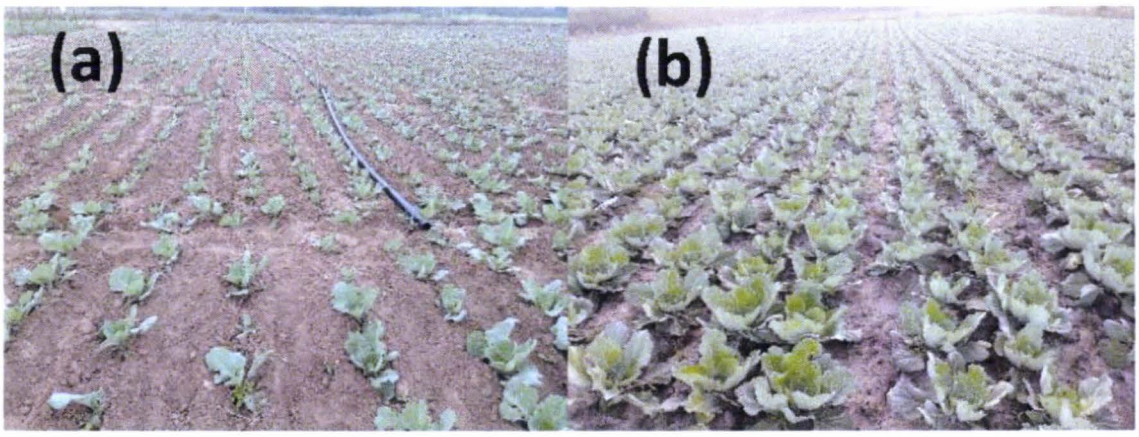

Figure 53 Cabbage crop growth stages (a) to (b).

Ragi (finger millet) is a type of millet grown in a rainfed condition during the kharif cropping season. It needs very less attention of the farmer and can grow with less rainy days. Figure 54 presents the growth stages of the ragi crop. The crop density of ragi crop is about nine bunches per m^2. In the last decade, ragi production has reduced in the watershed as the market price of maize/sunflower/sorghum was high compared to the ragi crop. Presently farmers' in the Berambadi watershed are cultivating ragi millet crop according to the requirement of the family.

Figure 54 Ragi crop growth stages from (a) to (c).

Solar bean is growing majorly during the rabi cropping season, and some farmer grows during kharif too. It needs irrigation facility with intensive care of farmer as it has to grow by hanging without contact with the soil like a tomato. Solar bean also has various harvestings after maturing during the crop growth. Figure 55 presents some crop growth stages of the solar bean. Majority of farmers are using a sprinkler to initiate solar bean and then switching to the drip irrigation till the final stage of the crop.

Figure 55 Solar bean crop growth stages from (a) to (c).

Country bean is a rainfed crop majorly growing in the kharif and rabi cropping seasons. Three and a half months after seeding, a farmer can do the first harvesting and then one or two more harvestings can depend on the crop growth. Country bean seeds have used a pulse and farmer not need to more intention if rain is good. Otherwise, as sown in Figure 56(a) farmer has to plough the soil and rotate it in the roots of the plants to retain soil moisture for the plant growth. Figure 56 shows various growth stages of the country bean crop in the watershed.

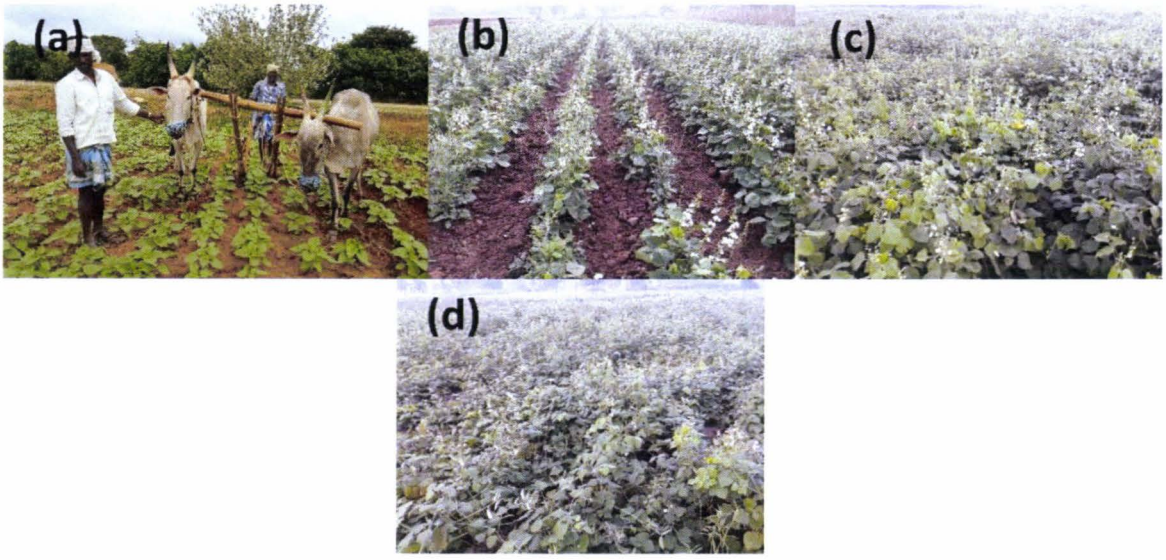

Figure 56 Country beans crop growth stages from (a) to (d).

Beetroot is an irrigated crop which is used as a vegetable or salad. The crop growth duration of beetroot is about three months. In the kharif cropping season majority of farmers are growing beetroot with turmeric as a double crop. During the rabi and summer cropping seasons, farmers are growing beetroot individually. Majority of farmers are using a sprinkler for the beetroot, but some farmers are using drip irrigation too. Figure 57 shows the various growth stages of the beetroot crop. Beetroot foliage cover is high during the mature stage with crop density approximately 12 crops per sqm.

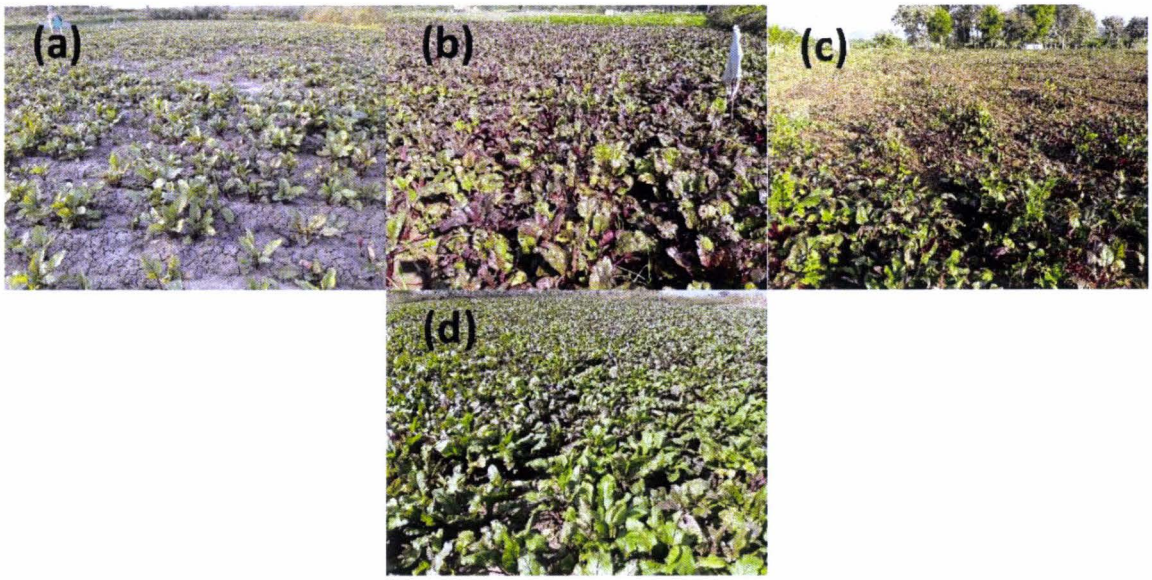

Figure 57 Beetroot crop growth stages from (a) to (d).

There are other several crops also grown in the Berambadi watershed, as shown in figure 58. The other major crops are chili, horse gram, beans, watermelon, black gram, pearl millet, cotton, pumpkin, groundnut, etc. In the kharif cropping season, chili (Figure 58(a)) is usually grown with the turmeric (Figure 58(a)), as both crop duration is of eight months. And farmer can get financial support with several harvesting of chilies. Some farmers are growing chili alone with drip irrigation facility. Horse gram (Figure 58(b)) is one of the major rainfed crops cultivating during the rabi cropping season. Horse gram is used as a pulse and farmer is not required to perform intensive farming practices, and the market rate is quite good. So, the majority of farmers prefer to grow horse gram during the rabi cropping season. During rabi cropping season some farmer prefers to cultivate various other beans (Figure 58(c)) together like kidney beans, peas, etc. Majorly, these beans are cultivating under rainfed condition in the Berambadi watershed. Watermelon (Figure 58(d)) can be seen in rabi and summer cropping seasons. Some farmers prefer to grow watermelon with banana (Figure 58(b)) as a mixed and some prefer to grow individual. Watermelon can cultivate only with irrigation facility. Majority of farmers are cultivating with drip irrigation with mulching (to maintain the soil moisture).

Chickpea (Figure 58(e)) is one of the major rainfed crops of the rabi cropping season. It is from the legume family, and it's also known as gram or Bengal gram. Chickpea is about four-month non-irrigated crop which can grow in rainfed conditions. Chickpea doesn't require intensive farming practices and farmers are getting a good market price as it's from the legume family. Due to this majority of farmers without irrigation facility are preferring chickpea to grow in rabi season. Few farmers are also cultivating pearl millet (Figure 58(f)) crop. Majorly, this is cultivating in rabi season to utilize a fodder for the livestock. Cotton (Figure 58(g)) is also one of the widely cultivated crops of rabi season. It is a non-irrigated crop majorly grown in sloppy terrain. Farmlands in sloppy terrain with sandy soil or soil with gravels use to cultivate cotton during the rabi season. Pumpkin (Figure 36(h)) is cultivating by a few farmers in the watershed during rabi and summer cropping seasons. In rabi season farmer prefer to grow pumpkin with banana (Figure 58(c)) and in summer they grow individually. Pumpkin is irrigated crop usually cultivating by drip irrigation. Some farmers use sprinkler irrigation too for the cultivation. Groundnut is also cultivating widely in the watershed during kharif and rabi seasons. It is a non-irrigated crop which can be cultivated in sandy or loamy soils.

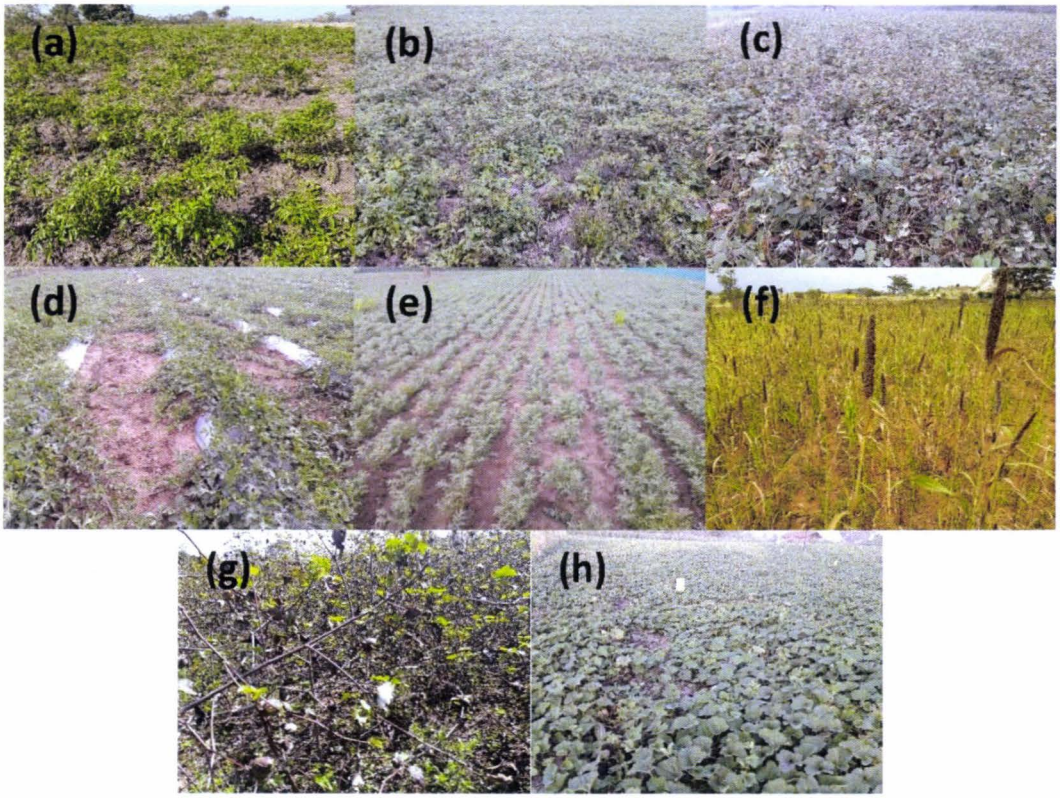

Figure 58 Other crops like Chilli (a), horse gram (b), beans (c), watermelon (d), chickpea (e), pearl millet (f), cotton (g) and pumpkin (h).

Farmlands without cultivation for particular cropping season or multiple seasons comes under the fallow land category. Farmers are letting their farmland fallow due to non-sufficient initial rainfall or lacking of irrigation resources or between two crop cultivation seasons or other personal factors. Figure 59 shows various types (six) of surface soil texture in the watershed. Apart from the high variability of surface soil texture, the surface soil roughness is also varied parcel to parcel. In figure 59 various combination of fallow land has been presented. The high variability in the surface soil texture and roughness makes system complex for study using microwave remote sensing (Bablet et al., 2018; Baghdadi et al., 2016; Renmin et al., 2016; Wang et al., 2015).

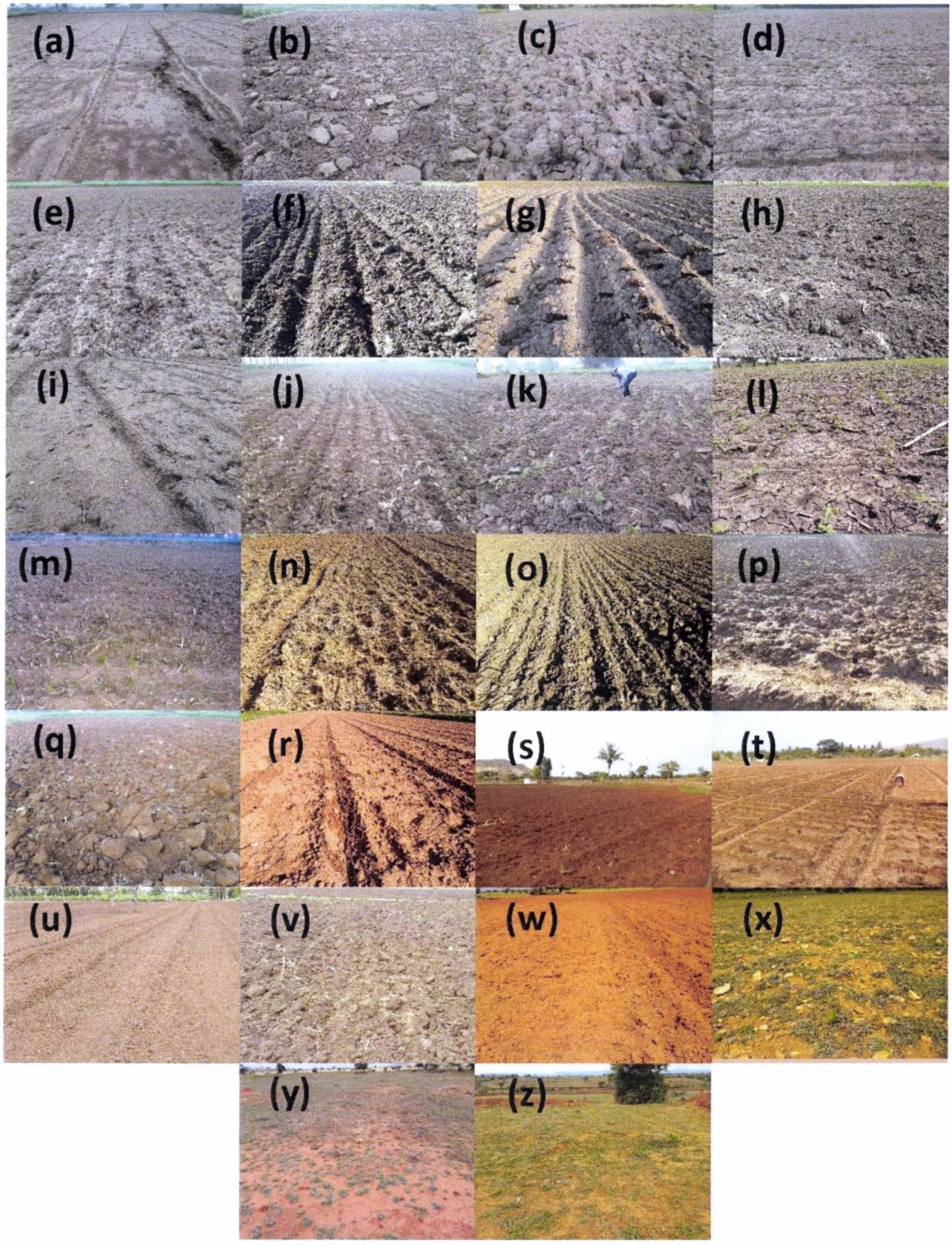

Figure 59 Fallow land variability (from (a) to (z)) in the Berambadi watershed.

2.2.3 Irrigation practices

Cropping practices in the Berambadi watershed depend on the rainfall and groundwater. Rainfall during two cropping seasons (kharif and rabi) assists farmers to cultivate the seasonal crops but the undulation in rainy days is compensating by the groundwater by partial irrigation. Farmers with rich in groundwater yield cultivate intensive irrigation crops (turmeric, banana, sugarcane, etc.) without being dependent on the rainfall. The spatial distribution of borewells in the watershed exists due to there is no other source of irrigation except groundwater in the watershed (Figure 60). The groundwater pumping borewell density is high in valleys of the watershed.

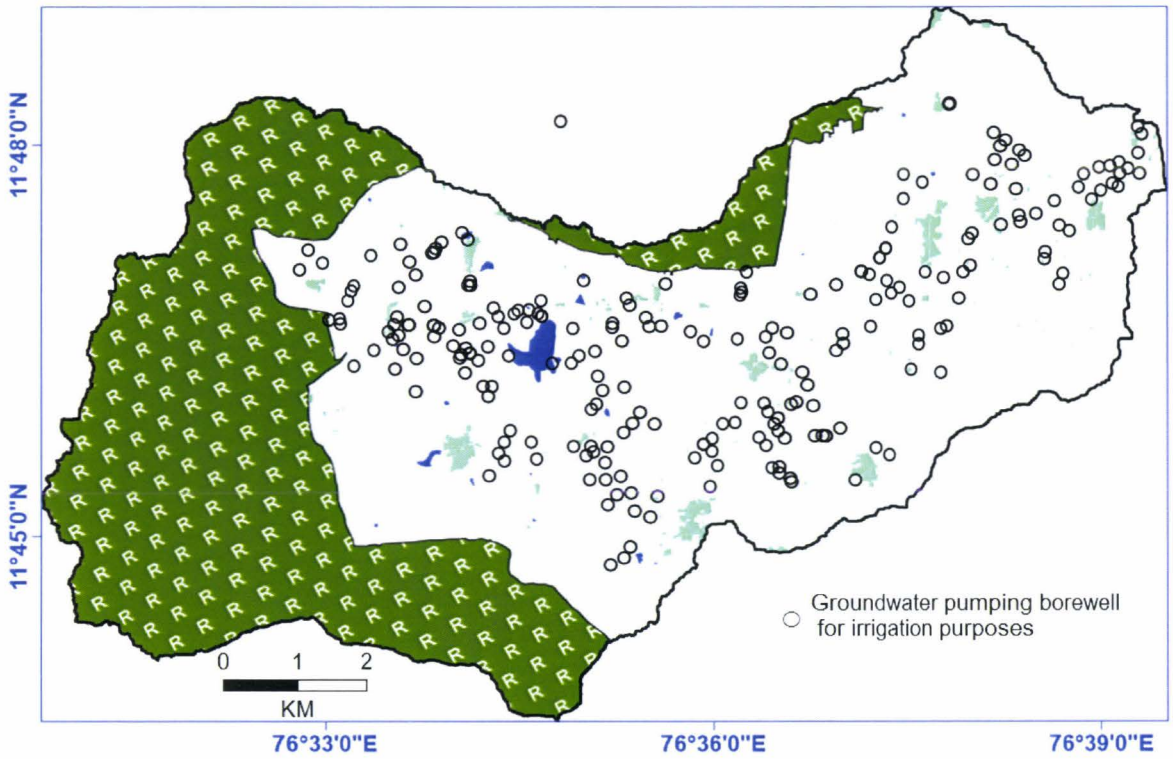

Figure 60 Groundwater is pumping borewell locations in the Berambadi watershed.

Most of the regions of India electricity for agricultural purposes is free (Shah et al., 2009). Farmers use to install highly dense borewells in/and surrounding valleys, and it was noticed that the depth of the borewell is varying from 50 m to 250 m. To pump the water from the 250 m depth to the earth surface most of the farmers have installed

motor of 7.5 KW. Government use to provide four-hour to eight-hour free electricity in the Berambadi watershed for agricultural purposes. Due to the short duration of electricity, farmers favour pumping the groundwater and store in an open water tank (Figure 61).

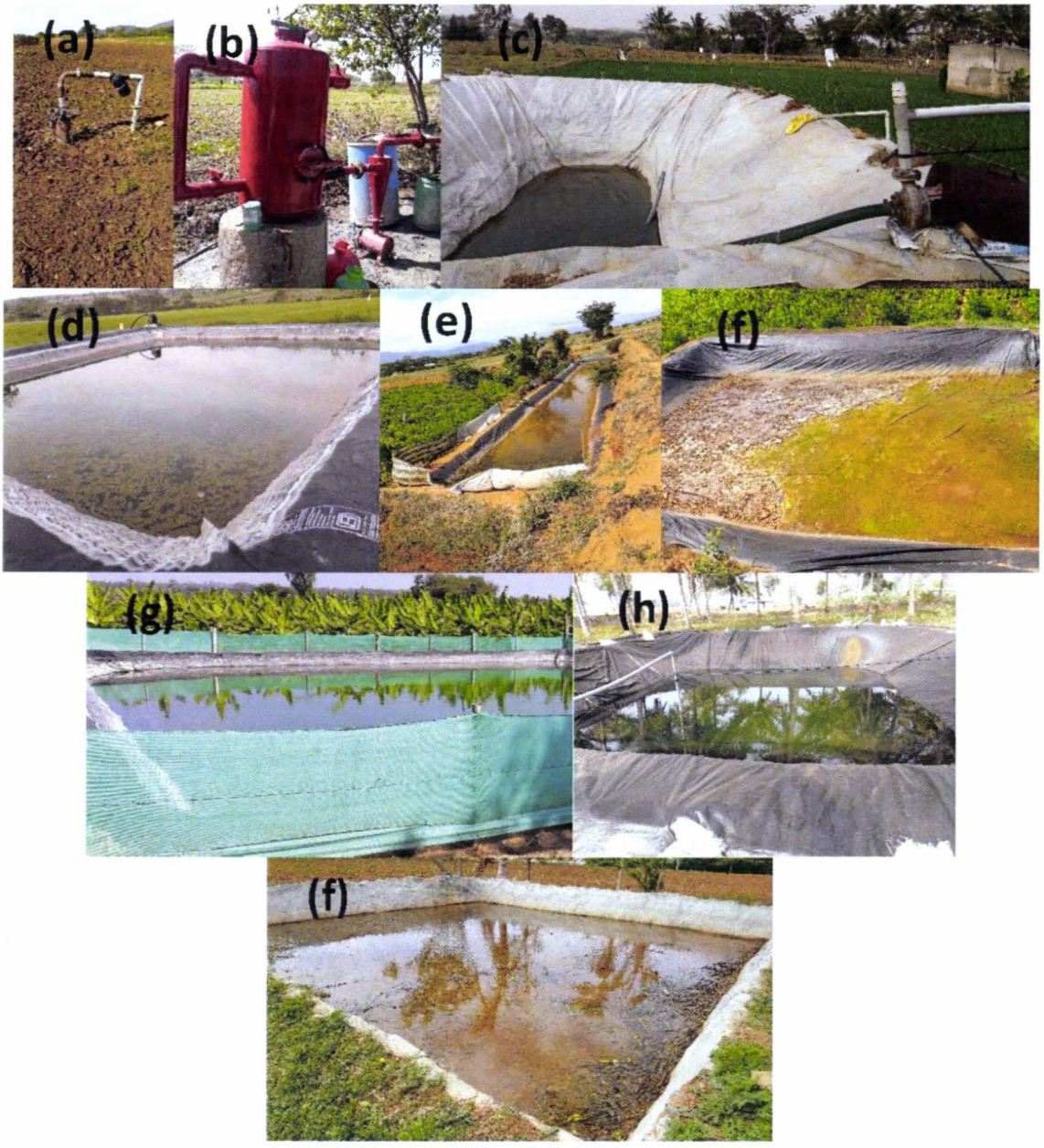

Figure 61 Groundwater pumping and storage in the tank.

The stored water later farmers are supplying to farmlands via various irrigation methods like a flood, drip, and sprinkler. Before supplying stored water to the drip or

sprinkler, farmers use to filter it to prevent choking in the irrigation system. Figure 62(b) shows the groundwater filtering mechanism. Pumping groundwater and storing in open water tank cause huge water loss by evaporation and high energy (electricity) loss (Badiani et al., 2012; Barik et al., 2016; Kumar et al., 2012; Shah et al., 2008, 2006).

From the year 1975 till 2000 small farmland holder showed their high-interest in diesel or electric pump for the irrigation purposes (Molle et al., 2003; Shah, 2007). With high-interest, India farmers have invested in pumps and it took the shape of green revolution (Molle et al., 2003). Due to intensive groundwater pumping in the watershed open wells or dug wells got dried. Figure 62 presents some of the dried open wells which were earlier utilized for the irrigation purposes.

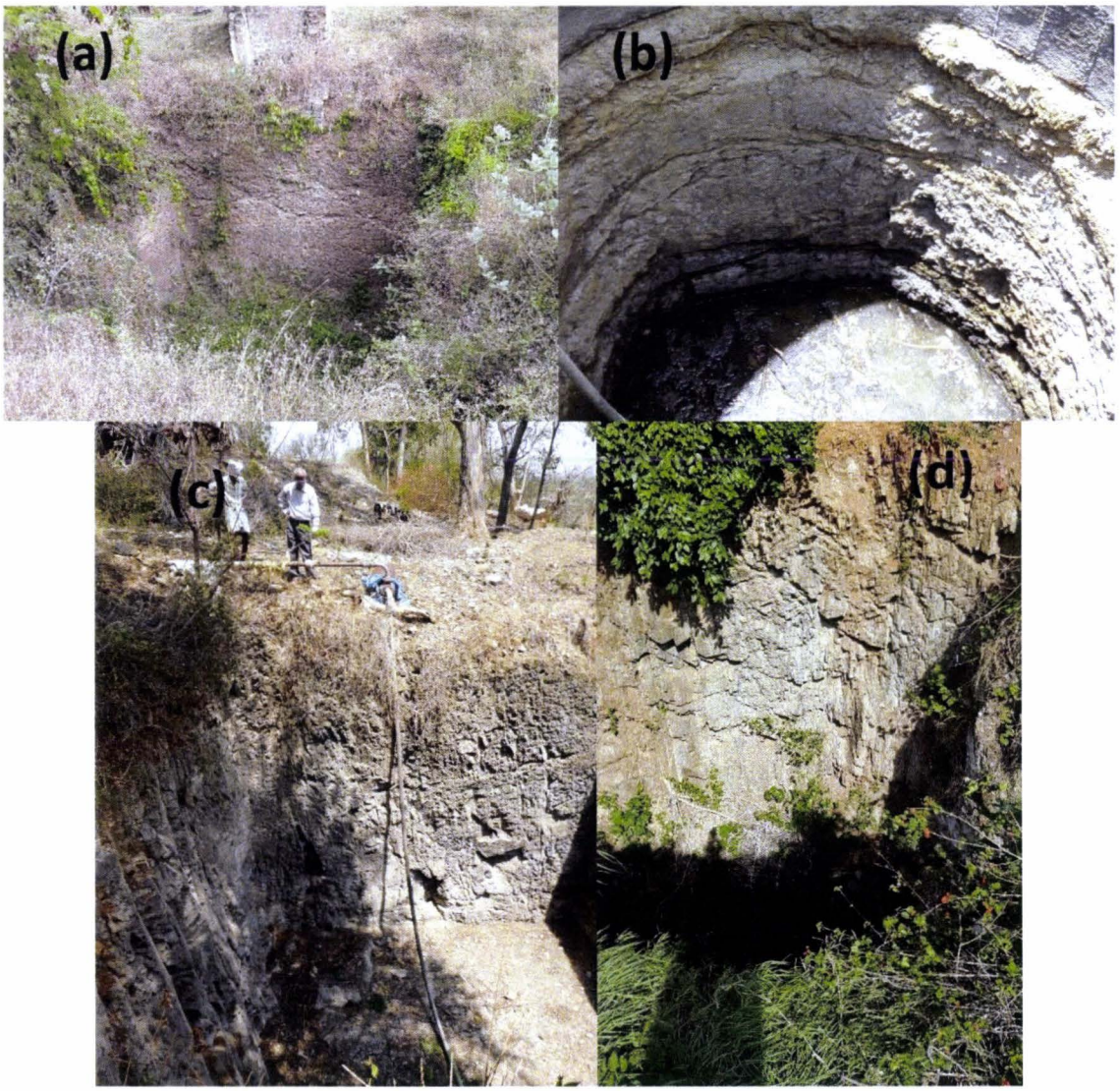

Figure 62 Dug wells which were used for the crop irrigation purposes.

With intensive groundwater pumping and starting cultivation in the drainage areas results disappearing of surface runoff and small water bodies started getting dried (Javeed, 2010; Sekhar M et al., 2011; Sreelash et al., 2013). Figure 63 shows some of the dried water bodies in the watershed. Figure 63 (c) shows that farmers are taking the tank soil and mixing in their farmlands as it is rich in minerals. But in some cases, these soils are becoming saline (figure 63 (d)) and farmers are losing their crops due to high saline soils (Kizza, 2016). With intensive groundwater irrigation farmers are also utilizing various kind of organic and inorganic fertilizers (Sriramulu et al., 2017b).

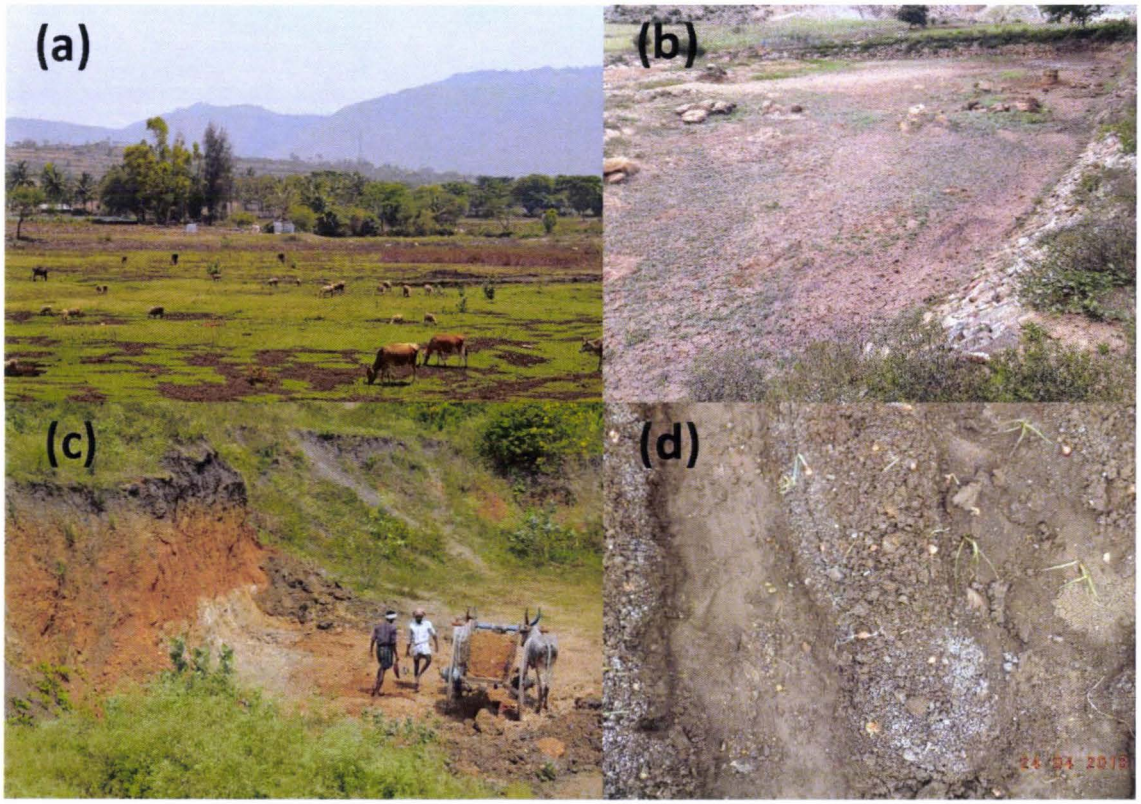

Figure 63 Dried water tanks (from (a) to (c)) and tank saline soil(d) mixed in the farmland.

The intensive groundwater irrigation leads to dug wells dried than surface water tanks dried and now huge amount of the borewells are getting dry (Fratzl, 2014; Robert et

al., 2018, 2017b; Sriramulu et al., 2017b). Figure 64 shows an example of dried borewells in the watershed.

Figure 64 Dried borewells in the watershed.

2.3 Ground observations and in-situ measurements

Ground observations have been realized in the framework to monitor land use practices the Berambadi watershed under the following research projects:

(i) AICHA (Adaptation of Irrigated agriculture to climate CHAnge) (IFCPAR-DST, Govt. of India) (Sekhar and Ruiz, 2010),

(ii) ATCHA (Accompanying The adaptation of irrigated agriculture to climate CHAnge) (ANR, Govt. of France) (Ruiz and Sekhar, 2016), and

(iii) Irriga-detection (TOSCA, CNES, Govt of France) (Corgne and Hubert-Moy, 2017).

All the research mentioned above projects were led by the Indo-French Cell for Water Sciences (IFCWS) based in Indian Institute of Sciences, Bangalore collaborated between Indian and French research institutes.

Ground campaigns were focused on organized to satisfy all funded research projects contribution for land use studies. The ground observations and *in-situ* measurements in the Berambadi watershed were broadly divided into three parts:

(i) history of land use practices in the watershed,

(ii) long-term intensive (15 to 24 days' interval) ground observation from spatial distributed 60 fixed identified parcels with focused to the Radarsat-2 satellite pass dates (Figure 67),

(iii) short-term (few days) random crop survey for various cropping season seasonal with an objective to monitor various cropping practices in the watershed.

The long-term crop monitoring for identified spatially distributed 60 parcels in the different soil types was performed from the year 2013 till 2017. The objectives of these ground observations and *in-situ* experiments were:

(i) to perform crop phenology and soil moisture measurements at 12 days' interval throughout the cropping season,

(ii) crop and water management practices information collection from farmers,

(iii) groundwater level monitoring from fixed identified 205 pumping borewells,

(iv) adaptive farmers are cropping decision in changing climate conditions at the watershed scale.

Short term crop surveys were conducted during kharif (monsoon) and rabi (post-monsoon) cropping seasons from the year 2013 till 2017 in the watershed. The objective of these crop monitor survey was to collect information on the spatial distribution of the various crops in the watershed includes the following variables:

(i) crop type,

(ii) crop height,

(iii) crop density,

(iv) soil color,

(v) rainfed or irrigated, and

(vi) if irrigated then the mode of irrigation (drip, sprinkler or flood)

Berambadi watershed is an excellent example of a highly complex agro-system, and it requires intensive and precise experimental studies (Corgne and Hubert-Moy, 2017; Ruiz and Sekhar, 2016; Sekhar and Ruiz, 2010). Agro-hydrological studies were performed by various fixed continuous monitoring sensors and portable manual measurements in the watershed (Sekhar et al., 2016). Figure 65 presents some of the

installed sensors and manual measurement apparatus. Land use monitoring in the Berambadi watershed were conducted for the surface soil moisture (Figure 65(f)) (Tomer et al., 2015), root zone soil moisture (Figure 65(b)) (Sreelash et al., 2017), *in-situ* flux tower for evapotranspiration studies (Figure 65(h)) (Eswar et al., 2016; Senay et al., 2016), leaf area index measurement for crop growth monitoring (Figure 65(g)), groundwater level monitoring (Figure 65(d)) (Sekhar M et al., 2011), GPS (Figure 65(e)), etc.

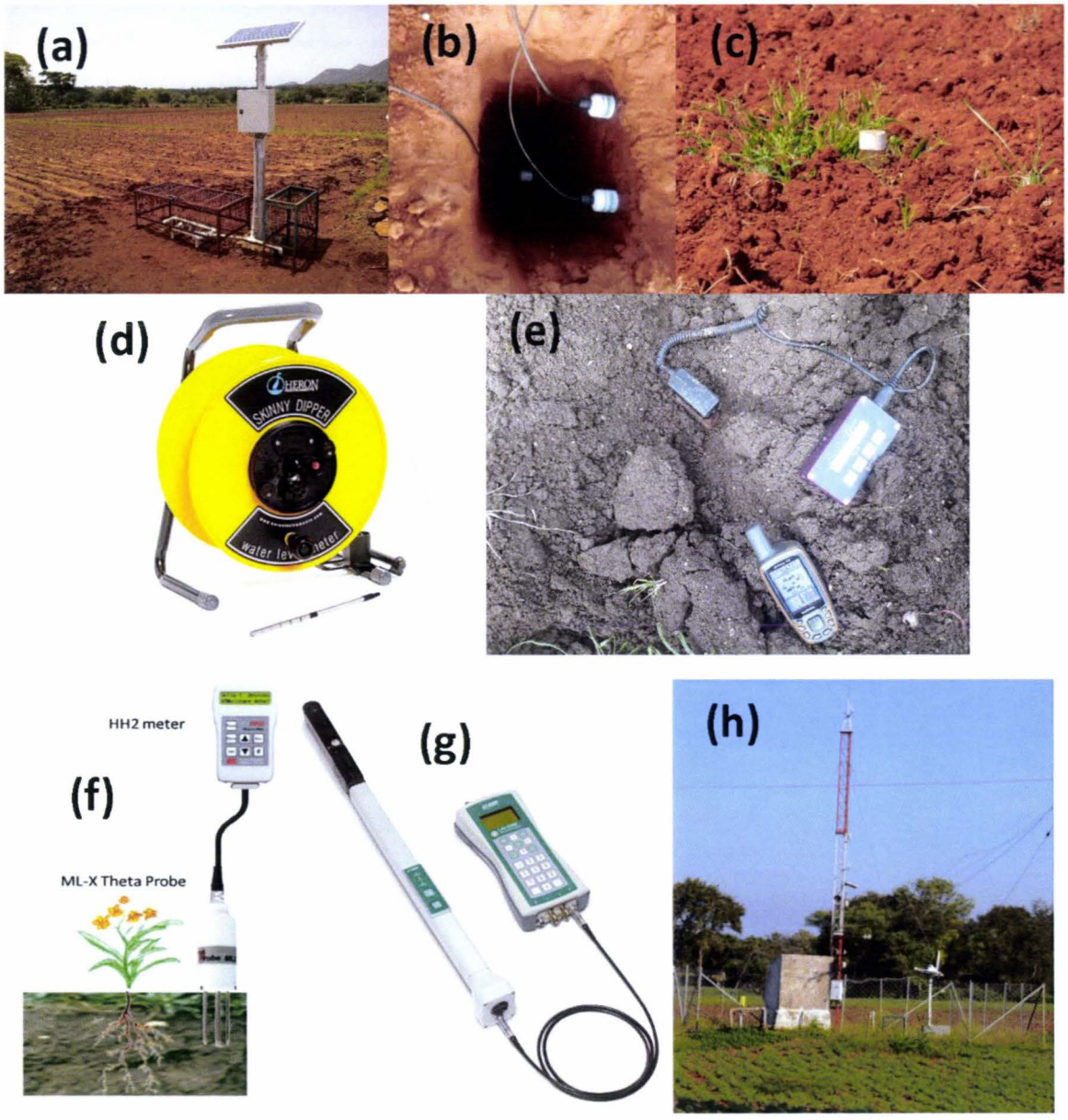

Figure 65 Instruments used for the soil (a, b, c, f), crop (e, g) and weather parameters (h) in the watershed.

2.3.1 Ground observation parcels identification

As mentioned in the above section the ground campaigns were divided into two main parts:

(i) long-term ground observation from fixed identified parcels and

(ii) random seasonal crop survey.

As presented in figure 66, spatially distributed 60 parcels were identified for long-term crop monitoring situated in different soil types and crop/water management practices. These 60 parcels are representing the land use practices in the watershed.

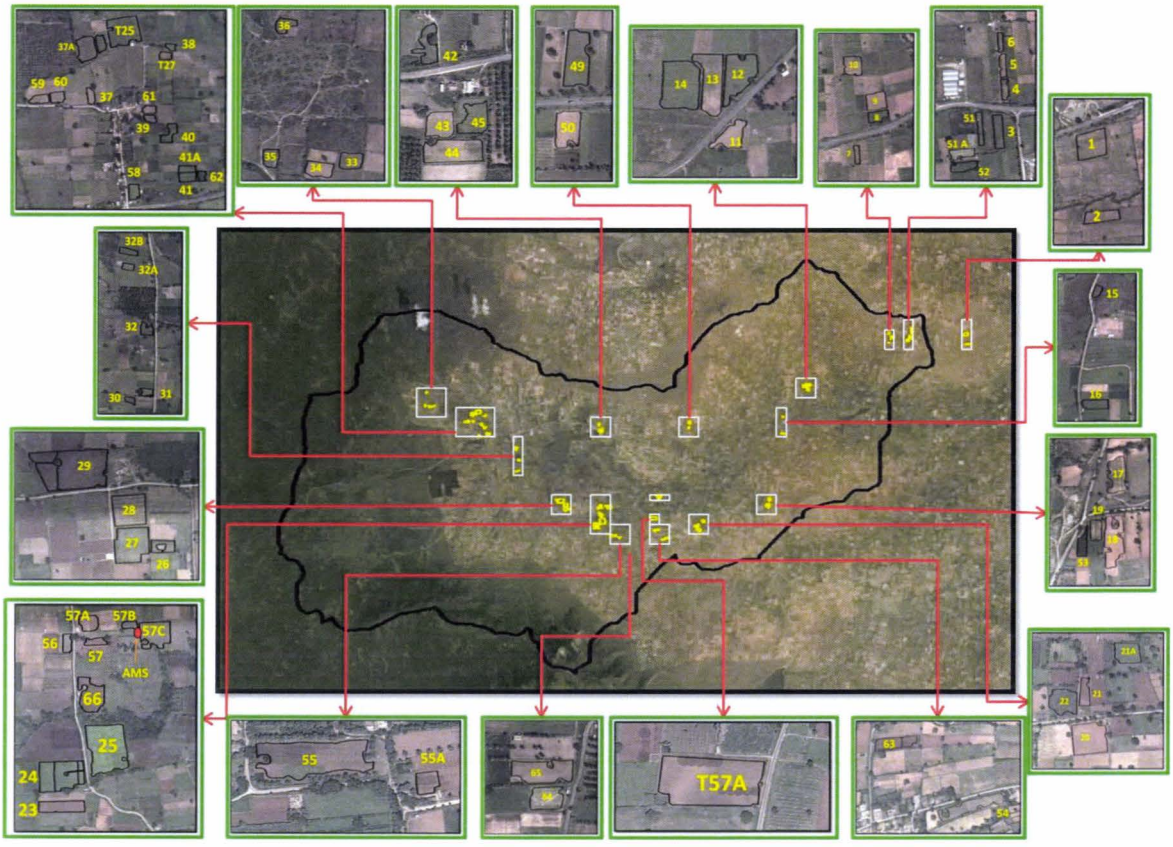

Figure 66 Long-term (for the year 2010-18) ground observation monitoring locations.

The short-term random surveys for kharif and rabi cropping seasons were conducted to understand the heterogeneity and complexity of cropping practices in the watershed. Mainly during kharif and rabi cropping seasons from the year 2013 till 2017

this kind of random surveys were performed to collect parcel scale crop/soil information like crop type, crop height, crop density, crop management practices, surface soil moisture, etc. (Mangiarotti et al., 2018, 2016; A K Sharma et al., 2018; Sharma et al., 2016).

2.3.2 Parcel digitization in the Berambadi watershed

Small land holding with a high diversity of crop types studies required precise parcel delineation (Dheeravath et al., 2010; Graesser and Ramankutty, 2017; Gumma et al., 2016; Sitokonstantinou et al., 2018). Farmers use to divide their croplands into small parcels to cultivate various crops. The parcel boundary delineation was performed using a google earth image of the year 2012 of 2 m spatial resolution. And then the reexamination and updating were done for the years 2014 and 2015 using IRS LISS IV 5 m spatial resolution and 2016 SPOT6 1.5 m spatial resolution. Approximately 20,100 land use/land cover polygons were examined, and approximately 19,000 agricultural parcels were precisely delineated in the watershed. Figure 67 shows the parcel boundary map in the Berambadi watershed. It was noticed by field survey that, big agricultural parcels with area > 1ha are mainly cultivated coconut, banana, sugarcane, etc. crops whereas small field is cultivating all types of crops.

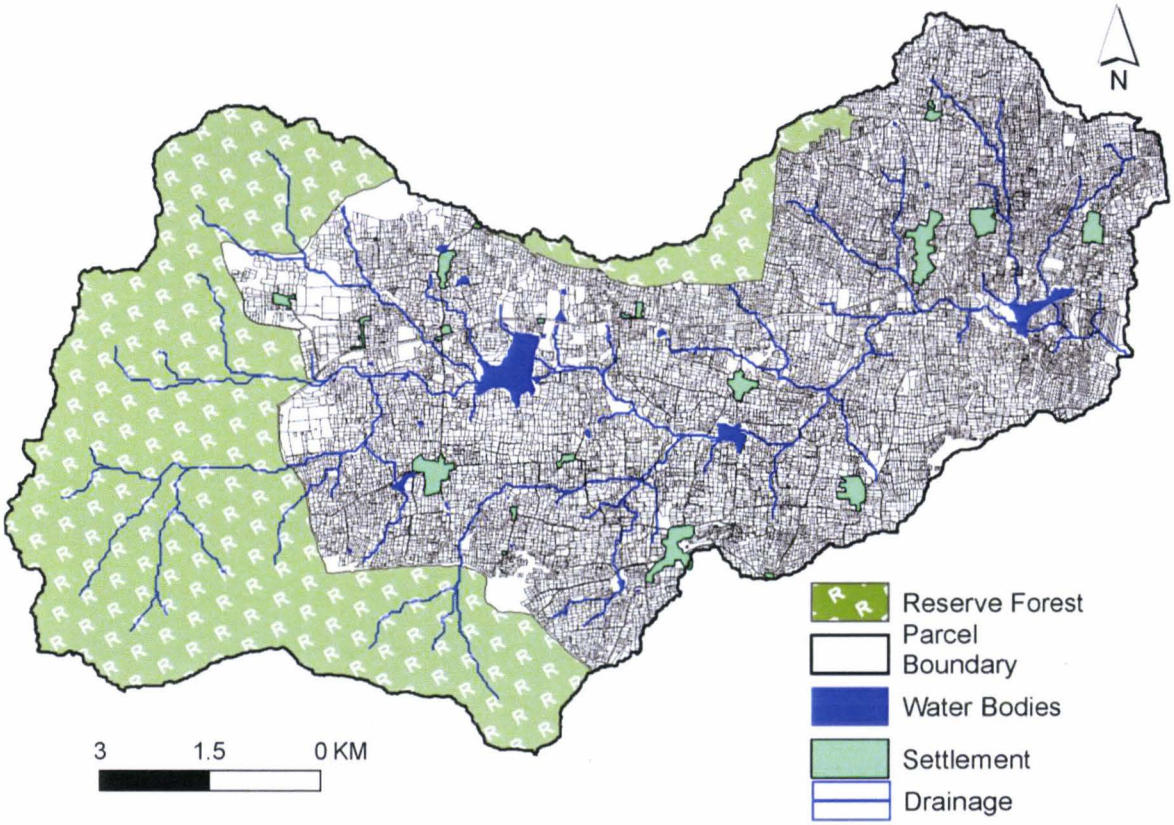

Figure 67 Parcel boundary delineation.

The histogram shows that the majority of parcels are falling around 0.2 ha area (Figure 68). The histogram shows that the farmers prefer to divide their farmlands into small parcels. Normally farmers are dividing their farmlands into small parcels according to their cultivation resources. If the farmer has an irrigation facility, then according to the groundwater yield farmer is deciding to divide into irrigated and non-irrigated parcels. In some cases, farmers are borrowing or purchasing water for irrigation purposes from the neighborhood. In these cases, farmers are deciding parcel size according to the possibility of irrigation to avoid crop loss (Robert, 2017). Farmers also decide the parcel size according to the government's aids like drip irrigation pipe distribution and other support. To normalize all possibilities of the cropping parcels, we have refined the parcel boundary with several year images. They are small, but it is clear that farmers are using these fixed parcels for the cultivation. Sometimes farmers are deciding the same crop cultivation in neighbor parcels too. These precise

parcel boundaries help to track farmer's cultivation strategy using remote sensing technique.

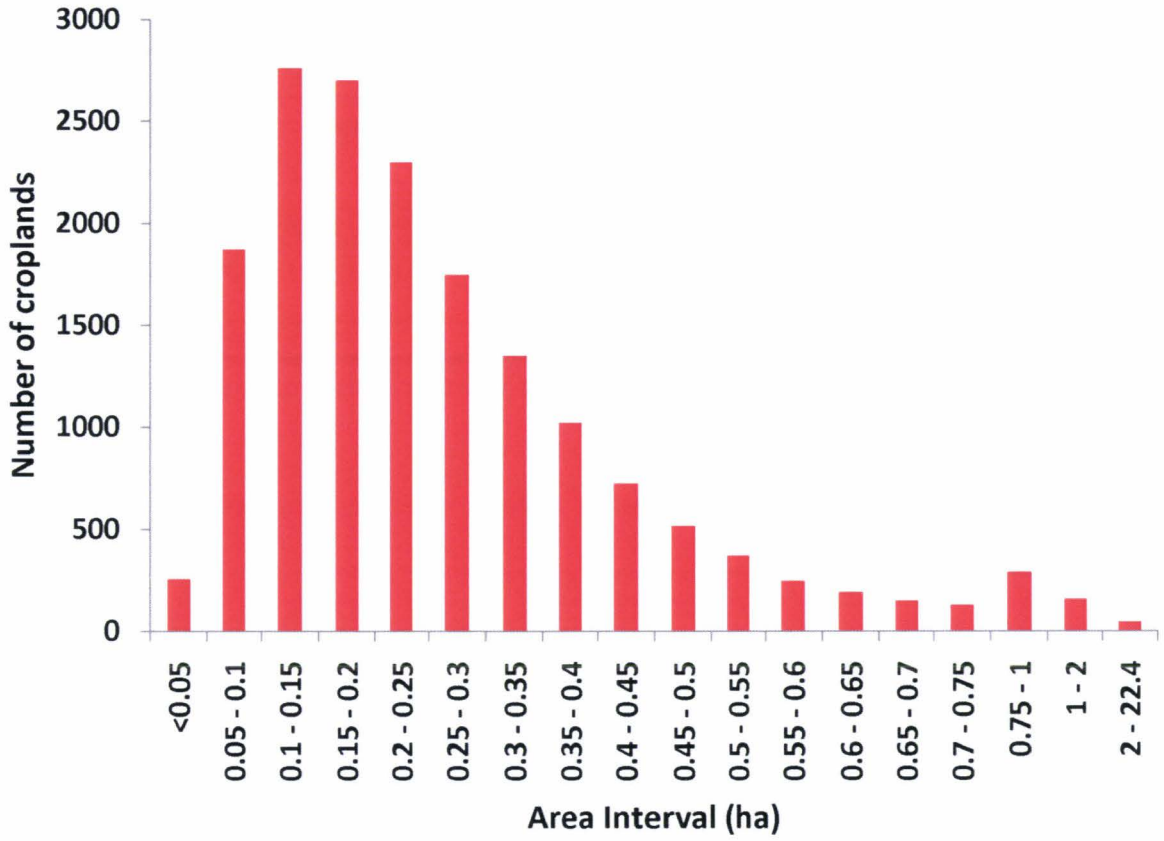

Figure 68 Parcel area histogram.

2.4 Remote sensing dataset

High spatial resolution (from 1 m to 30 m) time-series remote sensed images were procured for the land use monitoring in Berambadi experimental watershed. Images from optical, and microwave satellites were procured, and the ground observation was performed for the concern satellite pass date and time for precise land use identification and characterization.

2.4.1 Multispectral optical images

Cloud cover for two main cropping seasons (kharif and rabi) is noticed as the biggest obstacle for optical remote sensing (Hansen and Loveland, 2012; Sekhar et al., 2016). Figure 69 presents the available cloud free optical images were procured from multiple optical satellite platforms for cropping practices monitoring.

The study was performed into three sections using optical images:

(i) history of irrigation (from the year 1990 till 2016) using multitemporal optical satellite images,

(ii) the spatial distribution of irrigated croplands in the various cropping season for the year 2014-2016,

(iii) seasonal crop monitoring using optical satellite time-series of images for the year 2014-2016.

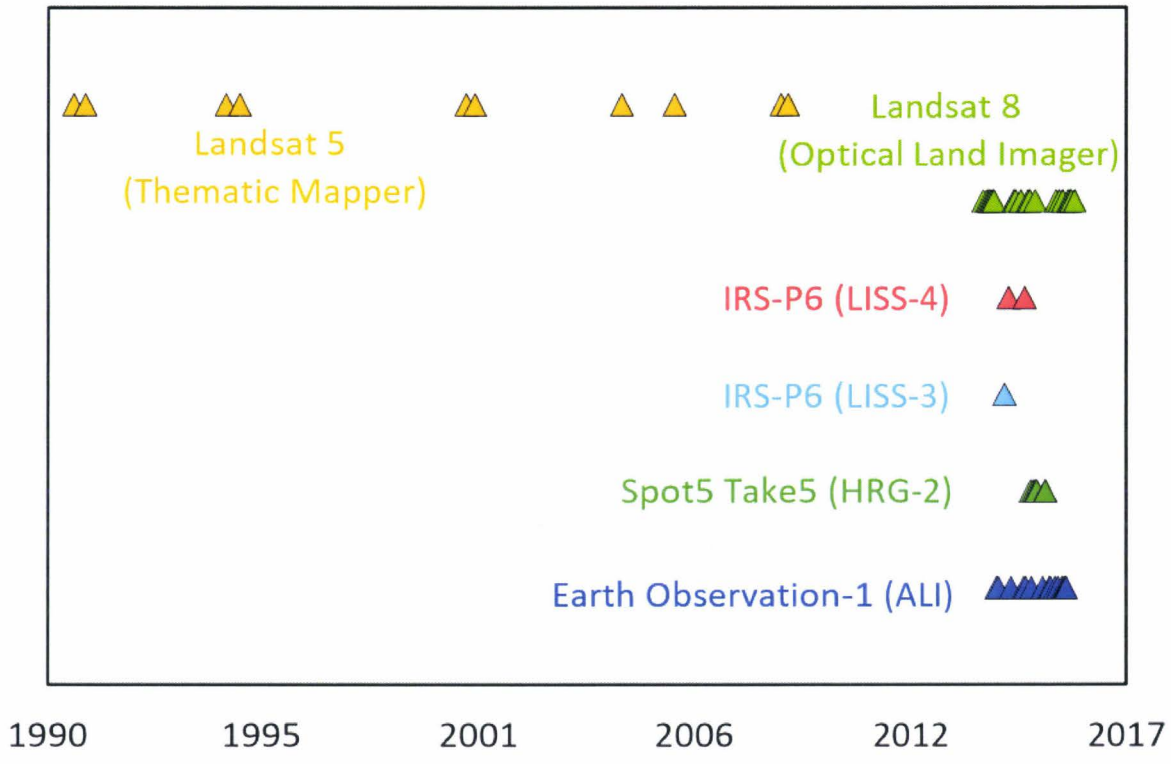

Figure 69 Optical satellite images.
Where LISS, HRG, and ALI represents to the Linear Imaging Self Scanning Sensor, High Resolution Geometrical, and Advance Land Imager.

The figure 70 shows for example a color composite image of the Berambadi watershed using 5*5 meters spatial resolution IRS LISS-4 sensor. We can see here the forest part in blue/red in the west on north part of watershed due to presence of active vegetation. As image was acquired during the summer period (January 2014), crops (in bright red color) are localised along to the drainage and majority of fields are not cultivated in the east part of the study area.

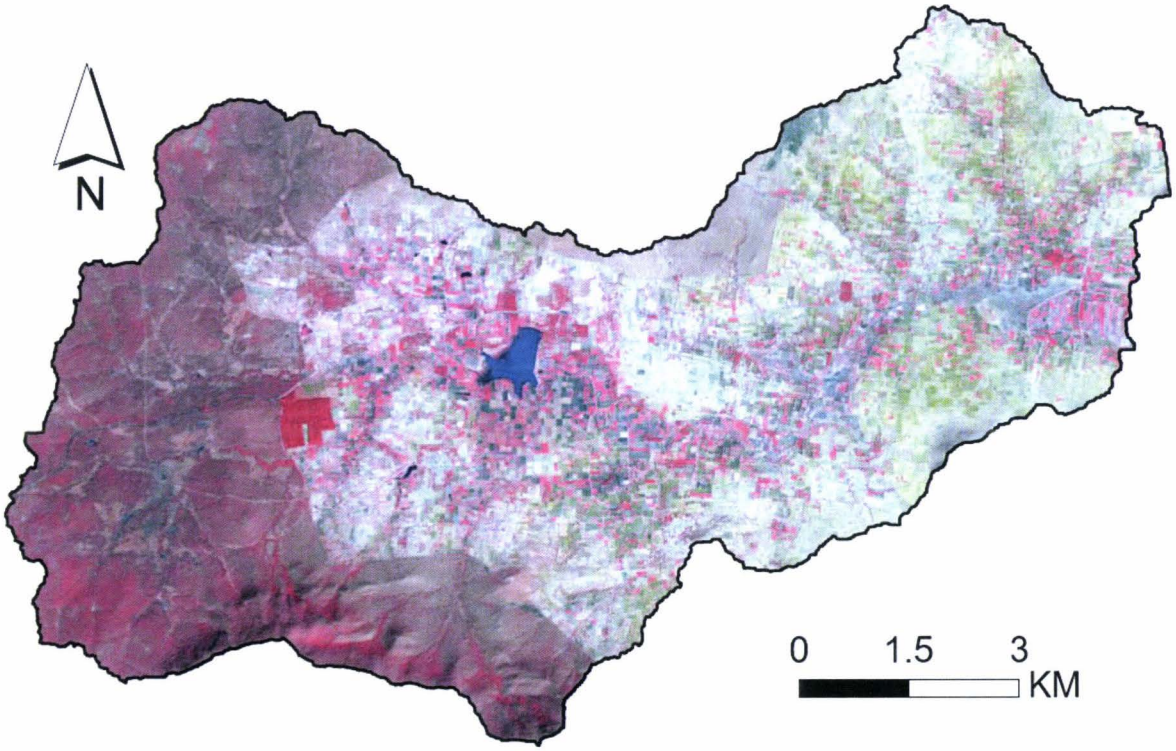

Figure 70 FCC (NIR Red Green) of IRS-LISS-4 satellite image (Date: 28th Jan 2014).

2.4.2 Synthetic Aperture Radar (SAR) images

Microwave images are the best available alternate of optical images to avoid cloud cover during two main cropping seasons (kharif and rabi). Radarsat-2 synthetic aperture radar (SAR) time-series images were procured from the year 2013 till 2017 (Figure 71). Ground observations were performed during all of the Radarsat-2 satellite pass date and time in the Berambadi watershed. All Radarsat-2 images procured (quad-pol or ultrafine HH-pol) were preferred to procure in descending mode only. As the descending mode satellite passes at 6 AM and the ascending mode satellite is passing at 6 PM. It was noticed that the anthropogenic activity like irrigating

farmlands, harvesting crops or any other farming practices, farmers use to perform in the evening. These anthropogenic activities bring bias in the ground observation data, apart from this due to evening temperature changes rapidly comparison to the morning. It was observed that the surface soil moisture uses to be constant for a long duration with comparison to the evening. Which gives us sufficient time to collect surface soil moisture from entire watershed. These reasons directed to prefer descending pass images for the Radarsat-2 data procurement.

We present here for example a color composite image of Radarsat-2 qual-polarization acquired the 8 june 2013 (figure 71). We have here Red, the HH polarization, in green the HV polarization and in blue the VV polarization. The forested area appears at the west part of the stufy area in green as HV is sensitive to volume scattering, in magenta, we have crops fields characterized by diferent types of surface scattering. We observed here in black the waterbody in the center of the image which have a specular scattering.

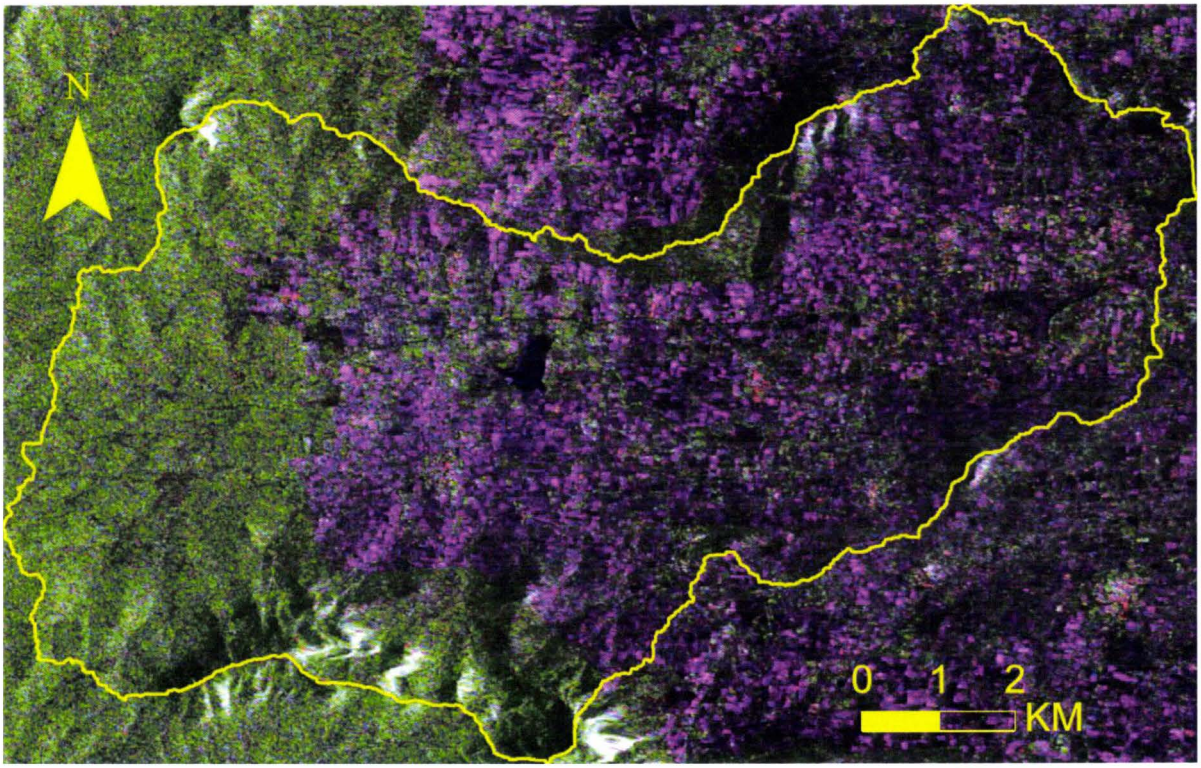

Figure 71 Multitemporal FCC of the SAR backscattering from HH HV and VV polarizations.

Radarsat-2 C-band SAR quad polarization (HH, HV, VH, VV) were procured for years 2013 and 2014 (Figure 72). For the year 2013 all images were procured with low incidence angle (incidence angle < 30°) with the objective of surface soil moisture estimation (Aubert et al., 2011; Srivastava et al., 2009; Tomer et al., 2015; Ulaby, 1975). The all procured images for year 2013 were having 24.55°and 26.43°near-incidence angle and far-incidence angle respective. The quad-pol SAR images procured for the year 2014 were having 39.26°and 40.71° near and far incidence angle respectively. The purpose of procuring high incidence angle (incidence angle > 30°) images were procured with an objective of crop monitoring (Hosseini and McNairn, 2017; Ulaby, 1975).

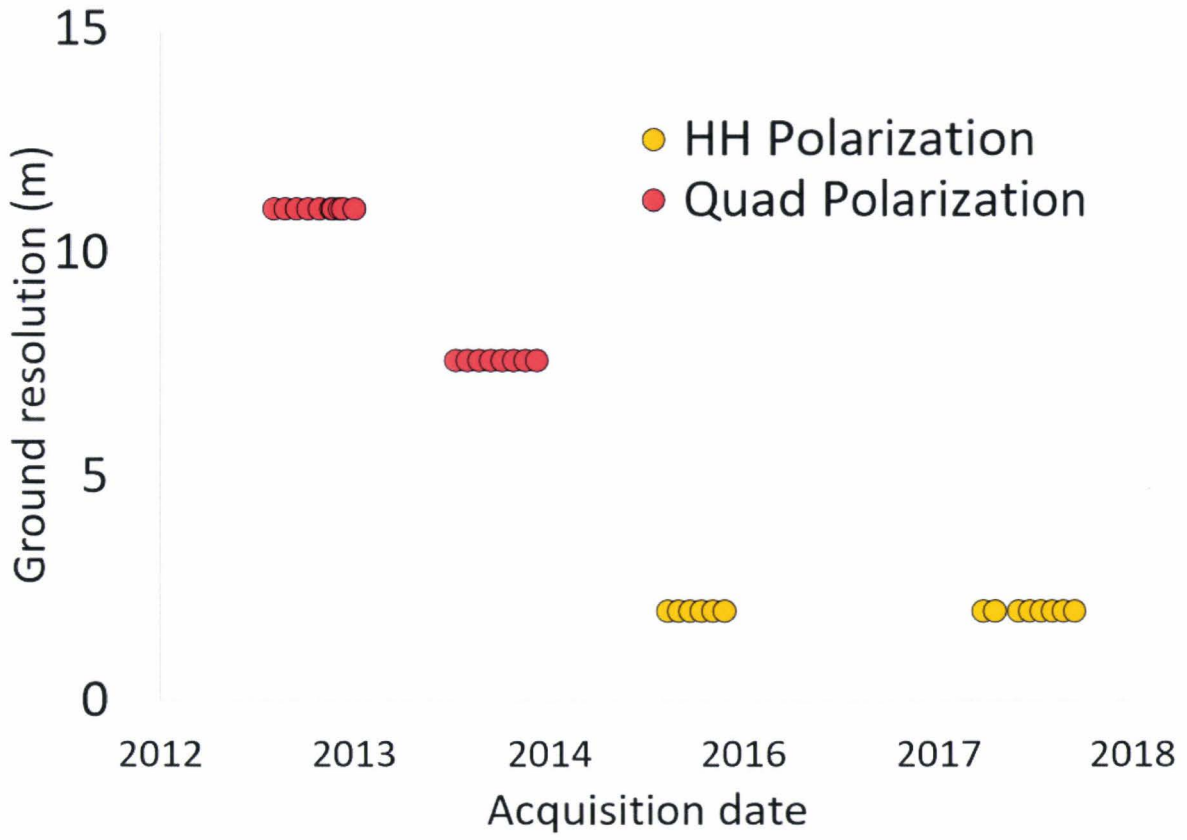

Figure 72 Radarsat-2 SAR quad polarization and ultrafine HH- polarization data.

Crop monitoring in small size parcel characterized watershed required high spatial resolution SAR images. The time-series of ultrafine HH-pol SAR Radarsat-2 satellites images for the years 2015 and 2017 were procured (Figure 72) with an objective of crop biophysical properties monitoring. All ultrafine images were procured with high incidence angle (incidence angle > 30deg) and fine spatial resolution.

2.5 Crop monitoring

Groundcontrol campaigns are required for precise crop monitoring (Löw et al., 2013; Sitokonstantinou et al., 2018; Zhao et al., 2014) to calibrate the satellite images and perform the image classification. The classified results can be further validated and their precision evaluated using the ground observations (Liu et al., 2014; Loosvelt et al., 2012; Mangiarotti et al., 2018; Sharma et al., 2016; Vuolo et al., 2018).

Several groundcontrol campaigns have been realized between 2013 and 2017 in the framework of the Indo-French Water Cell of Benaglore and several research programs as "AICHA", "ATCHA" and "Irriga-Detection". Groundcontrol campaigns were generally made during the Kharif and Rabi seasons with others research teams on the Berambadi watershed. For the thesis, we sampled about 80 to 100 fixed fields during Kharif and Rabi seasons where different type of informations were collected and randoms samples were also collected. As mention in figure 73, the ground observation or *in-situ* measurements for crop monitoring can be broadly divided into four sections: agronomy, irrigation, soil and hydrology, and others.

In the thesis, we didn't used all the database, as as for the agronomy part, we focused on crop type (CT), leaf area index (LAI), crop height (CH), crop density (CD) variables. For the irrigation practices, we noted first if at the field scale we have irrigation or non-irrigation. In the case of irrigation, the type of irrigation as drip irrigation, flood irrigation or sprinkler irrigation was mentionned. Soil and hydrology monitoring focused on surface soil moisture, root zone soil moisture information, groundwater level, depth of the borewell, power of the motor and total crop irrigation days, etc. During groundcontrol campaigns,we also realized interviews for a better undertsanting of farming management practises.

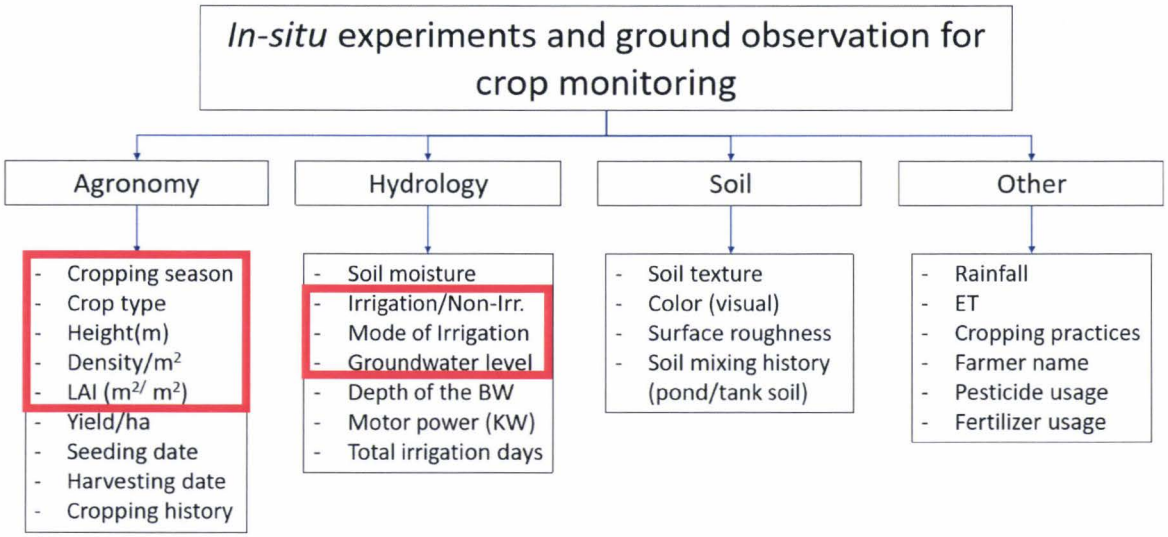

Figure 73 In-situ measurements and ground observation for crop monitoring (AICHA,ATCHA project and Irriga Detection), in red variables used in the thesis.

Conclusion

The objective of this chapter was to present the experimental Berambadi watershed and the data used for the research work. The Berambadi experimental agricultural watershed's location, topological variables, climatic variables, crop calendar, agricultural parcel delineation, and other informative components were presented in details. The satellite dataset with real-time ground observations like crop survey, groundwater monitoring, and other inputs to train and validate the satellite datasets is presented in the chapter. The chapter 2 shows that the Berambadi experimental agricultural watershed is a very complex agrosystem with very high spatiotemporal dynamics which represents an important challenge to monitor with remote sensing data.

CHAPTER 3: Historical evolution of irrigated cropland identification

Summary

This chapter aims to present the evolution of irrigated croplands in the experimental watershed using multitemporal optical satellite images. The study comprises spatial-temporal irrigated cropland ground observation and its used to evaluate irrigation history (1990-2016) in the watershed for two main irrigated cropping seasons (*Rabi* and *Summer*).

3.1 Introduction

Groundwater has rapidly evolved as a primary source for irrigation in Indian agriculture. Over-exploitation of the groundwater substantially depletes the natural water table and has negative impacts on the water resource availability. The overarching goal of the proposed research is to identify the historical evolution of irrigated cropland for the post-monsoon (rabi) and summer cropping seasons in the Berambadi watershed. Approximately five-year interval irrigated area maps were generated using 30 m spatial resolution Landsat satellite images for the period from 1990 to 2016. The potential of Support Vector Machine (SVM) was assessed to discriminate irrigated and non-irrigated croplands. Three indices, Normalized Difference Vegetation Index (NDVI), Normalized Difference Moisture Index (NDMI) and Enhanced Vegetation Index (EVI), were derived from multi-temporal Landsat satellite images. Spatially distributed intensive ground observations were collected for training and validation of the SVM models. The irrigated and non-irrigated croplands were estimated with high classification accuracy (kappa coefficient greater than 0.9). At the watershed scale, this approach allowed highlighting the contrasted evolution of multiple-cropping (two successive crops in rabi and summer seasons that often imply dual irrigation) with a steady increase in the upstream and a recent decrease in the downstream of the watershed. Moreover, the multiple-cropping was found to be

much more frequent in the valleys. These intensive practices were found to have significant impacts on the water resources, with a drastic decline in the water table level (more than 50 m). It also impacted the ecosystem: Groundwater level decline was more pronounced in the valleys, and the rivers are no more fed by the base flow.

3.2 Dataset used in the study

The irrigation history is developed using multi-temporal Landsat satellite images from the year 1990 to 2016. The study is focused on the post-monsoon (rabi) and summer (zaid) season, as the monsoon (kharif) season is mostly cloudy. The Shuttle Radar Topography Mission (SRTM) product 1 arc-second (30 m spatial resolution) Digital Elevation Model (DEM) was used for drainage and watershed delineation. Google Earth image, IRS (Indian Remote Sensing) LISS-IV (Linear Imaging Self Scanning Sensor) and SPOT-6 (Satellite Pour l'Observation de la Terre) images were used for cropland parcel delineation.

3.2.1 Remote sensing data used for the study

Multi-temporal Surface Reflectance (SR)-based products from Landsat (30 m spatial resolution) were used for irrigated vs. non-irrigated croplands classification. Twelve available cloud-free images (with approximately 5-year interval) were downloaded from the United States Geological Survey (USGS) website, includes ten Landsat 5 Thematic Mapper (TM) images and two Landsat 8 Optical Land Imager (OLI) images (Table 6). These twelve images span six agricultural years, with six rabi seasons and the following six summer seasons. Dates are towards the end of the respective seasons, corresponding to the stage of crop maturity. India being a tropical country cloud-free satellite images are rarely available during the Kharif cropping season. Therefore, while non-availability of images is the main limitation for using optical satellite images in monsoon regime contexts (Gumma et al., 2011), the present study is restricted to the rabi and summer cropping seasons.

Table 6 List of the dataset used with Day Of Year (DOY), season and sensor specifications (Thematic Mapper (TM), and Optical Land Imager (OLI)).

Year	Rabi Season	Summer Season
	Date (DOY (Sensor))	
1990–1991	26-12-1990 (360 (TM))	28-02-1991 (059 (TM))
1994–1995	05-12-1994 (339 (TM))	12-04-1995 (102 (TM))
2000–2001	21-12-2000 (356 (TM))	11-03-2001 (070 (TM))
2004–2006	16-12-2004 (351 (TM))	09-04-2006 (100 (TM))
2008–2009	27-12-2008 (362 (TM))	01-03-2009 (060 (TM))
2015–2016	31-12-2015 (365 (OLI))	20-12-2016 (080 (OLI))

3.2.2 Ground observation

The ground observation was divided into two parts: manual groundwater level data collection in various cropping seasons and irrigated/non-irrigated cropland survey with farmers. The intensive irrigated and non-irrigated cropland ground observation survey was conducted with the help of local farmers. The complete survey was done with individual interviews of around 80 to 120 farmers. The extensive field visit was undertaken to cover all land parcels in collecting the irrigation history in the watershed.

To maintain the survey accuracy, the information collected was cross-checked with the adjacent farmers. The questions include:

i. When was the borewell installed and/or re-installed?,
ii. How much deep the borewell is?,
iii. What are the pump specifications (motor power, etc.)?,
iv. Which crop was growing during the study period?,
v. What is the groundwater yield?,
vi. What are the borewell re-drilling and service history?,
vii. How much cropland area is cultivated using borewells?,
viii. The borewell yield is sufficient or not to cultivate the crops?, and
ix. Did farmer switch from traditional crops to other crop types? etc.

While doing a ground survey with farmers help, we noticed that in 90's the parcel size was bigger than present in the present (the year 2016). Farmers divided the irrigated cropland according to their financial resources and groundwater availability. As shown in Table 7, around 2500 parcels were used as samples for supervised classification using SVM algorithm. For the calibration of SVM model, 50% random and spatially distributed parcels were selected and remaining 50% random parcels were used for validation (Betbeder et al., 2015b; Jia et al., 2014). Care was taken to perform precise ground surveys and farmer interviews to obtain precise information on cropping and water management practices.

Table 7 Training and validation samples of irrigated and non-irrigated cropland in the Berambadi watershed.

Year	Irrigated	Non-Irrigated	Total
2015–2016	76	204	280
2008–2009	72	380	452
2004–2006	69	412	481
2000–2001	77	374	451
1994–1995	85	352	437
1990–1991	48	342	390

The groundwater level and borewell yield in the Berambadi watershed are monitored by spatially distributed 205 operational piezometers (Figure 74). Most of these piezometers belong to the farmers, who are using them for irrigation purposes. Monthly groundwater level monitoring is realized since May 2010 during non-pumping hours. The transect AA' is drawn to retrieve the groundwater level from upstream to downstream of the watershed. Inverse Distance Weighting interpolation was done at the watershed scale using distributed piezometers for three cropping seasons. Along the transect AA' the interpolated groundwater level was extracted for various cropping seasons with 100 m interval.

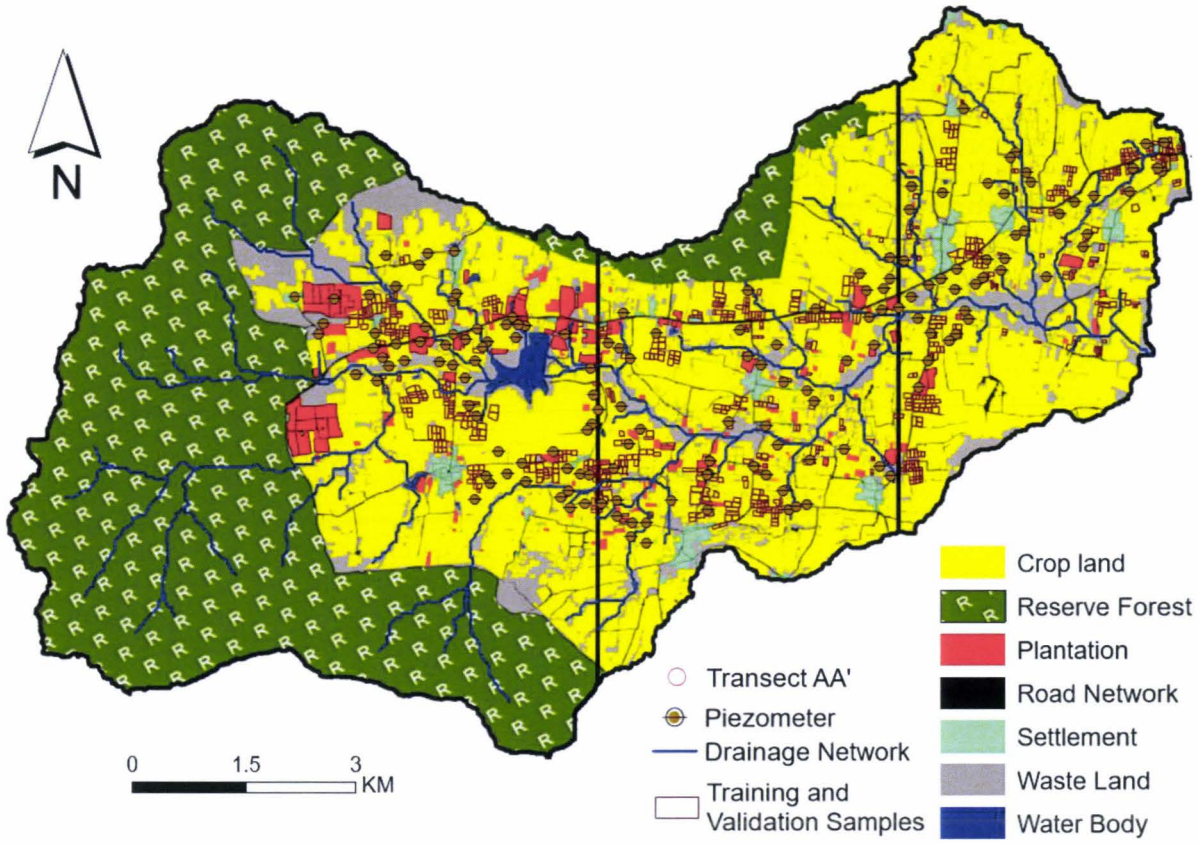

Figure 74 *Calibration and validation parcels in the watershed.* The X, Y, and Z belong to three regions which represent respectively upper, middle and downstream sections of the watershed.

All pre-processed (geo-referencing, atmospheric correction, optical indices estimation) Landsat images and indices were downloaded from ESPA (Earth Resources Observation and Science (EROS) centre Science Processing Architecture) project of USGS (USGS and U.S. Geological Survery, 2016). The downloaded indices were NDVI, NDMI, and EVI as presented in the table 8. The atmospheric correction was performed using the Landsat Ecosystem Disturbance Adaptive Processing System (LEDAPS) algorithm (USGS and U.S. Geological Survery, 2016). All optical indices were resampled using nearest neighbor (NN) resampling method to the pixel size 5 m spatial resolution for a better precise mean and standard deviation at agriculture parcel scale (Xu et al., 2015).

Table 8 Indices used were: Normalized Difference Vegetation Index (NDVI), Normalized Difference Moisture Index (NDMI), and Enhanced Vegetation Index (EVI).

Indices Name	Equation
NDVI	$NDVI = \frac{\rho NIR - \rho Red}{\rho NIR + \rho Red}$
EVI	$EVI = G\frac{\rho NIR - \rho Red}{\rho NIR + C1(\rho Red) - C2(\rho Blue) + L}$
NDMI	$NDMI = \frac{\rho NIR - \rho SWIR}{\rho NIR + \rho SWIR}$

Where G = 2.5 (the gain factor), ρ is the atmospherically corrected value for near-infrared (NIR), Red and Blue bands, C_1 and C_2 are coefficients with constant values 6.0 and 7.5 respectively, and L is the soil adjustment factor, and its value is 1.0 (Muhammad et al., 2016).

The overview of the comprehensive methodology to classify multi-temporal irrigated and non-irrigated cropland area is presented in Figure 75. The parcel scale median value (Tomer et al., 2015) and standard deviation (SD) were estimated for the various indices (NDVI, NDMI, and EVI) (Table 8). Parcel mean values were estimated for all 36 optical indices (3 indices × 12 multi-temporal products).

Support vector machines (SVM) classifier is a supervised non-parametric statistical learning mechanism. The Support vector machine classification was performed using the scikit-learn library (Pedregosa et al., 2011). Support vector machine classification was done individually for the various optical indices (NDVI, NDMI, and EVI) using 50% random spatially distributed intensive ground observed training samples. Remaining 50% random samples were used for the classification validation. The comprehensive methodology leads to identify irrigated and non-irrigated croplands. It was noticed that the indices together could perform better than the individual one to remove the classification overshoots. Therefore, the decision rule in the form of AND boolean operator was implemented on SVM classified outputs of these indices, and we have found that it removed the overshoot error of irrigated cropland outputs. After a generation of all irrigated cropland maps, the kappa coefficient was estimated. Kappa index is considered to be a better index for determining classification accuracy

from the confusion matrices (Cheema and Bastiaanssen, 2010; Ozdogan and Gutman, 2008). The primary results of irrigated and non-irrigated croplands were generated, and the kappa coefficient was calculated for all classified outputs. These individually classified outputs were further used to estimate irrigation history and to identify the evolution of dual season irrigated cropland (post-monsoon and summer cropping seasons) in the watershed. The validation of classified cropland parcels was done with randomly selected 50% (around 1250 parcels) of ground observed datasets.

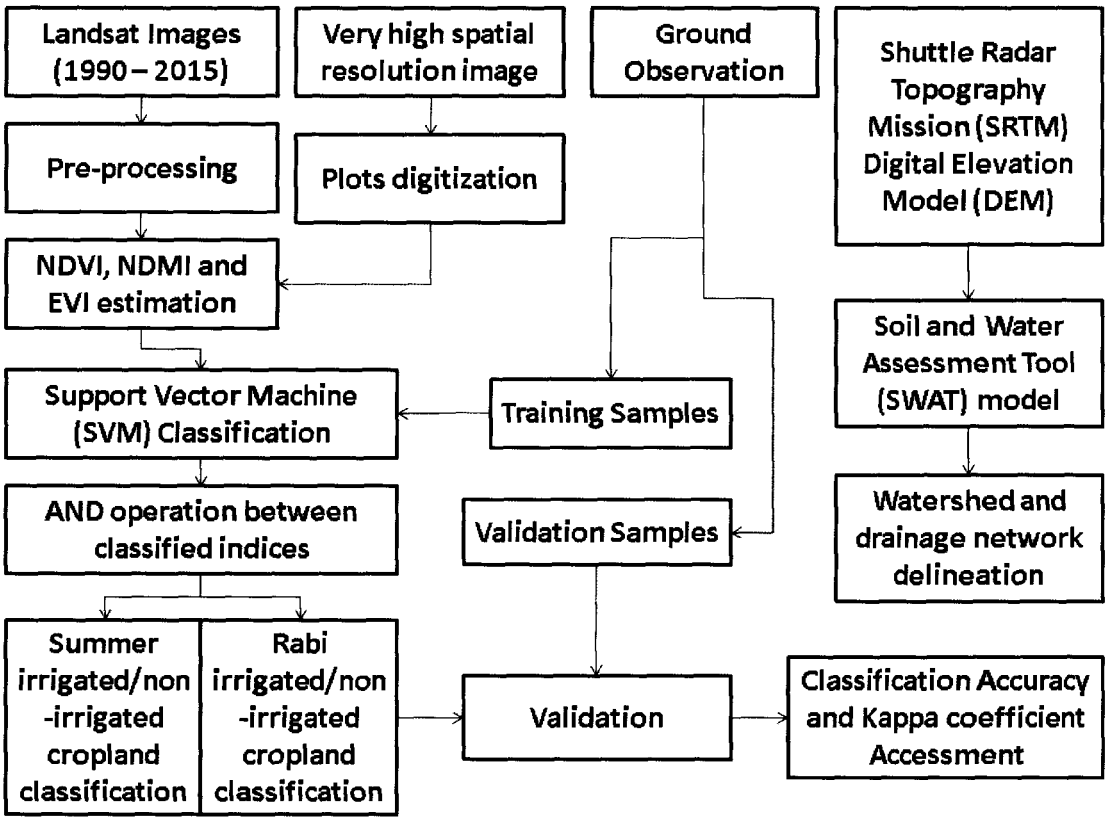

Figure 75 Workflow of the methodology.

After assigning 1 and 0 to respectively irrigated and non-irrigated croplands, the multitemporal values obtained for each parcel were summed to produce the irrigation intensity maps. The irrigation intensity maps were generated for the post-monsoon and summer cropping season by adding multitemporal images of concern seasons. The cumulative irrigation intensity map for the year 1990 to 2016 was generated by adding all 12 images, including both cropping seasons. This process gives a synoptic view of the spatial distribution of irrigated cropland intensity in the watershed.

3.3 Results and discussion

The first subsection explains about plot (parcels) delineation procedure and parcel size variation in the watershed. The second subsection shows the inter-comparison of results obtained from different indices for rabi and summer seasons. The third subsection is about spatiotemporal irrigated cropland evolution in the Berambadi watershed. The impact of intensive irrigation on groundwater is discussed in the fourth subsection.

3.3.1 Irrigated and non-irrigated cropland classifications

The kappa accuracy (%) of irrigated and non-irrigated cropland classification using NDVI, NDMI, and EVI, individually and together multitemporal images (36 images (12 dates × 3 indices)) of rabi and summer cropping seasons is shown in Figure 76. The classification was performed with SVM algorithm using EVI, NDMI, and NDVI indices. First, SVM algorithm was applied separately to each date and then to the rabi season dates and the summer season dates considered as two different datasets, and finally to all dates considered together as one dataset. It was evident in Figure 76 that, individually all three indices (EVI, NDVI, and NDMI) were given poor classification outputs when compared the same with combined indices. For the year 1990–1991, the classification results of each of the NDVI and NDMI were poor than EVI, even though combined indices performed further better than EVI. From 1994 to 2016 all indices improved the irrigated cropland classification performance with an error of 15 to 20%. However, indices performed higher classification accuracy together than the individual. Besides, these results confirm that SVM performs very well for the classification of irrigated cropland (Guzmán et al., 2018; Zheng et al., 2015).

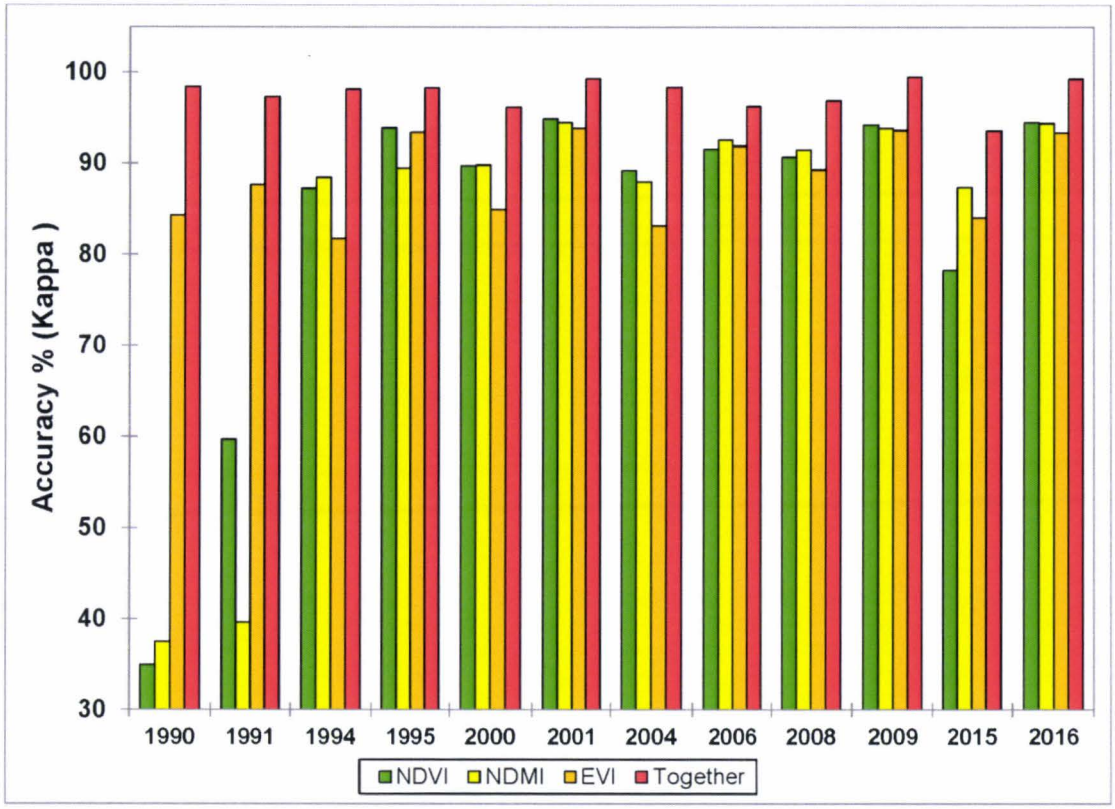

Figure 76 Accuracy assessment of SVM classified irrigated and non-irrigated croplands.

3.3.2 Irrigated and non-irrigated cropland analysis during Rabi season (post-monsoon)

The spatial distribution of irrigated and non-irrigated (or fallow land) cropland areas for the rabi cropping season depicted in Figure 77 with the approximately five-year interval from the year 1990 to 2015. It was noticed that in the 1990s few farmers (approximately 5%) with irrigation facility was cultivating in rabi season. In 1994, about 16% of irrigated cropland clustering was identified in the downstream of the watershed. The results show that the farmers were interested in growing irrigation crops in rabi season. As shown in Table 9, during the year 2015 rabi season irrigated cropland has reached 31%, compared to 21% in the year 2008, which requires a huge quantity of groundwater for the crop irrigation. The rabi season irrigated area in the up and middle stream regions has increased by 27% and 6%, respectively from 2008 to 2015 (Table 9). However, in the downstream, the irrigated area has been reduced by

2.5% for the same period. These figures indicate farmers' interest for rabi season irrigation in the upstream region.

Table 9 Rabi season irrigated cropland evolution from 1990 to 2015.

Year	Total Number of Parcels	Total Area (ha)	Irrigated Cropland Area (%) with Respect to the Total Agricultural Cropland			
			Upstream (X)	Middle Stream (Y)	Downstream (Z)	Total
1990	812	201.4	3.45	5.92	4.16	4.57
1994	2431	684.24	16.18	16.00	14.36	15.54
2000	3123	859.73	17.78	22.47	18.14	19.52
2004	2346	649.29	14.59	14.48	15.19	14.74
2008	3584	936.31	24.39	18.46	21.19	21.26
2015	4934	1380.36	51.13	24.15	18.81	31.34

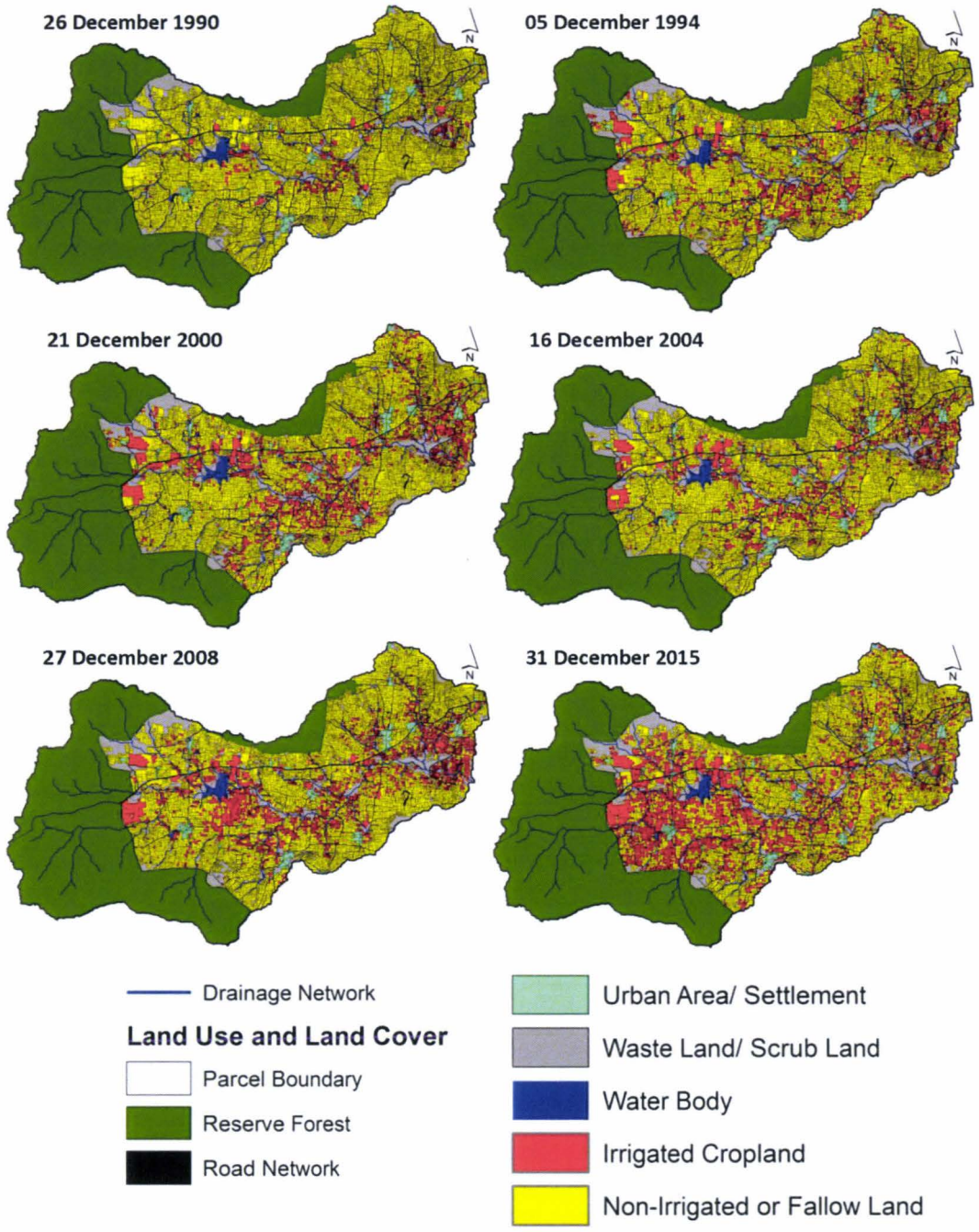

Figure 77 A temporal map of irrigated and non-irrigated croplands in Rabi season from 1990 to 2015.

The total irrigated cropland area was divided into the three zones upstream, middle stream and in downstream. The temporal variation of irrigated cropland was analyzed for the rabi season in these zones (regions). The regional irrigated cropland statistics gave an idea about their shifting towards upstream. The irrigated cropland in the upstream has significantly increased during the last decade (Figure 78). However, due

to tremendous depletion of groundwater in the downstream, the total rabi season irrigated cropland area of downstream got stabilized.

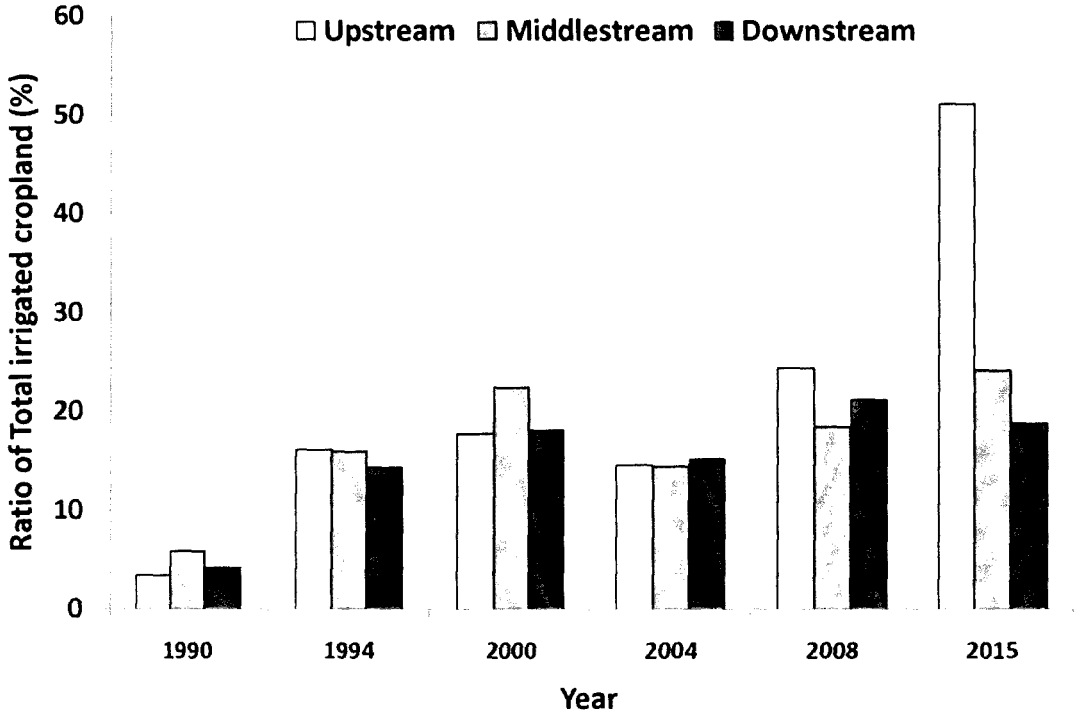

Figure 78 Rabi irrigated cropland evolution in the watershed.

The combined spatiotemporal map of the irrigated area was generated to distinguish the spatial distribution of high and less intensity irrigation practices. The light red to dark red color in the map shows the temporal intensity of irrigation (Figure 79). The irrigated croplands are clustered to the drainages and shifting towards upstream of the watershed. The shallow groundwater level in the upstream is attracting farmers to adapt irrigation practices during multiple cropping seasons. The irrigation intensity map (Figure 79) shows that new rabi irrigating cropland are emerging in the upstream. This tendency of farmers to adopt irrigation led them to pump an enormous amount of groundwater to fulfill the crop water requirement. This intensive irrigation activity can further deplete upstream groundwater, which can disconnect the baseflow and can disturb adjacent reserve forest ecology.

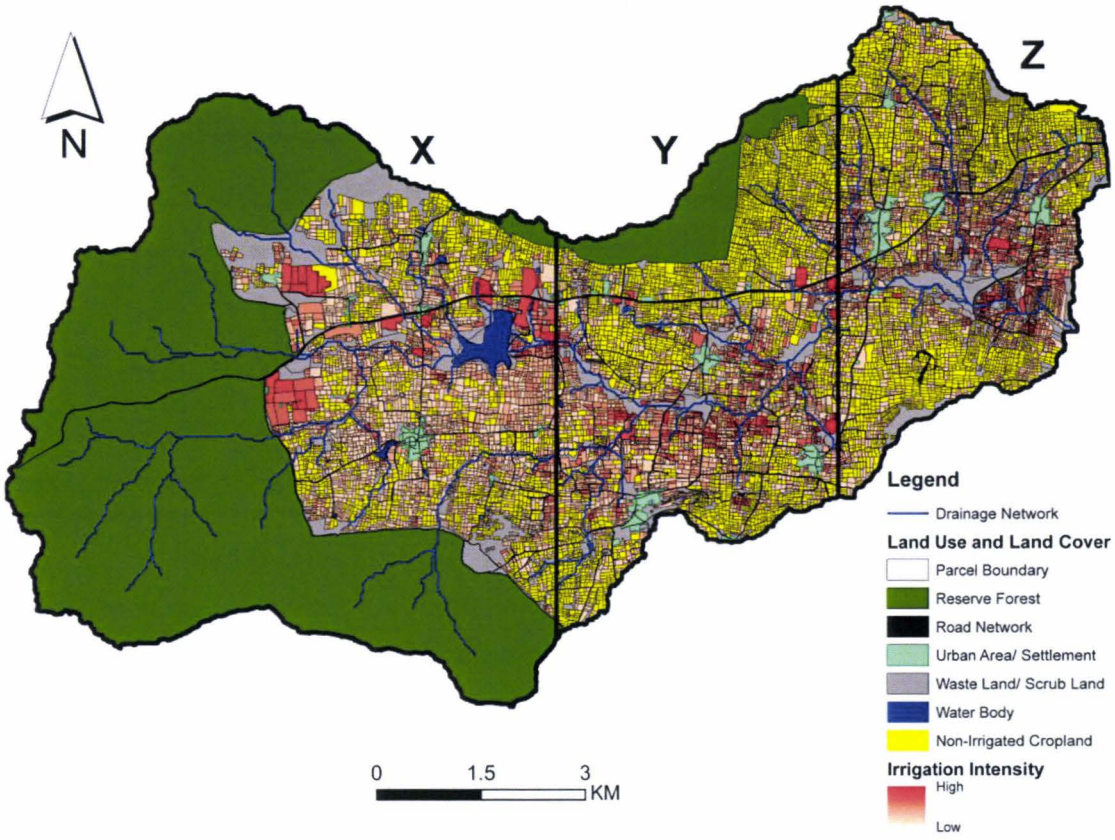

Figure 79 Spatiotemporal map of Rabi irrigated cropland for the duration 1990 to 2015.

3.3.3 Irrigated and non-irrigated cropland analysis during the summer season

Historical evolution of irrigated and non-irrigated cropland maps for summer cropping season (Figure 80) is also providing insightful information on spatial distribution and evolution of irrigation in the watershed. The detailed maps confirmed the observation that irrigation was preferentially developed along the valleys. Due to the insufficiency of high-resolution satellite images, a good number of studies used coarse resolution satellite images for the cropland classification with high definition gaps in rainfed and irrigated croplands (Dheeravath et al., 2010).

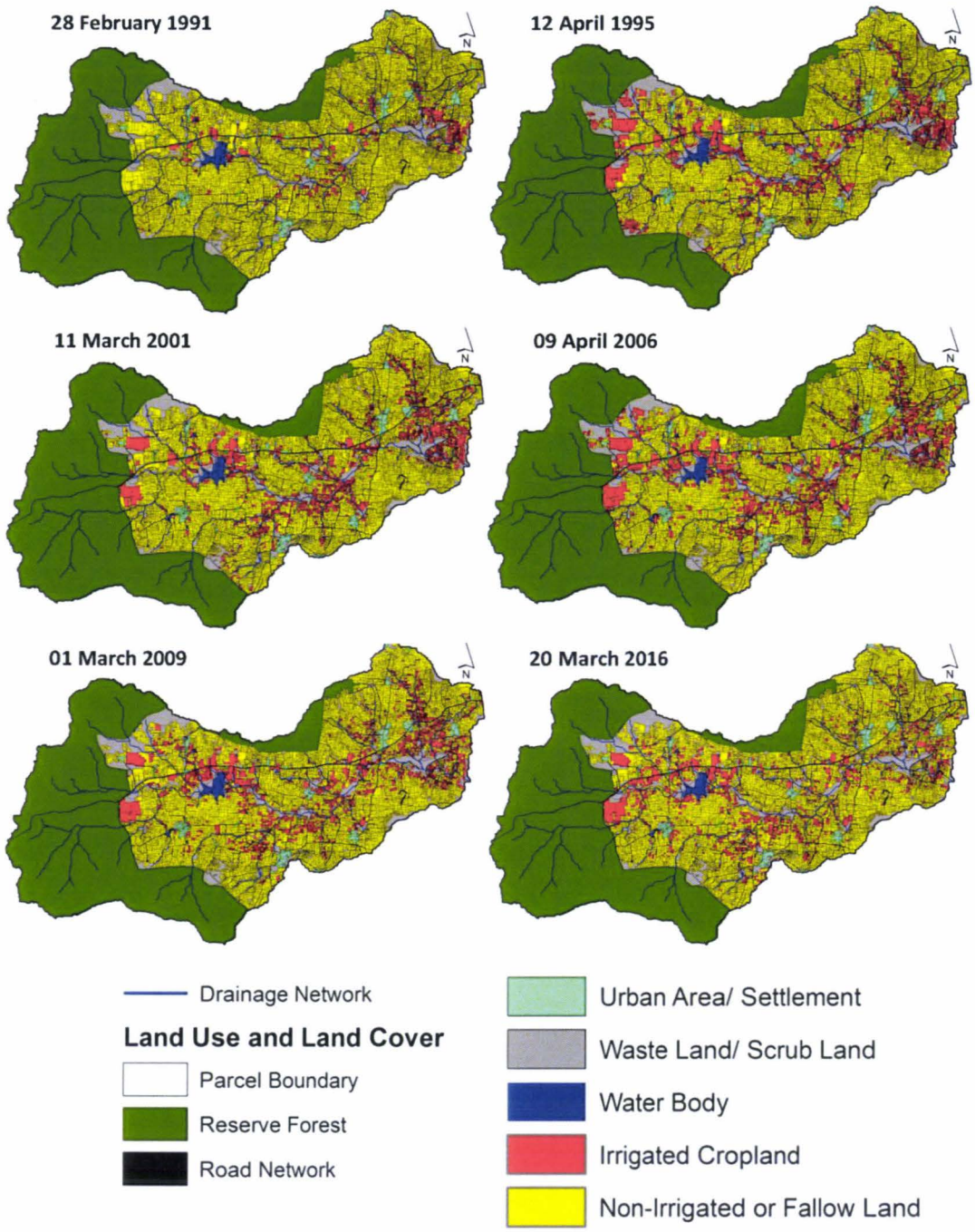

Figure 80 Temporal map of irrigated croplands in the Summer season from 1991 to 2016.

In 1991, few farmers with irrigation facility were growing summer crops. These farmlands existed for the most part near the outlet of the watershed. Slowly with time summer irrigated croplands moved towards upstream (Figure 80), but they were clustered around mainstream of the watershed. Summer irrigated cropland expansion

in the watershed was noticed from 1991 to 2016 (Figure 80). Due to intensive irrigation impact on groundwater farmers started quitting taking the risk of crop failure in the case of poor borewell yield (Sekhar et al., 2016). In 2016 most of the downstream farmers stopped summer irrigation, as groundwater depleted drastically. It is evident in the figure 80 that at present mostly summer irrigated cropland clusters exist in the upstream area of the watershed along the drainage. The total summer season irrigated area was increased threefold from 1991 to 1994, and after that, it got stabilize till 2009, and then it reduced to 2.5% in 2016 (Table 10).

Table 10 Summer season irrigated cropland evolution from 1991 to 2016.

Year	Total Number of Parcels	Total Area (ha)	Irrigated Cropland Area (%) with Respect to the Total Agricultural Cropland			
			Upstream (X)	Middle Stream (Y)	Downstream (Z)	Total
1991	816	210.55	2.74	4.76	6.92	4.78
1995	2406	694	19.82	13.31	14.52	15.76
2001	2560	684.4	14.24	16.39	16.06	15.54
2006	2837	789.64	21.69	16.66	15.65	17.93
2009	2805	723.79	16.79	15.48	17.23	16.43
2016	2170	616.24	19.06	13.60	9.28	13.99

Summer cropping is entirely dependent on the irrigation, and in the Berambadi watershed, there is no alternate source for the farmers except groundwater irrigation. Irrigated area has increased tremendously during 1991–1995 (Figure 81). From 1995 the upstream part of the watershed was leading in total irrigated cropland area as compared to downstream (Figure 81). Due to intensive groundwater and a huge number of borewells in the downstream, the farmers belong to the downstream region of watershed started quitting to grow summer season crops.

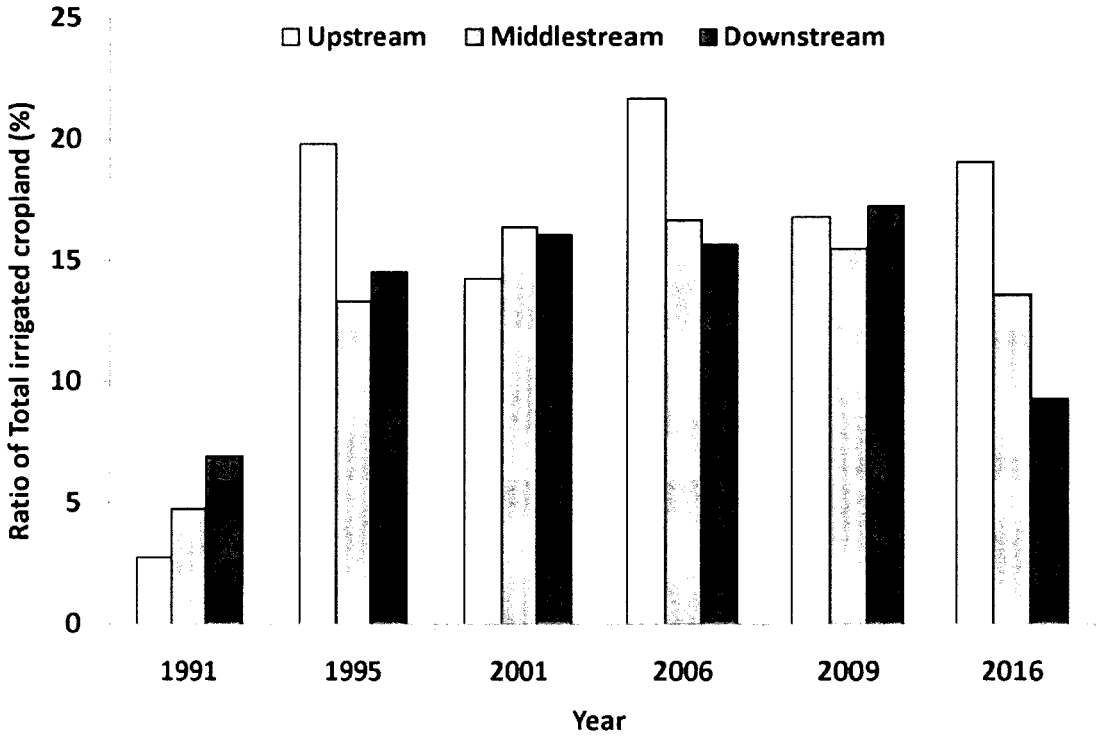

Figure 81 Summer irrigated cropland evolution in the watershed.

Summer season cropping is wholly dependent on the groundwater resources in the watershed. In 90's the irrigated cropland was mainly at downstream and slowly it clustered around all three main tanks of the watershed; however, presently all tanks are dried. The spatiotemporal map was generated from low intensity (once irrigated) to high intensity (always irrigated) (Figure 82). The non-irrigated croplands (rainfed croplands) are shown in yellow color. These croplands were not under any irrigation in summer cropping season during the year 1990–2016. In the absence of rainfall and no surface water availability during the summer cropping season, farmers generally irrigate the crops using groundwater.

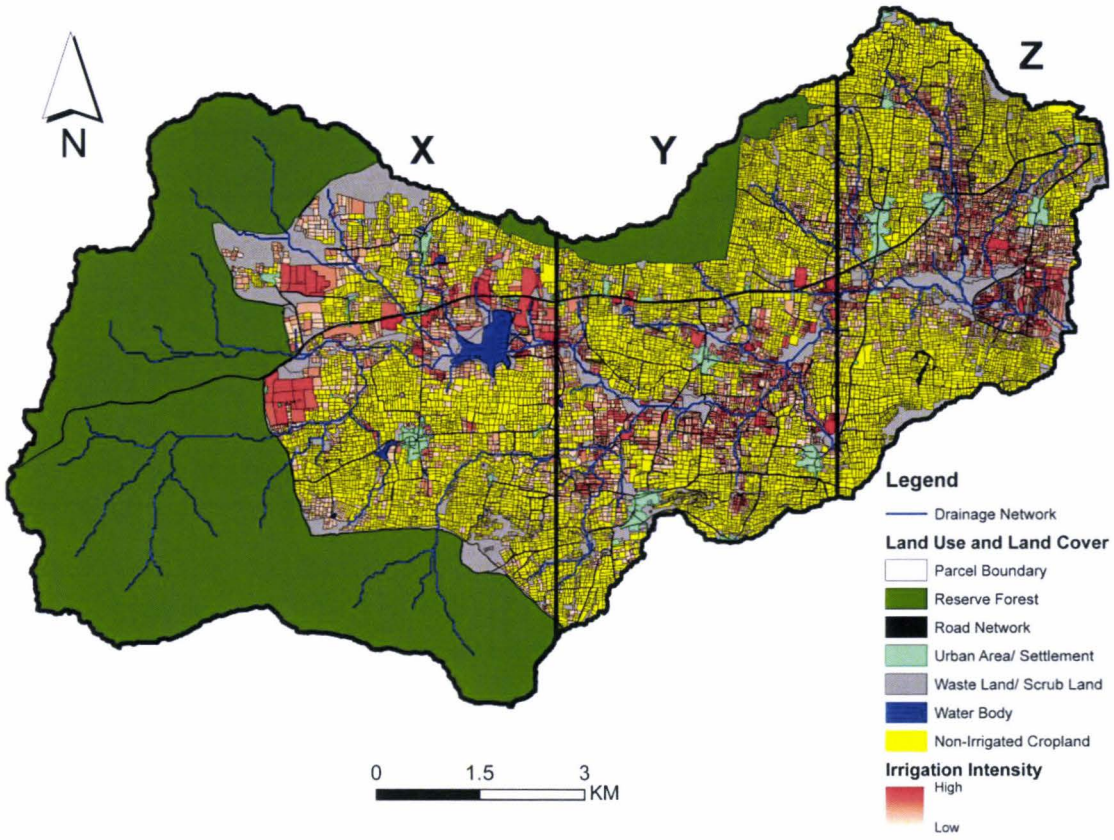

Figure 82 Spatiotemporal map of Summer irrigated area for the duration 1991 to 2016.

3.3.4 Dual season (Rabi and Summer) irrigated and non-irrigated cropland analysis

The total number of parcels of dual irrigated croplands has increased from 1990 to 2009, but during 2015–2016 the dual irrigated parcels have reduced (Table 11). At present farmers like to grow cash crops like turmeric, sugarcane, banana, onion, garlic, vegetables. All of these cash crops need intensive irrigation facility. Farmers with sufficient irrigation facility are switching to 2 or 3 irrigated crops per year. Apart from monsoon season, these farmers are cultivating crops in rabi and summer seasons. The total area is under dual irrigation, which is about 10% of total agricultural cropland (Table 11). These farmers have sufficient groundwater yield throughout the year for cultivation. These croplands are contributing maximum to the water loss in the watershed.

Table 11 Dual irrigated cropland evolution from 1990 to 2016.

Year	Total Number of Parcels	Total Area (ha)	Irrigated Cropland Area (%) with Respect to the Total Agricultural Cropland			
			Upstream (X)	Middle Stream (Y)	Downstream (Z)	Total
1990–1991	332	98.52	1.28	2.98	2.36	2.24
1994–1995	1072	356.4	11.34	6.51	6.60	8.09
2000–2001	1219	395.37	10.32	9.20	7.50	8.98
2004–2006	1028	345.26	10.41	6.75	6.50	7.84
2008–2009	1463	429.97	12.22	8.12	9.17	9.76
2015–2016	888	342.04	14.01	6.32	2.98	7.77

The temporal evolution of dual irrigated cropland in the upper stream, middle stream and downstream of the watershed are depicted in Figure 83. During 1994–1995 the dual irrigated cropland shoot-up in the upstream with an approximate 11% area occupation with respect to total cropland area of the upstream region. The high probability of groundwater yield in the upstream motivates farmers for dual season irrigation. As the groundwater of upstream region of the watershed is recharged by the adjacent humid reserve forest, this region helps to maintain dual irrigated cropland area from 1994–1995 to 2015–2016 (Figure 83). Middle stream and the downstream regions of the watershed has increased and stabilized their total irrigated cropland between 1994–1995 and 2008–2009. Intensive irrigation in the whole watershed depleted the groundwater by more than 50 m in downstream resulting the dual season irrigation depletion during 2015–2016. Due to over-exploitation of groundwater, many borewells were dried up, and farmers lost their crops in the last decade. After understanding the groundwater depletion pattern and poor borewell yield, the majority of farmers quit their plan for the summer crops in the downstream areas.

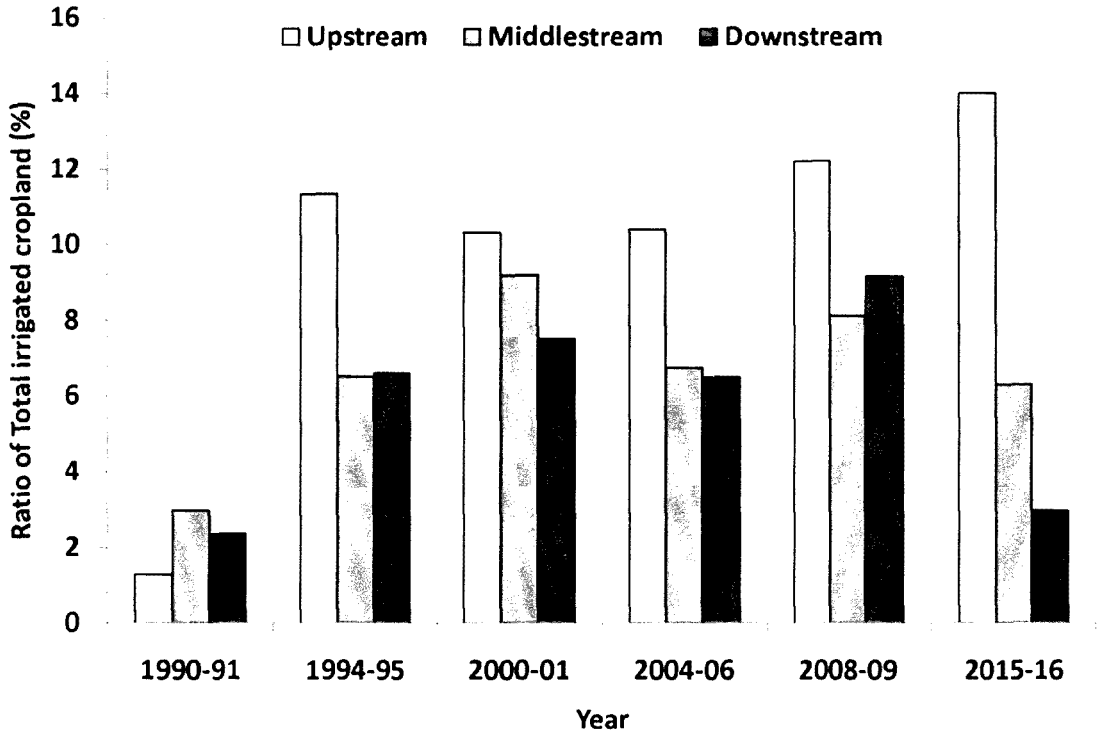

Figure 83 Dual (Rabi and Summer) irrigated cropland evolution in the watershed.

Figure 91 shows the spatial distribution of dual cropping season intensity from 1990 to 2016. In 90's the Berambadi watershed had three major water bodies in downstream near the outlet of the watershed, one at the middle stream and one at upstream (Figure 84). In 2017, the most significant perennial water body, which exists in the upstream of the watershed, also disappeared. Due to a continuous increase in irrigated cropland in the upstream, the farmers are exhausting their resources. In the 1990s the groundwater yield in the upstream was better, and surface flow also existed in monsoon and post-monsoon seasons. Economically strong farmers purchased big-sized farmlands (Figure 84) and started growing high water demanding crops like banana, sugarcane, coconut, turmeric, and vegetables. However, now these big farmers, as well as farmers in the middle stream and downstream, are dividing their croplands into smaller parcels for precision management and avoiding crop failure. Figure 91 represents dual (rabi and summer seasons) irrigation croplands evolution in the watershed. Other than cultivating in summer and rabi seasons, these farmers are also cultivating in the kharif season. Intensive cropping of three seasons in a year is

leading to extensive utilization of water resources, and use of various fertilizers is exerting significant negative impacts on the soil quality and groundwater availability (Sriramulu et al., 2017b). The major dual irrigated croplands are clustered along the drainages or valleys of the watershed (Figure 84).

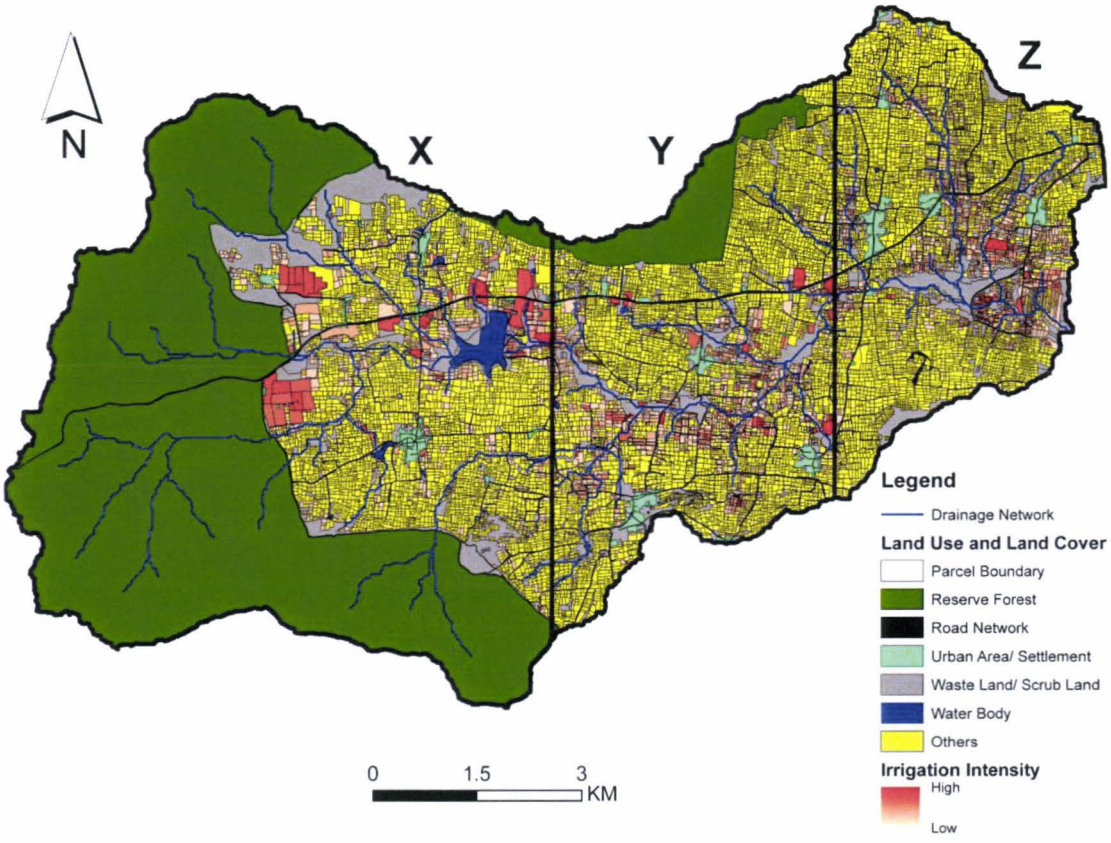

Figure 84 Spatiotemporal map of Dual (Rabi and Summer) irrigated cropland area for the duration 1990 to 2016.

Conclusions

Characterizing the spatiotemporal evolution of irrigated croplands is essential for sustainable resource exploitation in intensive agriculture areas. This study showed that available multitemporal remote sense data could be used to retrieve historical evolution of irrigation and its impact on groundwater resources for the last four decades. While we used Landsat multi-temporal imagery, it would be interesting in future studies to apply our approach to Sentinel 2 time-series to compare the results

obtained with these two different types of datasets. We have shown that the combined use of multispectral indices like NDVI (vegetation), EVI (soil impact correction to vegetation) and NDMI (moisture) could provide accurate classification of irrigated cropland. Using SVM algorithm (trained with intensive ground sample dataset) allowed us to generate irrigated cropland statistics for the past four decades in a semi-arid watershed in South India, which was a challenge considering with the small parcel dimensions (less than 0.5 ha). The resulting irrigated and non-irrigated cropland classified maps were generated for rabi and summer seasons with high classification accuracy and kappa coefficient. Results show the contrasted spatial distribution of irrigated cropland in the watershed and its evolution over time: while irrigation was developed very early in the valley areas in the East (downstream), it expanded recently to all the upstream areas while decreasing in the East. This was found consistent with the observed evolution of groundwater resources in the watershed: while in the East part groundwater was severely depleted since 2010, the decline in water table levels is more recent in the West. The constructed irrigated cropland statistics can be used as an input to groundwater models for understanding the interactions between climate, agricultural practices, and water resources. *Kharif* or monsoon cropping season is the most cultivated among all cropping season, but the limitation of optical satellite is the cloud cover. The kharif cropping season irrigated cropland monitoring using polarimetric SAR images is presented in the following chapter.

CHAPTER 4: Irrigated cropland identification

Summary

This chapter aims to monitor spatial distribution of irrigated cropland in the Berambadi watershed for all cropping seasons. The chapter is divided into two main sections: Evaluation of Radarsat-2 quad-pol SAR time series images for monitoring groundwater irrigation, and Seasonal intensive groundwater irrigated cropland identification using multiple satellites NDVI time-series images. In the first section use of various polarization indices obtained from radarsat-2 SAR data used for the irrigated cropland monitoring is demonstrated. In the section two, the use of multiple optical satellite images during the all cropping seasons for the experimental watershed for the irrigated cropland monitoring is demonstrated.

4.1 Evaluation of Radarsat-2 quad-pol SAR time series images for monitoring groundwater irrigation

Groundwater assists farmers to irrigate crops for fulfilling the crop-water requirement. Indian agriculture system is characterized by three cropping seasons known as kharif (monsoon), rabi (post-monsoon) and summer (pre-monsoon). Optical and microwave remote sensing provides an opportunity to monitor the irrigated croplands with high spatial and temporal resolution. In this chapter the irrigated cropland monitoring using Radarsat-2 quad-pol SAR microwave and multi-satellite optical time-series images is presented for the Berambadi watershed.

In this section of the chapter, the strength of C-band polarimetric Synthetic Aperture Radar (SAR) time series images were evaluated to classify groundwater irrigated croplands for the kharif and rabi cropping seasons of the year 2013. The present study was performed in the Berambadi experimental watershed of Kabini river basin, southern peninsular India. A total of fifteen polarimetric variables were estimated includes four backscattering coefficients (HH, HV, VH, VV) and eleven polarimetric

indices for all Radarsat-2 SAR images. The cumulative temporal sum (seasonal and dual-season) of these parameters was supervised classified using Support Vector Machine (SVM) classifier with intensive ground observation samples. Classification results using the best equation (highest accuracy and kappa) shows that the kharif, rabi and irrigated double croplands are respectively 10.1 km² (21.7%), 10.5 km² (22.6%) and 6.2 km² (13.4%) with a kappa coefficient respectively 0.82, 0.79 and 0.94.

4.1.1 Ground observation

The ground observation was carried out at Berambadi watershed (Figure 85) (Ruiz et al., 2016; Sekhar and Ruiz, 2010). The southwest (SW) and northeast (NE) monsoon seasons are assisting farmers to grow non-irrigated crops during respectively kharif and rabi cropping seasons. Groundwater irrigation is fulfilling the crop water requirement partially or fully for the irrigated crops (Robert et al., 2017b; A K Sharma et al., 2018; Sriramulu et al., 2017a). The Berambadi watershed is having three main cropping seasons, known as monsoon (kharif), post-monsoon (rabi) and summer (pre-monsoon) season.

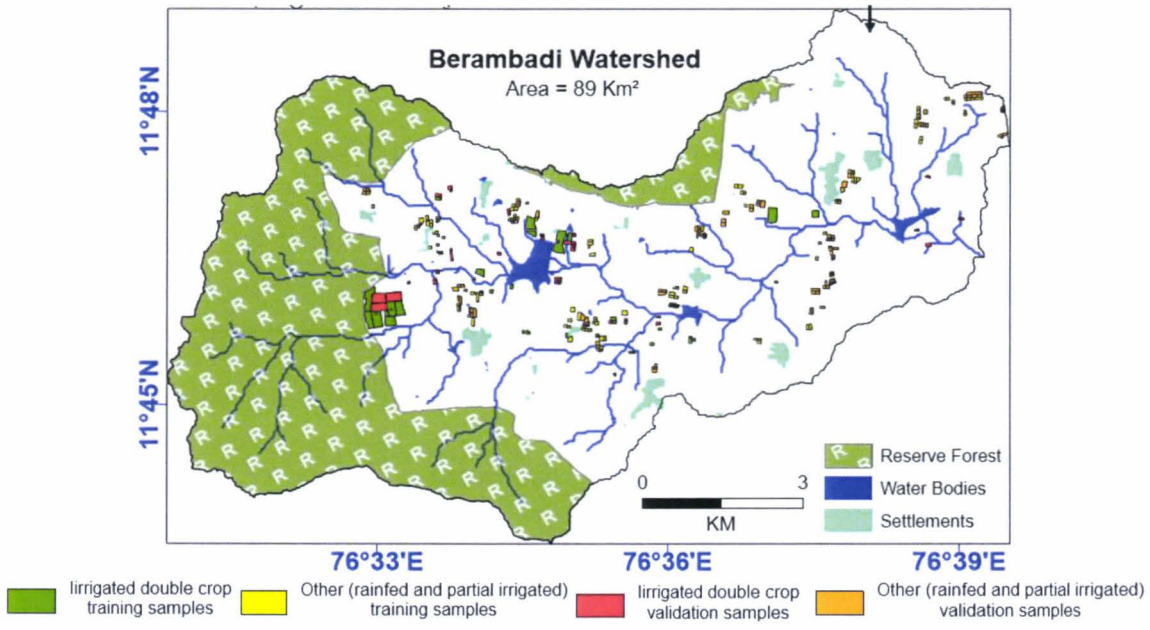

Figure 85 Study area and ground observation locations.

Crops like solar beans, garlic, tomato, beetroot, cabbage, turmeric, sugarcane, and banana need irrigation. Summer cropping season comprises of 100% irrigated cash crops. The major summer crops in the watershed are cabbage, beetroot, onion, vegetables, watermelon, sugarcane, and banana (A K Sharma et al., 2018). In Berambadi watershed groundwater is the only source of irrigation, due to unavailability of canals and restriction to pump water from the water bodies (tanks). The dug wells and open wells almost disappear in the Berambadi watershed due to the groundwater level is approximately 30m from the surface (Sekhar et al., 2016). Farmers are using drip, sprinkler, or furrow irrigation techniques based on the individual financial condition, availability of borewells, groundwater yield and the support from the government.

4.1.2 Satellite images used for the study

Radarsat-2 is an active SAR (synthetic aperture radar) microwave satellite with a payload of C-band (frequency = 5.4 GHz) (MacDonald Dettwiler and Associates Ltd., 2014). Nine Radarsat-2 satellite quad pol (HH, HV, VH, VV) images at fine-quad (FQ6) mode were acquired for the period from June 2013 to December 2013 (Table 12). The quad pol images consist of four polarization combinations (quad pol) includes horizontal transmission & horizontal receiving (HH pol), horizontal transmission & vertical receiving (HV pol), vertical transmission & vertical receiving (VV pol) and vertical transmission & horizontal receiving (VH pol). The low incidence angle (~25°) with 5.3 GHz frequency antenna (C-band SAR) is one of the ideal conditions to estimate surface soil moisture (Tomer et al., 2015; Zribi et al., 2014). Low incidence angle has the least attenuation with the crop canopy, and the backscattering coefficient is mainly representing the surface soil humidity (Srivastava et al., 2009; Ulaby, 1975). The ground and azimuth resolutions for all acquired images were respectively 10.9m and 4.7m. More characteristics of the satellite images were presented in Table 12.

Table 12 *Characteristics and dates of acquired Radarsat-2 satellite images.*

Radarsat-2 satellite images characteristics	
Ground resolution	10.99m
Azimuth resolution	4.7m
Polarization	Quad pol (HH, HV, VH, and VV)
Mode	Fine quad (descending)
Incidence angle	24.6 (near) – 26.4 (far)
Data acquisition dates	08- 06-2013
	02-07-2013
	26-07-2013
	19-08-2013
	12-09-2013
	06-10-2013
	30-10-2013
	23-11-2013
	17-12-2013

4.1.3 Ground observations

A ground survey was carried out during kharif and rabi cropping seasons to collect field data. A total of 301 samples were collected which include 74 samples for irrigated croplands and 227 samples for others category includes rainfed or partially irrigate fields (Figure 86). Ground control campaign was conducted for the kharif and rabi cropping seasons on the day of Radarsat-2 satellite passes. The intensively irrigated parcels represent long duration (eight months or more) irrigated crops (viz. banana, sugarcane, turmeric, and plantations) or irrigated crops during two consecutive cropping seasons for the kharif and rabi (viz. beetroot, cabbage, garlic, onion, watermelon, etc.). The other cropland includes either partially irrigated in the absence of rainfall or cultivation under only in rainfed condition for both cropping seasons. The summer cropping season is not included in the analysis due to non-availability of Radarsat-2 dataset. The data collected on crop type, irrigation type (drip, sprinkler or furrow) and groundwater level measurement for the better understanding the

cropping practices in the watershed. The randomly selected calibration and validation samples of irrigated and other croplands were presented in four categories (Figure 85):

i. irrigated double crop training samples (groundwater irrigated cropland samples (performed irrigation in kharif and rabi cropping seasons) used to train SVM classifier),
ii. other (rainfed and partial irrigated) training samples (the rainfed in both cropping seasons or partial irrigated cropland samples (performed irrigation activity in absence of rainfall according to groundwater availability) used to train SVM classifier),
iii. irrigated double crop validation samples (groundwater irrigated cropland samples (performed irrigation in kharif and rabi cropping seasons) used for the validation of SVM classified output and,
iv. other (rainfed and partial irrigated) validation samples (the rainfed in both cropping seasons or partial irrigated cropland samples (performed irrigation activity in absence of rainfall according to groundwater availability) used for the validation of SVM classified output).

Agricultural parcels of the Berambadi watershed were manually digitized using google earth image of the year 2012 and updated using 1.5m spatial resolution SPOT-6 (Satellite Pour l'Observation de la Terre) satellite image (A K Sharma et al., 2018). Total 18,500 agricultural parcels were identified in the Berambadi watershed out of the total approximately 19,600 parcels. It was noticed that the majority of agricultural parcels were of approximately 0.2ha area.

Berambadi watershed is having a high number of rainy days during southwest monsoon (kharif cropping season) compare to the northeast monsoon (rabi cropping season) (Figure 86). The daily rainfall data was observed during the Radarsat-2 satellite data acquisition period. In the year 2013, total rainfall during kharif and rabi cropping seasons was respectively 602.5mm and 227.5mm.

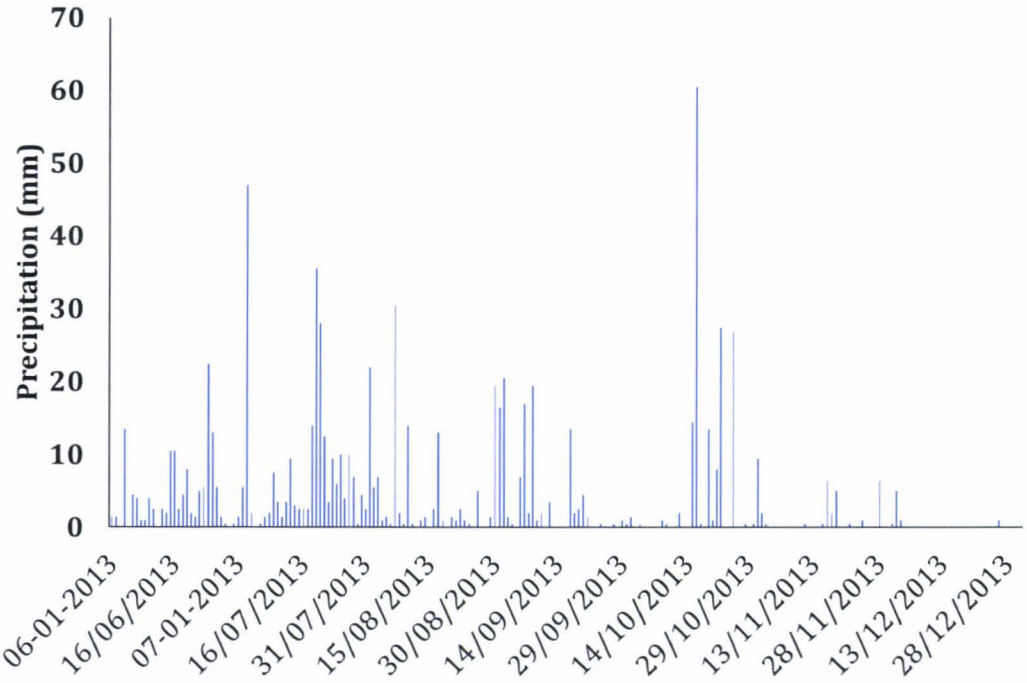

Figure 86 Daily rainfall of the Berambadi watershed for the Radarsat-2 pass duration

Image pre-processing consists of radiometric calibration, speckle filtering and geometric correction (Battude et al., 2014). The radiometric calibration was done for all Radarsat-2 images to extract backscattering coefficients σ◦HH, σ◦HV, σ◦VH and σ◦VV (Betbeder et al., 2014a).

The Lee sigma speckle filter (Duguay et al., 2016; Lee, 1983; Lee et al., 2009) with 4 look intensity, 5 x 5 window size, sigma=0.9, and target window 3 x 3 was used to reduce speckle noise. The improved Lee sigma speckle filter's characteristics were quantitatively evaluated and validated with SAR images (Lee et al., 2009). All SAR images were geocoded using 3sec SRTM (shuttle radar topographic mission) DEM (digital elevation model). After geocoding all SAR images were geometrically corrected with ground survey locations with UTM (Universal Transverse Mercator) projection and 43rd Zone of North hemisphere.

4.1.4 Image processing

On the basis of the current state of the art, total 11 polarization indices (PI's) using polarimetric backscattering coefficients (σ°HH, σ°HV, σ°VH, and σ°VV) and individually all four backscattering coefficients (σ°HH, σ°HV, σ°VH, and σ°VV) are extracted. As presented in the figure 87 for all nine Radarsat-2 images acquisition dates (Table 12) during kharif and rabi cropping seasons were processed to classify irrigated cropland in the watershed. These PI's are representing various combinations of polarimetric backscatter coefficients (Figure 87). The parcels mean values of various polarimetric indices and backscattering coefficients were calculated using digitized agricultural parcel boundaries for all nine acquisition dates (9 dates * 15 indices = 145 outputs).

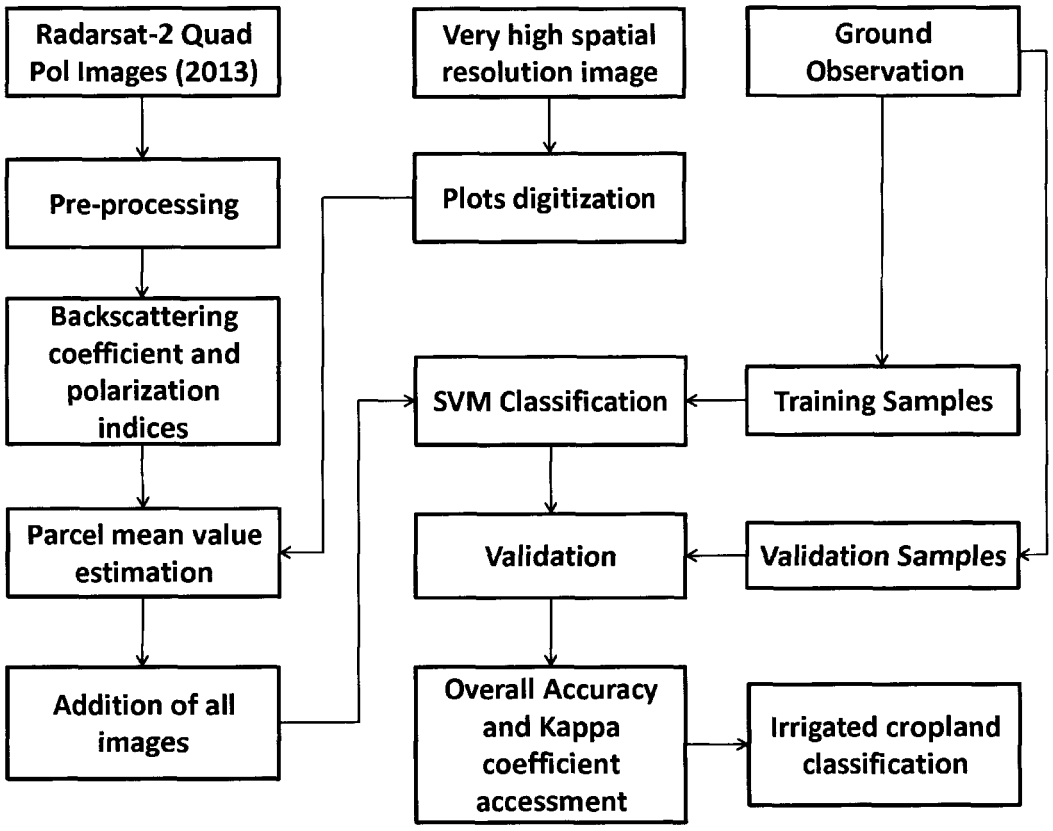

Figure 87 Image processing workflow.

To classify groundwater irrigated double croplands the parcel scale cumulative sums output (Eq^{n} 31) were calculated from the time series images (during kharif and rabi

cropping seasons). This double cropping season cumulative sum was estimated for all four backscattering coefficients and eleven polarimetric indices (Eq^n 31 to Eq^n 45).

$$\sum_{i=1}^{9} \sigma°hh(i) = \sigma°hh\,(08June) + \sigma°hh\,(02July) + \sigma°hh\,(26July) + \sigma°hh\,(19Aug) + \sigma°hh\,(12Sept) + \sigma°hh\,(06Oct) + \sigma°hh\,(30Oct) + \sigma°hh\,(23Nov) + \sigma°hh\,(17Dec) \quad \textit{Equation 31}$$

The equation Eq^n 31 till Eq^n 34 are representing the polarization backscattering coefficients and the Eq^n 31 till Eq^n 45 are representing the various polarization indices. The proposed cumulative backscattering coefficients and polarization indices are:

$$\sum_{i=1}^{9} \sigma°hv(i) \quad \text{Equation 32}$$

$$\sum_{i=1}^{9} \sigma°vv(i) \quad \text{Equation 33}$$

$$\sum_{i=1}^{9} \sigma°vh(i) \quad \text{Equation 34}$$

$$\sum_{i=1}^{9} \frac{(\sigma°vh(i))}{(\sigma°vv(i))} \quad \text{Equation 35}$$

$$\sum_{i=1}^{9} \frac{(\sigma°hv(i))}{(\sigma°hh(i))} \quad \text{Equation 36}$$

$$\sum_{i=1}^{9} \frac{(\sigma°hh(i))}{(\sigma°hv(i))} \quad \text{Equation 37}$$

$$\sum_{i=1}^{9} \frac{(\sigma°vv(i))}{(\sigma°hh(i))} \quad \text{Equation 38}$$

$$\chi_{v} = \sum_{i=1}^{9} \sigma°vh(i) - \sigma°vv(i) \quad \text{Equation 39}$$

$$\sum_{i=1}^{9} \sigma°vv(i) - \sigma°hh(i) \quad \text{Equation 40}$$

$$\sum_{i=1}^{9} \sigma°hh(i) + \sigma°vh(i) \quad \text{Equation 41}$$

$$\sum_{i=1}^{9} \frac{(\sigma°hh(i) - \sigma°vv(i))}{(\sigma°hh(i) + \sigma°vv(i))} \quad \text{Equation 42}$$

$$\sum_{i=1}^{9} \frac{(\sigma°hh(i) - \sigma°hv(i))}{(\sigma°hh(i) + \sigma°hv(i))} \quad \text{Equation 43}$$

$$RVI = \sum_{i=1}^{9} \frac{(8 * \sigma°hv(i))}{\left(\sigma°hh(i) + \sigma°vv(i) + (2 * \sigma°hv(i))\right)} \quad \text{Equation 44}$$

$$\sum_{i=1}^{9} \frac{(\sigma°vv(i) - \sigma°hh(i))}{\sqrt{(\sigma°vv(i))2 - (\sigma°hh(i))2}}. \quad \text{Equation 45}$$

Backscattering coefficients (Eq^n 31 to Eq^n 34) were used for the soil moisture and crop classification (Betbeder et al., 2014a; Canisius et al., 2018; Susan Moran et al., 2012;

Yusoff et al., 2017). The co-polarized correlation coefficient (ρvvhh) represents the correlation between co-polarized channels like HH and VV. Eq^{n} 37 (Betbeder et al., 2014a), Eq^{n} 38 (Canisius et al., 2018), Eq^{n} 40 (Susan Moran et al., 2012), Eq^{n} 42 (Haldar et al., 2016) and Eq^{n}45 (Gherboudj et al., 2011) are computed with co-polarized backscattering coefficients for various crops and soil moisture studies. De-polarization (χ_v) (Eq^{n} 39) calculated using VH and VV backscattering coefficients (Gherboudj et al., 2011; Ulaby et al., 1983) which is used for agro-hydrological applications and to calibrate water-cloud model (Gherboudj et al., 2011). The cross-polarized indices like Eq^{n} 35 and Eq^{n} 36 (Canisius et al., 2018), Eq^{n} 41 and Eq^{n} 44 (Canisius et al., 2018; Kim et al., 2012a) and Eq^{n} 43 (Haldar et al., 2016) have also been used widely to understand the crop phenology and the surface soil moisture. The scikit-learn library (Pedregosa et al., 2011) was used to perform SVM supervised classification. Out of total 301 ground observed samples, randomly selected 50% samples were used for the training (supervised learning) and remaining 50% samples used for the validation of classified output.

The individual cumulative sum for all 15 polarization indices were fed to the SVM classifier with intense ground observed training samples and followed with validation of SVM classification outputs by remaining ground observed samples (Figure 87). The validation of classification outputs was performed by confusion matrix, user's accuracy, producer's accuracy, overall accuracy and kappa coefficients estimation (Gumma et al., 2016; Olofsson et al., 2013; Yan and Roy, 2016). The polarization parameter with highest classification accuracy and kappa coefficient for the irrigated double crop classification is further used to classify seasonal (kharif and rabi individually) irrigated croplands.

4.1.5 Results

Irrigated double cropland for the kharif and rabi cropping seasons were classified using SVM classifier. Total fifteen classified outputs were generated using indices mentioned above (four backscattering coefficients and eleven polarisation indices). These classified outputs were representing parcels which were under irrigation for the

two consecutive cropping seasons (kharif and rabi seasons). These classified irrigated cropland outputs were calibrated and validated using respectively 149, and 152 ground observed sampling parcels. The classified outputs were validated by calculating producer's accuracy, user's accuracy, overall classification accuracy and kappa coefficient with the confusion matrix (Table 16) (Foody et al., 2006; Gumma et al., 2016). The SVM classification calibration and validation were performed at pixel scale (5m spatial resolution), and the confusion matrix was generated in percentage (Gao et al., 2018; Hill et al., 2005). Validation of the classification output was performed by dividing samples into two categories known as:

i. irrigated double crop (irrigated parcels during both kharif and rabi cropping seasons) and
ii. the other croplands (rainfed croplands during both kharif and rabi cropping seasons and partial irrigation in the absence of rainfall according to the groundwater availability).

Out of fifteen classified outputs from the above mention equations for irrigated double crop classification, five classified outputs (Eq^n 31, Eq^n 34, Eq^n 39, Eq^n 43, and Eq^n 46) has a zero-kappa coefficient and 62.6% classification accuracy. These five classifications outputs were able to classify other croplands precisely but not able to classify irrigated double crop. The precise classification of other croplands and not able to classify irrigated double crop satisfies the validation for only one category. For these (five equations Eq^{n}31, Eq^{n}34, Eq^{n}39, Eq^{n}43, and Eq^{n}46) classified outputs the precise classification of the other cropland category bags the classification accuracy of 62.6%, but the irrigated double croplands were not classified precisely in these outputs, which makes kappa accuracy 0%.

The kappa classification accuracy for the six classified outputs (Eq^n 35, Eq^n 36, Eq^n 37, Eq^n 41, Eq^n 43, and Eq^n 44) were less than 70%, and for two classification outputs (Eq^{n}32 and Eq^n 34) the kappa classification accuracies were more than 70% but less than 80%. Only Eq^n 39 and Eq^n 40 classified the irrigated double crop and other croplands precisely with a kappa classification accuracy respectively 93.9% (OA = 97.2%) and 93.3% (OA = 96.9%) (Table 16). The errors of omission (producer's

accuracy) and errors of commission (user's accuracy) for highest kappa classification accuracy output (Eq^{n} 39) were respectively for the irrigated double crop 0.94 and 0.98, whereas for other croplands respectively 0.99% and 0.97% were estimated (Dheeravath et al., 2010; Du et al., 2013; Lunetta et al., 2006; Thenkabail et al., 2008; Yan and Roy, 2014) were also respectively highest for the Eqn9 and Eqn10.

Table 13 The table presents confusion matrix, user's accuracy, producer's accuracy, overall classification accuracy (OA), and the kappa coefficient for all SVM classified outputs from various polarization indices.

Eq^{n} No.	Polarization Indices	Confusion Matrix (%)				User's Accuracy (%)	Producer's accuracy (%)	Overall Accuracy (%)	Kappa (%)
			a	b	Total				
31	$\sum_{i=1}^{9} \sigma^{\circ}\mathrm{hh}(i)$	a	0	0	0	a=0, b=0.63	a=0, b=1	62.6	0
		b	37.4	62.6	100				
		Total	37.4	62.6	62.6				
32	$\sum_{i=1}^{9} \sigma^{\circ}\mathrm{hv}(i)$	a	27.2	0.6	27.8	a=0.98, b=0.86	a=0.73, b=0.99	89.2	75.8
		b	10.2	62.0	72.2				
		Total	37.4	62.6	89.2				
33	$\sum_{i=1}^{9} \sigma^{\circ}vv(i)$	a	0	0	0	a=0, b=0.63	a=0, b=1	62.6	0
		b	37.3	62.6	100				
		Total	37.4	62.6	62.6				
34	$\sum_{i=1}^{9} \sigma^{\circ}vh(i)$	a	27.9	0.6	28.5	a=0.98, b=0.87	a=0.75, b=0.99	89.9	77.3
		b	9.4	62.1	71.0				
		Total	37.4	62.6	90.0				
35	$\sum_{i=1}^{9} \frac{\sigma^{\circ}\mathrm{vh}\ (\mathrm{i})}{\sigma^{\circ}\mathrm{vv}\ (\mathrm{i})}$	a	27.2	5.7	32.9	a=0.83, b=0.85	a=0.73, b=0.91	84.11	65.2
		b	10.1	57.0	67.1				
			37.4	62.6	84.2				
36	$\sum_{i=1}^{9} \frac{\sigma^{\circ}\mathrm{hv}\ (\mathrm{i})}{\sigma^{\circ}\mathrm{hh}\ (\mathrm{i})}$	a	28.3	7.3	35.6	a=0.79, b=0.86	a=0.76, b=0.88	83.5	64.5
		b	9	55.4	64.4				
			37.4	62.6	83.7				
		a	28.8	7	35.8	a=0.81,	a=0.77,	84.4	66.4

37	$\sum_{i=1}^{9} \frac{\sigma^{\circ}\mathrm{hh}\ (\mathrm{i})}{\sigma^{\circ}\mathrm{hv}\ (\mathrm{i})}$	b	8.5	55.7	64.2	b=0.87	b=0.89		
			37.4	62.6	84.5				
38	$\sum_{i=1}^{9} \frac{\lvert\sigma^{\circ}\mathrm{vv}\ (\mathrm{i})\rvert^2}{\lvert\sigma^{\circ}\mathrm{hh}\ (\mathrm{i})\rvert^2}$	a	0	0	0	a=0, b=0.63	a=0, b=1	62.6	0
		b	37.3	62.6	100				
			37.4	62.6	62.6				
39	$\sum_{i=1}^{9} \sigma^{\circ}vh(i) - \sigma^{\circ}vv(i)$	a	35.3	0.7	36	a=0.98, b=0.97	a=0.94, b=0.99	97.2	93.9
		b	2	62.0	64				
			37.4	62.6	97.3				
40	$\sum_{i=1}^{9} \sigma^{\circ}vv(i) - \sigma^{\circ}\mathrm{hh}(i)$	a	35.3	1.2	36.5	a=0.97, b=0.97	a=0.95, b=0.98	96.9	93.3
		b	2	61.5	63.5				
			37.4	62.6	96.8				
41	$\sum_{i=1}^{9} \sigma^{\circ}\mathrm{hh}(i) + \sigma^{\circ}vh(i)$	a	6.2	0	6.2	a=1, b=0.67	a=0.17, b=1	68.93	20.07
		b	31.1	62.7	93.8				
		Total	37.4	62.6	68.9				
42	$\sum_{i=1}^{9} \frac{(\sigma^{\circ}\mathrm{hh}(i) - \sigma^{\circ}vv(i))}{(\sigma^{\circ}\mathrm{hh}(i) + \sigma^{\circ}vv(i))}$	a	0	0	0	a=0, b=0.63	a=0, b=1	62.6	0
		b	37.3	62.6	100				
		Total	37.4	62.6	62.6				
43	$\sum_{i=1}^{9} \frac{(\sigma^{\circ}\mathrm{hh}(i) - \sigma^{\circ}\mathrm{hv}(i))}{(\sigma^{\circ}\mathrm{hh}(i) + \sigma^{\circ}\mathrm{hv}(i))}$	a	28.3	6.5	34.8	a=0.82, b=0.86	a=0.76, b=0.9	84.4	66.3
		b	9	56.2	65.2				
		Total	37.4	62.6	84.5				
44	$\sum_{i=1}^{9} \frac{(8 * \sigma^{\circ}\mathrm{hv}(i))}{(\sigma^{\circ}\mathrm{hh}(i) + \sigma^{\circ}vv(i) + (2 * \sigma^{\circ}\mathrm{hv}(i)))}$	a	27.5	6.4	33.9	a=0.9, b=0.85	a=0.73, b=0.9	83.7	64.4
		b	9.8	56.3	66.1				
		Total	37.4	62.6	83.8				
45	$\sum_{i=1}^{9} \frac{(\sigma^{\circ}vv(i) - \sigma^{\circ}\mathrm{hh}(i))}{\sqrt{(\sigma^{\circ}vv(i))2 - (\sigma^{\circ}\mathrm{hh}(i))2}}$	a	0	0	0	a=0, b=0.63	a=0, b=1	62.6	0
		b	37.3	62.6	100				
		Total	37.4	62.6	62.6				

Where a and b represent respectively irrigated double-croplands (irrigated in kharif and rabi cropping seasons) and other (partial groundwater irrigation during or rainfed) croplands.

4.1.5.1 Irrigated double cropland classification

The dual season (kharif and rabi cropping seasons) irrigated cropland is classified using the equation with highest kappa coefficient and overall classification accuracy (Figure 88). The Eq^{n}39 represents the cumulative sum of the difference between VH and VV backscattering coefficients. The proposed research shows that the dual season cumulative sum from Eq^{n}39 (subtraction between cross-polarized backscattering coefficient and co-polarised backscattering coefficient) is performing irrigated double cropland classification with the highest overall classification accuracy and kappa coefficient. Total area estimated using Eq^{n}39 under dual season (kharif and rabi cropping seasons) irrigation is 6.22 km^2 and this irrigated double cropland area is 13.4% of the total cropland area in Berambadi watershed.

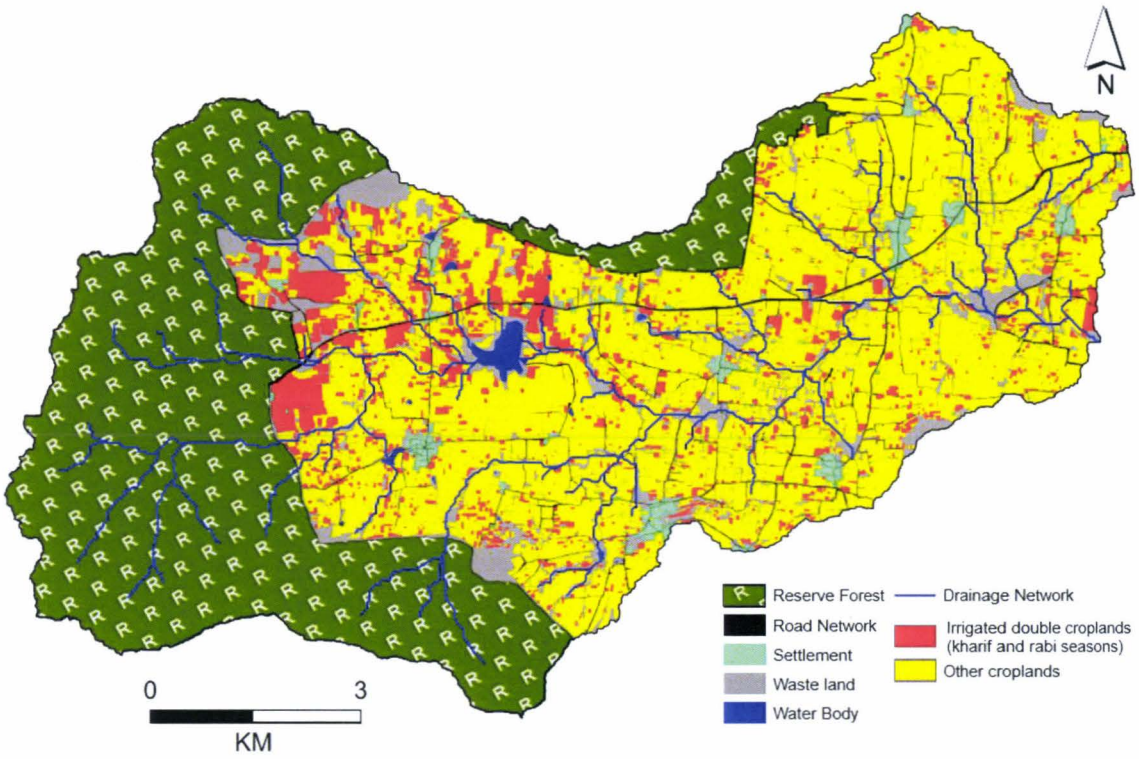

Figure 88 *Spatial distribution of dual-irrigation in the Berambadi watershed in 2013.*

Where the other croplands are partially groundwater irrigated in the absence of rainfall or grown under only rainfed condition.

The overall classification accuracy and kappa coefficient for the classification output using Eq^{n}39 are respectively 97.2% and 0.94 (Table 14). The user's accuracy and producer's accuracy for the irrigated double cropland (a) estimated respectively 0.98

and 0.94 (Table 14). For the other croplands (b) user's accuracy and producer's accuracy were estimated respectively 0.97 and 0.99. The Eqn9 bags the highest overall classification accuracy, kappa coefficient, user accuracy, and producer accuracy, with highest diagonal value (97.3%) (Table 14).

Table 14 Total irrigated area and classification accuracy for the dual-irrigation practices in the Berambadi watershed. Were a and b are representing respectively irrigated croplands and other (rainfed and fallow) croplands.

Cropping Season	Irrigated area (km^2)	Irrigated area (%)	User's Accuracy (%)	Producer's accuracy (%)	Overall accuracy (%)	Kappa Coef.
Dual (Kharif+Rabi) 2013-14	6.2	13.4	a=0.98, b=0.97	a=0.94, b=0.99	97.2	0.94

4.1.5.2 Kharif cropping season irrigated cropland classification

The spatial distribution of irrigated croplands in the Berambadi watershed for the kharif cropping season is presented in figure 89. As the Eq^n 39 bags the highest overall classification accuracy, kappa coefficient, user accuracy and producer accuracy for the irrigated double cropland identification, the same equation is used to classify kharif season irrigated cropland. The cumulative sum of Eq^n 39 outcomes for the all kharif season four Radarsat-2 SAR images (Table 15) was performed SVM classification with the same training and validation samples (Figure 89) to generate classification output and the accuracy assessment. It was noticed from the classification output (Figure 89) that the high concentration of the kharif season irrigated cropland is in the North-West (NW) region of the watershed. The NW region of the watershed is in the upstream which is between reserve forest and the biggest waterbody of the Berambadi watershed.

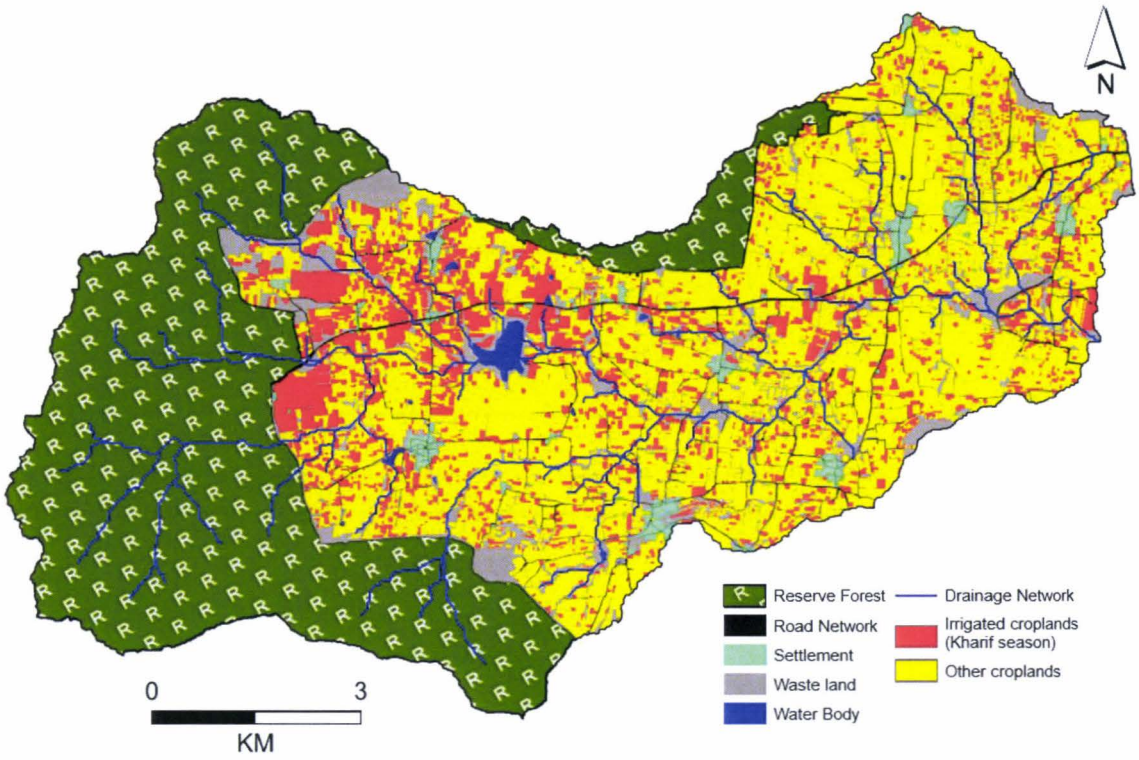

Figure 89 Spatial distribution of irrigated croplands during kharif cropping season. where the other croplands are partially groundwater irrigated in the absence of rainfall or grown under only rainfed condition.

The total irrigation area under kharif cropping season is 10.1 km² and approximately 21.7% area of the total cropland. The overall classification accuracy and kappa coefficient for the kharif irrigated cropland classification are respectively 91.4% and 0.82 (Table 15). The user's accuracy and producer's accuracy for the kharif season irrigated cropland (a) estimated respectively 0.85 and 0.94 (Table 15). For the other croplands (b) user's accuracy and producer's accuracy were estimated respectively 0.96 and 0.9.

Table 15 Total irrigated area and classification accuracy for the kharif cropping season. Were a and b are representing respectively irrigated croplands and other (rainfed and fallow) croplands.

Cropping Season	Irrigated area (km^2)	Irrigated area (%)	User's Accuracy (%)	Producer's accuracy (%)	Overall Acc. (%)	Kappa Coef.
Kharif 2013	10.1	21.7	a=0.85, b=0.96	a=0.94, b=0.9	91.4	0.82

4.1.5.3 Rabi cropping season irrigated cropland classification

The rabi cropping season spatial distribution of irrigated croplands in the Berambadi watershed is presented in figure 90. As the Eqn9 bags the highest overall classification accuracy, kappa coefficient, user accuracy and producer accuracy for the irrigated double cropland identification. The same equation is used to classify rabi season irrigated cropland classification. The cumulative sum of Eq^n 39 outcomes for the all rabi season five Radarsat-2 SAR images (Table 12) was undergone with SVM classification with the same training and validation samples (Figure 90) to generate classification output and the accuracy assessment. The rabi cropping season irrigated cropland is spread in all parts of the Berambadi watershed (Figure 90). The NW and the west region of the watershed is in the upstream of the Berambadi watershed are respectively having big irrigated parcels.

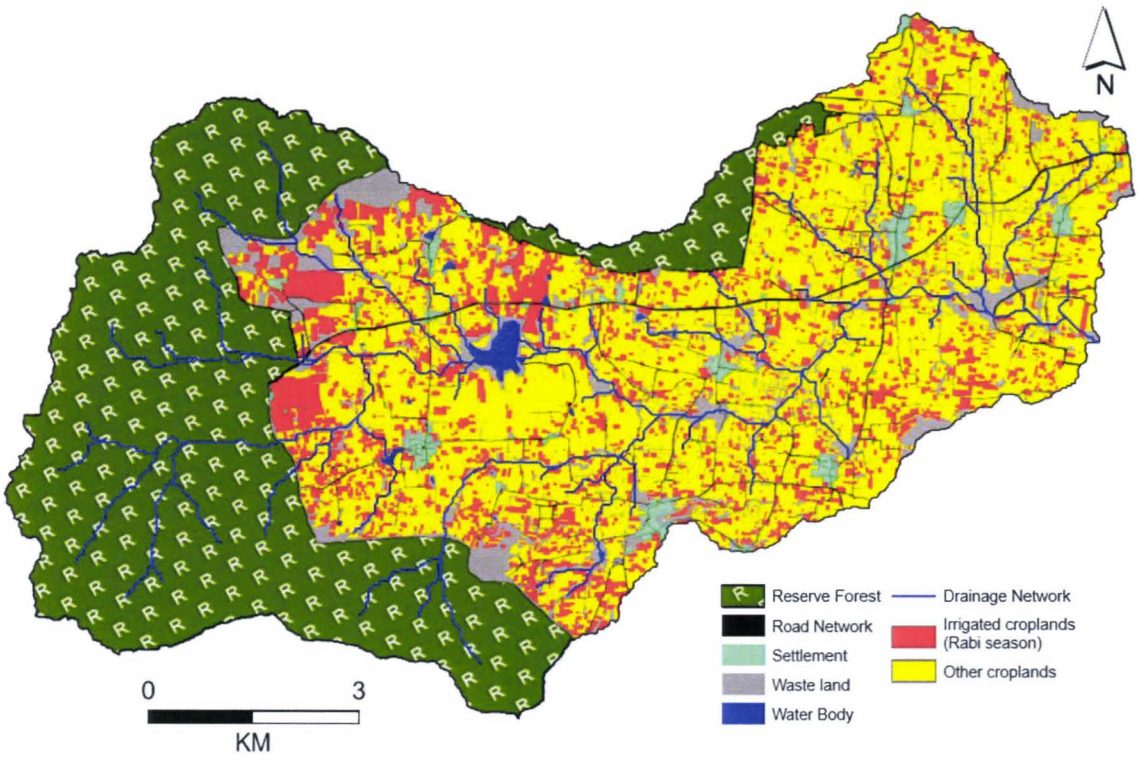

Figure 90 *Spatial distribution of rabi cropping season irrigated croplands.* The other croplands are partially groundwater irrigated in the absence of rainfall or grown under only rainfed condition.

The total area under rabi season irrigation is 10.5 km² and approximately 22.6% area of the total cropland in the watershed. The overall classification accuracy and kappa coefficient for the rabi irrigated cropland classification are respectively 90.4% and 0.79 (Table 16). The user's accuracy and producer's accuracy for the rabi season irrigated cropland (a) estimated respectively 0.88 and 0.86 (Table 16). Rabi season other croplands (b) user's accuracy and producer's accuracy were estimated respectively 0.92 and 0.94.

Table 16 Total irrigated area and classification accuracy for the rabi cropping season.

Cropping Season	Irrigated area (km^2)	Irrigated area (%)	User's Accuracy (%)	Producer's accuracy (%)	Overall Acc. (%)	Kappa Coef.
Rabi 2013-14	10.5	22.6	a=0.88, b=0.92	a=0.86, b=0.94	90.4	0.79

4.1.6 Discussion

In this study, the main objective was to evaluate the strength of C-band polarimetric SAR time series images to identify groundwater irrigated croplands. For that purpose, we classified polarimetric indices and backscattering coefficients calculated from Radarsat-2 quad-pol SAR images using SVM classifier.

The Berambadi watershed is mostly covered with clouds during kharif and rabi cropping seasons; the microwave remote sensing is the only available solution to map the spatial distribution of irrigated croplands in the watershed (Mangiarotti et al., 2018). Microwaves remote sensing uses respectively longer wavelengths (2.7 mm to 1.2 m) than optical wavelengths (0.435µm to 12.5µm) (https://landsat.usgs.gov/what-are-band-designations-landsat-satellites) which are not sensitive to atmospheric conditions (clouds, aerosols, etc.) (Hosseini et al., 2015; Karthikeyan et al., 2017; Ouchi, 2013). The Radarsat-2 data was used for the present study, (i) the unavailability of other high spatial resolution satellite images during the study period and (ii) Radarsat-2 is a quad pol satellite whereas Sentinel-1satellite is dual-pol (Engelbrecht et al., 2017). Nevertheless, the study can be extended using freely available Sentinel-1timeseries images for all three cropping seasons (kharif, rabi, and summer) and intra-annual analysis.

4.1.6.1 Selection of the polarimetric indices and backscattering coefficients for irrigated cropland mapping

The use of single polarimetric backscattering coefficient for crop monitoring or irrigated cropland monitoring is quite limited (Blaes et al., 2006). Radarsat-2 satellite products are comprising of four polarizations, which assists for multiple polarimetric combinations or polarimetric indices (Yang et al., 2017). The widely recognized polarimetric backscattering coefficients and polarimetric indices for crop and soil parameters monitoring were reviewed and implemented to identify seasonal irrigated croplands (Li and Lampropoulos, 2016; Yonezawa et al., 2012). The best index (Eqn9) to identify dual cropping season groundwater irrigated croplands is identified with the highest overall classification accuracy (97.2%) and kappa coefficient (0.94). The same equation (Eqn9) is further implemented to classify kharif and rabi cropping season groundwater irrigated croplands. For the kharif cropping season, the overall classification accuracy and kappa coefficients were respectively 91.4% and 0.82. Whereas for the rabi cropping season the overall classification accuracy and kappa coefficients were respectively 90.4% and 0.79.

4.1.6.2 Methodological considerations and study area complexity

In the Berambadi watershed majority of farmers are fully dependent on kharif and rabi cropping seasons. Farmers with borewell facility and good borewell yield are cultivating crops which require long term irrigation (e.g., turmeric, banana and sugarcane). Others are growing short duration irrigated cash crops (e.g., onion, garlic, beetroot, etc.) or non-irrigated crops (e.g., marigold, sunflower, maize, etc.). Very few farmers with good groundwater yield are growing water-intensive long duration crops (e.g., banana and sugarcane).

The spatial distribution of intensive groundwater irrigation in the Berambadi watershed (Sekhar et al., 2016) for the two main cropping season can be identified from the present study. The classified irrigated double croplands are majorly occupying with turmeric, sugarcane, banana, dual-season irrigated vegetables (e.g., onion, garlic, beetroot, chili, tomato, etc.), and the plantations. In the Berambadi

watershed, the groundwater is recharging from the rainfall during SW and NE monsoons and declining after the rabi cropping season (Maréchal et al., 2010). After recharging during SW and NE monsoons, groundwater table becomes shallow from the mid of kharif season till the end of the rabi cropping season. With the high possibility to supply water through borewells during these two cropping seasons enables the farmers to irrigate their crops which are comparably not possible during the summer season. Only farmers with multiple borewell facilities and shallow groundwater level are adapting long duration annual crops (A K Sharma et al., 2018). The depth of the groundwater from the surface in the watershed for the year 2013 was approximately between 15 m to 30 m (Sekhar et al., 2016).

In the year 2010, the World Bank has notified that in India approximately 36% (581 x 103 km²) of the total agricultural croplands (160 x 104 km²) are reliably irrigating. In the Karnataka state, the total groundwater irrigated area is approximately 10% (https://en.wikipedia.org/wiki/Irrigation_in_India). The proposed study shows that the dual cropping season groundwater irrigated croplands are approximately 13.4%, and for the individual kharif and rabi cropping season total irrigated areas are respectively 21.7% and 22.6%. The study can extend for the summer cropping season irrigated cropland monitoring. Excessive use of groundwater in the downstream areas of the watershed, the upstream of the watershed has shallow groundwater level with a comparison to the downstream (A K Sharma et al., 2018; Sriramulu et al., 2017b). Moreover, the downstream groundwater is highly contaminated with a high amount of nitrate (Sriramulu et al., 2017b). As the groundwater table become shallow in the upstream, farmers are started growing long duration irrigated crops.

4.1.7 Conclusion

Our study demonstrated the potential of using time series of Radarsat-2 quad-pol data to identify irrigated croplands in the context of south India. This constitutes an important advance, as kharif and rabi cropping seasons are very difficult to monitor with optical satellite imagery due to quasi-permanent cloud cover during the South West and North East monsoon. The SVM classifier has been proved to be a potential

candidate in order to classify irrigated double crop with 97.2% overall classification and 93.9% kappa classification accuracies. The result shows 13.4% croplands are cultivating irrigated double crops with intensive groundwater irrigation. However, due to the small parcel size (less than 0.5 ha), the high diversity of crop types and crop management practices in the watershed, crop classification remains a challenging task. The study brought out the uneven spatial distribution of irrigated double crop areas in the watershed. It is an important input for understanding the interactions between groundwater dynamics and cropping systems. This information retrieved will be crucial for constraining groundwater models such as the one being used in the Berambadi watershed, which will allow recommending suitable practices that need to be adopted by the farmers to ensure the sustainability of their farming systems. The situation can further lead to groundwater depletion and contamination in the upstream region too. The methodology used in this study could be applied at regional or national scales using freely available Sentinel-1 datasets for seasonal or annual irrigated cropland monitoring. Indeed, socio-economic sustainability and food security of this region depends on the judicious use of the groundwater and planning the cropping sequence with optimal utilization of groundwater resources in critical to reaching this goal.

4.2 Seasonal intensive groundwater irrigated cropland identification using NDVI time-series images

The overarching goal of this section is to monitor seasonal intensive irrigated croplands using multiple optical satellite NDVI time series images at watershed scale. Cloud cover during the crop growth is the biggest obstacle for optical remote sensing studies. Cloud-free images from the same satellite during complete cropping season is difficult in semi-arid or humid regions. Multiple optical satellite images can fill the gap for crop monitoring during various cropping seasons. The cloud-free images of LS-8, EO-1, IRS-P6, and Spot5Take5 satellites were collected from various payloads over Berambadi watershed, southern peninsular India. Optical images were procured for the all three cropping seasons from summer of the year 2014 till the summer of the year 2016. All images were atmospheric and geometric corrected followed with resampling at 5m spatial resolution. The Normalized Differential Vegetation Index (NDVI) values were estimated for all images at parcel scale, and seasonal cumulative NDVI products were generated at the parcel scale. The novel algorithm is aimed to identify seasonal intensive irrigated croplands like beetroot, cabbage, turmeric, sugarcane, banana, etc. Support Vector Machine (SVM) classification algorithm was implemented on seasonal cumulative NDVI images with intensive ground observations. The kappa coefficient was between 0.81 to 0.96 for summer, kharif and rabi of the year 2014-15 for the classified outputs. The kappa coefficient for the summer, kharif, and rabi of the year 2015-16 were between 0.62 to 0.89, and for the summer of the year 2016 kappa was 1. Results show that the intensive groundwater irrigation during various cropping seasons in the Berambadi watershed is between 5% to 20%.

4.2.1 Dataset used for the study

The study aimed to identify groundwater irrigated cropland using time-series of optical images from the summer cropping season of the year 2014 till the year 2016 summer cropping season. The study was conducted in the Berambadi watershed of southern peninsular India under research projects titled "Assimilation of Multi-

satellite data at Berambadi watershed for Hydrology And land Surface experiment" (AMBHAS) (Sekhar and Ruiz, 2010). Clouds are the biggest obstacle to use the same satellite images for the complete study period. To avoid the data gap, we have procured multiple optical sensor images of the study area for the monitoring period. The spatially distributed throughout the watershed intensive ground survey was done for the various monitored cropping seasons. Detail of the study area used datasets, and the methodology is presented in this section.

4.2.1.1 Remote sensing data collection and image pre-processing

Cloud cover during cropping seasons is the biggest obstacle for optical remote sensing for earth observation studies. To overcome the unavailability of same satellite time-series images we have procured optical images from various platforms like Landsat-8, Spot-5 (Take5), Earth Observation-1 (EO-1) and IRS-P6 (Figure 91). Optical Land Imager (OLI) sensor images from the Landsat-8 satellite, Advance Land Imagine (ALI) sensor images from the EO-1 satellite, High Resolution Geometrical (HRG-2) sensor images from Spot5 satellite and Linear Imaging Self Scanning Sensor (LISS-3 and LISS-4) sensor images from the Indian Remote Sensing (IRS) satellite IRS-P6 (Resourcesat-2) were procured from summer cropping of the year 2014 till summer season of the year 2016. All procured images were pre-processed for atmospheric correction using Second Simulation of a Satellite Signal in the Solar Spectrum (6S) (Claverie et al., 2015; USGS and U.S. Geological Survery, 2016; Vermote et al., 1997) radiative transfer model followed to the geometric correction. Figure 98 presents total 43 optical satellite cloud fee images from various platforms were procured and resampled at 5m spatial resolution without changing the pixel values (Roy et al., 2014; A K Sharma et al., 2018).

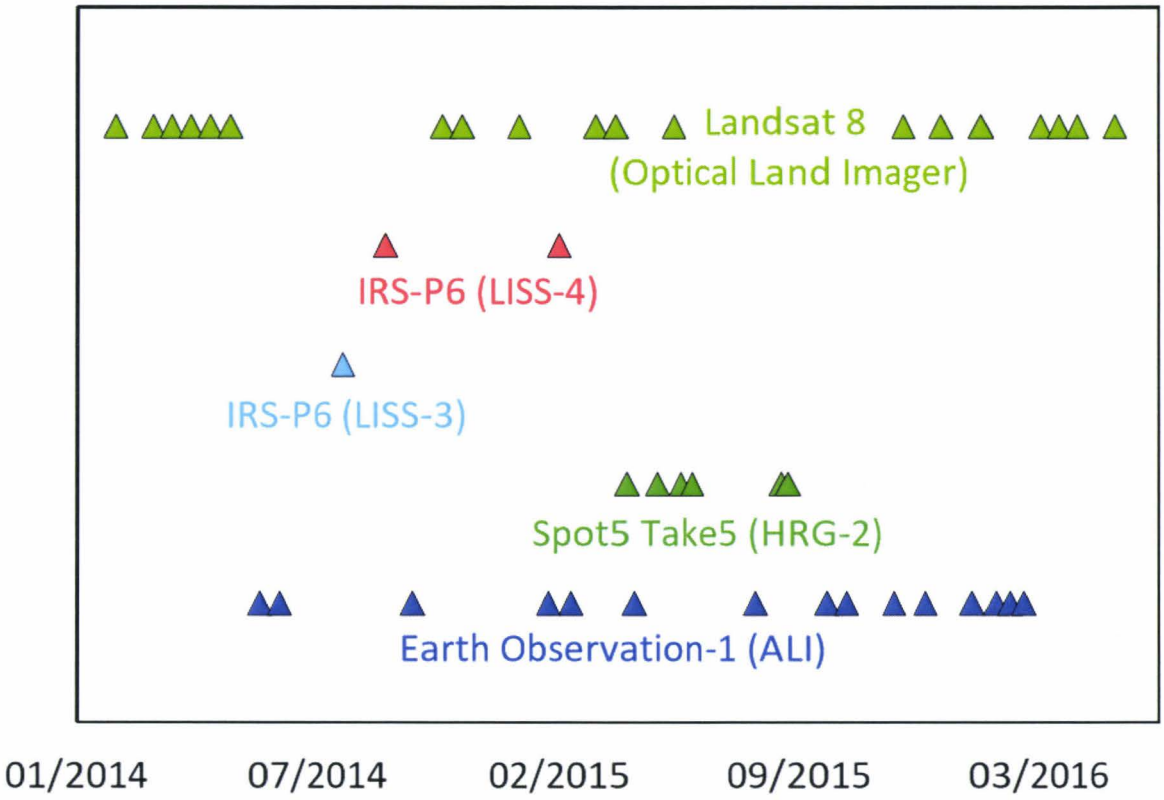

Figure 91 Multi-satellite images used for the study.

Berambadi watershed is characterized mainly with the parcels of an area less than a hectare. A total number of parcel in the Berambadi watershed are approximately 19,600, and total agricultural cropland is 18,500 (A K Sharma et al., 2018). All procured 43 satellite images were resampled at 5 m spatial resolution using the nearest neighbour (NN) resampling method without changing the original pixel values (Xu et al., 2015).

4.2.1.2 Ground observation data

Ground observation information was collected from the farmers and personally for all monitored cropping seasons (summer 2014, kharif 2014, rabi 2014-15, summer 2015, kharif 2015, rabi 2015-16 and summer 2016). Due to the limited funds, the ground survey was performed in mid of kharif and rabi cropping seasons of the year 2014 and 2015. During these surveys summer cropping of the year 2014 and 2015 were also collected from the farmers. Summer 2016 crop information was collected in the kharif season of the year 2016. While doing the filed survey quality of the collected

information is maintained (like if the farmer is sure, then only the information is collected). The ground survey was performed in the Berambadi watershed with an objective to collect maximum information about crop management practices and the water management practices at field (parcel) scale. Various information's were collected from the field survey to keep in knowledge while processing the datasets and result generation.

The main information's noticed during the field survey were:

(i) seasonal crop type,
(ii) irrigation practices information (number of irrigations, etc.),
(iii) crop seeding date,
(iv) crop harvesting dates (marigold has multiple harvesting and farmers use to cultivate mixed crops like onion, chili, and beetroot with the turmeric),
(v) weather crop is irrigated or rainfed or partial irrigated, and
(vi) source of the irrigation (own borewell or neighbor's borewell used for the irrigation) were collected.

The intensive spatially distributed survey was done throughout the watershed. It was noticed while survey that the farmers are performing unplanned partial irrigation during crop growth in the absence of rainfall, according to their groundwater facility (Sharma et al., 2019). After finishing all surveys to minimize the heterogeneity of cropping practices in the watershed, the datasets were divided into two categories:

(i) annual irrigated croplands (irrigated during all cropping seasons like summer, kharif, and rabi), and
(ii) others (rainfed, partially irrigated and left fallow for a cropping season).

Total 628 parcels were surveyed for the year 2014-15, 731 parcels were surveyed for the year 2015-16, and 604 parcels were surveyed for the year 2016 (Table 17). The intensively irrigated crops are long duration crops during all three cropping seasons (like banana, sugarcane, irrigated coconut, irrigated plantation, etc.), irrigated during two season and followed with summer irrigation (like turmeric (kharif and rabi) and summer crop

(like beetroot, cabbage, carrot, vegetables, etc.)), and individual three irrigation crops like onion, garlic, beetroot, cabbage, carrot, watermelon, vegetables, etc.

Table 17 Training and validation samples of intensively irrigated cropland and other croplands.

Year	Intensive irrigated	Others	Total
2014–2015	182	446	628
2015–2016	218	513	731
2016	152	452	604

Spatially distributed intensive irrigated croplands were surveyed for the years 2014, 2015 and 2016 in the Berambadi watershed. Figure 92 shows the training (calibration) and validation samples locations for all years. The training and validation samples were randomly divided 50-50% from the total collected samples of table 17. These training and validation further used to classify the irrigated croplands and to validate the classification outputs.

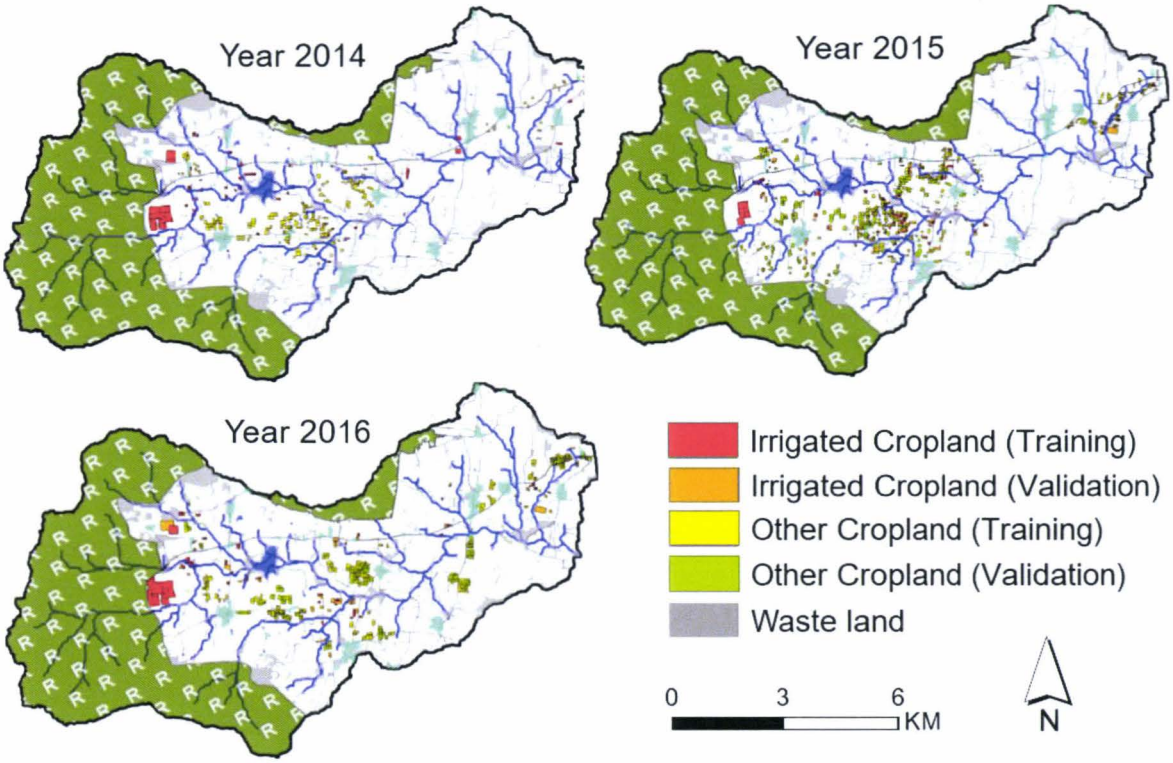

Figure 92 Ground observed training (calibration) and validation parcels of annual (summer + kharif + rabi) irrigated (intensive irrigation) and other (partial irrigation

in the absence of rainfall, rainfed only and fellow land) croplands for the years 2014, 2015 and 2016.

4.2.1.3 Monthly rainfall and its relation to cropping practices in the Berambadi watershed

The Berambadi watershed is characterized in three main cropping seasons known as summer, kharif, and rabi. Figure 93 shows the monthly rainfall for various cropping seasons from summer-2014 till summer-2016. The kharif cropping season is also known as monsoon season, and major farming practices are depending on the SW rainfall. The rainfed (non-irrigated) crop seeding during kharif season depends on the first rainfall of the season. Farmers with irrigation facility are sometimes doesn't wait for the first rain and sometimes they are starting seeding crops like turmeric (with onion and beetroot) in the first week of May also. The rabi cropping season is also known as post-monsoon cropping season as it credits with the NE monsoon rainfall for the crop cultivation. Less rainy days during the NE rainfall (for the example year 2014) is having a direct impact on the total cultivation. According to the groundwater condition farmers with the borewell facility are selecting the crop for seeding in the concern cropping season. During summer cropping season thunders may come but as there is no surety of the rainfall, only farmers with completely depends on the groundwater irrigation only.

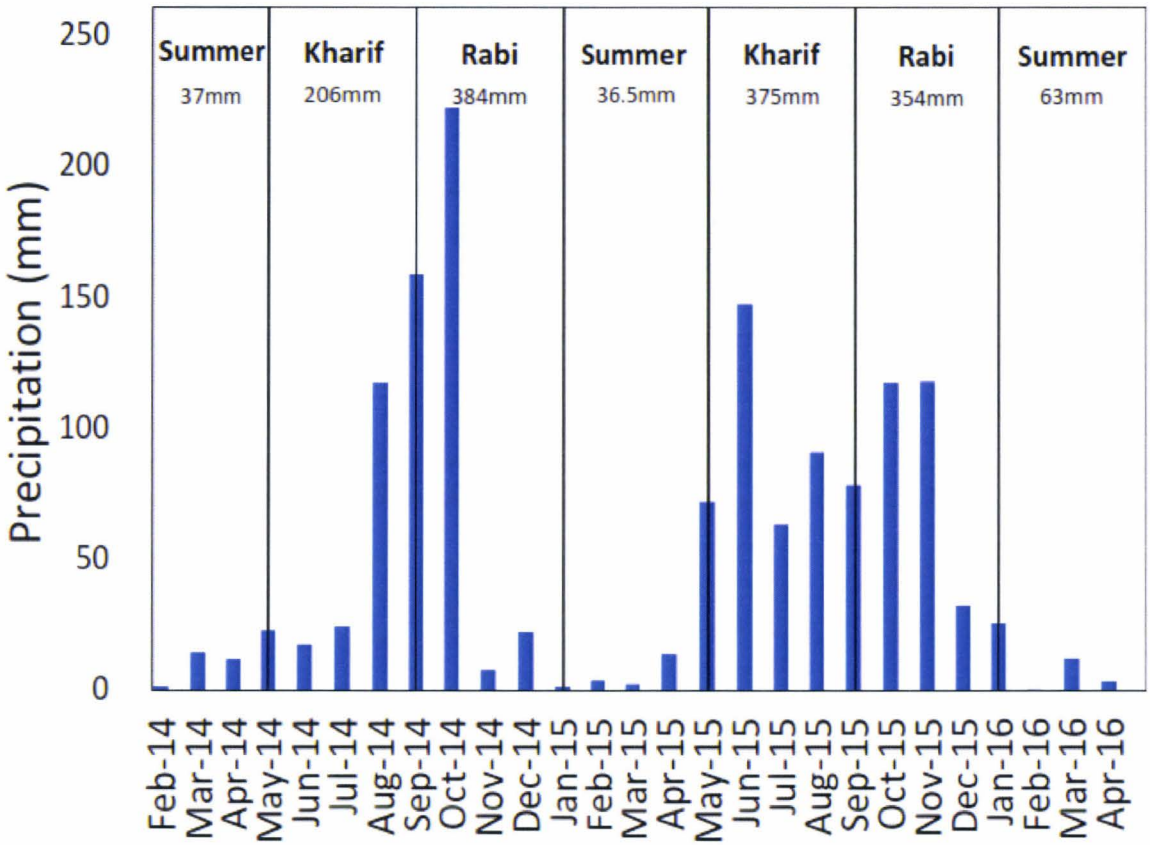

Figure 93 Monthly rainfall during cropping seasons for the year 2014-16.

The figure 93 shows the SW monsoon's weaker (monthly rainfall ~ 25 mm) starting and high rainfall (approximate 150 mm) at the end. Due to the weaker starting of the SW monsoon majority of rainfed farmers quit cultivating crops this year. The SW monsoon plays a major role to recharge groundwater (A K Sharma et al., 2018), but due to weaker monsoon the groundwater got depleted more than 50 m in downstream villages of the watershed (Sekhar et al., 2016).

4.2.2 Methodology

Hierarchical diagram of the comprehensive methodology to classify seasonal intensive irrigated croplands using multiple satellite images is presented in Figure 94. The pre-processed and resampled 5 m spatial resolution images further used to estimate NDVI time-series. The seasonal cumulative NDVI values at agricultural parcel scale were further used to classify the irrigated croplands for the concern cropping seasons.

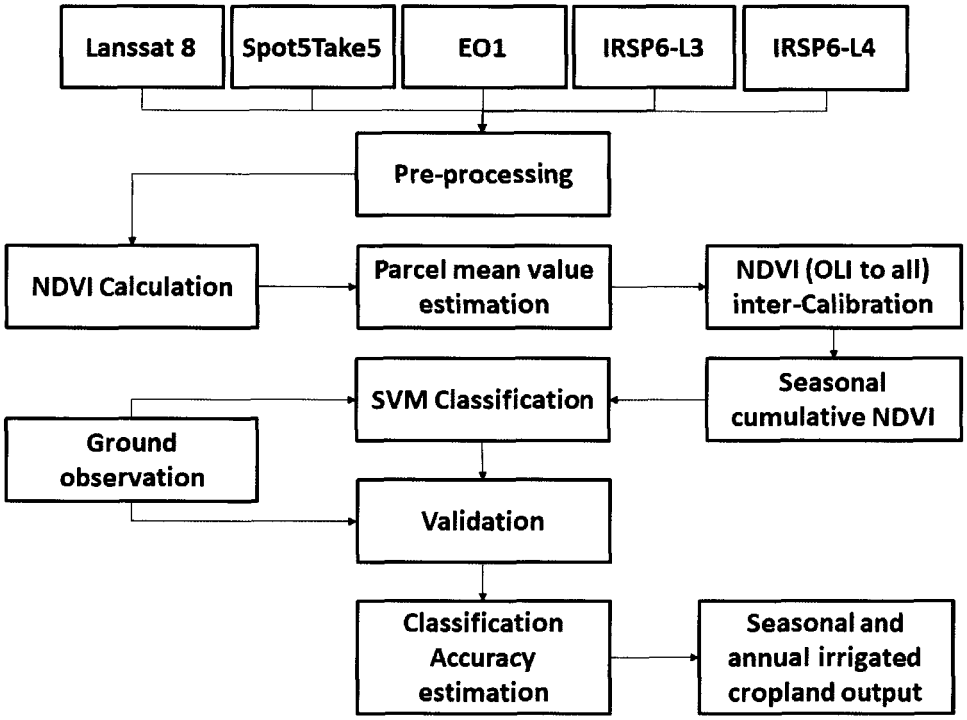

Figure 94 Methodology flow chart.

Available cloud-free Landsat-8, IRS-P6 (LISS-3 and LISS-4), EO-1 and Spot-5 (Take5) images of the Berambadi watershed were procured during the study period. The spatial resolution of various satellite images was varying from 5 m to 30 m. All images were resampled at 5 m spatial resolution using NN resampling method without changing the pixel value (Borra-Serrano et al., 2015). The parcel means NDVI values were estimated for all satellite dates using manually digitized parcel boundary (A K Sharma et al., 2018). The NDVI equation is presented below, here NIR represents to the Near InfraRed spectral band. The Figure 95 shows satellite derived NDVI for the different acquisition dates from the various satellite sensors.

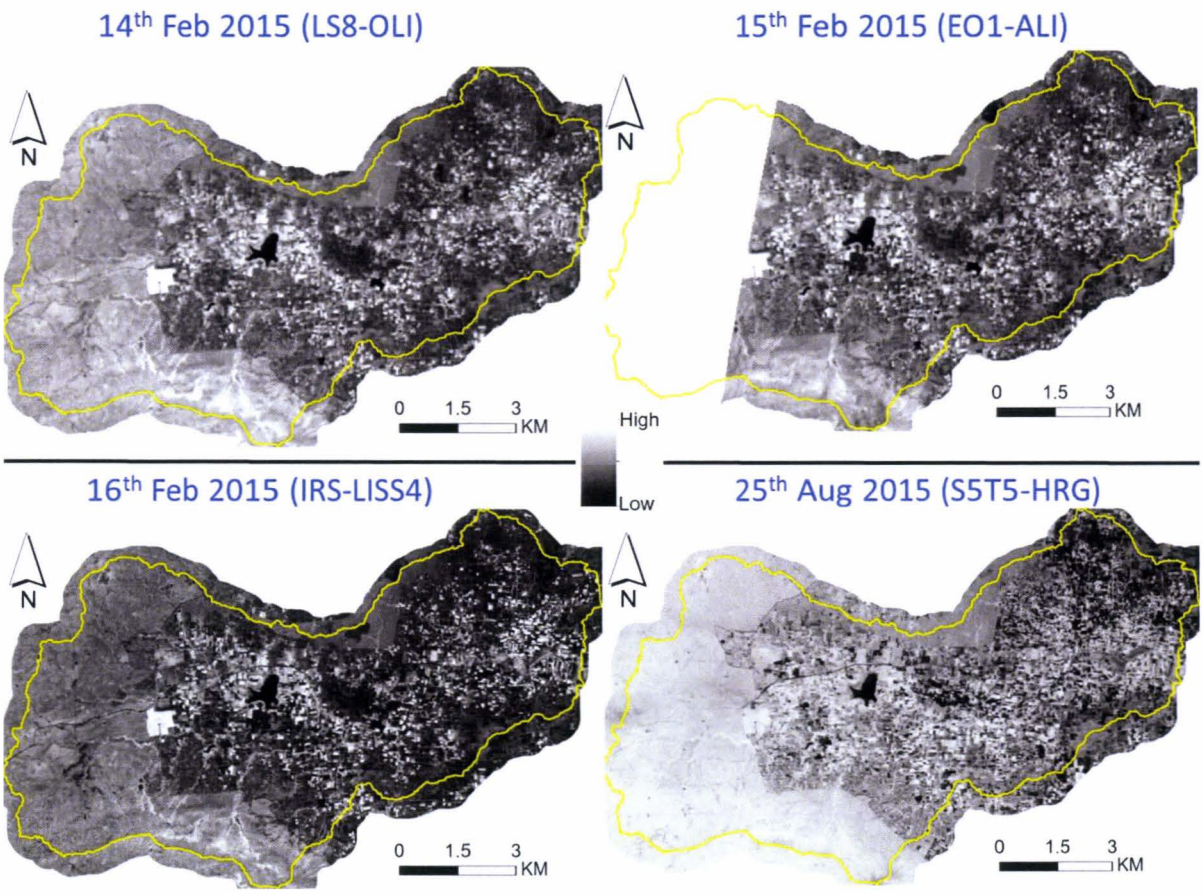

Figure 95 Pre-processed NDVI obtained from various sensors.

The uncertainty between various satellite sensors needs to be taken care to avoid sensor errors (Ke et al., 2015; Roy et al., 2016). These sensor uncertainties are causing due to:

(i) the spectral response differences between different sensors,
(ii) surface and atmospheric differences between the satellite sensors pass dates, and
(iii) the bi-directional reflectance effects.

The parcel scale linear regression was performed between LS8 NDVI values with other satellite NDVI values (using only cloud-free images) for the same or nearby date. This exercise was performed to bring all NDVI products from various satellite to an equal platform. This NDVI correction is reducing the uncertainty between various NDVI products (Hwang et al., 2011; Ke et al., 2015). Figure 96 shows the high regression

coefficient of determination (R^2) for all corrected NDVI values (generated from various sensors) with respect to the LS-8 NDVI values at the parcel scale. The same day procured satellite images from Spot-5 (Take-5), and EO-1 satellites were presents high regression coefficient of determination with $R^2 > 0.85$. Due to the IRS LISS-3 and IRS LISS-4 were procured with two days interval the regression coefficient of determination estimated $R^2 > 0.67$.

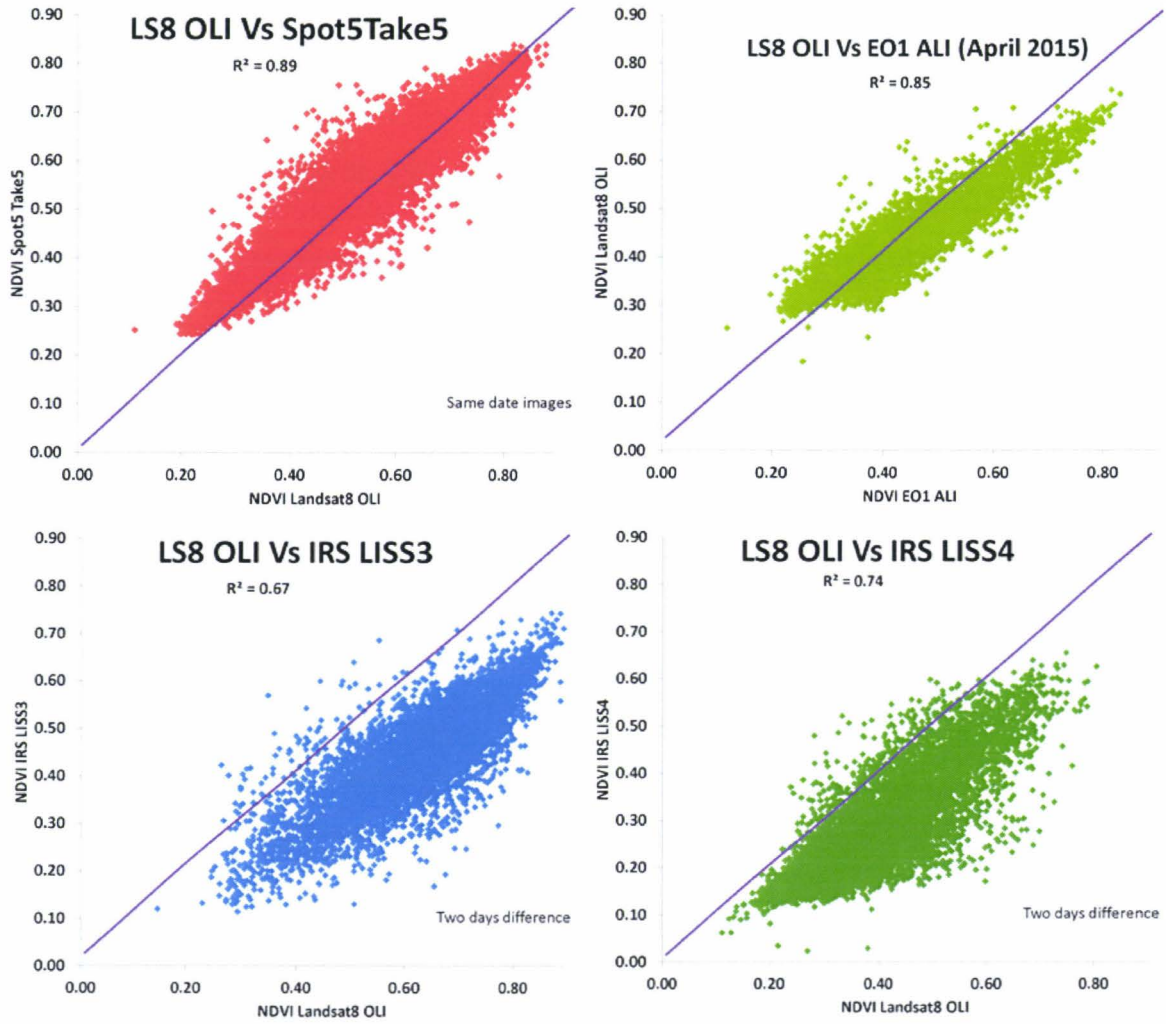

Figure 96 Linear relation between LS8 OLI NDVI and other corrected NDVI values.

Once the individual linear regression equations were established, then these linear regression equations were implemented on the other satellite NDVI datasets. Eq^n 46

to Eq^{n} 49 are presenting the exact values which were used to correct other satellite (except LS-8) NDVI products values, with respect to the Landsat-8 OLI NDVI values.

$$LS8\_OLI = -0.1557063196349761+1.398225916340921*EO1\text{-}ALI \quad \textit{Equation 46}$$

$$LS8\_OLI = 0.021738909990993+0.9348793197749551*S5T5 \quad \textit{Equation 47}$$

$$LS8\_OLI = 0.2951758962359471+0.9527610765128951*IRS\text{-}L3 \quad \textit{Equation 48}$$

$$LS8\_OLI = 0.1254527538943421+0.9257467137568071*IRS\text{-}L4 \quad \textit{Equation 49}$$

Multi-source corrected temporal NDVI for the various main crops of the experimental watershed is presented in the figure 97. Sugarcane and banana are the annual crops and if the cultivation started in the last rabi season it will harvest in the respective next rabi cropping season. As presented in the figure 97, sugarcane NDVI is high (~0.5) in the summer and it harvest in the rabi cropping season due to it was cultivated in the last rabi season. Turmeric is cultivating alone or with other short (3 months) crops like onion, beetroot, etc. As the turmeric crop duration is of eight months so some farmers are seeding turmeric with other crops and by the time turmeric leaves are becoming big the other short duration crops are getting harvest. Figure 104 shows the cultivation NDVI time-series of turmeric crop alone and turmeric with onion cultivation. The sorghum, marigold, maize, sunflower, and country beans (beans) are four-month crops and these crops are commonly cultivating under rainfed condition only.

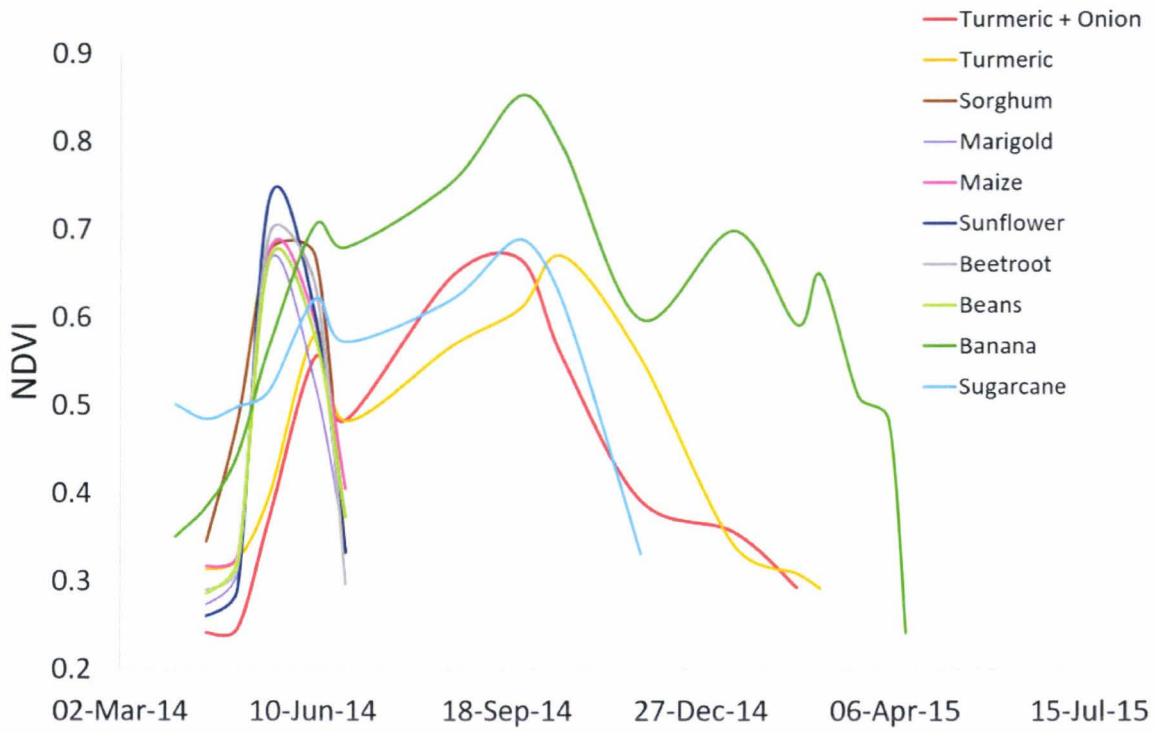

Figure 97 The re-constructed temporal NDVI for various crops in the watershed.

4.2.2.1 SVM image classification

The support vector machine (SVM) algorithm (Betbeder et al., 2014a; Xiong et al., 2017) with the scikit-learn library (Pedregosa et al., 2011) was used to classify intensively irrigated croplands for the all cropping seasons. The 50% random ground observed samples (Figure 92) from both categories (intensive irrigated and other croplands) were used to train the SVM classifier and classified the seasonal irrigated maps. The remaining 50% random samples (Figure 92) were used to validate the SVM classified outputs. The seasonal cumulative NDVI from various satellite sensors at parcel scale were used to classify intensively irrigated cropland in the watershed. The SVM classifier is the best example of supervised non-parametric discriminative statistical classifiers (Li et al., 2007). The supervised classification using SVM classifier discriminates training samples with multidimensional hyperplanes in the feature space (Mavroforakis and Theodoridis, 2006).

4.2.3 Results and discussion

Seasonal irrigated cropland and successive double and triple cropping season irrigation are classified using SVM classifier. Due to the cloud cover its difficult to procure the same satellite products for the multiple cropping seasons during crop growth. These clouds are hiding the crop growth period during two main cropping seasons. To overcome this challenge, we have used multiple satellite missions together for the seasonal irrigated cropland monitoring. The intensive spatial distributed ground observation was performed for all cropping seasons from summer 2014 till summer 2016. These intensive ground observations were further used for the training of SVM classifier and to validate the classified outputs. The classified outputs were validated by calculating producer's accuracy, user's accuracy, overall accuracy, and the kappa coefficient (Gumma et al., 2016; Olofsson et al., 2013). First, the cumulative seasonal NDVI, dual season NDVI and annual NDVI were estimated. Then the parcel boundary of the Berambadi watershed (A K Sharma et al., 2018) is used to estimate mean cumulative NDVI at parcel scale. These parcels mean cumulative NDVI further used for the SVM classifications.

Using multiple satellite cloud-free images and intensive ground observations (table 20), all cropping seasons were analysed to identify intensively irrigated croplands in the Berambadi watershed. In this study, the major focus was to demarcate intensively irrigated croplands for various cropping seasons. The seasonal cumulative NDVI outputs were generated at agricultural parcel scale to classify seasonal intensive irrigated croplands. During the kharif cropping season, major focus was to identify croplands with the cultivation of long duration irrigated crops like turmeric, banana, sugarcane, chili, and two irrigated crops in a season (like onion followed with beetroot). During rabi cropping season all kharif crops like turmeric, banana, sugarcane, chili, etc. are extending with the new cultivation of tomato, banana, and sugarcane for the further cropping season. Some farmers during rabi season are cultivating short duration crops (two to three months) like beetroot, garlic or cabbage just after turmeric harvesting. During summer cropping season banana and sugarcane are extending from the last season, and farmers with irrigation facility are cultivating short duration crops like cabbage, beetroot, watermelon, etc. During the summer

season cultivation, it completely depends on the irrigation facility of the farmer. So, the farmers with groundwater facility are only plans to cultivate in this cropping season. All classified outputs are presenting a high concentration of intensively irrigated croplands in the upstream of the Berambadi watershed. This section is dividing into subsections to provide a concise and precise description of the experimental results and their interpretation followed with the experimental conclusions.

4.2.3.1 Irrigated cropland classification for the year 2014-15

Three progressive cropping seasons for the year 2014-15 were analyzed to identify intensively irrigated croplands in the watershed. Table 18 shows that during summer, kharif and rabi cropping seasons respectively 6.3%, 9.2%, and 15.7% croplands are performing intensive irrigation. The croplands performing dual season irrigation are approximately 5% to 7% of the total cultivation area in the Berambadi watershed. About 4.6% croplands are cultivating throughout the year; these croplands are cultivating banana, sugarcane, plantation, etc.

Table 18 Classification accuracy assessment of intensively irrigated cropland and other croplands for the year 2014-15. Where Irr and Oth represents to the Irrigated and other cropland respectively.

Cropping Season	Irrigated area (km^2)	Irrigated area (%)	Error of Omission	Error of Commission	Kappa Coef.	Overall Acc. (%)
Summer 2014	2.87	6.27	Irr=9.17 Oth=2.05	Irr=2.87 Oth=6.67	0.90	94.87
Kharif 2014	4.18	9.15	Irr=2.14 Oth=6.15	Irr=7.6 Oth=1.71	0.91	95.59
Rabi 2014-15	7.18	15.72	Irr=4.52 Oth=6.04	Irr=7.65 Oth=3.54	0.89	94.62
Summer AND Kharif 2014	2.34	5.12	Irr=14.3 Oth=1.9	Irr=2.82 Oth=9.99	0.85	92.75

Kharif AND Rabi 2014-15	3.17	6.95	Irr=10.57 Oth=3.58	Irr=5.19 Oth=8.05	0.87	93.31
Summer AND Kharif AND Rabi 2014-15	2.09	4.57	Irr=18.39 Oth=1.89	Irr=2.96 Oth=12.49	0.81	90.28

In the upstream region of the watershed, the groundwater is shallow compared to the downstream (Figure 98). Due to the shallow groundwater scenario in the upstream farmers are likely to cultivate intensive irrigation in the upstream (Figure 98). Summer season cultivation can be performed by only groundwater irrigation. Kharif cropping season is mainly occupied with rainfed cultivation. During rabi cropping season irrigation is dominant after getting groundwater recharge by the monsoon season (Figure 98).

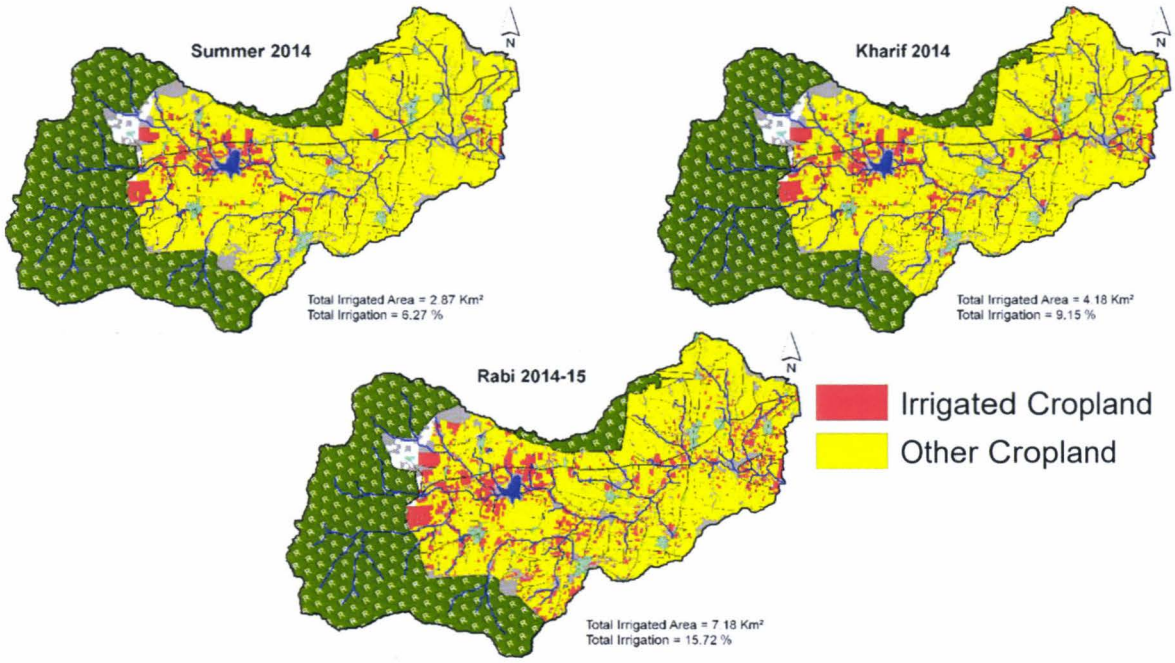

Figure 98 Seasonal intensive irrigated cropland classification for the year 2014-15.

Dual season irrigation in the watershed requires good groundwater availability. Figure 99 shows that the dual and annual irrigated croplands are situated in the upstream of

the watershed. The high concentration of irrigated croplands in the upstream is due to the shallow groundwater scenario (Figure 99). During kharif and rabi season dual irrigation parcels can be found in the downstream and middle of the watershed. These dual irrigated croplands can be of turmeric crop.

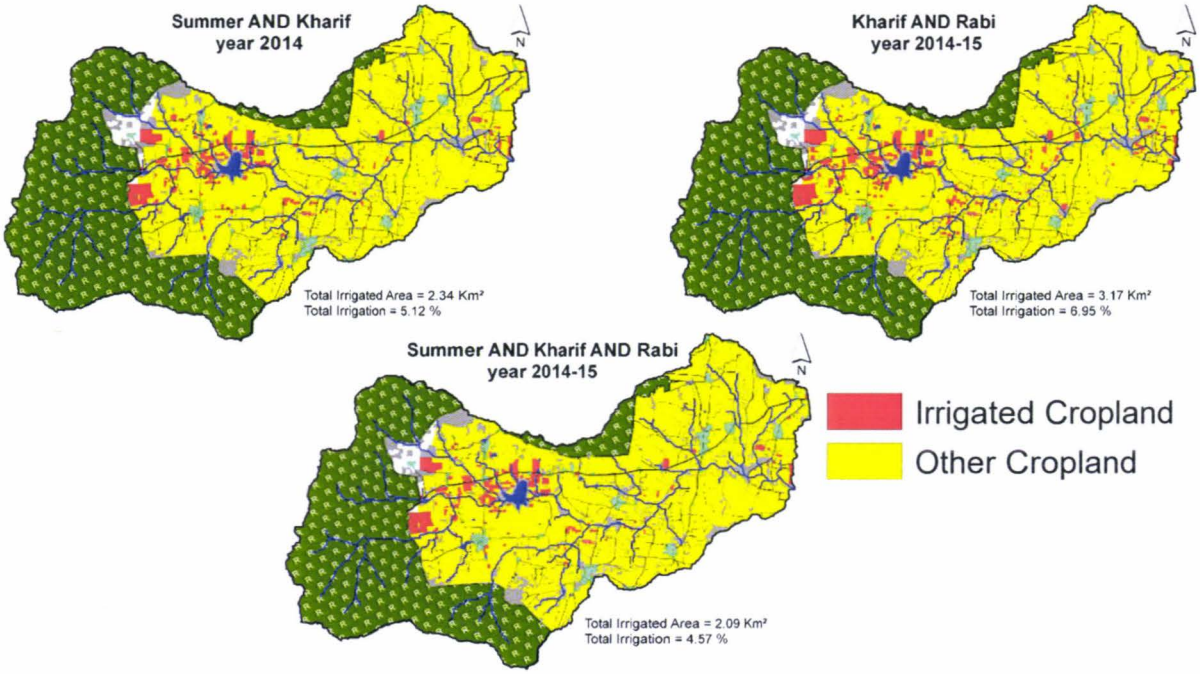

Figure 99 Dual and annual irrigated cropland classification for the year 2014-15.

4.2.3.2 Irrigated cropland classification for the year 2015-16

Intensively irrigated croplands for the cropping seasons in the year 2015-16 are reasonably more than the year 2014-15 (Table 19). For the summer kharif and rabi cropping seasons of the year 2015-16 respectively 15.9%, 16.5%, and 14% croplands are performing intensive irrigation. The dual season irrigated croplands for the summer and kharif seasons of the year 2015 were 10.6%. For kharif and rabi cropping season dual irrigation was in 9.4% croplands. The annual irrigated croplands in the watershed was occupying around 7.3% area.

Table 19 Classification accuracy assessment of intensively irrigated cropland and other croplands for the year 2015-16. Where Irr and Oth represents to the Irrigated and other cropland respectively.

Cropping Season	Irrigated area (km^2)	Irrigated area (%)	Error of Omission	Error of Commission	Kappa Coef.	Overall Acc. (%)
Summer 2015	7.16	15.86	Irr=22.98 Oth=6.25	Irr=9.92 Oth=15.29	0.72	86.66
Kharif 2015	7.43	16.47	Irr=13.73 Oth=3.53	Irr=5.26 Oth=9.48	0.84	92.15
Rabi 2015-16	6.43	13.98	Irr=21.43 Oth=4.57	Irr=7.32 Oth=14.19	0.76	88.28
Summer AND Kharif 2015	4.76	10.55	Irr=35.75 Oth=2.11	Irr=4.3 Oth=21.05	0.65	83.69
Kharif AND Rabi 2015-16	4.23	9.43	Irr=35.56 Oth=0.9	Irr=1.88 Oth=20.77	0.67	84.47
Summer AND Kharif AND Rabi 2015-16	3.27	7.28	Irr=41.06 Oth=0.57	Irr=1.3 Oth=23.17	0.62	82.34

During summer all cropping season for the year 2015-16 the irrigation croplands were intensified in all regions of the watershed (downstream, middle-stream and the upstream). Figure 100 shows the intensity of irrigated croplands is following the main drainage network of the watershed.

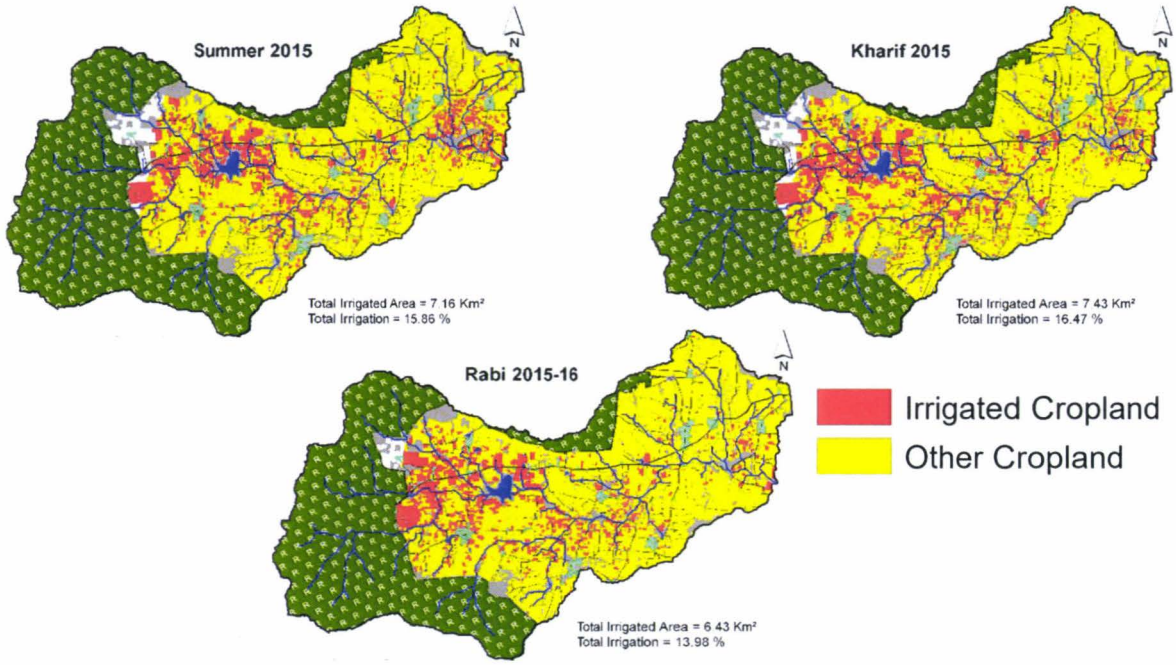

Figure 100 Seasonal intensive irrigated cropland classification for the year 2015-16.

Dual irrigation and annual irrigation is mainly intensified in the upstream of the watershed (Figure 101). The high intensity in the upstream is due to shallow groundwater level in the upstream and groundwater recharge by neighbor reserve forest.

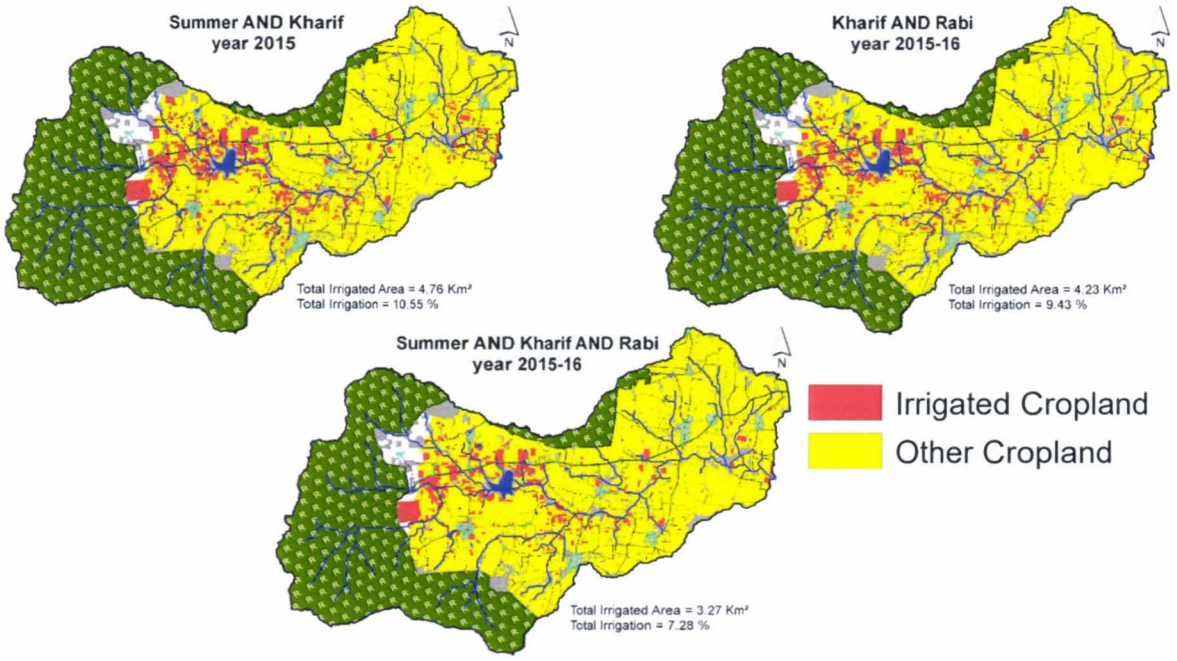

Figure 101 Dual and annual irrigated cropland classification for the year 2015-16.

4.2.3.3 Irrigated cropland classification for Summer 2016

In the Berambadi watershed, during the summer cropping seasons cultivation can only be possible by groundwater irrigation. The croplands cultivating in this season are having sufficient groundwater resources for irrigation purposes. During the summer season of the year, 2016 12.8% croplands cultivate their crops with groundwater facility (Table 20).

Table 20 Classification accuracy assessment of intensively irrigated cropland and other croplands for the year 2016.

Cropping Season	Irrigated area (km^2)	Irrigated area (%)	Error of Omission	Error of Commission	Kappa Coef.	Overall Acc. (%)
Summer 2016	5.88	12.78	Irr=0 Oth=0	Irr=0 Oth=0	1.0	100

The irrigated cropland in the summer season of the year 2016 is distributed along to drainage in the watershed (Figure 102). The Downstream and middle-stream regions of the watershed are also cultivated in the summer 2016 season after good groundwater recharge in kharif and rabi seasons of the year 2015-16. The kharif (SW-monsoon) and rabi (NE- monsoon) season rainfall for the year 2015-16 were respectively 375mm and 354mm. And for the summer season of year 2016 total rainfall was 63mm. Due to the good rainfall during SW and NE monsoons the ground water is recharged and spatially distributed intensive irrigated parcels can be seen in the figure 102.

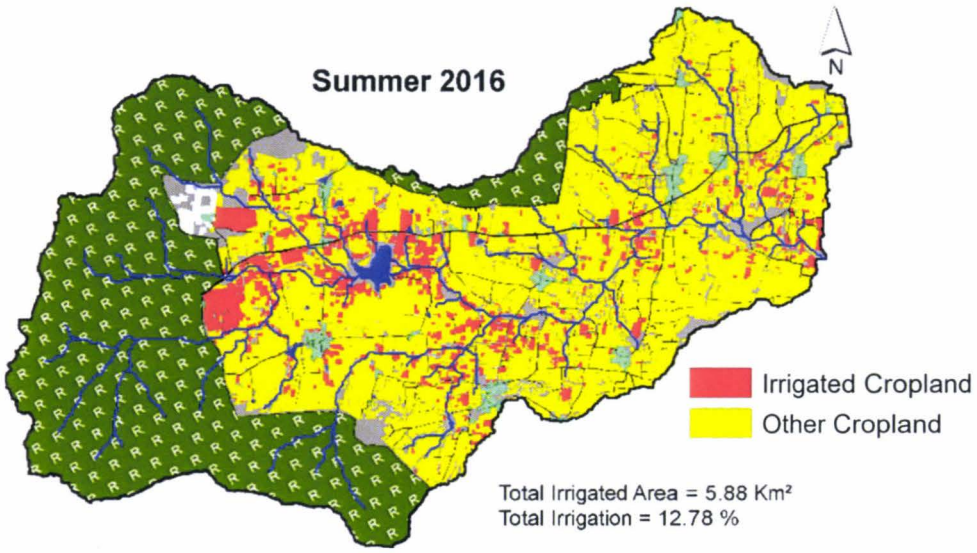

Figure 102 Summer irrigated cropland classification for the year 2016.

4.2.3.4 Irrigated cropland classification validation

The present study used spatially distributed annual irrigated cropland ground observed samples for the training and validation. The classification was performed with high accuracy even though the uncertainty has increased in present samples due to we used annual irrigated cropland, which can have three possibilities of irrigated cropland:

i. short duration crops (like onion, garlic, beetroot, cabbage, etc.) of three months each with fifteen days to a month gap between progressive crops,
ii. one moderate duration crop (like turmeric) of eight-month duration followed with short duration crop of three months,
iii. or annual crop like banana, sugarcane, and coconut.

The purpose of using a spatially distributed vast number of annual irrigated samples was to validate the proposed methodology's sensitivity for seasonal irrigated croplands classification.

The seasonal irrigated cropland classification outputs using the proposed methodology was validated with Sharma et al. (2018) seasonal training & validation samples and vice versa. Table 21 shows the kappa coefficient and overall classification accuracies for the methodology proposed in Sharma et al. (2018) and the present work. The total irrigated area for the rabi cropping season of year 2015 in the study Sharma et al. (2018) was 31.34% and with the present methodology total intensive irrigated cropland estimated is 14%. The remaining about 17% irrigated cropland were seasons partial irrigation which was not estimated by the present study.

Table 21 Validation of the proposed study.

Cropping Season	Sharma et al. (2018)		Proposed classification	
	using annual irrigated samples	using seasonal irrigated samples	using annual irrigated samples	using seasonal irrigated samples
Rabi 2015	Kappa = 0.32 OA = 71.1%	Kappa = 0.94 OA = 96.9%	Kappa = 0.76 OA = 88.28%	Kappa = 0.80 OA = 89.81%
Summer 2016	Kappa = 0.94 OA = 97.2	Kappa = 0.99 OA = 99.7%	Kappa = 1.0 OA = 100%	Kappa = 0.83 OA = 91.7%

The kappa coefficient for the Sharma et al. (2018) for rabi 2015 irrigated cropland classification was very low due to the training and validation samples were collected from annual irrigated croplands. The possibility of fallow land between two cropping seasons is high, which feeds the error to classification outputs. The rabi cropping season starts in mid-September and finishes in mid-January, so the possibility of harvesting short duration crops like onion, garlic, beetroot, and cabbage is high in November-end or December-starting. But crops like turmeric, banana, sugarcane, coconut exist due to they are long duration crops. The proposed classification methodology is stable (Table 21) for both annual and seasonal samples to monitor irrigated cropland during rabi and summer cropping seasons.

Conclusion

Groundwater on the Beramabadi watershed is becoming scared due to uncontrolled pumping for irrigation purposes. We presented here an approach to precisely identificate the presence of irrigation for different cropping seasons. In absence of same optical satellite images for complete cropping season, multiple satellite images (Landsat-8, SPOT-5, EO-1and IRS-P6) have been used to identify irrigated cropland. Overall classification accuracy from NDVI timeseries using SVM classifier for all studied cropping seasons was higher than 0.82 when considering irrigation. The study shows that the majority of farmers are performing groundwater irrigation along drainages which impact the surface flow in the major part of the watershed. The study shows less irrigated cropland during various cropping seasons of the year 2014-15 compared to cropping seasons of the year 2015-16 due to a severe drought. The methodology presents the way to identify irrigated cropping areas in the scarcity of the same satellite time series images. The study can further perform partial irrigation and rainfed cropland identification. The intensive groundwater irrigation can be further related to the groundwater quality and quantity of concern cropping seasons.

CHAPTER 5: Crop type monitoring and characterization

Summary

This chapter aims to monitor agricultural crop physical properties (crop height) and classify turmeric crop using SAR and optical data with ground observation. The chapter is divided into two main sections: Sensitivity analysis of Radarsat-2 SAR ultrafine multitemporal images with the crop growth is presented, and turmeric crop monitoring is performed using Radarsat-2 quad pol SAR and Landsat-8 time series images.

5.1 Sensitivity analysis of multitemporal Radarsat-2 (UF) images with crop growth

Farmers in the Berambadi watershed are cultivating various irrigated and non-irrigated crops according to their availability of irrigation resources. The groundwater is only source of irrigation in the watershed and the non-irrigated farmlands are completely depending upon the rainfall. During less rainy days or undulation in the monsoon, the rainfed farmers also uses partial irrigation ton save their crops. Optical remote sensing facing the limitation of cloud cover which is overcoming with the microwave remote sensing images. In the present study we have used time-series of Radarsat-2 ultrafine SAR images to monitor crop growth during the Kharif season in 2017 on the Berambadi watershed. The objective of this study is to investigate the potential of ultrafine (UF) synthetic aperture radar (SAR) images for crop growth monitoring. HH polarized multitemporal images of the Radarsat-2 UF SAR images with high incidence angle (~36°) were procured for the year 2017 over Berambadi watershed, southern peninsular India. A total of two images were acquired for the kharif cropping season, and one image was acquired for the rabi cropping season. Field observations were performed according to three Radarsat-2 satellite pass dates. It was observed that six major crops of the watershed have a strong positive correlation with

the SAR backscattering coefficients. The six major crops were maize (R^2 ~ 0.83), marigold (R^2 ~ 0.85), sorghum (R^2 ~ 0.68), sunflower (R^2 ~ 0.70), banana (R^2 ~ 0.61), and turmeric (R^2 ~ 0.72). The study also demonstrated the intra-crop heterogeneity of crop height in the Berambadi watershed but demonstrated nevertheless the potential of Radarsat-2 SAR UF data for crop growth monitoring.

5.1.1 Ground observation locations

The crop survey was performed two times in the kharif cropping season and once in rabi cropping season. Three ground control campaigns were performed at the same time of the Radarsat-2 satellite pass on the Berambadi watershed. While performing crop survey the crop type, crop height, crop density, crop yield per plant, leaf area index (LAI) and information about crop management practices were collected. A total of 562 crop parcels were surveyed together all three surveys, which includes 79 turmeric parcels, 71 banana parcels, 123 maize parcels, 90 sorghum parcels, 78 marigold parcels, and 121 sunflower parcels (Figure 103). The watershed is consisting of huge variety of crop types with several water management practices and with a combination of six major soil types.

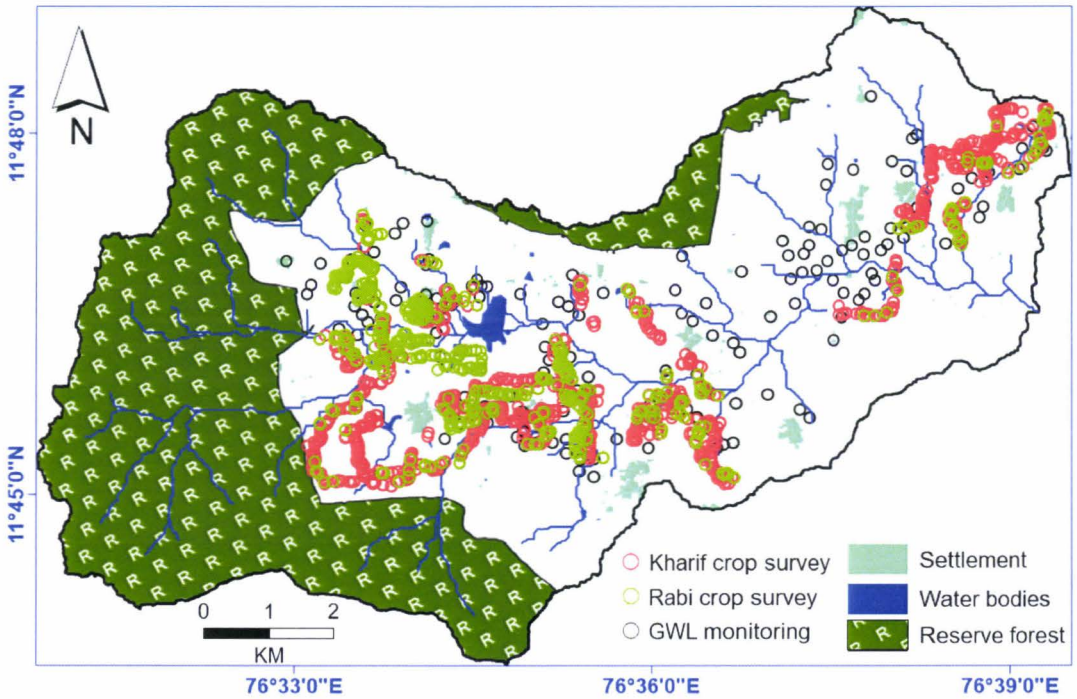

Figure 103 Ground observation locations during kharif and rabi cropping seasons in 2017.

5.1.2 Materials and methods

Kharif and Rabi are the two main cropping seasons in Berambadi watershed with the majority of farmlands cultivation. To avoid the cloud cover obstacle Radarsat-2 SAR ultrafine HH-polarization images with high incidence angle (Lee and Pottier, 2009; Srivastava et al., 2009) were procured. Two SAR images are acquired during the kharif season and one image during the rabi season in the framework of VIGISAT program (Table 22).

Table 22 Characteristics and dates of the acquired Radarsat-2 UF satellite images.

Radarsat-2 satellite images characteristics	
Ground resolution	1.99m
Azimuth resolution	1.56m
Polarization	HH
Mode	Ultrafine (descending)
Incidence angle	35.5 (near) - 36.8 (far)
Data acquisition dates	05-06-2017
	29-06-2017
	16-08-2017

The RGB color composite of ultrafine (UF) HH-polarization for the three dates were estimated at pixel scale (Figure 104). This RGB color composite represents the spatial distribution of three dates combined image in the Berambadi watershed. We can see here clearly the forest at west part of the watershed in grey, blue colour on the false composite image indicate highest level of backscattering in HH polarization the 16th of August, in red, highest level of backscattering for the 5th of June, etc.

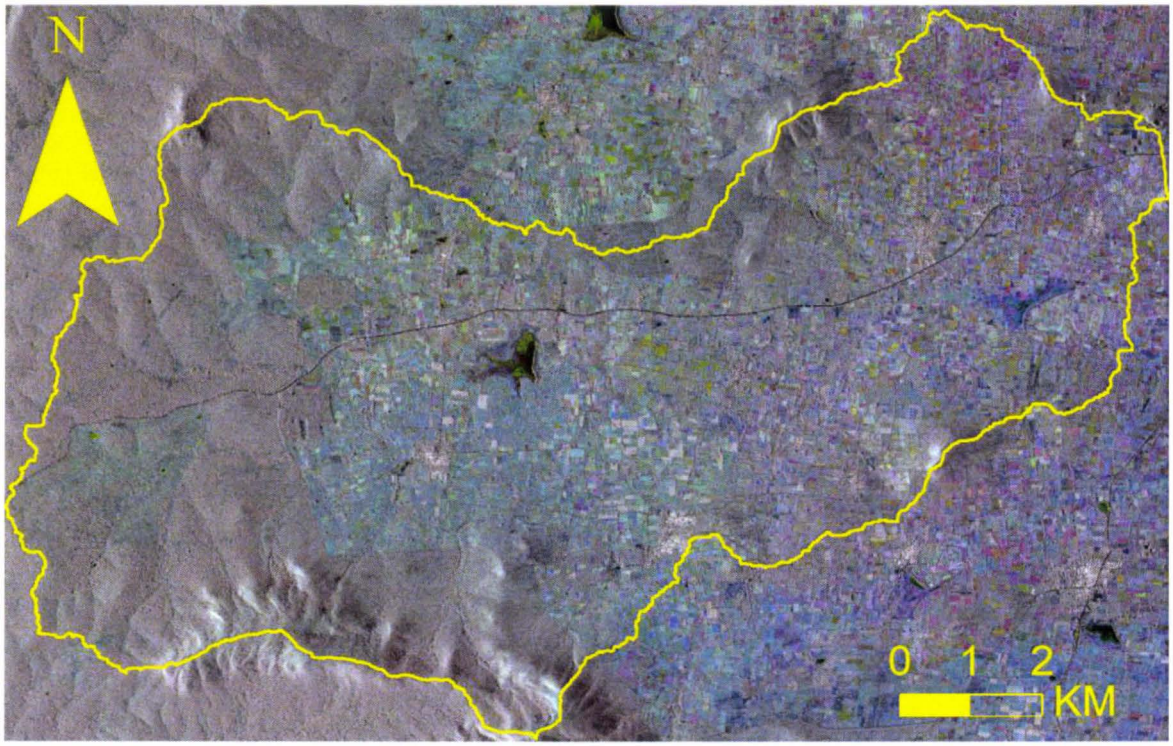

Figure 104 Multitemporal composite color of Radarsat-2 UF images (in red : 05th June 2017, in green : 29th June 2017 , in blue : 16th Aug 2017).

The two irrigated crops (turmeric and banana) and four non-irrigated crops (maize, sorghum, marigold, and sunflower) were analysed for the present study as shown in Figure 105. Turmeric crop is normally seeding in the May second or third week; banana is seeding every year in rabi cropping season. And maize, sorghum, and sunflower are seeding in the month June first week, depending on the first rain of the cropping season. Marigold is first seeding in a nursery then planting in the field during the first or second week of June. For, Rabi cropping season, seeding is realized in mid of the September month.

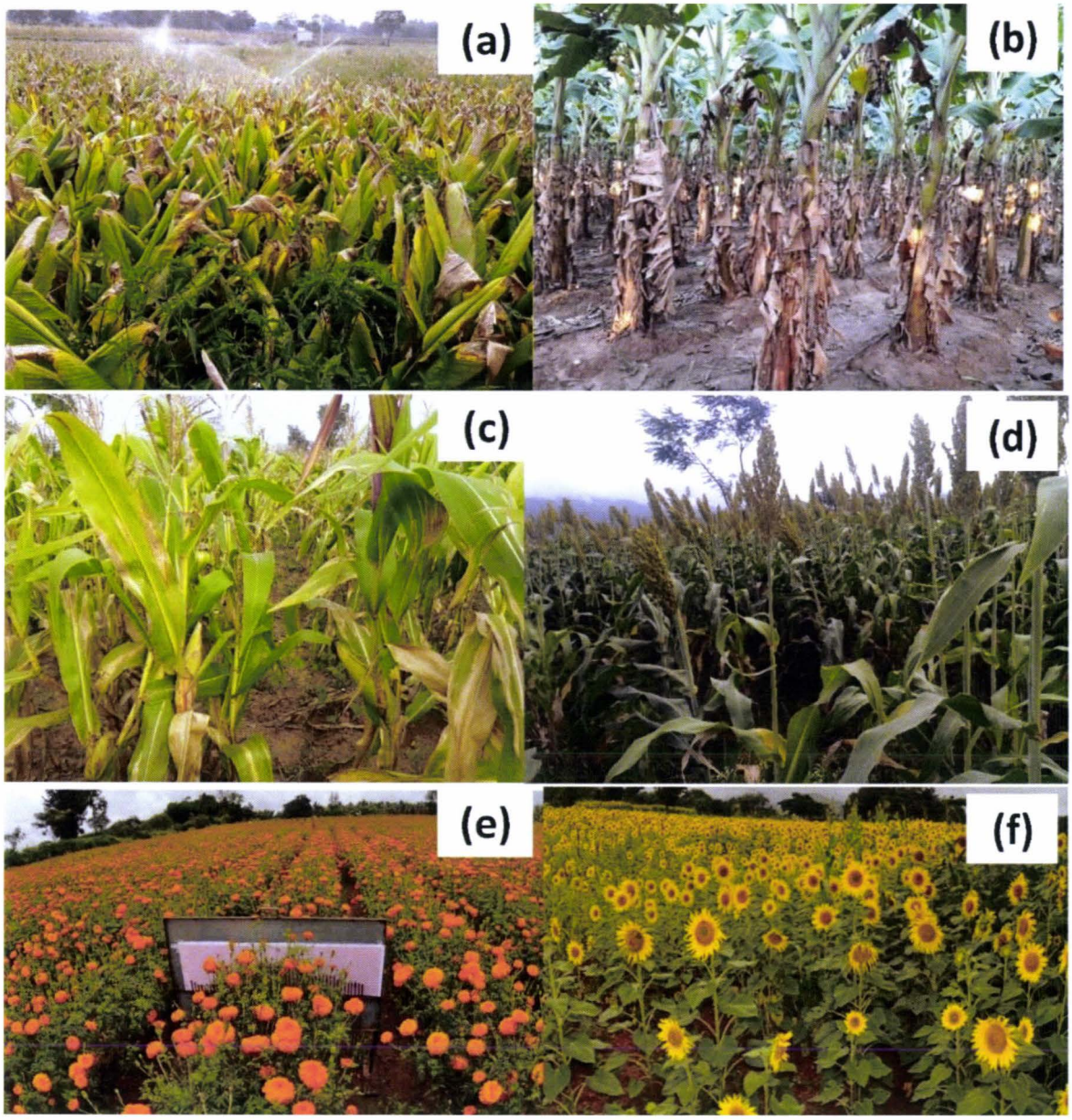

Figure 105 Major crops (turmeric (a), banana (b), maize (c), sorghum (d), marigold (e), and sunflower (f)) grown in the Berambadi watershed.

Radiometric calibration was done for all procured Radarsat-2 images. The backscattering coefficient for HH were estimated in decibels (dB) and the Lee sigma speckle filter (Duguay et al., 2016; Lee, 1983; Lee et al., 2009) with 4 look intensity, 5x5 window size, sigma=0.9 and target window 3x3 is used to reduce speckle noise. The improved Lee sigma speckle filter's characteristics were quantitatively evaluated and validated with SAR images (Lee et al., 2009). All images were geocoded using 3sec SRTM (shuttle radar topographic mission) DEM (digital elevation model). After

geocoding all SAR images were geometrically corrected with ground survey locations with UTM (Universal Transverse Mercator) projection and 43rd Zone of North hemisphere. The parcel mean backscattering coefficient at the parcel scale was evaluated for all three Radarsat-2 images. All parcel mean values were then representing at a field scale by calculating mean backscattering coefficients of pixels inside the digitized plots, an example of false colour composite is presented on the Figure 106.

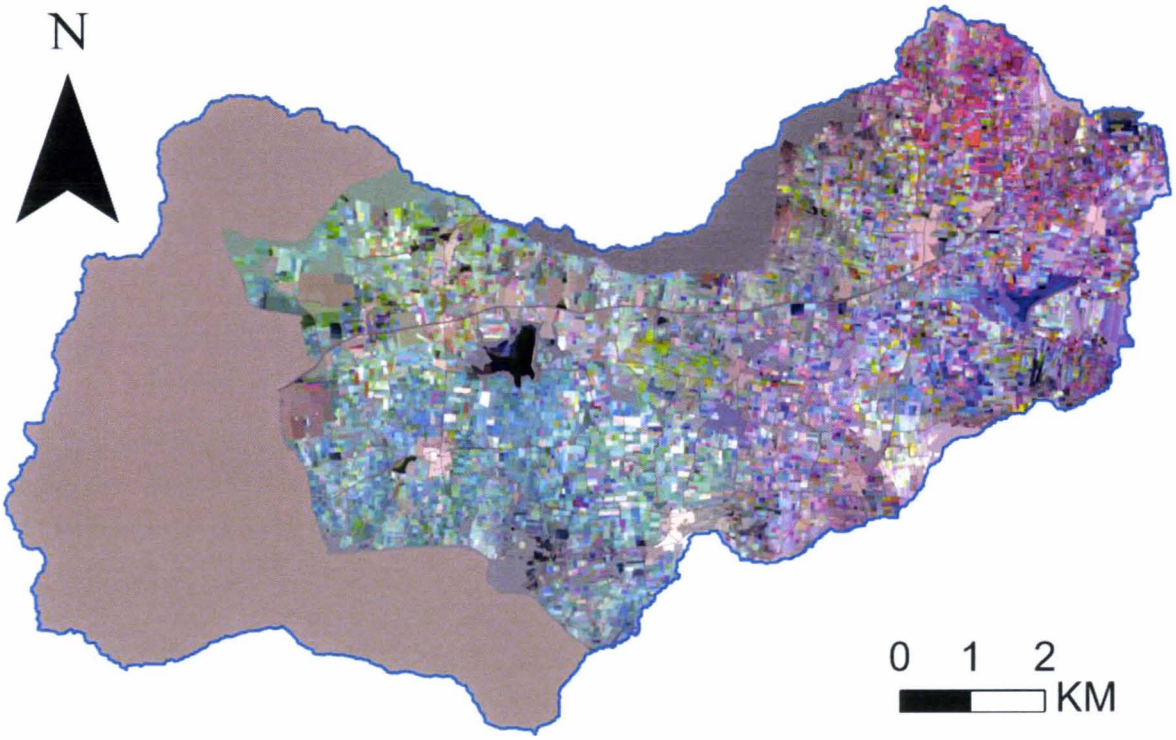

Figure 106 Multitemporal composite color of Radarsat-2 UF images parcel mean values (in red : 05th June 2017, in green : 29th June 2017 , in blue : 16th Aug 2017)

5.1.3 Results and discussion

A total of 562 parcels were surveyed together for kharif and rabi cropping seasons. The mean backscattering coefficient of HH polarization was extracted for surveyed 562 parcels. And then for surveyed six crops (turmeric, banana, maize, sorghum, marigold, and sunflower), the linear relation between parcel mean HH backscattering coefficient and crop height has been established. The correlations between crop height and backscattering coefficient are detailed in Figure 107.

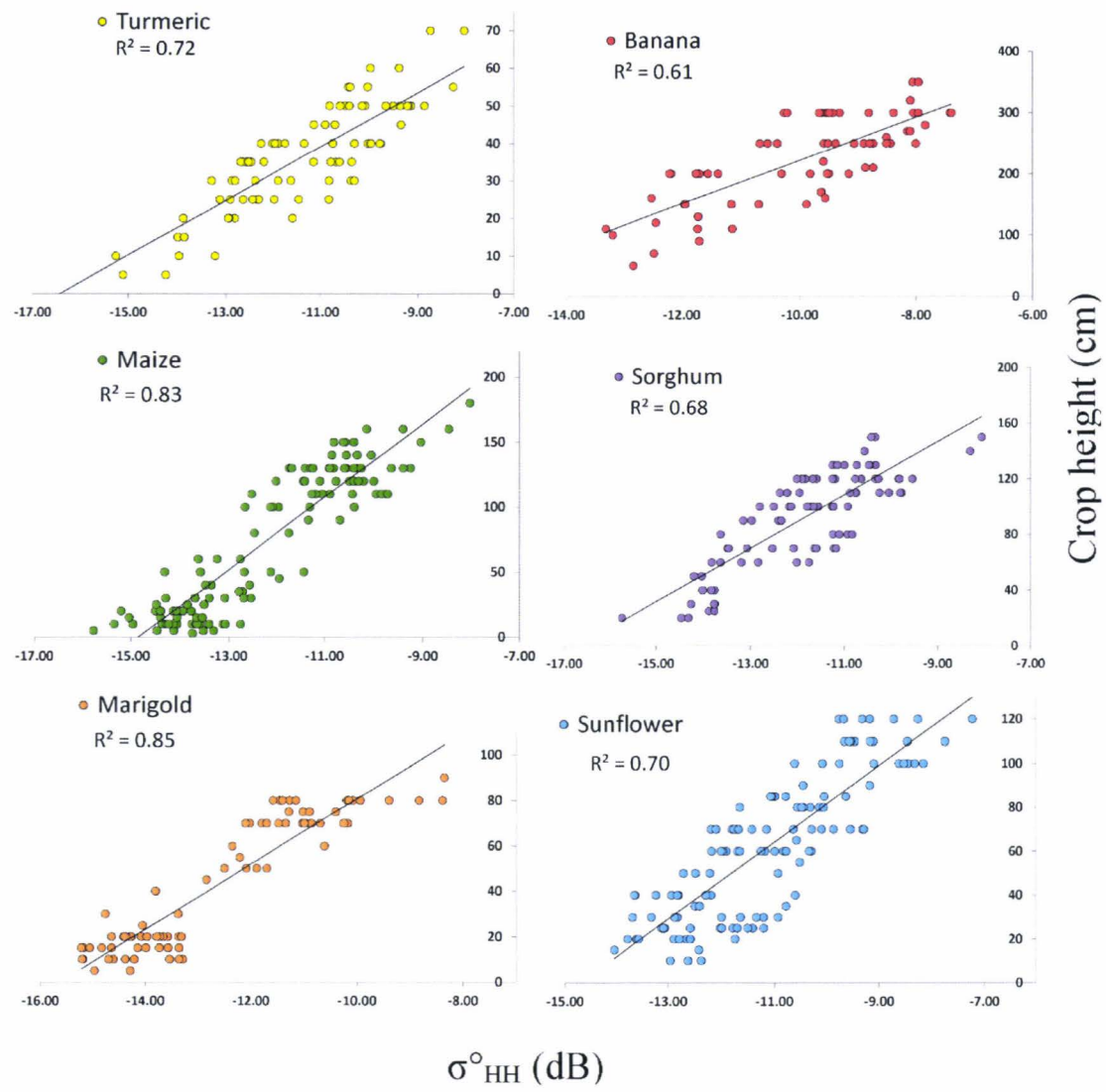

Figure 107 Linear relation between ground observed crop height and the parcel mean HH backscattering coefficient value.

Figure 107 presents individual sensitiveness with crop height for various crop types with coefficient of determination (R^2) between 0.61 to 0.85. Here maize and marigold crops are showing $R^2 > 0.83$, and other crops like turmeric, banana, sorghum, sunflower are showing R^2 between 0.61 and 0.72. The linear regression between the all surveyed crops (six-crop) height and their corresponding parcel mean backscattering coefficients were established (Figure 108). The linear and exponential relation is not marquant with a coefficient of determination respectively of r^2=0.5 and 0.6. This huge heterogeneity is due to intra-parcel heterogeneity height and especially different

phenological stages for similar crops due to planting delays according to farmers' agricultural practices.

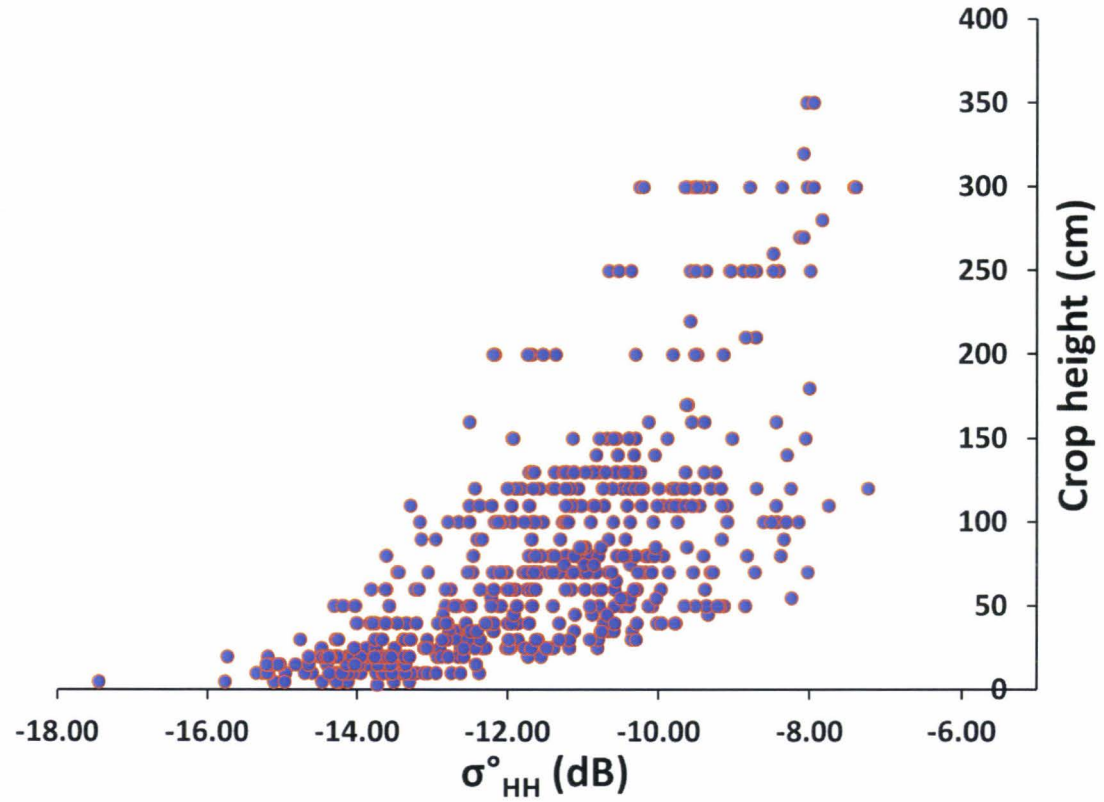

Figure 108 Relationship between the ground observed crop height (irrespective to the crop type) and parcel mean backscatter value.

Crop height (cm), crop land area (ha) and σ^{o} HH backscattering variability is presented in Figure 109. The banana crop is noticed with highly heterogeneous crops heights in the watershed characterized by various water management practices as drip, sprinkler or flood irrigation (El Hajj et al., 2016). Due to the high variability crop height, it is having a weaker relation with mean backscattering coefficient comparison to the other crop types. High heterogeneity concerned also maize height and backscattering coefficient because of phenological stages differences observed on the watershed. Turmeric is characterized by the fewest variations in terms of height and cropland areas because of a homogeneous agricultural practise for this crop. No conclusions can be done for the interpretation of the backscattering coefficients values even if we can note that we obtain the highest value for banana and sunflower and the lower value for marigold.

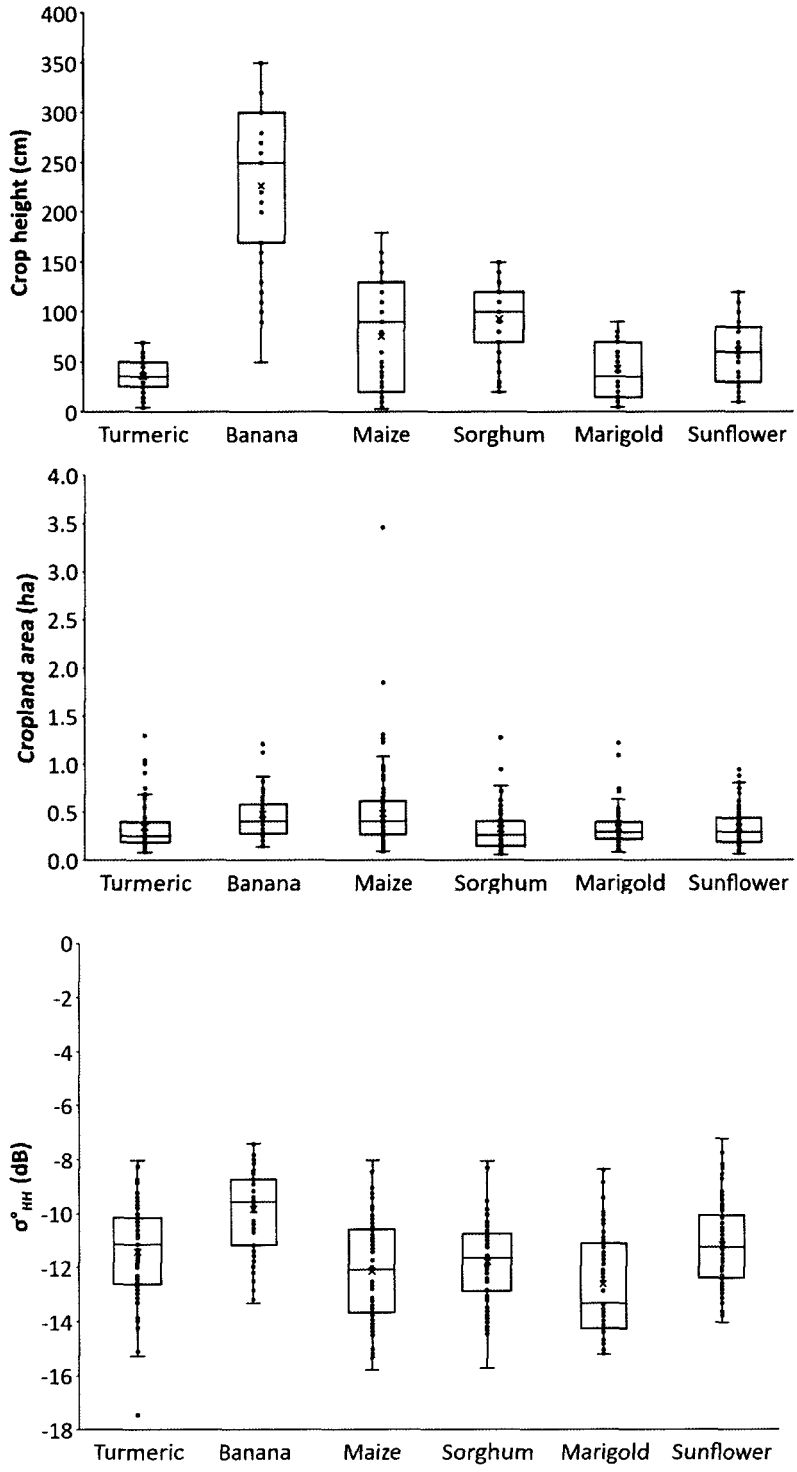

Figure 109 Crop height and surface heterogeneity representation for samples fields of turmeric, banana, maize, sorghum, marigold, sunflower and backscattering coefficients values .

5.2 Turmeric monitoring using Radarsat-2 (QuadPol) and Landsat-8 time series images

The objective of this study is to evaluate the combined use of time-series optical and SAR data for precise turmeric crop monitoring in the Berambadi watershed of southern peninsular India. Turmeric is considered as an important "cash crop" on the Berambadi watershed with a cycle of 8 months which necessitate specifics agricultural practises as irrigation, thus, his monitoring at a field scale represents an important stakeholder for local users and managers. To monitor turmeric crop, information's on phenological stages were taking during entire growth duration in 2014. Backscattering coefficients and polarimetric indicators were derived from the seven time-series quad-pol SAR RADARSAT-2 images. The NDVI and LAI were derived from four Landsat-8 OLI optical images. The analysis of covariance (ANCOVA) was applied to all the time-series parameters to identify the best informative variables which can discriminate turmeric and non-turmeric parcels. These informative variables were further classified using the Support Vector Machine (SVM) algorithm. Results show that in the absence of optical images, polarimetric parameters derived from SAR time-series can be used for precise turmeric crop identification. The combined use of SAR and optical parameters can further improve the classification accuracy to identify turmeric crop.

5.2.1 Introduction

Precise crop type monitoring is the key input variables for a sustainable management system of agricultural landscapes (Atzberger, 2013; Betbeder et al., 2016b). Groundwater is the biggest freshwater resource and is used as a principal irrigation resource in several parts of the world including India (Bhaduri et al., 2012; Gorelick and Zheng, 2015; Lee et al., 2018; Peña-Arancibia et al., 2016). Excess use of this resource for irrigation purposes has led to widespread depletion and affected crop yields (Rodell et al., 2009; Roy and Shah, 2002; Sekhar M et al., 2011; Shah et al., 2006). It is required to identify and monitor the groundwater irrigated crop types to apply improved water management plans and save these irrigated crops from the impact of water stress. Precise crop type classification remains a challenge as in India approximately 94 % of farmers have small farm holdings (Ambika et al., 2016; Robert

et al., 2017a; Shah, 2007). Challenge begins with small parcel size, mixed cropping practices and two-three cropping seasons annually. Assessing irrigated crop identification may be performed using time-series of optical remote sensing images with a high spatial resolution (Ameline et al., 2016; Betbeder et al., 2016a; Fieuzal and Baup, 2016; Rolim et al., 2016; Waske and Van Der Linden, 2008). The objective of this study is to evaluate the combined use of high spatial resolution multi-temporal optical and radar images to improve the precision of crop identification by taking into account information on crop phenological stages.

5.2.2 Ground observation and dataset

At the time and dates of the Radarsat-2 satellite pass, the ground observations were conducted. As the objective of this study is to discriminate turmeric crop with other crop types, two data sets were collected on only turmeric crop parcels and the other, with mixed land use categories. A total of 100 parcels were used for the study, includes 62 turmeric parcels and 38 non-turmeric parcels (Figure 110).

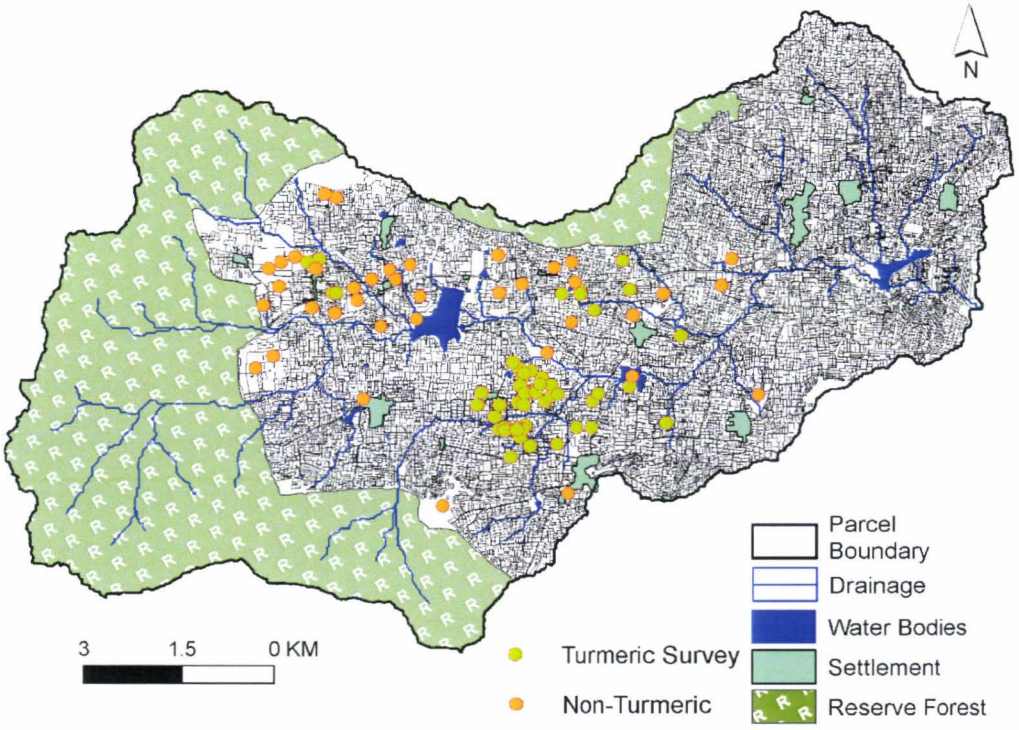

Figure 110 Ground survey location of turmeric and non-turmeric parcels during kharif and rabi cropping season of the year 2014.

5.2.2.1 LAI growth curve for the turmeric crop

The phenological stages of turmeric crop can be represent by temporal LAI. Figure 111 shows the ground monitored LAI from the 11 turmeric parcels. The monitored turmeric LAI was between 0.8 to 5.2. Mostly parcels were having high LAI in the month of July and Aug except parcel number 57D and 41.

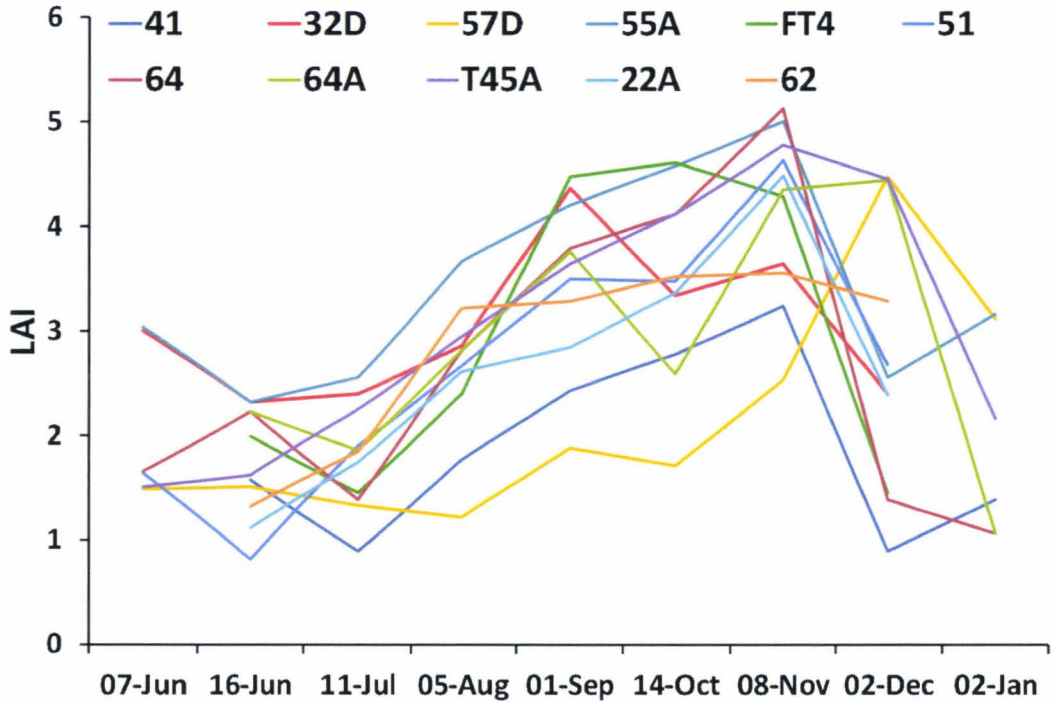

Figure 111 Measured LAI growth curves for the monitored turmeric parcels.

5.2.2.2 Satellite data

As shown in table 23, a series of seven quad-pol SAR Radarsat-2 images (from June 2014 to November 2014) and four Landsat-8 cloud-free images were acquired during the monsoon cropping season. The time-series of SAR images were covering the complete growth stages of turmeric crop.

Table 23 Optical and SAR satellite images.

	SAR images RADARSAT-2		Optical images LANDSAT-8
Dates	17-06-2014	21-09-2014	18-05-2014
	11-07-2014	15-10-2014	22-08-2014
	04-08-2014	08-11-2014	23-09-2014
	28-08-2014		09-10-2014
Spatial resolution (m)	Ground resolution: 7.6 m Azimuth resolution: 5 m		30 m
Spectral, geometric and polarimetric characteristics	C-Band (5.23 cm, 9.65 GHz) Quad polarization (HH, VV, HV, VH) Fine-Quad-Pol mode Incidence angle: from 39.43° (Descending)		Operational Land Imager (OLI) B3: 0.53 – 0.59 µm (Green) B4: 0.64 – 0.67 µm (Red) B5: 0.85 – 0.88 µm (NIR)

5.2.3 Methodology

The two-step methodology used in this study to identify turmeric using optical and SAR multi-temporal data are summarized in Figures 112 (a) and (b). The first step consisted of pre-processing optical and radar images. Optical images were corrected from radiometric and atmospheric perturbations using the 6S model (USGS and U.S. Geological Survery, 2016; Vermote et al., 1997). They were then geometrically corrected to the Universal Transverse Mercator (UTM) datum-WGS 1984 zone-43N. Normalized Differential Vegetation Index (NDVI) and Modified Triangular Vegetation Index (MTVI2) were derived from the optical images. MTVI2 was used to estimate the Leaf Area Index (LAI) using the empirical relationship described by equation 50 (Betbeder et al., 2016a; Liu et al., 2012):

$$LAI = -6.247 \times \ln(0.943 - 0.643 \times MTVI2) \qquad \text{Equation 50}$$

The Figure 113 shows the multitemporal composite colour combination of three dates estimated LAI values. In red colour in the figure 113, we have land use with the highest LAI value during November, in green the highest LAI value during September and in blue, the highest LAI value in May.

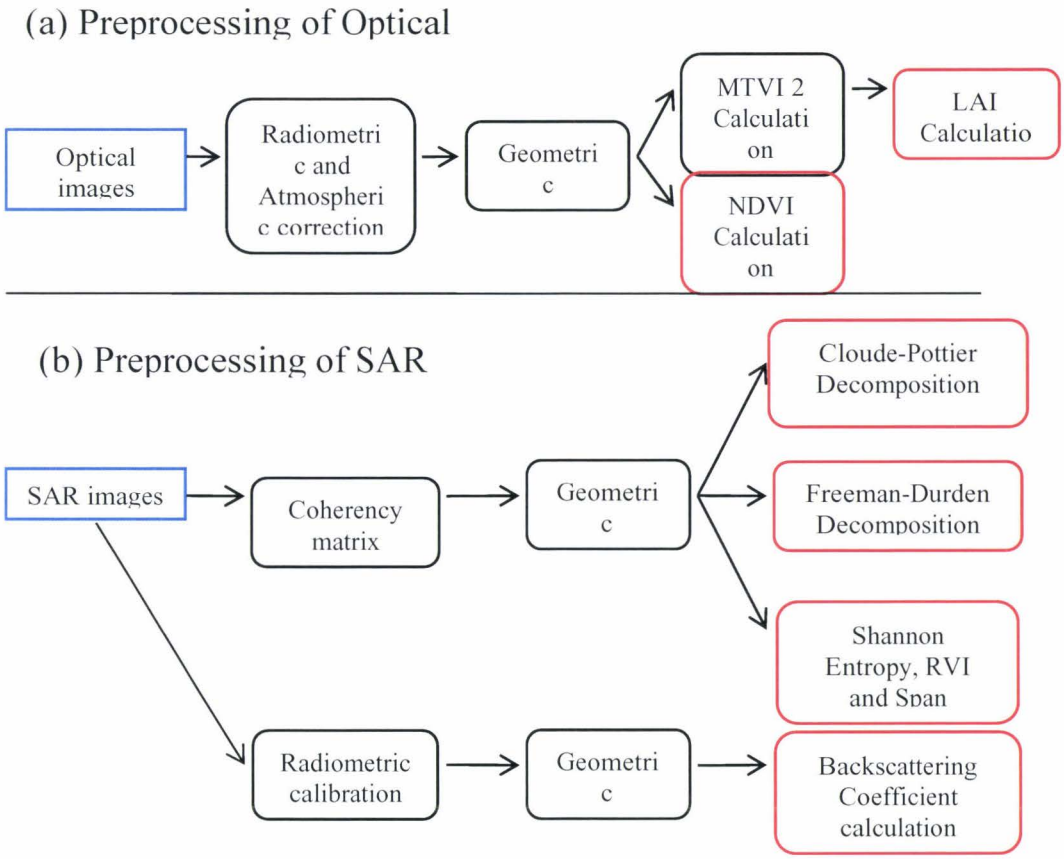

Figure 112 Image pre-processing workflows for optical and SAR datasets.

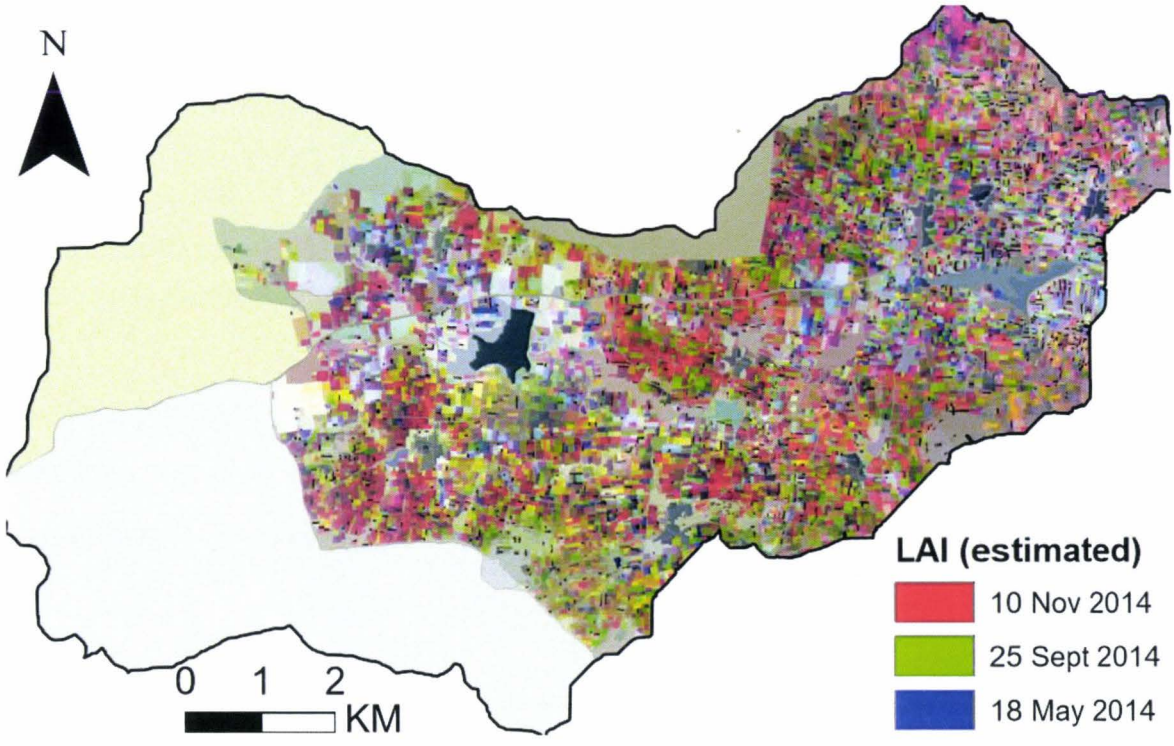

Figure 113 *Estimated LAI RGB color composite of the three dates*

SAR images were firstly radiometrically calibrated to extract the backscattering coefficients (σ^oHH, σ^oVV, and σ^oHV) according to (Baghdadi et al., 2017b). The images were then geocoded using the Shuttle Radar Topography Mission (SRTM) data to correct the topographic deformations (geometric correction accuracy less than 1 pixel) and projected into the Universal Transverse Mercator (UTM) datum-WGS 1984 zone-43N.

The most used polarimetric parameters were extracted from each RADARSAT-2 image(Betbeder et al., 2015a). First, the coherency matrix (T3) was extracted from the scattering matrix (Lee et al., 1994; Pottier et al., 2012). The T11, T22 and T33 elements of the diagonal were used to estimate single-bounce, double-bounce, and volume scattering (Figure 114) mechanisms, respectively. Both Cloude-Pottier (eigenvector-eigenvalue) (Furtado et al., 2016) and Freeman-Durden decompositions were performed on the T3 coherency matrix (Lee and Pottier, 2009; Pottier et al., 2012; Yamaguchi et al., 2005).

Standard deviation (SD) and parcel mean values were calculated for the all SAR and optical variables to take in account intra parcel heterogeneity of backscattering signals. The SD was calculated using below mention formula

$$\sigma = \sqrt{\frac{1}{N}\sum_{i=1}^{N}(x_i - \mu)^2}$$

here σ, N, i, x, and μ are representing respectively to the standard deviation, total number of observations, initial value, observed values, and mean value of these observations.

As examples, Figure 114 and 115 are representing respectively the T33 component of T3 matrix and Volume scattering from Freeman-Durden values at a pixel, mean and standard deviation scales, for a Radarsat-2 Quad pol acquired the 11th July 2014.

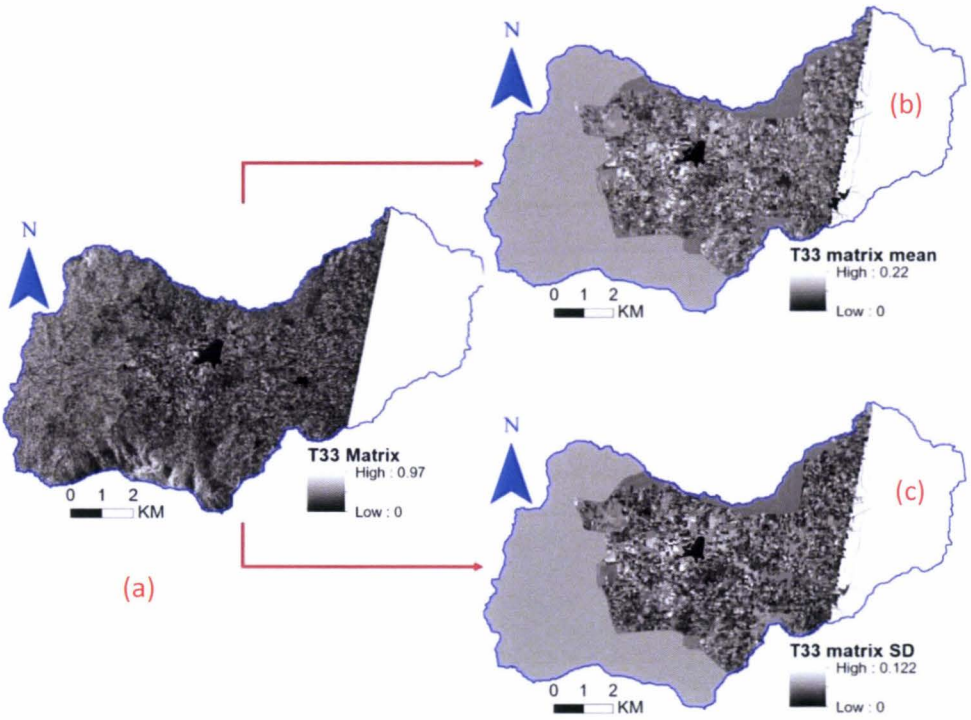

Figure 114 Example of the representation of the T33 component issue of Radarsat-2 Quad Pol data at a pixel (a), plot mean (c) and plot standard deviation (c) scales (11th July 2014).

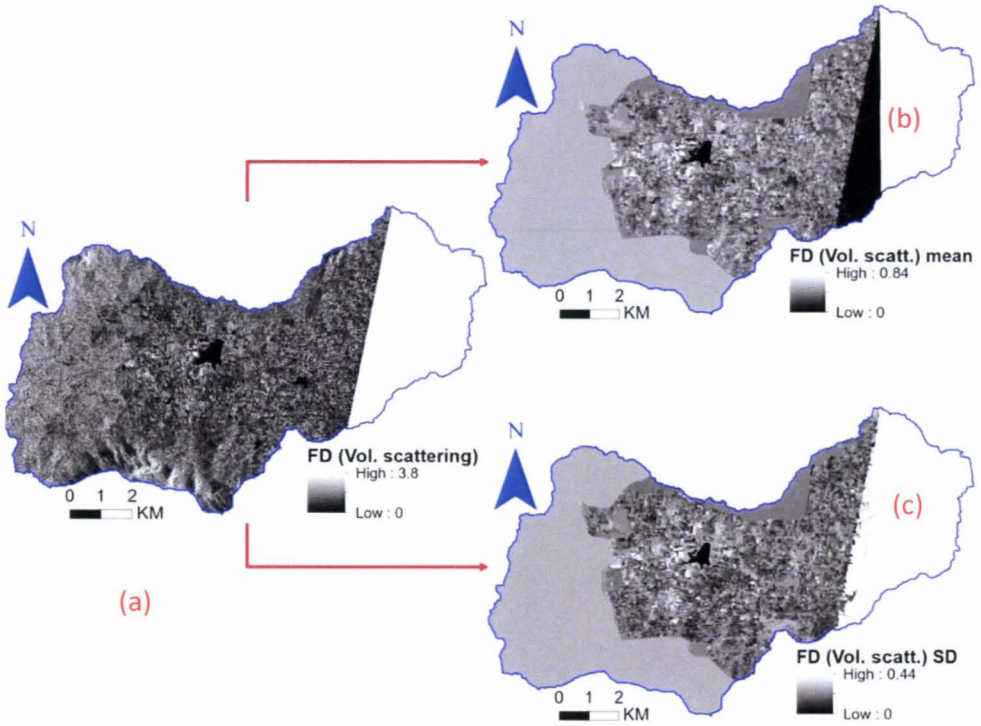

Figure 115 Example of the representation of the Freeman Durden volume scattering intensity of Radarsat-2 Quad Pol data at a pixel (a), plot mean (c) and plot standard deviation (c) scales (11th July 2014).

Three parameters [entropy (H), Alpha angle (α) and Anisotropy (A)] were also derived from the Cloude-Pottier decomposition and three parameters [Freeman single-bounce (FD_SB), Freeman double-bounce (FD_DB) and Freeman volume-scattering (FD_Vol)] were extracted from the Freeman-Durden decomposition. Moreover, other polarimetric parameters including the SPAN, the Shannon entropy (SE) and the radar vegetation index (RVI) (Betbeder et al., 2016b; Kim et al., 2012b) were estimated (Figure 116).

The second step of the methodology consisted of processing the 14 time-series parameters derived from the optical and SAR time-series (Figure 117). The time-profile mean and standard deviation were calculated at the parcel scale for the parameters. To select the best parameter to discriminate turmeric crops, an analysis of covariance (ANCOVA) was applied to all the time-series parameters using 100 field samples (62 for turmeric and 38 for other crops). ANCOVA is evaluating whether the parcel or pixel mean value of a dependent variable are equal across level of a categorical independent variable or not. This statistically controlling the effects of other continuous variables (known as covariates or nuisance variable) that are not of primary interest. The ANOVA model assumes a linear relation between the response and covariate values. Below mention equation represents the mathematical representation of ANCOVA model.

$$y_{ij} = \tau_i + B\left(x_{ij} - \bar{x}\right) + \varepsilon_{ij}$$

here, the dependent variable, $y_{ij}$is the j^{th}observation under the i^{th}categorical group and the covariates, x_{ij} is the j^{th} observation of the covariate under the i^{th} group. Variables in the ANCOVA model derived from the observed data: μ (the grand mean) and $\bar{x}$ (the global mean for covariate x). The variables to be fitted are τ_i, B, and ε_{ij}, these variables are respectively representing to the effect of i^{th} level of independent variable, the slope of the line, and the associated unobserved error term for j^{th} observation in i^{th} group.

The best informative variable were selected using ANCOVA and integrated to the SVM supervised machine learning classification (figure 117) (Betbeder et al., 2014a; Pal and Mather, 2005). The classification results were validated using confusion matrices and kappa coefficients (Lunetta et al., 2006).

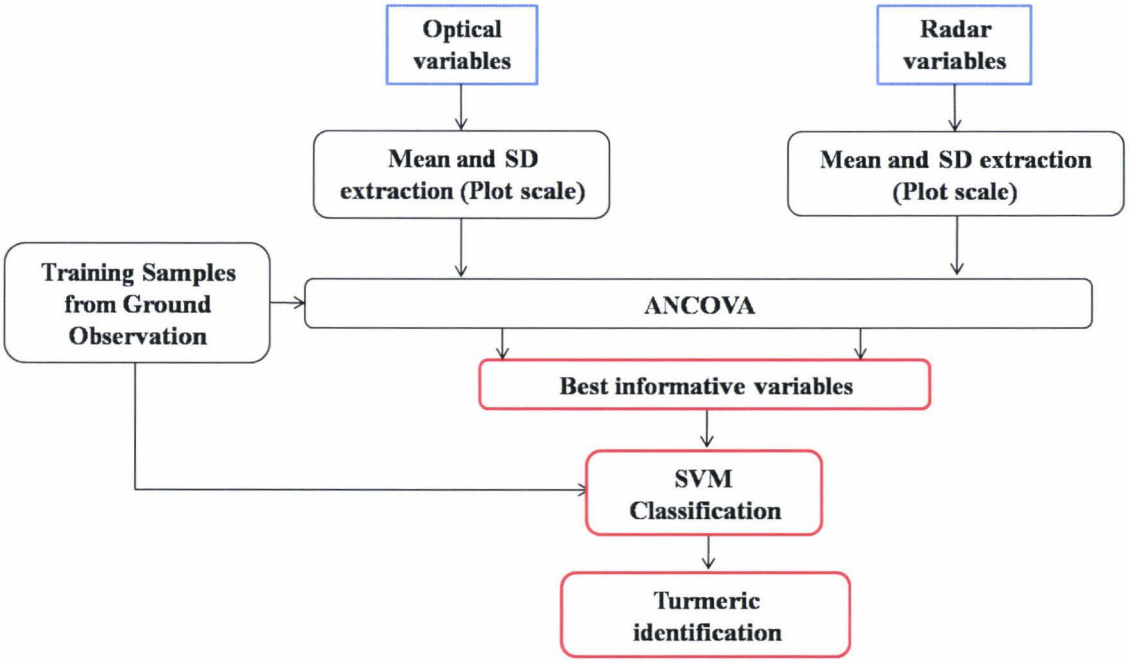

Figure 116 ANCOVA implementation and SVM classification.

5.2.4 Results and discussion

The mean NDVI values for all 62 parcels of the turmeric crop phenology were extracted and plotted with time (Figure 117). The NDVI standard deviation (SD) is high during crop growth but after September all parcels were presenting least heterogeneity. After the mature stage in August and September with a NDVI mean at 0.56, we observed a strong decrease of the NDVI for all turmeric parcels till December asscociated with a weaker Standard Deviation.

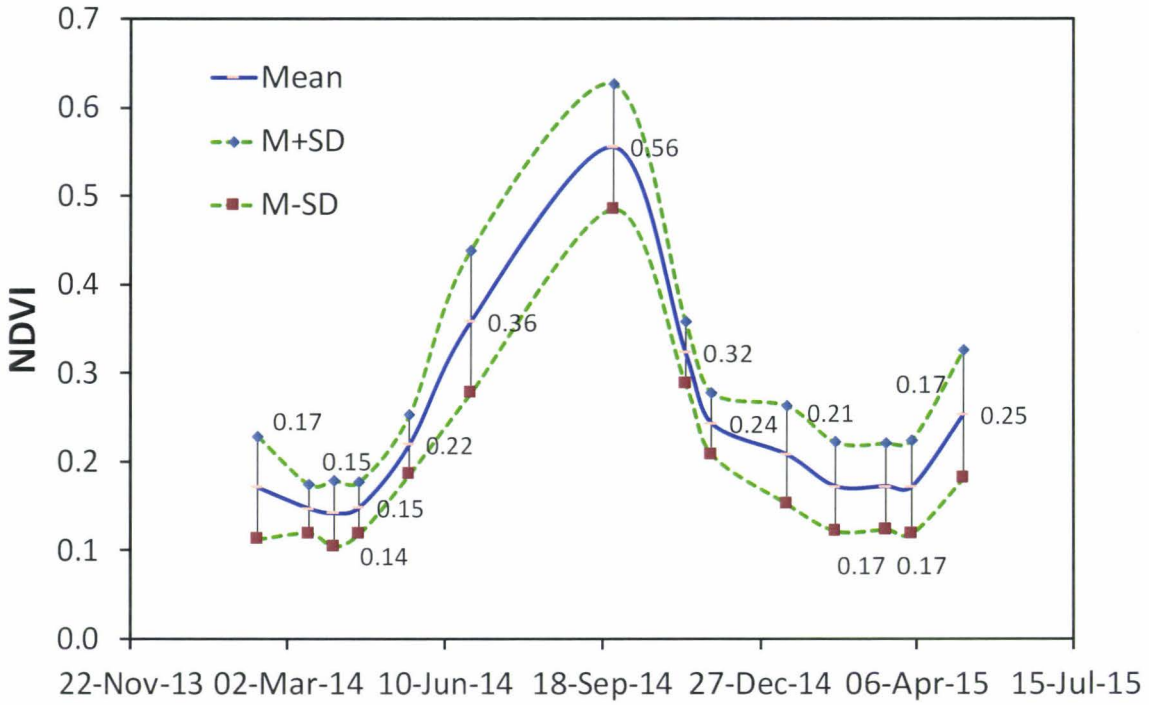

Figure 117 Turmeric NDVI curve evolution

The linear correlation between ground observed LAI with satellite NDVI and LAI show a positive correlation in figure 118 with respectively a R^2 of 0.65 for the NDVI and 0.79 for LAI variables.

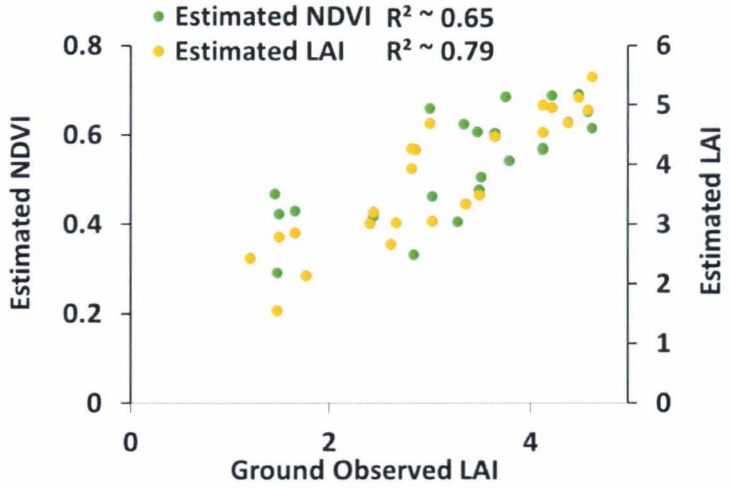

Figure 118 Satellite NDVI and LAI relation with ground observed LAI

For polarimetric variables, the correlations are lower. Correlations between Ground observed LAI with T11, Shannon entropy, Shannon Entropy Intensity (SEI) and span have respectively a coefficient of determination (R^2) of 0.61, 0.64, 0.57 and 0.53 (figure 119).

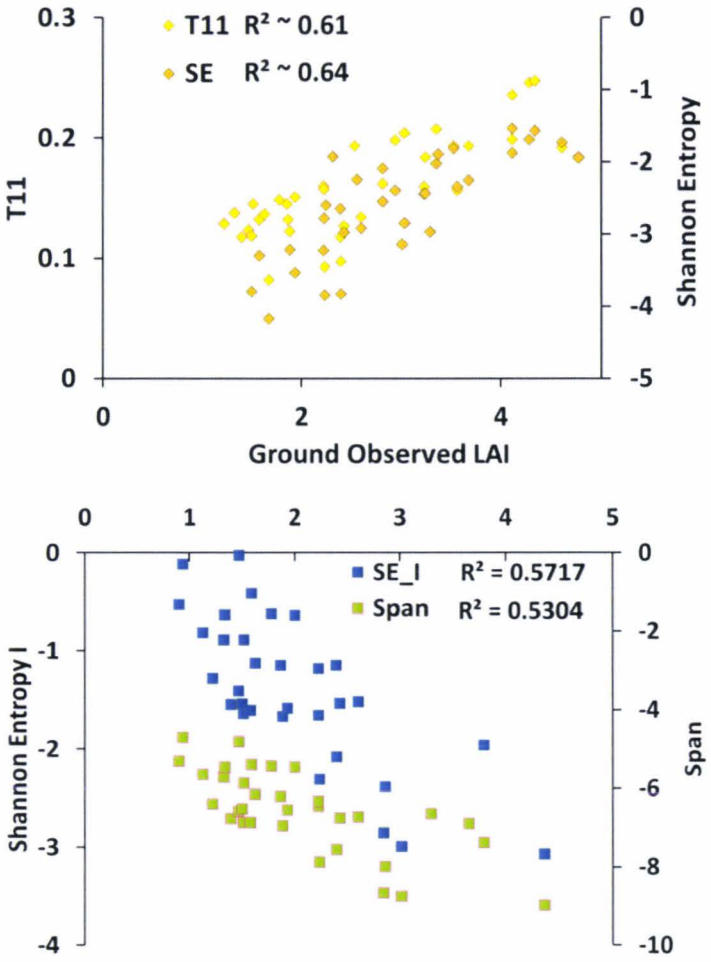

Figure 119 Relation between polarimetric decomposition variables and ground observed LAI relation. where SE_I and T11 represents to the Shannon Entropy (Intensity) and single-bounce diagonal component intensity of the Coherency matrix respectively.

The ANCOVA results indicate that 8 out of 14 time-series parameters (one optical and seven polarimetric parameters) are discriminant to identify turmeric crop (LAI, T33, σ^{o}_{HV}, Freeman-Durden Volume, Alpha angle, Shannon Entropy, T22 and Entropy).

Since the correlation with ground reference data is higher ($R^2 \geq 0.6$) to these variables, these variables were selected and integrated in the SVM algorithm for turmeric / non-turmeric classification.

Results are satisfactory with Kappa ≥ 0.79 for more than half of these eight parameters (Table 24). We can notice that the biophysical parameter (LAI) derived from the time-series of Landsat-8 images is highly suitable to identify turmeric (Kappa = 0.87). Moreover, the results show that polarimetric parameters and backscattering coefficients can detect turmeric crop with a high level of precision. They also point out that the three most discriminant radar parameters are all related to volume scattering mechanism.

Table 24 Estimation of the kappa coefficient.

Variable	Kappa coefficient
LAI	0.87
T33	0.95
σ^0_{HV}	0.79
FD_Vol	0.75
Alpha	0.75
Shannon Entropy	0.76
T22	0.79
Entropy	0.80

The T33, which is sensitive to volume scattering, appears as the more explicative variable with the highest kappa coefficient to classify turmeric crop parcels from non-turmeric crop parcels.

Conclusion

This chapter focused first on crop height sensitivity to multiple Radarsat-2 UF data. A simple approach has been tested to estimate crop height. The crop growth can be

modelled using ultrafine SAR images as for Marigold with one R^2=0.85 between backscattering coefficients and crop height. Secondly, turmeric monitoring is performed with Radarsat-2 and Landsat-8 images. A total of twelve polarimetric variable and two optical variables were analysed. Among them, LAI variable appears as the optical variable the more informative to discriminate turmeric crop from other crops.

CHAPTER 6: Assessing impact of intensive irrigation on groundwater resources

Summary

This chapter presents the relation between gridded mean depth of the groundwater table and total irrigated area percentage for the same grid. The purpose of this chapter is to contribute of a better understanding of the relation between groundwater table and total irrigated area in the Berambadi experimental watershed. Total number of borewells in the various villages of the watershed is also compared with the manually monitored present depth of the groundwater table at upper-stream, middle-stream and downstream of the watershed.

6.1 Introduction

In this study, we investigated relations between groundwater levels and evolution of irrigated areas on the Berambadi watershed. Three analysis are proposed here. The first one focus on the study of spatial relationships between the groundwater level and irrigated areas for the years 2015 (Rabi) and 2016 (Summer). Second analysis aimed to analyse the evolution of total number of borewells according to the evolution of irrigated areas (outputs from the Chapter 3). The third one used a transect from the upper stream to the downstream of the watershed in order to analyse groundwater level fluctuations for various cropping seasons.

6.2 Material and methods

The Figure 120 presents the general methodology to achieve our 3 objectives. Three types of data are used: (1) The irrigated evolution maps were produced in the chapter 3, they spatialized irrigates and non-irrigated plots between 1990 to 2016; (2) groundwater levels issued of agricultural borewells and (3) borewells evolution.

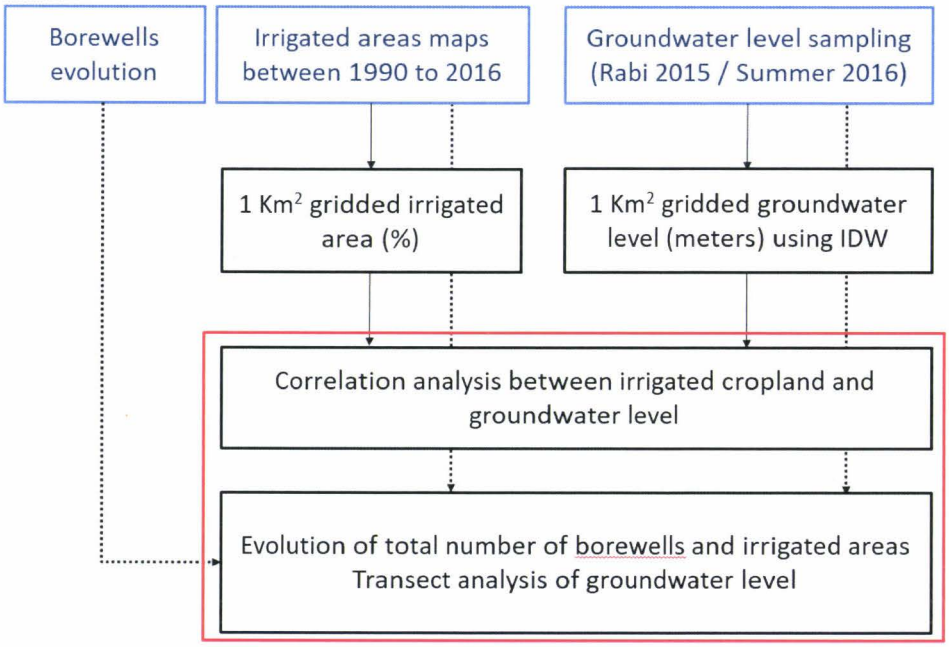

Figure 120 Methodology to assess the impact of intensive irrigation on groundwater resources.

Groundwater levels have been sampled the Berambadi watershed (Figure 122).

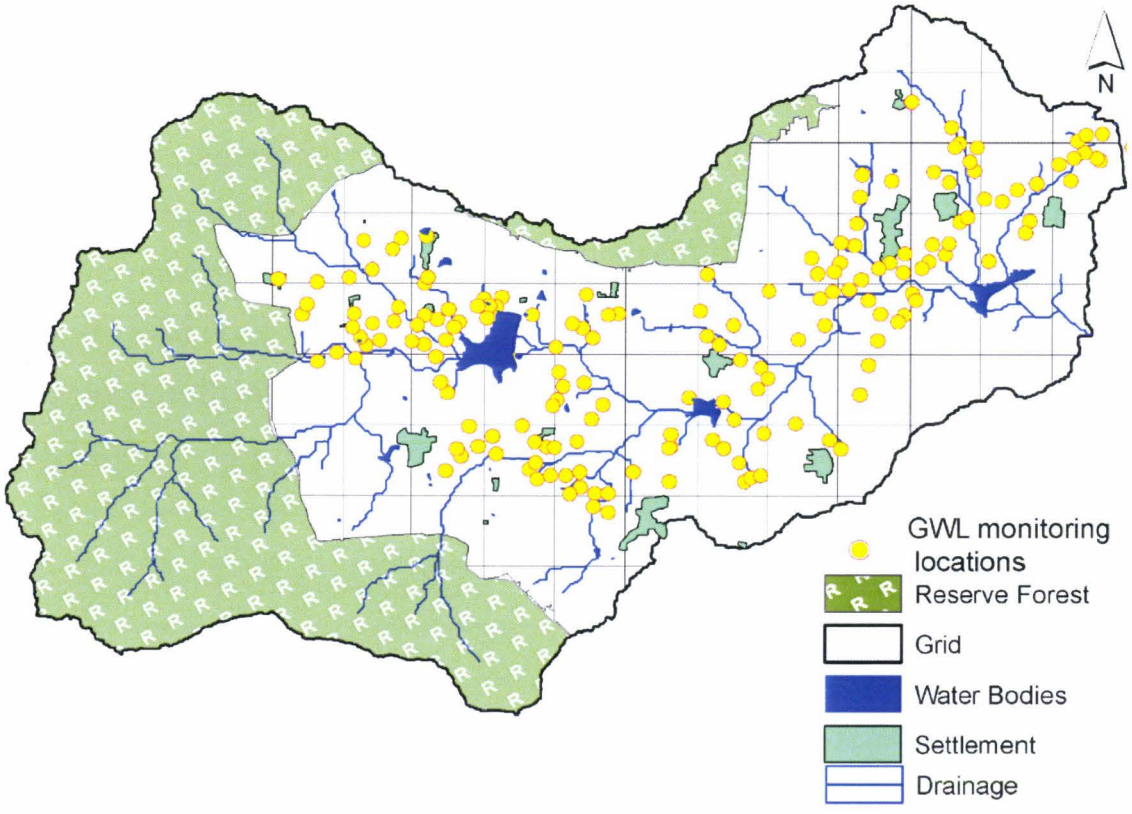

Figure 121 Borewell monitoring location in 2015 and 2016.

A total of 205 borewells were monitored during non-pumping hours. All borewells were monitored in December 2015 (rabi cropping season) and in March 2016 (summer cropping season) with four/five days' uncertainty in measurement. To collect the groundwater level data, we monitored before farmer pumps for the day because of once farmer started the pumping, groundwater fluctuates very rapidly. During collecting the groundwater level from borewells, we have taken care of the knowledge of electricity provided for these wells to obtain unaffected groundwater level measurements (Sekhar et al., 2016; Sekhar M et al., 2011). The groundwater level from agricultural borewells in Berambadi watershed were collected with respect to the earth surface. It was noticed that some borewell were at height from the earth surface which was further reduced to maintain the data quality and equality. For borewells evolution, they have been collected from the Central Groundwater Board (Dhiman, 2012a).

For interpolation, as presented in the Figure 121, 1 Km^2 grids were used to estimate total irrigated area in the grid as it is the scale used for agro hydrological modelling developed in the framework of ATCHA project. Interpolation method of the data in these grid represent an important stake for the interpretation of results. Spatio-temporal distribution of any physical and socio-economic phenomenon can be approximated by functions depending on the sampling locations in a multi-dimensional space, as a multivariate scaler, vector, or a tensor field (Mitas and Mitasova, 2005). The selection of an appropriate interpolation methods is challenged as the modelled fields are usually very complex due to the data is spatially heterogeneous, data often based on far from optimal sampling, and data may contain significant noise or discontinuities. Broadly interpolators can be divided into two categories: deterministic, and stochastic. These interpolators are using a function with a combination of known functions with different weighting and neighbouring methods. The closer data to the interpolation point is having more influence (weight) during computation with comparison to the faraway data, according to the first law of Geography (Garnero and Godone, 2013; Tobler, 1970). As presented in the figure 122, commonly used interpolation methods are Voronoi polygons, TIN-based linear interpolation, Inverse Distance Weighing (IDW), Kriging (spherical variogram),

spline with tension and stream enforcement, and regularised spline with tension smoothing.

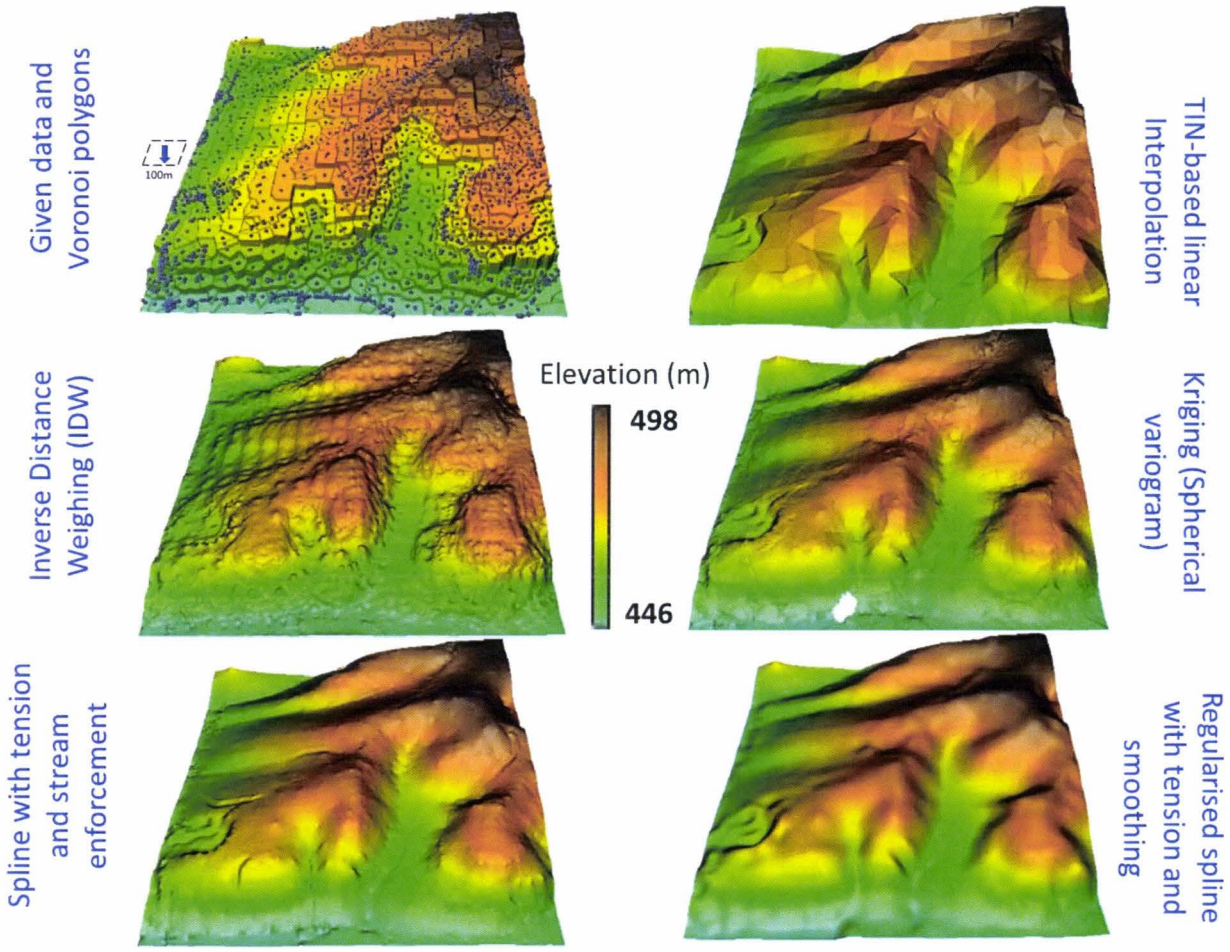

Figure 122 Various interpolation methods implementation on scattered elevation point data.
Source: (Mitas and Mitasova, 2005)

The Inverse Distance Weighing (IDW) was choosen for the study as it is an interpolator based on an assumption that the value at an unsampled point can be approximated as a weighted average of the certain cut-off *n* closest values. Tomeczak et al. (2003) presented that the IDW is particularly suitable for narrow datasets, where other interpolation techniques may be getting affected by the errors. The IDW interpolation is highly flexible and it allows to estimate dataset with trends and anisotropy (Garnero and Godone, 2013). The formula of IDW interpolation can be represents as:

$$Z_j = \frac{\sum_{i=1}^{n} \frac{Z_i}{(h_{ij} + \delta)^{\beta}}}{\sum_{i=1}^{n} \frac{1}{(h_{ij} + \delta)^{\beta}}}$$

where Z_j, Z_i, β, δ, and h_{ij} are respectively value at the unsampled location, known values, weight, smoothing parameter, and separation distance.

The h_{ij} is the distance between known and unknown point, which can be measured with Euclidean distance: $h_{ij} = \sqrt{(\Delta x)^2 + (\Delta y)^2}$

where Δx and Δy are the distances between the unknown point j and the sampled location i, with respect to the reference axes.

The interpolated groundwater level of the watershed was converted to the gridded mean values for the Rabi 2015 (Figure 123) and Summer 2016 (Figure 124) cropping seasons. As shown in figure 123, groundwater level of downstream of the watershed is depleted up to 50m from the surface and in the upstream groundwater level is touching to the topological surface. Upstream of the watershed is also getting a recharge from the adjacent reserve forest.

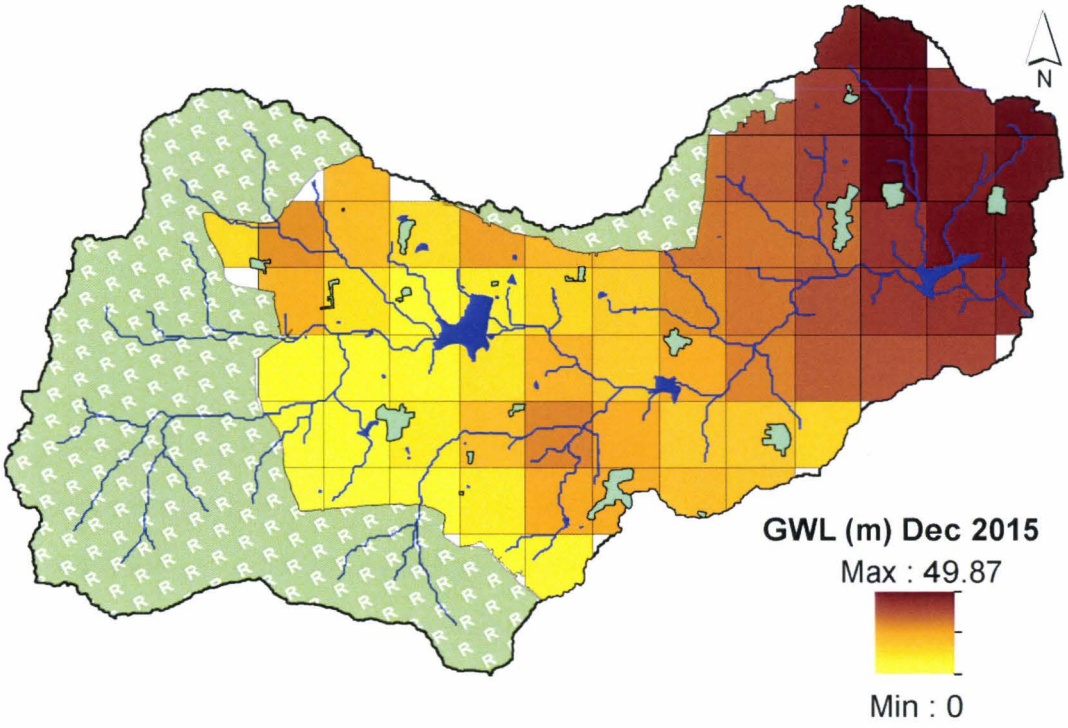

Figure 123 Gridded means of groundwater level (GWL in meters) in December 2015.

The gridded mean groundwater level map for the watershed was generated from the interpolated groundwater level data (Figure 125). As rabi cropping season, in summer season also downstream grids of the watershed have deeper groundwater than the upstream grids. We note also that the maximum level of groundwater is about 55 meters during summer at the east part of the watershed against 50 meters in rabi season.

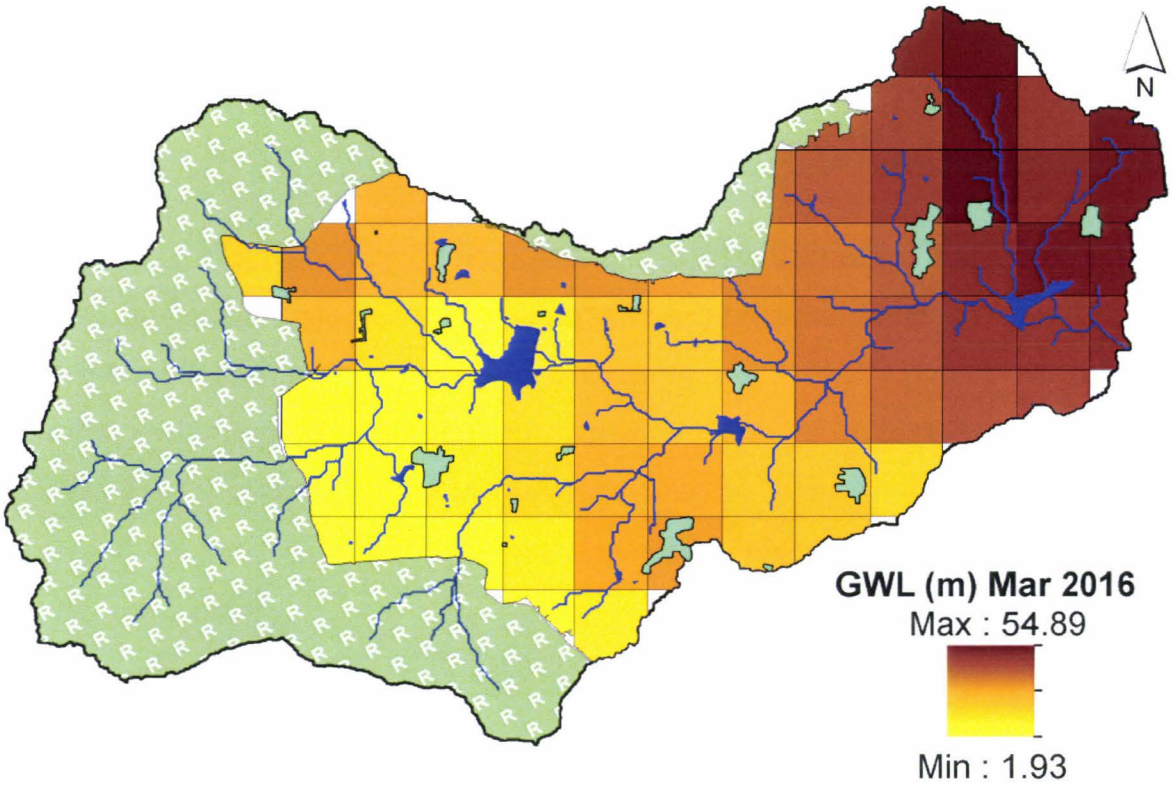

Figure 124 Gridded mean value of groundwater level in the summer of the year 2016.

For irrigated areas evolution, the gridded percentage irrigated cropland was generated for both studied cropping seasons: Rabi 2015 (Figure 125) and Summer 2016 (Figure 126) in the Berambadi experimental watershed. Due to some gridded are not fully occupied by the watershed boundary, the irrigated cropland percentage was preferred to relate with gridded mean groundwater level. It was noticed that the irrigated percentage was varying from 1% to approximately 64% in the watershed (Figure 125).

The upstream of the watershed was having a high percentage of irrigated area compare to the downstream (Figure 125).

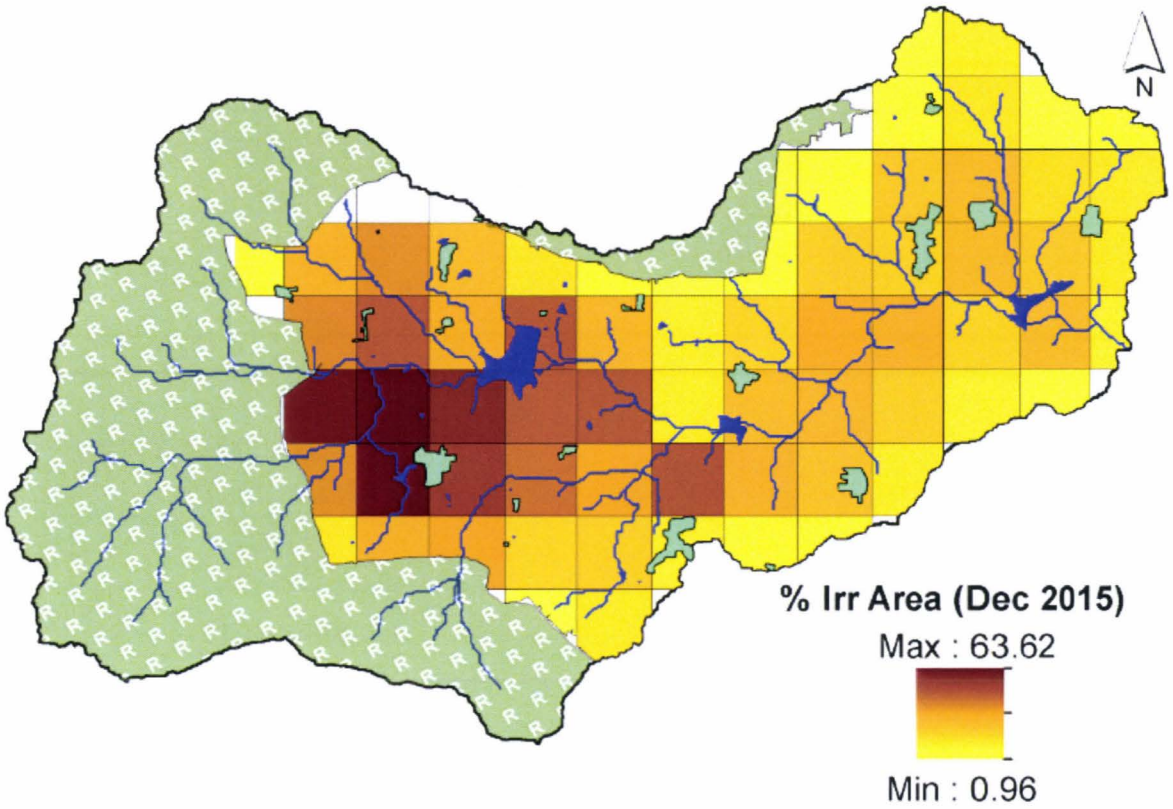

Figure 125 Gridded percentage of irrigated cropland in rabi 2015.

During the summer cropping season the gridded irrigated cropland was variating between 0.11% to 51.58% (Figure 126). And it was noticed from the figure 126 that these highly irrigated grids are along to the drainage network. The gridded irrigated cropland percentage and gridded mean groundwater level were further related to the study.

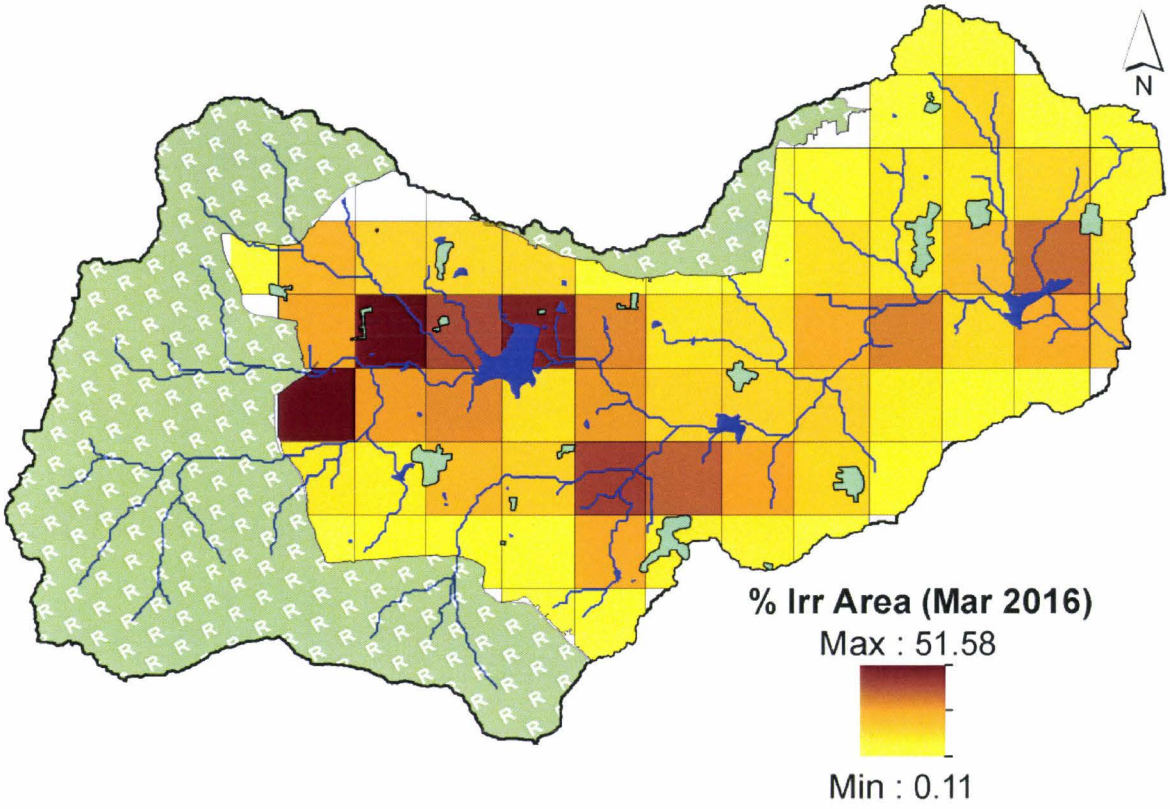

Figure 126 Gridded percentage of irrigated cropland in summer 2016.

Finally, AA' transect (100 meter interval) was drawn as shown in figure 127, to retrieve the spatially distributed groundwater level and elevation data as it was noticed by the survey during the last three decades that's huge number of farmers switch from rainfed to irrigated cropping. It have been built using a DEM (SRTM, 30*30 meters) and interpolated groundwater level in 2015 and 2016.

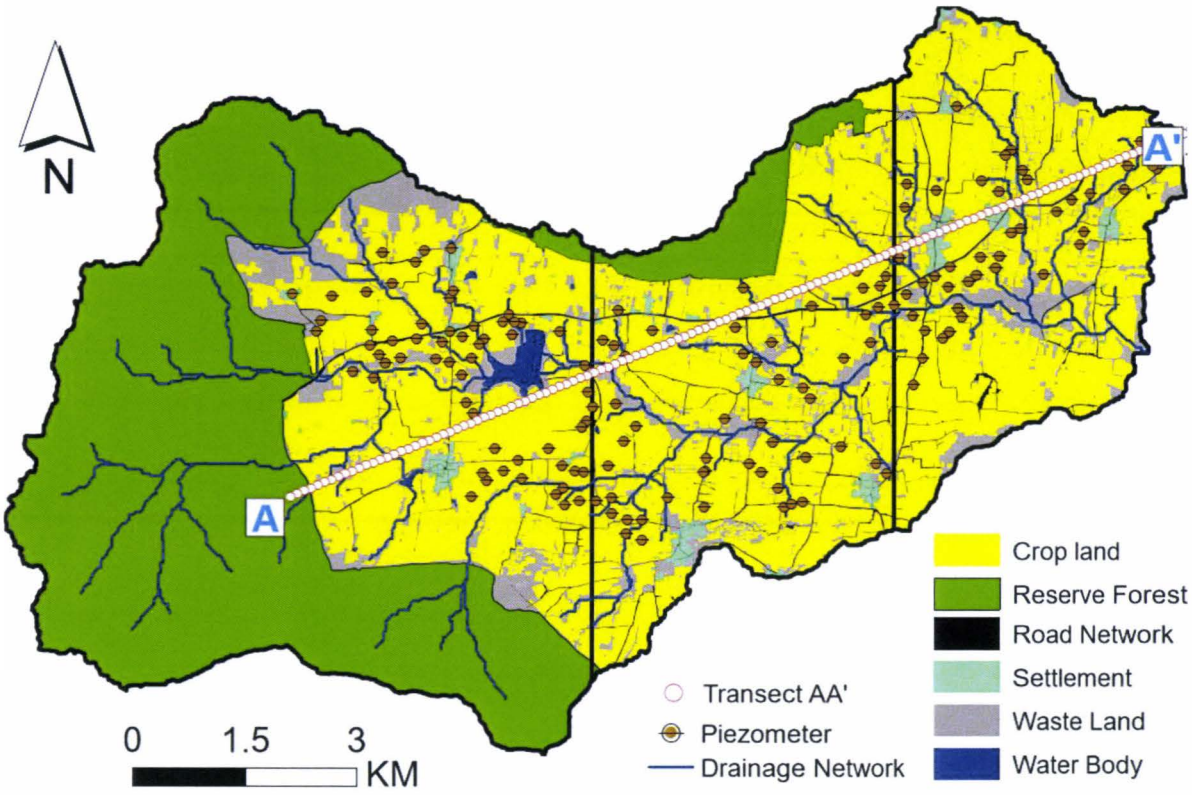

Figure 127 Sampled borewell locations and the transect from upstream towards downstream of the watershed.

6.3 Results and discussion

Berambadi watershed is categorized for three main cropping seasons known as kharif or monsoon (mid-May to mid-Sept), rabi or post-monsoon (mid-Sept to mid-Jan) and summer (mid-Jan to mid-May). Farmers are following these cropping for the cultivation in the watershed. Sometimes, due to delayed rainfall in the kharif cropping season and different agricultural practises, we note difference between seeding dates for the same crop. Rabi cropping season is partially benefitted with North-East rainfall but both the Rabi and summer cropping seasons are majorly depending on groundwater resources. The presented results show the possibility of relation between total irrigated cropland and mean groundwater level at gridded scale in the watershed.

6.3.1 Relation between irrigated cropland and groundwater level.

As the Rabi cropping seasons begins after the monsoon and due to during monsoon majority of crops are rainfed, the groundwater is getting a recharge at this time. With positive economic conditions and disponibilty of groundwater, farmers are cultivating either annual crops like banana and sugarcane or cultivating in rabi and summer season continuously like garlic and vegetable respectively. Farmers with partial facility condition for groundwater extraction may plan for short duration crop like garlic, beetroot, cabbage, watermelon, etc. Finally, a farmer without any groundwater is cultivating non-irrigated crops like gram, maize, ragi, etc.

The gridded irrigated areas are distributed between 5% to 65% in the watershed and the gridded groundwater level mean were between 5m to 50m (Figure 128). It was noticed from the study that the watershed is having very high spatial variability in terms of groundwater level and the total irrigation. Results shows that the intensive irrigated grids (gridded irrigation > 30%) are not available in deeper groundwater grids (mean groundwater level > 15m). The relation tells high possibility of irrigated cropland in the shallow groundwater level zones in the Rabi cropping season.

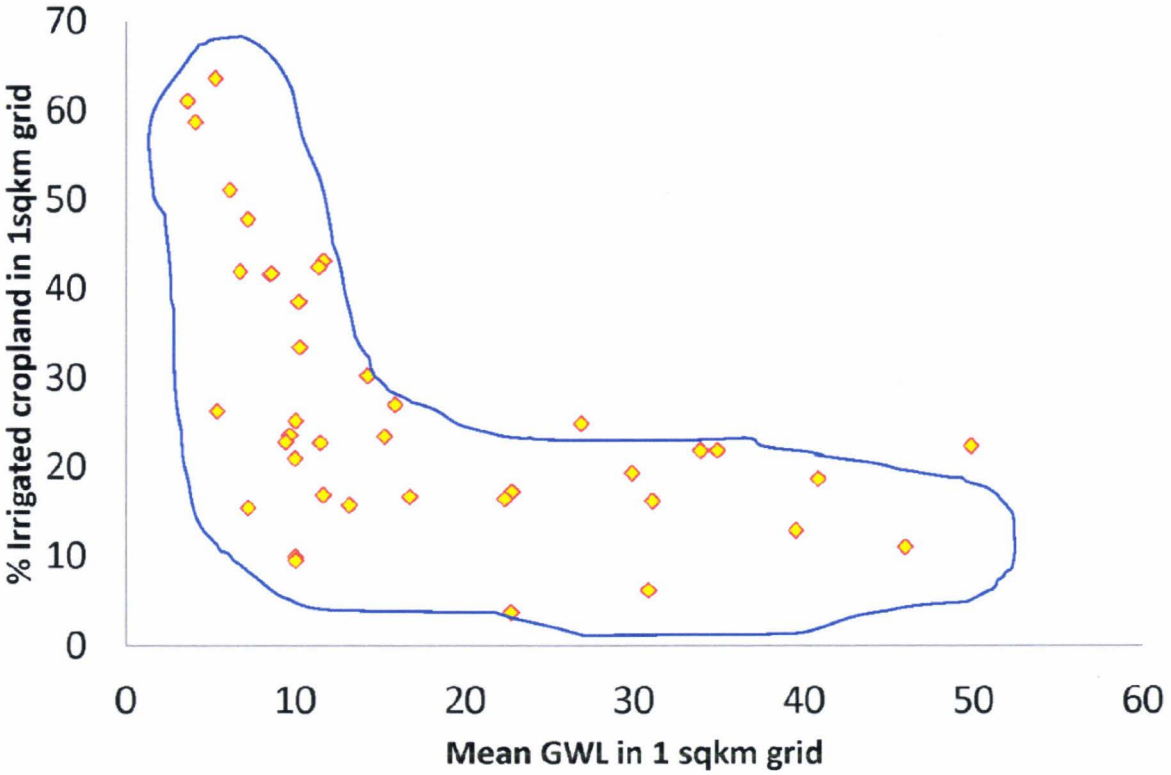

Figure 128 Relation between gridded mean groundwater and percentage irrigated area for rabi 2015 (in yellow, the grid cells).

The summer season cultivation completely depends on groundwater resources and farmer's economic condition. So the farmers with sufficient groundwater availability and good economic condition only plan for the crop cultivation in this season. During summer season, either the annual crop like banana and sugarcane (which is extending from last season) or short-duration crops like vegetables or watermelon were commonly seen during this cropping season. In summer season of the year 2016, the gridded irrigation is distributed between from 0.1% to 30% mainly, and the gridded mean groundwater level is between 7 m to 55 m (Figure 129). It was noticed that the irrigated grids with 10% to 25 % are having majority in the watershed, so the intensive irrigated grids like Rabi cropping season do not exist in this cropping season.

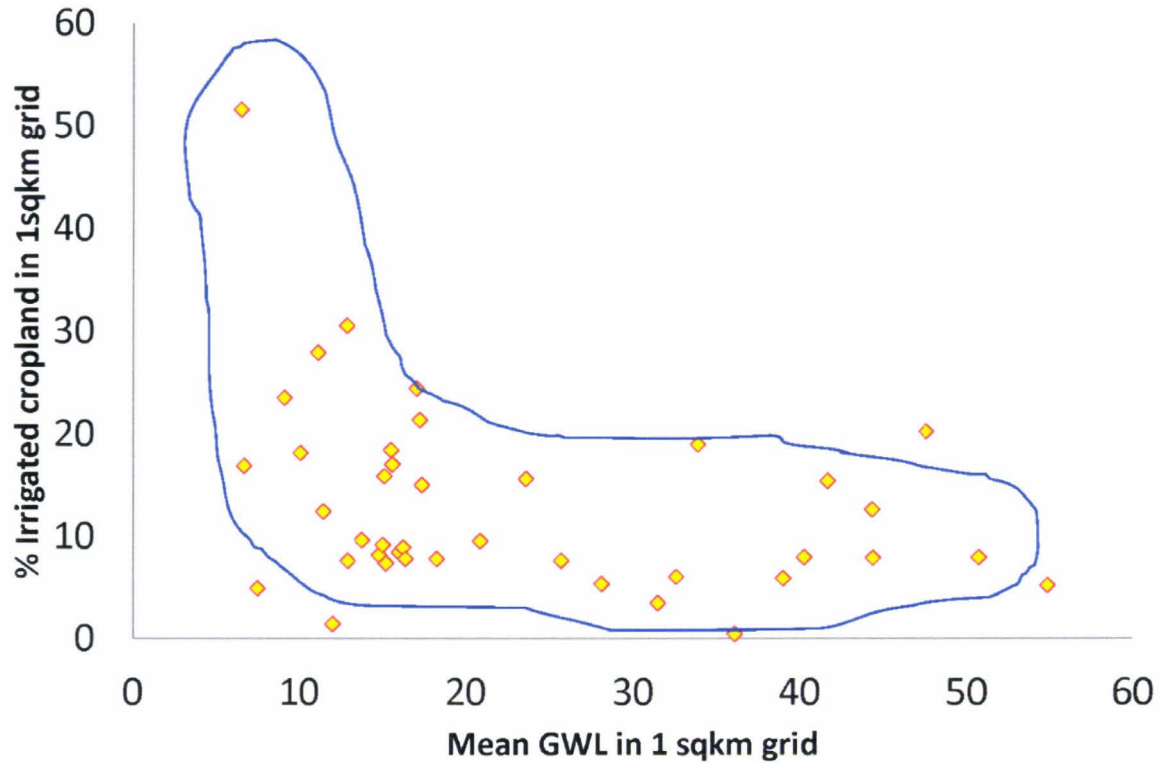

Figure 129 Relation between gridded mean groundwater and percentage irrigated area for summer 2016 (in yellow, the grid cells).

6.3.2 Relation of borewell evolution and intensive irrigation

As per the Census of India 2011, the area under irrigation in the Gundulupet taluk is 27% of the net sown area with borewell density of 11 borewells/km² (Ruiz and Sekhar, 2016; Sekhar M et al., 2011). Figure 130 shows growth of the temporal cumulative number of borewells in the Berambadi watershed with annual cumulative rainfall and total irrigated cropland area estimated for the multitemporal summer and rabi cropping seasons. The temporal increment of groundwater pumping borewell and increment in total irrigated cropland is noticed in the watershed. Results shows that, in the year 2012, the total number of borewells in the watershed were approximately 1300 and approximated 22% of croplands were under irrigation.

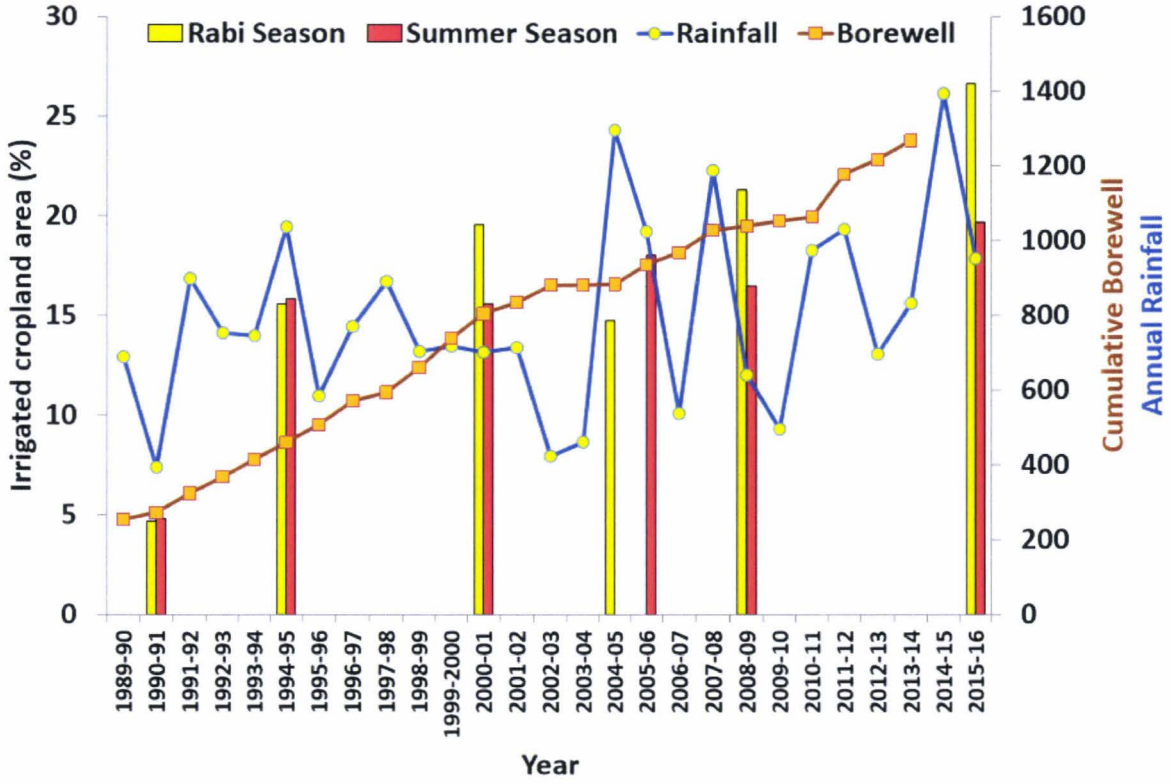

Figure 130 Evolution of total number of borewells in the watershed with cumulative annual rainfall and corresponding total irrigated area.

During weak monsoon, farmers keep borewell option open as an alternative (Sekhar et al., 2016). A total of 13 villages exist in the watershed, and we have found the number of borewells is on the rise. Figure 131 highlights the large change in groundwater levels due to the rapid addition of borewells. Downstream groundwater depleted by 40 to 50 m due to intensive irrigation history and drainages runs dry. Now irrigated cropland clustered in the valleys and shifted towards upstream of the watershed. This uncontrolled growth in several borewells can cause further groundwater depletion in the upstream region of the watershed and will have a severe impact on the adjacent reserve forest groundwater level located in the upstream area. It was observed that the valley portions are having deeper groundwater levels, while in the topographically higher zones have relatively shallow groundwater level (Figure 132). This pattern of groundwater base flow is non-classical in hydrogeology. Figure 132 also shows that borewell density in the valleys, and now the borewell failure rate is also increased significantly in the valleys of the watershed.

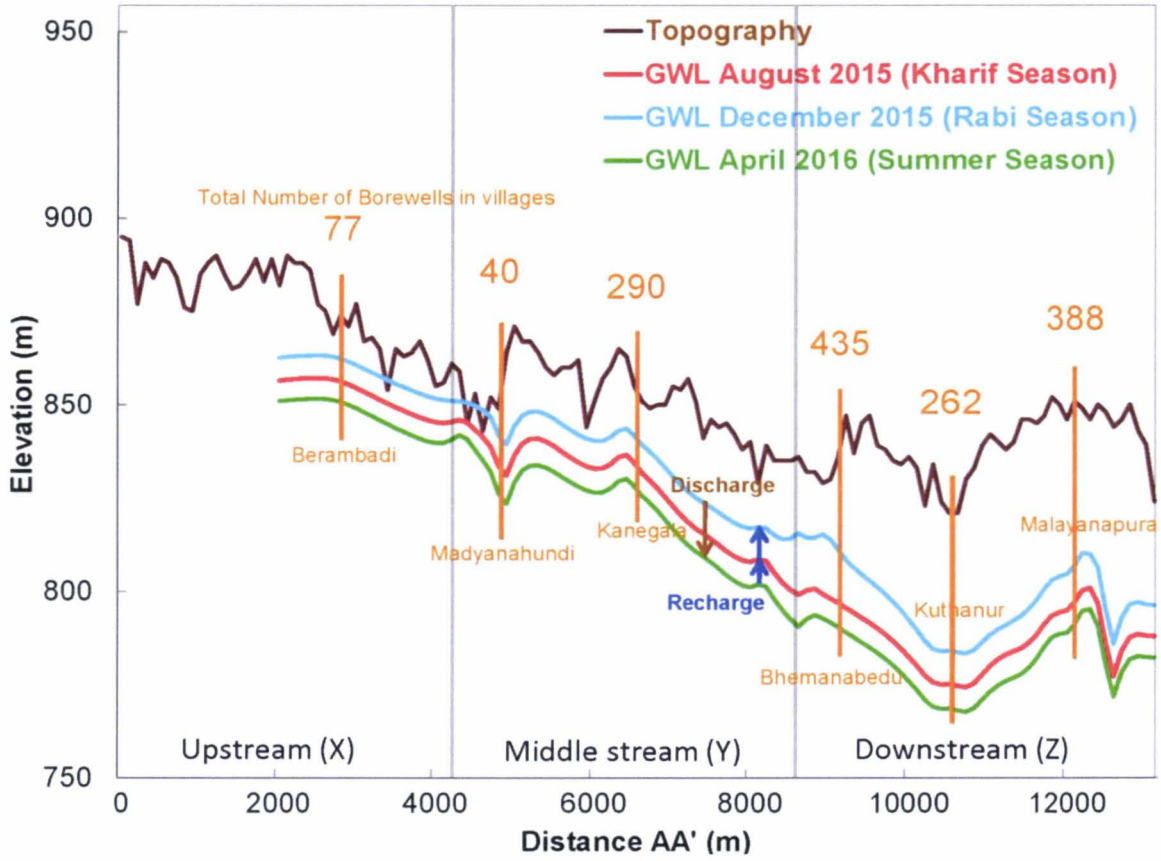

Figure 131 Groundwater level (GWL) along transect AA' for the Kharif, Rabi and Summer season and the total number of borewells in villages of the experimental watershed in 2015.

The extracted interpolated groundwater level was plotted in Figure 132, with a total number of groundwater pumping borewells in villages, passes through the transect AA'. It is observed that the valleys are having a maximum number of borewells, as there is more probability of getting good borewell yield. The groundwater recharging in the monsoon (Kharif) cropping season and the groundwater level is at its highest level in a post-monsoon (rabi) season. This increased groundwater level tempts the farmers to plant banana and sugarcane in the rabi season.

Conclusion

The relationship between groundwater level and irrigated cropland area was presented for the rabi and summer cropping seasons. In both seasons, it was noticed that farmers are performing irrigation according to the seasonal groundwater level conditions. It is individual farmers decision that for the particular cropping season he would like to cultivate crop in irrigation or rainfed condition (Robert et al., 2017b, 2017a; Sriramulu et al., 2016). During the Rabi cropping season of the year 2015, for the shall groundwater level grids (from 5m to 15m), the irrigated cropland percentage grids were distributed from 10% to 64% of irrigation. Whereas, in summer cropping season for shallow groundwater grids (from 5m to 15m), major dense irrigated cropland grids were distributing from 0.1% to 30%. It is clear that farmer decision for the irrigated crop cultivation not only depends on groundwater condition but also on other factors as climate, socio-economy, etc. Majority of summer irrigated cropland situated in the valleys of the watershed and neighborhood of water tank area. This overexploitation of groundwater and occupying the valleys for cropping obstructs the surface flow. At present, the surface flow in the Berambadi watershed is disappeared and all water bodies are getting dry, it happens first time in history after the construction of the Berambadi water tank. This intensive irrigation is also contributing to obstacle base flow and groundwater table in the valleys are depleting with time. This overexploitation of groundwater is affecting the ecosystem and creating various environmental issues. With the intensive groundwater irrigation, farmers also utilizing various organic and inorganic fertilizes in the watershed (Sriramulu et al., 2017b, 2016). The present study can also extend to relate the groundwater contamination zones with total irrigated cropland. This kind of result to relate irrigated cropland area with groundwater level situation or groundwater condition can be extended for regional or national scale. These studies can help in the directions for sustainable agriculture adaptation to climate change conditions.

CHAPTER 7: Conclusion and Perspectives

This Ph.D. thesis explores approaches to monitor irrigated areas using multi source data (remote sensing, ground control campaigns...) on an experimental watershed located in Karnataka India characterized with important stakes for water resource management in the framework of the climate change.

The first chapter presents literature review of the context of irrigation in India with a special focus to see the impacts of the *green revolution* on water resources management. It was noticed that the India is world leader in groundwater abstraction for the irrigation purposes. Furthermore, basics of optical and SAR remote sensing which appear relevant for irrigation monitoring is presented. It was noticed that to monitor irrigated cropland in a tropical country like India at a local scale, it is required to process high spatial and temporal optical and SAR variables associated with ground control campaigns. Irrigated watersheds in India are effectively characterized by very complex spatiotemporal dynamics which necessitate to use multi source remote sensing data (SAR for data acquisition during monsoon). Furthermore, to understand agricultural practises and land use dynamics during crop seasons, it is required to realized intensive ground observation.

Second chapter presents geographical characteristics of the experimental Berambadi watershed which by his location represents an interesting study area to analyse irrigation evolution in the framework of global change. Located in the south west of Karnataka near the western Ghats, it is situated in a semi-arid region and his agriculture has known an important evolution due to groundwater exploitation. Crop management and water management practises are then presented and show high variability of crops according to seasons and high dependence of the monsoon and groundwater resources. For this thesis, only optical and SAR data are used with ground observation study irrigated crops at different temporal scales. Ground campaign have been realized according to different satellites data acquisitions and

permit to obtain spatialized information on land use, biophysical variables and groundwater level which will permit the evaluation of the satellite database for mains objectives of the thesis.

Thus, the third chapter of the thesis presents the use of optical remote sensing for irrigated cropland evolution mapping. The main conclusions of this chapter show that Landsat data could be used to retrieve historical evolution of irrigation. The combined use of multispectral vegetation index (NDVI), soil moisture index (NDMI) and soil impact correction to vegetation index (EVI) are relevant to monitor irrigated croplands. The SVM classification algorithm is used and permit to monitor the seasonal irrigated cropland parcels over decades. Results show the contrasted spatial distribution of irrigated cropland in the watershed and its evolution over time. Irrigation was developed in the early 90s in the valley areas of the watershed, and it expanded recently to the upstream areas.

As southern peninsular India is characterized as a dual monsoon region, the Southwest (SW) and the Northeast (NE) (Douglas et al., 2009; Sekhar et al., 2016; Shah, 2009), cloud cover during two main cropping seasons (kharif and rabi) is the biggest obstacle for optical remote sensing to monitor the cropping practices. Microwave remote sensing can be the best alternate solution for land use studies in cloudy or diverse climatic condition (Dusseux et al., 2014; Lievens et al., 2016). The fourth chapter of the thesis presents two evaluations to overcome the cloudy conditions to monitor irrigated croplands. The first is by the use of only microwave time-series images and the second one by using multi-source optical satellite images. Main results to monitor irrigated croplands using SAR time-series images are that various polarization indices can be used to classify seasonal irrigated croplands using time-series of Radarsat-2 quad pol images. Furthermore, the polarizations variables for dual season irrigated croplands offer interesting results with 0.82 kappa coefficient for two classes: irrigated areas and non-irrigated areas. The second evaluation aims to classify seasonal irrigated cropland using multiple and multisource optical satellite time-series images. A simple methodology base on NDVI temporal analysis to identify seasonal irrigated croplands, dual irrigated croplands, and annual irrigated croplands in the Berambadi watershed was developed. Results show overall classification

accuracy higher than 0.82 when considering irrigation areas. The study shows high heterogeneity between years with for example less irrigated cropland during various cropping seasons of the year 2014-15 compared to cropping seasons of the year 2015-16 due to a severe drought.

At a field scale, very few studies are realized in India to characterize irrigated areas as mean surface of fields are about 0.2 ha. Chapter 5 shows a possible way to monitor crop growth using ultrafine Radarsat-2 SAR images (2*2 meters of spatial resolution, HH polarization) to identify the turmeric crop using optical and SAR data. We focus here first, on crop growth and a coefficient of determination (R^2) from 0.61 to 0.85 is obtained for various six crops (Turmeric, Banana, Sorghum, Maize, Marigold, and Sunflower). Secondly, we analyse turmeric crop as it is the famous cash crop of the Berambadi watershed which necessitates important water resource extraction. The NDVI time series values for the turmeric gave a synoptic view of the turmeric phenological stages. The linear regression between ground observed LAI from eleven turmeric parcels with satellite estimated LAI, NDVI, SE, SE-I, and Span showed a coefficient of determination (R^2) between 0.53 to 0.79. Eight best informative variables issued of optical and radar variables (LAI, T33, σ_0HV, FD_Vol, Alpha, SE, T22, and Entropy) were able to classify turmeric crop with kappa coefficient greater than 0.7.

The intensive groundwater irrigation over decades is becoming a global challenge for the freshwater availability and quality (Böhlke, 2002; Gorelick and Zheng, 2015; Sriramulu et al., 2017b). The sixth chapter is focused on understanding the relationship of irrigation on groundwater level in the Berambadi watershed. It was noticed by the field survey that the farmer decisions to irrigate their farmland for the crop cultivation does not only depend on groundwater condition but also on the farmer's financial condition and government aides. The conclusions of the sixth chapter show that during the rabi cropping season, the irrigated cropland grids between 10% to 64% were distributed in shallow groundwater level grids (from 5 m to 15 m). Whereas, during the summer cropping season the shallow groundwater grids (from 5m to 15m) were having up to 30% of irrigated cropland. In both cropping seasons, it was noticed that farmers are performing irrigation according to the seasonal groundwater level conditions. It is individual farmer's decision that for the

particular cropping season he would like to cultivate crop in irrigation or rainfed condition.

This Ph.D. thesis opens numerous operational, methodological or thematic perspectives for earth observation studies applied to irrigated cropland monitoring. High spatial and temporal satellite images (inferior to 1 m) can be used for further studies of irrigated cropland monitoring and crop type classification. Freely available Sentinel-1, 2 or 3 time-series images could be used for present years to monitor various cropping seasons. Future satellite missions like Fluorescence Explorer (FLEX), Biomass, EarthCARE, etc. can be used for crop biophysical property studies. The simple logical approach that tested the capacity of HH-pol SAR to detect crop height precisely could be further implemented on other crops. The scattering phenomena should be studied to monitor farm management practices and crop physical properties. The proposed results were limited to estimate intensively irrigated croplands, whereas the partial irrigation and precise non-irrigated cropland area estimation were not considered. The study can further implement to perform partial irrigation and rainfed cropland identification. With the intensive groundwater irrigation, farmers also utilizing various organic and inorganic fertilizes in the watershed (Sriramulu et al., 2017b, 2016). The study could further expend to relate the groundwater contamination zones with total irrigated cropland. This kind of result to relate irrigated cropland area with groundwater level situation or groundwater condition could be extended for regional or national scale. The outcomes of thesis could also be used use for a better estimation of the groundwater pumping during these critical agronomic periods. They will be integrated to the AMBHAS groundwater model (Sekhar and Tomer, 2018), and can be used to study the relationship between irrigated cropland area with surface soil and groundwater contamination (Sriramulu et al., 2017b).

References

Abbas, A., Khan, S., Hussain, N., Hanjra, M.A., Akbar, S., 2013. Characterizing soil salinity in irrigated agriculture using a remote sensing approach. Phys. Chem. Earth 55–57, 43–52. https://doi.org/10.1016/j.pce.2010.12.004

Aeschbach-hertig, W., Gleeson, T., 2012. Regional strategies for the accelerating global problem of groundwater depletion. Nat. Geosci. 5, 853–861. https://doi.org/10.1038/ngeo1617

Agarwal, A., Marian S. delos Angeles, R.B., Chéret, I., Davila-Poblete, S., Falkenmark, M., Villarreal, F.G., Jønch-Clausen, T., Kadi, M.A., Kindler, J., Rees, J., Roberts, P., Rogers, P., Solanes, M., Wright, A., 2000. Integrated Water Resources Management.

Alex, Duncan; Stephen, J., 1993. Agricultural Marketing and Pricing Reform : A Review of Experience. World Dev. 21, 1495–1514. https://doi.org/10.1016/0305-750X(93)90129-W

Alexandridis, T.K., Zalidis, G.C., Silleos, N.G., 2008. Mapping irrigated area in Mediterranean basins using low cost satellite Earth Observation. Comput. Electron. Agric. 64, 93–103. https://doi.org/10.1016/j.compag.2008.04.001

Alrababah, M.A., Alhamad, M.N., 2006. Land use/cover classification of arid and semi-arid Mediterranean landscapes using Landsat ETM. Int. J. Remote Sens. 27, 2703–2718. https://doi.org/10.1080/01431160500522700

Ambika, A.K.., Wardlow, B.., Mishra, V.., 2016. Data Descriptor : Remotely sensed high resolution irrigated area mapping in India for 2000 to 2015. Sci. data 3, 1–14. https://doi.org/10.1038/sdata.2016.118

Ameline, M., Fieuzal, R., Betbeber, J., Berthoumieu, J.-F., Baup, F., 2016. Assimilation of SAR and optical data into an agro-meteorological model for monitoring yield of corn. Int. Congr. Environ. Model. Softw.

Anuraga, T.S., Ruiz, L., Kumar, M.S.M., Sekhar, M., Leijnse, A., 2006. Estimating groundwater recharge using land use and soil data: A case study in South India. Agric. Water Manag. 84, 65–76. https://doi.org/10.1016/j.agwat.2006.01.017

Assadian, N.W., Esparza, L.C., Fenn, L.B., Ali, A.S., Miyamoto, S., Figueroa, U. V., Warrick, A.W., 1998. Spatial variability of heavy metals in irrigated alfalfa fields in the upper Rio Grande River basin. Agric. Water Manag. 36, 141–156. https://doi.org/10.1016/S0378-3774(97)00054-1

Atzberger, C., 2013. Advances in remote sensing of agriculture: Context description, existing operational monitoring systems and major information needs. Remote

Sens. 5, 949–981. https://doi.org/10.3390/rs5020949

Aubert, M., Baghdadi, N., Zribi, M., Douaoui, A., Loumagne, C., Baup, F., El Hajj, M., Garrigues, S., 2011. Analysis of TerraSAR-X data sensitivity to bare soil moisture, roughness, composition and soil crust. Remote Sens. Environ. 115, 1801–1810. https://doi.org/10.1016/j.rse.2011.02.021

Bablet, A., Vu, P.V.H., Jacquemoud, S., Viallefont-Robinet, F., Fabre, S., Briottet, X., Sadeghi, M., Whiting, M.L., Baret, F., Tian, J., 2018. MARMIT: A multilayer radiative transfer model of soil reflectance to estimate surface soil moisture content in the solar domain (400–2500 nm). Remote Sens. Environ. 217, 1–17. https://doi.org/10.1016/j.rse.2018.07.031

Badiani, R., Jessoe, K.K., Plant, S., 2012. Development and the Environment: The Implications of Agricultural Electricity Subsidies in India. J. Environ. Dev. 21, 244–262. https://doi.org/10.1177/1070496512442507

Baghdadi, N., Choker, M., Zribi, M., Hajj, M. El, Paloscia, S., Verhoest, N.E.C., Lievens, H., Baup, F., Mattia, F., 2017a. New empirical model for radar scattering from bare soils. Int. Geosci. Remote Sens. Symp. 2017-July, 4139–4142. https://doi.org/10.1109/IGARSS.2017.8127912

Baghdadi, N., Choker, M., Zribi, M., Hajj, M., Paloscia, S., Verhoest, N., Lievens, H., Baup, F., Mattia, F., 2016. A New Empirical Model for Radar Scattering from Bare Soil Surfaces. Remote Sens. 8, 920. https://doi.org/10.3390/rs8110920

Baghdadi, N., Cresson, R., El Hajj, M., Ludwig, R., La Jeunesse, I., 2012. Estimation of soil parameters over bare agriculture areas from C-band polarimetric SAR data using neural networks. Hydrol. Earth Syst. Sci. 16, 1607–1621. https://doi.org/10.5194/hess-16-1607-2012

Baghdadi, N., Hajj, M. El, Zribi, M., Bousbih, S., 2017b. Calibration of the Water Cloud Model at C-Band for winter crop fields and grasslands. Remote Sens. 9, 1–13. https://doi.org/10.3390/rs9090969

Baghdadi, N., Zribi, M., 2016. Characterization of soil surface properties using radar remote sensing. L. Surf. Remote Sens. Cont. Hydrol. 1–39. https://doi.org/10.1016/B978-1-78548-104-8.50001-2

Bank, W., 2010. Deep Wells and Prudence : Towards Pragmatic Action for Addressing Groundwater Overexploitation in India. Tech. Rep.

Banwart, S.A., J., C., J., G., D., S., T., W., S., A., A., A., S., B., S.L, B., O., C., W.E., D., C., D., M., G., K., L., N.P, N., K.V, R., 2013. Sustaining Earth ' s Critical Zone Basic Science and Interdisciplinary Solutions for Global Challenges.

Bargiel, D., 2017. A new method for crop classification combining time series of radar images and crop phenology information. Remote Sens. Environ. 198, 369–383. https://doi.org/10.1016/j.rse.2017.06.022

References

Barik, B., Ghosh, S., Sahana, A.S., Pathak, A., Sekhar, M., Saheer Sahana, A., Pathak, A., Sekhar, M., 2016. Water Food Energy Nexus : Changing Scenarios in India during recent Decades. Hydrol. Earth Syst. Sci. Discuss. 21, 1–30. https://doi.org/10.5194/hess-2016-647

Battude, M., Al Bitar, A., Brut, A., Tallec, T., Huc, M., Cros, J., Weber, J.J., Lhuissier, L., Simonneaux, V., Demarez, V., 2017. Modeling water needs and total irrigation depths of maize crop in the south west of France using high spatial and temporal resolution satellite imagery. Agric. Water Manag. 189, 123–136. https://doi.org/10.1016/j.agwat.2017.04.018

Battude, M., Morin, D., Laurence, S., Valero, S., Marais Sicre, C., Dejoux, J.-F., Huc, M., Hagolle, O., Cros, J., Veloso, A., Inglada, J., Weiss, M., Courault, D., Demarez, V., 2014. Cartography of irrigated crops and estimation of biophysical variables with high spatial and temporal resolution images. GV2M Glob. Veg. Monit. Model.

Baup, F., Villa, L., Fieuzal, R., Ameline, M., 2016. Sensitivity of X-Band (σ 0 , γ) and Optical (NDVI) Satellite Data to Corn Biophysical Parameters. Adv. Remote Sens. 5, 103–117.

Beddington, J.R., Asaduzzaman, M., Clark, M.E., Fernández Bremauntz, A., Guillou, M.D., Howlett, D.J.B., Jahn, M.M., Lin, E., Mamo, T., Negra, C., Nobre, C.A., Scholes, R.J., Van Bo, N., Wakhungu, J., 2012. Agriculture: What next for agriculture after Durban? Science (80-.). 335, 289–290. https://doi.org/10.1126/science.1217941

Bégué, A., Arvor, D., Bellon, B., Betbeder, J., de Abelleyra, D., Ferraz, R.P.D., Lebourgeois, V., Lelong, C., Simões, M., Verón, S.R., 2018. Remote sensing and cropping practices: A review. Remote Sens. 10, 1–32. https://doi.org/10.3390/rs10010099

Betbeder, J., 2015. Evaluation of remote sensing data for identification and characterization of ecological continuities l ' identification et la caract '.

Betbeder, J., Corpetti, T., Corgne, S., Hubert-Moy, L., Rapinel, S., Corpetti, T., Pottier, E., Corgne, S., Hubert-Moy, L., 2014a. Multitemporal classification of TerraSAR-X data for wetland vegetation mapping. J. Appl. Remote Sens. 8, 1–16. https://doi.org/10.1117/1.JRS.8.083648

Betbeder, J., Fieuzal, R., Baup, F., 2016a. Assimilation of LAI and Dry Biomass Data from Optical and SAR Images into an Agro-Meteorological Model to Estimate Soybean Yield. IEEE J. Sel. Top. Appl. Earth Obs. Remote Sens. 9, 2540–2553. https://doi.org/10.1109/JSTARS.2016.2541169

Betbeder, J., Fieuzal, R., Philippets, Y., Ferro-Famil, L., Baup, F., 2016b. Contribution of multitemporal polarimetric synthetic aperture radar data for monitoring winter wheat and rapeseed crops. J. Appl. Remote Sens. 10, 026020. https://doi.org/10.1117/1.JRS.10.026020

Betbeder, J., Fieuzal, R., Philippets, Y., Ferro-Famil, L., Baup, F., 2015a. Estimation of crop parameters using multi-temporal optical and radar polarimetric satellite data 9637, 963702. https://doi.org/10.1117/12.2194781

Betbeder, J., Nabucet, J., Pottier, E., Baudry, J., Corgne, S., Hubert-Moy, L., 2014b. Detection and characterization of hedgerows using TerraSAR-X imagery. Remote Sens. 6, 3752–3769. https://doi.org/10.3390/rs6053752

Betbeder, J., Rapinel, S., Corgne, S., Pottier, E., Hubert-Moy, L., 2015b. TerraSAR-X dual-pol time-series for mapping of wetland vegetation. ISPRS J. Photogramm. Remote Sens. 107, 90–98. https://doi.org/10.1016/j.isprsjprs.2015.05.001

Bhaduri, A., Amarasinghe, U., Shah, T., 2012. An Analysis of Groundwater Irrigation Expansion in India. Int. J. Environ. Waste Manag. 9, 372–387. https://doi.org/10.1504/IJEWM.2012.046399

Bhanja, S.N., Mukherjee, A., Rangarajan, R., Scanlon, B.R., Malakar, P., Verma, S., 2019. Long-term groundwater recharge rates across India by in situ measurements. Hydrol. Earth Syst. Sci. 23, 711–722. https://doi.org/10.5194/hess-23-711-2019

Bhavani, P., Roy, P.S., Chakravarthi, V., Kanawade, V.P., 2017. Satellite Remote Sensing for Monitoring Agriculture Growth and Agricultural Drought Vulnerability Using Long-Term (1982–2015) Climate Variability and Socio-economic Data set. Proc. Natl. Acad. Sci. India Sect. A - Phys. Sci. 87, 733–750. https://doi.org/10.1007/s40010-017-0445-7

Biazin, B., Sterk, G., 2013. Drought vulnerability drives land-use and land cover changes in the Rift Valley dry lands of Ethiopia. Agric. Ecosyst. Environ. 164, 100–113. https://doi.org/10.1016/j.agee.2012.09.012

Biggs, T.W., Thenkabail, P.S., Gumma, M.K., Scott, C.A., Parthasaradhi, G.R., Turral, H.N., Thenkabail, P.S., Gumma, M.K., Scott, C.A., 2006. Irrigated area mapping in heterogeneous landscapes with MODIS time series, ground truth and census data, Krishna Basin, India. Int. J. Remote Sens. 27, 4245–4266. https://doi.org/10.1080/01431160600851801

Biswas, A.K., Tortajada, C., 2009. Water Crisis: Myth or Reality?, Global-is-Asian.

Blaes, X., Defourny, P., Wegmüller, U., Member, S., Vecchia, A. Della, Guerriero, L., Ferrazzoli, P., Member, S., 2006. C-Band Polarimetric Indexes for Maize Monitoring Based on a Validated Radiative Transfer Model 44, 791–800.

Böhlke, J.K., 2002. Groundwater recharge and agricultural contamination. Hydrogeol. J. 10, 153–179. https://doi.org/10.1007/s10040-001-0183-3

Bonilla-Moheno, M., Redo, D.J., Aide, T.M., Clark, M.L., Grau, H.R., 2013. Vegetation change and land tenure in Mexico: A country-wide analysis. Land use policy 30, 355–364. https://doi.org/10.1016/j.landusepol.2012.04.002

Borra-Serrano, I., Peña, J.M., Torres-Sánchez, J., Mesas-Carrascosa, F.J., López-Granados, F., 2015. Spatial quality evaluation of resampled unmanned aerial vehicle-imagery for weed mapping. Sensors (Switzerland) 15, 19688–19708. https://doi.org/10.3390/s150819688

Bourgeau-Chavez, L.L., Leblon, B., Charbonneau, F., Buckley, J.R., 2013. Evaluation of polarimetric Radarsat-2 SAR data for development of soil moisture retrieval algorithms over a chronosequence of black spruce boreal forests. Remote Sens. Environ. 132, 71–85. https://doi.org/10.1016/j.rse.2013.01.006

Brisco, B., Murnaghan, K., Wdowinski, S., Hong, S.H., 2015. Evaluation of RADARSAT-2 Acquisition Modes for Wetland Monitoring Applications. Can. J. Remote Sens. 41, 431–439. https://doi.org/10.1080/07038992.2015.1104636

Brown, J.C., Kastens, J.H., Coutinho, A.C., Victoria, D. de C., Bishop, C.R., 2013. Classifying multiyear agricultural land use data from Mato Grosso using time-series MODIS vegetation index data. Remote Sens. Environ. 130, 39–50. https://doi.org/10.1016/j.rse.2012.11.009

Campos-Taberner, M., García-Haro, F.J., Camps-Valls, G., Grau-Muedra, G., Nutini, F., Busetto, L., Katsantonis, D., Stavrakoudis, D., Minakou, C., Gatti, L., Barbieri, M., Holecz, F., Stroppiana, D., Boschetti, M., 2017. Exploitation of SAR and optical sentinel data to detect rice crop and estimate seasonal dynamics of leaf area index. Remote Sens. 9, 1–17. https://doi.org/10.3390/rs9030248

Campos-Taberner, M., García-Haro, F.J., Camps-Valls, G., Grau-Muedra, G., Nutini, F., Crema, A., Boschetti, M., 2016a. Multitemporal and multiresolution leaf area index retrieval for operational local rice crop monitoring. Remote Sens. Environ. 187, 102–118. https://doi.org/10.1016/j.rse.2016.10.009

Campos-Taberner, M., García-Haro, F.J., Confalonieri, R., Martínez, B., Moreno, Á., Sánchez-Ruiz, S., Gilabert, M.A., Camacho, F., Boschetti, M., Busetto, L., 2016b. Multitemporal monitoring of plant area index in the valencia rice district with PocketLAI. Remote Sens. 8, 1–17. https://doi.org/10.3390/rs8030202

Canisius, F., Shang, J., Liu, J., Huang, X., Ma, B., Jiao, X., Geng, X., Kovacs, J.M., Walters, D., 2018. Tracking crop phenological development using multi-temporal polarimetric Radarsat-2 data. Remote Sens. Environ. 210, 508–518. https://doi.org/10.1016/j.rse.2017.07.031

Cao, F., Deledalle, C.A., Nicolas, J.M., Tupin, F., Denis, L., Ferro-Famil, L., Pottier, E., López-Martínez, C., 2011. Influence of speckle filtering of polarimetric SAR data on different classification methods. Int. Geosci. Remote Sens. Symp. 1052–1055. https://doi.org/10.1109/IGARSS.2011.6049376

Capodici, F., Maltese, A., Ciraolo, G., D'Urso, G., Loggia, G. La, 2017. Power sensitivity analysis of multi-frequency, multi-polarized, multi-temporal SAR data for soil-vegetation system variables characterization. Remote Sens. 9. https://doi.org/10.3390/rs9070677

Chalise, S., Naranpanawa, A., 2016. Climate change adaptation in agriculture: A computable general equilibrium analysis of land-use change in Nepal. Land use policy 59, 241–250. https://doi.org/10.1016/j.landusepol.2016.09.007

Chandrasekar, K., Sai, M.V.R.S., Roy, P.S., Sesha Sai, M.V.R., Roy, P.S., Dwevedi, R.S., 2010. Land Surface Water Index (LSWI) response to rainfall and NDVI using the MODIS vegetation index product. Int. J. Remote Sens. 31, 3987–4005. https://doi.org/10.1080/01431160802575653

Cheema, M.J.M., Bastiaanssen, W.G.M., 2010. Land use and land cover classification in the irrigated Indus Basin using growth phenology information from satellite data to support water management analysis. Agric. Water Manag. 97, 1541–1552. https://doi.org/10.1016/j.agwat.2010.05.009

Chen, J., Li, H., Han, Y., 2016. Potential of RADARSAT-2 data on identifying sugarcane lodging caused by typhoon. 5th Int. Conf. Agro-Geoinformatics, Agro-Geoinformatics 2016. https://doi.org/10.1109/Agro-Geoinformatics.2016.7577665

Chen, K., Huang, W.P., 1996. Classification of multifrequency polarimetric SAR imagery using a dynamic learning neural network. Geosci. Remote ... 34, 814–820. https://doi.org/10.1109/36.499786

Chen, K.S., Yen, S.K., Huang, W.P., 1995. A simple model for retrieving bare soil moisture from radar-scattering coefficients. Remote Sens. Environ. 54, 121–126. https://doi.org/10.1016/0034-4257(95)00129-O

Chen, L., Ren, C., Zhang, B., Wang, Z., Xi, Y., Chen, L., Ren, C., Zhang, B., Wang, Z., Xi, Y., 2018. Estimation of Forest Above-Ground Biomass by Geographically Weighted Regression and Machine Learning with Sentinel Imagery. For. 2018, Vol. 9, Page 582 9, 582. https://doi.org/10.3390/F9100582

Chen, Y., Dou, P., Yang, X., 2017. Improving land use/cover classification with a multiple classifier system using AdaBoost integration technique. Remote Sens. 9. https://doi.org/10.3390/rs9101055

Claverie, M., Demarez, V., Duchemin, B., Hagolle, O., Ducrot, D., Marais-Sicre, C., Dejoux, J.F., Huc, M., Keravec, P., Béziat, P., Fieuzal, R., Ceschia, E., Dedieu, G., 2012. Maize and sunflower biomass estimation in southwest France using high spatial and temporal resolution remote sensing data. Remote Sens. Environ. 124, 844–857. https://doi.org/10.1016/j.rse.2012.04.005

Claverie, M., Vermote, E.F., Franch, B., Masek, J.G., 2015. Evaluation of the Landsat-5 TM and Landsat-7 ETM+ surface reflectance products. Remote Sens. Environ. 169, 390–403. https://doi.org/10.1016/j.rse.2015.08.030

Cloude, S.R., Member, S., Pottier, E., 1997. An Entropy Based Classification Scheme for Land Applications of Polarimetric SAR 35, 68–78.

Corgne, S., Hubert-Moy, L., 2017. Irriga-Detection : Détection et caractérisation des cultures irriguées à partir d'une série d'images radar et optique à haute résolution spatiale et temporelle : Application au site expérimental du Berambadi en Inde. TOSCA/CNES 1–14.

Corgne, S., Hubert-Moy, L., Betbeder, J., 2016a. Monitoring of Agricultural Landscapes Using Remote Sensing Data. L. Surf. Remote Sens. Agric. For. 221–247. https://doi.org/10.1016/B978-1-78548-103-1.50006-6

Corgne, S., Hubert-moy, L., Mercier, G., 2016b. Land cover change prediction with a new theory of plausible and paradoxical reasoning.

Dash, J., 2012. Remote sensing of global cropland for food security. Int. J. Remote Sens. 33, 3321–3322. https://doi.org/10.1080/01431161.2010.516720

Del Frate, F., Ferrazzoli, P., Schiavon, G., 2003. Retrieving soil moisture and agricultural variables by microwave radiometry using neural networks. Remote Sens. Environ. 84, 174–183. https://doi.org/10.1016/S0034-4257(02)00105-0

Del Frate, Fabio, Schiavon, G., Solimini, D., Borgeaud, M., Hoekman, D.H., Vissers, M.A.M., 2003. Crop classification using multiconfiguration C-band SAR data. IEEE Trans. Geosci. Remote Sens. 41, 1611–1619. https://doi.org/10.1109/TGRS.2003.813530

Dheeravath, V., Thenkabail, P.S., Chandrakantha, G., Noojipady, P., Reddy, G.P.O., Biradar, C.M., Gumma, M.K., Velpuri, M., 2010. Irrigated areas of India derived using MODIS 500 m time series for the years 2001-2003. ISPRS J. Photogramm. Remote Sens. 65, 42–59 Contents. https://doi.org/10.1016/j.isprsjprs.2009.08.004

Dhiman, S.C., 2012a. Aquifer Systems of India. CGWB, Minist. Water Resour. Gov. India.

Dhiman, S.C., 2012b. Groundwater Information Booklet. CGWB, Minist. Water Resour. Gov. India.

Di Luzio, M., Srinivasan, R., Arnold, J.G., 2002. Integration of Watershed Tools and SWAT Model into Basins. JAWRA J. Am. Water Resour. Assoc. 38, 1127–1141. https://doi.org/10.1111/j.1752-1688.2002.tb05551.x

Dominique, C., Valérie, D., Martine, G., Michel, L.P., Vincent, S., Sylvain, F., Amanda, V., 2016. Contribution of Remote Sensing for Crop and Water Monitoring, in: Land Surface Remote Sensing in Agriculture and Forest. pp. 113–177. https://doi.org/10.1016/B978-1-78548-103-1.50004-2

Dore, N., 2014. Polarimetric multi- incidence angle analysis over the archaeological site of Samarra by means of RADARSAT-2 and satellites dataset s. Univ. RENNES 1.

Dorigo, W., De Jeu, R., Chung, D., Parinussa, R., Liu, Y., Wagner, W., Fernández-

Prieto, D., 2012. Evaluating global trends (1988-2010) in harmonized multi-satellite surface soil moisture. Geophys. Res. Lett. 39, 3–9. https://doi.org/10.1029/2012GL052988

Douglas, E.M., Beltrán-Przekurat, A., Niyogi, D., Pielke, R.A., Vörösmarty, C.J., 2009. The impact of agricultural intensification and irrigation on land-atmosphere interactions and Indian monsoon precipitation - A mesoscale modeling perspective. Glob. Planet. Change 67, 117–128. https://doi.org/10.1016/j.gloplacha.2008.12.007

Du, P., Liu, S., Xia, J., Zhao, Y., 2013. Information fusion techniques for change detection from multi-temporal remote sensing images. Inf. Fusion 14, 19–27. https://doi.org/10.1016/j.inffus.2012.05.003

Du, P., Xia, J., Zhang, W., Tan, K., Liu, Y., Liu, S., 2012. Multiple classifier system for remote sensing image classification: A review. Sensors 12, 4764–4792. https://doi.org/10.3390/s120404764

Duguay, Y., Bernier, M., Lévesque, E., Domine, F., 2016. Land Cover Classification in SubArctic Regions Using Fully Polarimetric RADARSAT-2 Data. Remote Sens. 8, 697. https://doi.org/10.3390/rs8090697

Dusseux, P., 2014. Exploitation de séries temporelles d'images satellites à haute résolution spatiale pour le suivi des prairies en milieu agricole.

Dusseux, P., Corpetti, T., Hubert-moy, L., Corgne, S., 2014. Combined Use of Multi-Temporal Optical and Radar Satellite Images for Grassland Monitoring 6163–6182. https://doi.org/10.3390/rs6076163

Dusseux, P., Hubert-Moy, L., Corpetti, T., Vertès, F., 2015. Evaluation of SPOT imagery for the estimation of grassland biomass. Int. J. Appl. Earth Obs. Geoinf. 38, 72–77. https://doi.org/10.1016/j.jag.2014.12.003

E. D. Spratt, S.L.C., 1978. Indian Council of Agricultural Research (ICAR), All India Coordinated Research Project devised to help farmers make better use of soil and climatic resources . Descrip- tions of cropping seasons , crop types and production methods for the various region. F. Crop. Res. 1, 103--126.

El Hajj, M., Baghdadi, N., Belaud, G., Zribi, M., Cheviron, B., Courault, D., Hagolle, O., Charron, F., 2014. Irrigated grassland monitoring using a time series of TerraSAR-X and COSMO-SkyMed X-Band SAR data. Remote Sens. 6, 10002–10032. https://doi.org/10.3390/rs61010002

El Hajj, M., Baghdadi, N., Zribi, M., Belaud, G., Cheviron, B., Courault, D., Charron, F., 2016. Soil moisture retrieval over irrigated grassland using X-band SAR data. Remote Sens. Environ. 176, 202–218. https://doi.org/10.1016/j.rse.2016.01.027

El Hajj, M., Bégué, A., Guillaume, S., Martiné, J.F., 2009. Integrating SPOT-5 time series, crop growth modeling and expert knowledge for monitoring agricultural

practices - The case of sugarcane harvest on Reunion Island. Remote Sens. Environ. 113, 2052–2061. https://doi.org/10.1016/j.rse.2009.04.009

Endo, A., Tsurita, I., Burnett, K., Orencio, P.M., 2017. A review of the current state of research on the water, energy, and food nexus. J. Hydrol. Reg. Stud. 11, 20–30. https://doi.org/10.1016/j.ejrh.2015.11.010

Engelbrecht, J., Theron, A., Vhengani, L., Kemp, J., 2017. A simple normalized difference approach to burnt area mapping using multi-polarisation C-Band SAR. Remote Sens. 9, 9–11. https://doi.org/10.3390/rs9080764

Erlangung, Z., 2016. AN ADVANCED SYSTEM FOR THE TARGETED MULTI-TEMPORAL SAR IMAGERY.

Erten, E., Lopez-Sanchez, J.M., Yuzugullu, O., Hajnsek, I., 2016. Retrieval of agricultural crop height from space: A comparison of SAR techniques. Remote Sens. Environ. 187, 130–144. https://doi.org/10.1016/j.rse.2016.10.007

Esch, S., Reichenau, T.G.T.G., Schneider, K., Esch, S., Korres, W., Reichenau, T.G.T.G., Schneider, K., Esch, S., Korres, W., Reichenau, T.G.T.G., Schneider, K., Esch, S., Korres, W., Reichenau, T.G.T.G., Schneider, K., 2018. Soil moisture index from ERS-SAR and its application to the analysis of spatial patterns in agricultural areas. J. Appl. Remote Sens. 12, 1. https://doi.org/10.1117/1.JRS.12.022206

Eswar, R., Sekhar, M., Bhattacharya, B.K., 2016. Disaggregation of LST over India: comparative analysis of different vegetation indices. Int. J. Remote Sens. 37, 1035–1054. https://doi.org/10.1080/01431161.2016.1145363

F. S. Nakayama, D.A.B., 1991. Water quality in drip / trickle irrigation : A review. Irrig Sci 187–192.

Famiglietti, J.S., 2014. The global groundwater crisis. Nat. Clim. Chang. 4, 945–948. https://doi.org/10.1038/nclimate2425

FAO, 2016. Full-Text. AQUASAT 8–9.

FAO, 2006. Farm power and mechanization for small farms in sub-Saharan Africa. Agric. FOOD Eng. Tech. Rep. 3 3.

Feng, X., Li, J., Cheng, W., Fu, B., Wang, Y., Lü, Y., Shao, M., 2017. Evaluation of AMSR-E retrieval by detecting soil moisture decrease following massive dryland re-vegetation in the Loess Plateau, China. Remote Sens. Environ. 196, 253–264. https://doi.org/10.1016/j.rse.2017.05.012

Feola, G., Lerner, A.M., Jain, M., Montefrio, M.J.F., Nicholas, K.A., 2015. Researching farmer behaviour in climate change adaptation and sustainable agriculture: Lessons learned from five case studies. J. Rural Stud. 39, 74–84. https://doi.org/10.1016/j.jrurstud.2015.03.009

Ferrant, S., Bustillo, V., Burel, E., Salmon-Monviola, J., Claverie, M., Jarosz, N., Yin, T., Rivalland, V., Dedieu, G., Demarez, V., Ceschia, E., Probst, A., Al-Bitar, A., Kerr, Y., Probst, J.-L., Durand, P., Gascoin, S., 2016. Extracting Soil Water Holding Capacity Parameters of a Distributed Agro-Hydrological Model from High Resolution Optical Satellite Observations Series. Remote Sens. 8, 154. https://doi.org/10.3390/rs8020154

Ferrant, S., Selles, A., Le Page, M., Herrault, P.A., Pelletier, C., Al-Bitar, A., Mermoz, S., Gascoin, S., Bouvet, A., Saqalli, M., Dewandel, B., Caballero, Y., Ahmed, S., Maréchal, J.C., Kerr, Y., 2017. Detection of irrigated crops from Sentinel-1 and Sentinel-2 data to estimate seasonal groundwater use in South India. Remote Sens. 9. https://doi.org/10.3390/rs9111119

Fieuzal, R., Baup, F., 2016. Estimation of leaf area index and crop height of sunflowers using multi-temporal optical and SAR satellite data. Int. J. Remote Sens. 37, 2780–2809. https://doi.org/10.1080/01431161.2016.1176276

Filion, R., Bernier, M., Paniconi, C., Chokmani, K., Melis, M., Soddu, A., Talazac, M., Lafortune, F.X., 2016. Remote sensing for mapping soil moisture and drainage potential in semi-arid regions: Applications to the Campidano plain of Sardinia, Italy. Sci. Total Environ. 543, 862–876. https://doi.org/10.1016/j.scitotenv.2015.07.068

Fishman, R., 2018. Groundwater depletion limits the scope for adaptation to increased rainfall variability in India. Clim. Change 147, 195–209. https://doi.org/10.1007/s10584-018-2146-x

Fishman, R., Devineni, N., Raman, S., 2015. Can improved agricultural water use efficiency save India's groundwater? Environ. Res. Lett. 10. https://doi.org/10.1088/1748-9326/10/8/084022

Fletcher, R., Ecology, S., Modeling, C., 2018. Land-Cover Pattern and Change.

Foody, G.M., 2002. Status of land cover classification accuracy assessment. Remote Sens. Environ. 80, 185–201. https://doi.org/10.1016/S0034-4257(01)00295-4

Foody, G.M., Mathur, A., 2004. A Relative Evaluation of Multiclass Image Classification by Support Vector Machines. IEEE Trans. Geosci. Remote Sens. 42, 1335–1343. https://doi.org/10.1109/TGRS.2004.827257

Foody, G.M., Mathur, A., Sanchez-Hernandez, C., Boyd, D.S., 2006. Training set size requirements for the classification of a specific class. Remote Sens. Environ. 104, 1–14. https://doi.org/10.1016/j.rse.2006.03.004

Fratzl, P., 2014. When wells run dry. Nature 516, 9–10.

Frost, V.S., Member, S., Stiles, J.A., Member, S., 2012. A Model for Radar Images and Its Application to Adaptive Digital Filtering of Multiplicative Noise 8, 231–239.

Furtado, L.F. de A., Silva, T.S.F., Novo, E.M.L. de M., 2016. Dual-season and full-polarimetric C band SAR assessment for vegetation mapping in the Amazon várzea wetlands. Remote Sens. Environ. 174, 212–222. https://doi.org/10.1016/j.rse.2015.12.013

Gandhi, V.P., Namboodiri, N. V, 2009. Groundwater Irrigation in India : Gains , Costs and Risks.

Gao, Q., Zribi, M., Escorihuela, M.J., Baghdadi, N., Segui, P.Q., 2018. Irrigation Mapping Using Sentinel-1 Time Series at Field Scale. Remote Sens. 10, 1495. https://doi.org/10.3390/rs10091495

Gao, S., Niu, Z., Huang, N., Hou, X., 2013. Estimating the Leaf Area Index, height and biomass of maize using HJ-1 and RADARSAT-2. Int. J. Appl. Earth Obs. Geoinf. 24, 1–8. https://doi.org/10.1016/j.jag.2013.02.002

Garnero, G., Godone, D., 2013. Comparisons between different interpolation techniques. Int. Arch. Photogramm. Remote Sens. Spat. Inf. Sci. - ISPRS Arch. 40, 139–144. https://doi.org/10.5194/isprsarchives-XL-5-W3-139-2013

Gherboudj, I., Magagi, R., Berg, A.A., Toth, B., 2011. Soil moisture retrieval over agricultural fields from multi-polarized and multi-angular RADARSAT-2 SAR data. Remote Sens. Environ. 115, 33–43. https://doi.org/10.1016/j.rse.2010.07.011

Gibbs, H.K., Ruesch, A.S., Achard, F., Clayton, M.K., Holmgren, P., Ramankutty, N., Foley, J.A., 2010. Tropical forests were the primary sources of new agricultural land in the 1980s and 1990s. Proc Natl Acad Sci USA 107, 1–6. https://doi.org/10.1073/pnas.0910275107

Gitelson, A.A., Kaufman, Y.J., Stark, R., Rundquist, D., 2002. Novel algorithms for remote estimation of vegetation fraction. Remote Sens. Environ. 80, 76–87. https://doi.org/10.1016/S0034-4257(01)00289-9

Goldewijk, K.K., Beusen, A., Doelman, J., Stehfest, E., 2017. Anthropogenic land use estimates for the Holocene - HYDE 3.2. Earth Syst. Sci. Data 9, 927–953. https://doi.org/10.5194/essd-9-927-2017

Goodman, J.W., 1976. Some fundamental properties of speckle * 94305, 1145–1150.

Gorelick, S.M., Zheng, C., 2015. Global change and the groundwatermanagement challenge Steven. Water Resour. Res. 3031–3051. https://doi.org/10.1002/2014WR016825.Received

Government of India, 2015. Agricultural Statistics at a Glance, 2014. https://doi.org/http://eands.dacnet.nic.in/PDF/Agricultural_Statistics_At_Glance-2015.pdf

Graesser, J., Ramankutty, N., 2017. Detection of cropland field parcels from Landsat imagery. Remote Sens. Environ. 201, 165–180.

https://doi.org/10.1016/j.rse.2017.08.027

Grisso, R., Alley, M., Holshouser, D., Thomason, W., 2009. Precision farming tools: soil electrical conductivity. Virginia Coop. Ext. 442, 1–6.

Guidici, D., Clark, M.L., 2017. One-dimensional convolutional neural network land-cover classification of multi-seasonal hyperspectral imagery in the San Francisco Bay Area, California. Remote Sens. 9. https://doi.org/10.3390/rs9060629

Gumma, M., Pyla, K., Thenkabail, P., Reddi, V., Naresh, G., Mohammed, I., Rafi, I., 2014. Crop Dominance Mapping with IRS-P6 and MODIS 250-m Time Series Data. Agriculture 4, 113–131. https://doi.org/10.3390/agriculture4020113

Gumma, M.K., Thenkabail, P.S., Muralikrishna, I. V., Velpuri, M.N., Gangadhararao, P.T., Dheeravath, V.V.., Biradar, C.M., Nalan, S.A., Gaur, A., Krishna Gumma, M., Thenkabail, P.S., Muralikrishna, I. V., Velpuri, M.N., Gangadhararao, P.T., Dheeravath, V.V.., Biradar, C.M., Acharya Nalan, S., Gaur, A., Gumma, M.K., Thenkabail, P.S., Muralikrishna, I. V., Velpuri, M.N., Gangadhararao, P.T., Dheeravath, V.V.., Biradar, C.M., Nalan, S.A., Gaur, A., Krishna Gumma, M., Thenkabail, P.S., Muralikrishna, I. V., Velpuri, M.N., Gangadhararao, P.T., Dheeravath, V.V.., Biradar, C.M., Acharya Nalan, S., Gaur, A., Gumma, M. K.; Thenkabail, P. S.; Muralikrishna, I. V.; Velpuri, M. N.; Gangadhararao, P.T.., Dheeravath, V.V.., Biradar, C. M.; Nalan, S.A.., Gaur, A., Gumma, M.K., Thenkabail, P.S., Muralikrishna, I. V., Velpuri, M.N., Gangadhararao, P.T., Dheeravath, V.V.., Biradar, C.M., Nalan, S.A., Gaur, A., Krishna Gumma, M., Thenkabail, P.S., Muralikrishna, I. V., Velpuri, M.N., Gangadhararao, P.T., Dheeravath, V.V.., Biradar, C.M., Acharya Nalan, S., Gaur, A., Gumma, M.K., Thenkabail, P.S., Muralikrishna, I. V., Velpuri, M.N., Gangadhararao, P.T., Dheeravath, V.V.., Biradar, C.M., Nalan, S.A., Gaur, A., Krishna Gumma, M., Thenkabail, P.S., Muralikrishna, I. V., Velpuri, M.N., Gangadhararao, P.T., Dheeravath, V.V.., Biradar, C.M., Acharya Nalan, S., Gaur, A., 2011. Changes in agricultural cropland areas between a water-surplus year and a water-deficit year impacting food security, determined using MODIS 250 m time-series data and spectral matching techniques, in the Krishna river basin (India). Int. J. Remote Sens. 32, 3495–3520. https://doi.org/10.1080/01431161003749485

Gumma, M.K., Thenkabail, P.S., Nelson, A., 2000. Mapping Irrigated Areas Using MODIS 250 Meter Time-Series Data: A Study on Krishna River Basin (India). Water 3, 113–131. https://doi.org/10.3390/w3010113

Gumma, M.K., Thenkabail, P.S., Teluguntla, P., Rao, M.N., Mohammed, I.A., Whitbread, A.M., 2016. Mapping rice-fallow cropland areas for short-season grain legumes intensification in South Asia using MODIS 250 m time-series data. Int. J. Digit. Earth 9, 981–1003. https://doi.org/10.1080/17538947.2016.1168489

Gun, J. van der, 2012. Groundwater and Global Change: Trends, Opportunities and Challenges.

Gun, J. Van Der, Vasak, S., Reckman, J., Richts, A., Struckmeier, W.F., Zaepke, M., 2011. Sustaining Groundwater Resources 159–173. https://doi.org/10.1007/978-90-481-3426-7

Guzmán, S.M., Paz, J.O., Tagert, M.L.M., Mercer, A.E., Pote, J.W., 2018. An integrated SVR and crop model to estimate the impacts of irrigation on daily groundwater levels. Agric. Syst. 159, 248–259. https://doi.org/10.1016/j.agsy.2017.01.017

Haboudane, D., Miller, J.R., Pattey, E., Zarco-Tejada, P.J., Strachan, I.B., 2004. Hyperspectral vegetation indices and novel algorithms for predicting green LAI of crop canopies: Modeling and validation in the context of precision agriculture. Remote Sens. Environ. 90, 337–352. https://doi.org/10.1016/j.rse.2003.12.013

Haldar, D., Rana, P., Yadav, M., Hooda, R.S., Chakraborty, M., 2016. Time series analysis of co-polarization phase difference (PPD) for winter field crops using polarimetric C-band SAR data. Int. J. Remote Sens. 37, 3753–3770. https://doi.org/10.1080/01431161.2016.1204024

Hansen, M.C., Loveland, T.R., 2012. A review of large area monitoring of land cover change using Landsat data. Remote Sens. Environ. 122, 66–74. https://doi.org/10.1016/j.rse.2011.08.024

Hazaymeh, K., K. Hassan, Q., 2016. Remote sensing of agricultural drought monitoring: A state of art review. AIMS Environ. Sci. 3, 604–630. https://doi.org/10.3934/environsci.2016.4.604

Heller, E., Rhemtulla, J.M., Lele, S., Kalacska, M., Badiger, S., Sengupta, R., Ramankutty, N., 2012. Mapping Crop Types, Irrigated Areas, and Cropping Intensities in Heterogeneous Landscapes of Southern India Using Multi-Temporal Medium-Resolution Imagery. Photogramm. Eng. Remote Sens. 78, 815–827. https://doi.org/10.14358/PERS.78.8.815

Hill, M.J., Ticehurst, C.J., Lee, J. Sen, Grunes, M.R., Donald, G.E., Henry, D., 2005. Integration of optical and radar classifications for mapping pasture type in Western Australia. IEEE Trans. Geosci. Remote Sens. 43, 1665–1680. https://doi.org/10.1109/TGRS.2005.846868

Hoang, H.K., Bernier, M., Member, S., Duchesne, S., Tran, Y.M., 2016. Rice Mapping Using RADARSAT-2 Dual- and Quad-Pol Data in a Complex Land-Use Watershed : Cau River Basin (Vietnam) 9, 3082–3096.

Hoekman, D.H., Vissers, M.A.M., Tran, T.N., 2011. Unsupervised Full-Polarimetric SAR Data Segmentation as a Tool for Classification of Agricultural Areas. IEEE J. Sel. Top. Appl. Earth Obs. Remote Sens. 4, 402–411. https://doi.org/10.1109/JSTARS.2010.2042280

Hong, G., Zhang, A., Zhou, F., Brisco, B., 2014. Integration of optical and synthetic aperture radar (SAR) images to differentiate grassland and alfalfa in Prairie area.

Int. J. Appl. Earth Obs. Geoinf. https://doi.org/10.1016/j.jag.2013.10.003

Hosseini, M., McNairn, H., 2017. Using multi-polarization C- and L-band synthetic aperture radar to estimate biomass and soil moisture of wheat fields. Int. J. Appl. Earth Obs. Geoinf. 58, 50–64. https://doi.org/10.1016/j.jag.2017.01.006

Hosseini, M., McNairn, H., Merzouki, A., Pacheco, A., 2015. Estimation of Leaf Area Index (LAI) in corn and soybeans using multi-polarization C- and L-band radar data. Remote Sens. Environ. 170, 77–89. https://doi.org/10.1016/j.rse.2015.09.002

Houghton, R.A., Nassikas, A.A., 2017. Global and regional fluxes of carbon from land use and land cover change 1850–2015. Global Biogeochem. Cycles 31, 456–472. https://doi.org/10.1002/2016GB005546

Huete, A.R., 1988. A soil-adjusted vegetation index (SAVI). Remote Sens. Environ. 25, 295–309. https://doi.org/10.1016/0034-4257(88)90106-X

Huete, A.R., Hua, G., Qi, J., Chehbouni, A., van Leeuwen, W.J.D., 1992. Normalization of multidirectional red and NIR reflectances with the SAVI. Remote Sens. Environ. 41, 143–154. https://doi.org/10.1016/0034-4257(92)90074-T

Huete, A.R., Justice, C., Liu, H., 1994. Development of Vegetation and Soil Indexes for Modis-EOS. Remote Sens. Environ. 49, 224–234. https://doi.org/Doi 10.1016/0034-4257(94)90018-3

Hütt, C., Waldhoff, G., 2018. Multi-data approach for crop classification using multitemporal, dual-polarimetric TerraSAR-X data, and official geodata. Eur. J. Remote Sens. 51, 62–74. https://doi.org/10.1080/22797254.2017.1401909

Hwang, T., Song, C., Bolstad, P. V., Band, L.E., 2011. Downscaling real-time vegetation dynamics by fusing multi-temporal MODIS and Landsat NDVI in topographically complex terrain. Remote Sens. Environ. 115, 2499–2512. https://doi.org/10.1016/j.rse.2011.05.010

Idol, T., Haack, B., Mahabir, R., 2016. An evaluation of Radarsat-2 individual and combined image dates for land use/cover mapping. Geocarto Int. 31, 1108–1122. https://doi.org/10.1080/10106049.2015.1120351

Inoue, Y., Sakaiya, E., Wang, C., 2014. Capability of C-band backscattering coefficients from high-resolution satellite SAR sensors to assess biophysical variables in paddy rice. Remote Sens. Environ. 140, 257–266. https://doi.org/10.1016/j.rse.2013.09.001

Jain, M., Mondal, P., DeFries, R.S., Small, C., Galford, G.L., 2013. Mapping cropping intensity of smallholder farms: A comparison of methods using multiple sensors. Remote Sens. Environ. 134, 210–223. https://doi.org/10.1016/j.rse.2013.02.029

Jain, M., Naeem, S., Orlove, B., Modi, V., DeFries, R.S., 2015. Understanding the

causes and consequences of differential decision-making in adaptation research: Adapting to a delayed monsoon onset in Gujarat, India. Glob. Environ. Chang. 31, 98–109. https://doi.org/10.1016/j.gloenvcha.2014.12.008

Jain, M., Srivastava, A.K., Balwinder-Singh, Joon, R.K., McDonald, A., Royal, K., Lisaius, M.C., Lobell, D.B., 2016. Mapping smallholder wheat yields and sowing dates using micro-satellite data. Remote Sens. 8, 1–18. https://doi.org/10.3390/rs8100860

Javeed, Y., 2010. Analysis of Groundwater Dynamics in Semi-Arid Regions : Effect of Rainfall Variability and Pumping. Dr. Philos. , Indian Inst. Sci.

Javeed, Y., Sekhar, M., Bandyopadhyay, S., Mangiarotti, S., 2009. EOF and SSA analyses of hydrological time series to assess climatic variability and land-use effects: a case study in the Kabini River basin of South India. Int. Assoc. Hydrol. Sci. 329, 167–176.

Jawak, S.D., Kulkarni, K., Luis, A.J., 2015. A Review on Extraction of Lakes from Remotely Sensed Optical Satellite Data with a Special Focus on Cryospheric Lakes. Adv. Remote Sens. 04, 196–213. https://doi.org/10.4236/ars.2015.43016

Jha, S.K., Bharti, A., n.d. Frequently Asked Questions (FAQ). Indian Meteorol. Dep. 1–64.

Jia, K., Liang, S., Zhang, L., Wei, X., Yao, Y., Xie, X., 2014. Forest cover classification using Landsat ETM+ data and time series MODIS NDVI data. Int. J. Appl. Earth Obs. Geoinf. 33, 32–38. https://doi.org/10.1016/j.jag.2014.04.015

Jiao, X., Kovacs, J.M., Shang, J., Mcnairn, H., Walters, D., Ma, B., Geng, X., 2014. Object-oriented crop mapping and monitoring using multi-temporal polarimetric RADARSAT-2 data. ISPRS J. Photogramm. Remote Sens. 96, 38–46. https://doi.org/10.1016/j.isprsjprs.2014.06.014

Jin, S., Sader, S.A., 2005. Comparison of time series tasseled cap wetness and the normalized difference moisture index in detecting forest disturbances. Remote Sens. Environ. 94, 364–372. https://doi.org/10.1016/j.rse.2004.10.012

Jin, X., Kumar, L., Li, Z., Feng, H., Xu, X., Yang, G., Wang, J., 2018. A review of data assimilation of remote sensing and crop models. Eur. J. Agron. 92, 141–152. https://doi.org/10.1016/j.eja.2017.11.002

Karthikeyan, L., Pan, M., Wanders, N., Kumar, D.N., Wood, E.F., 2017. Four decades of microwave satellite soil moisture observations: Part 1. A review of retrieval algorithms. Adv. Water Resour. 109, 106–120. https://doi.org/10.1016/j.advwatres.2017.09.006

Katharine, J., Mach, Planton, S., Broome, J.A., Church, Australia, L., Jan, 2014. IPCC Glossary. Robert Sch. (South Africa) 117–130. https://doi.org/10.1017/CBO9781107415324

Ke, Y., Im, J., Lee, J., Gong, H., Ryu, Y., 2015. Characteristics of Landsat 8 OLI-derived NDVI by comparison with multiple satellite sensors and in-situ observations. Remote Sens. Environ. 164, 298–313. https://doi.org/10.1016/j.rse.2015.04.004

Kenduiywo, B.K., Bargiel, D., Soergel, U., 2017. Higher Order Dynamic Conditional Random Fields Ensemble for Crop Type Classification in Radar Images 1–17.

Khan, S., Hanjra, M.A., 2009. Footprints of water and energy inputs in food production - Global perspectives. Food Policy 34, 130–140. https://doi.org/10.1016/j.foodpol.2008.09.001

Khandelwal, A., Karpatne, A., Marlier, M.E., Kim, J., Lettenmaier, D.P., Kumar, V., 2017. An approach for global monitoring of surface water extent variations in reservoirs using MODIS data. Remote Sens. Environ. 202, 113–128. https://doi.org/10.1016/j.rse.2017.05.039

Kim, Y., Jackson, T., Bindlish, R., Lee, H., Hong, S., 2012a. Radar Vegetation Indices for Estimating the Vegetation Water Content of Rice and Soybean Radar Vegetation Indices for Estimating the Vegetation Water Content of Rice and Soybean 9, 564–568.

Kim, Y., Jackson, T., Bindlish, R., Lee, H., Hong, S., 2012b. Radar vegetation index for estimating the vegetation water content of rice and soybean. IEEE Geosci. Remote Sens. Lett. 9, 564–568. https://doi.org/10.1109/LGRS.2011.2174772

Kizza, T., 2016. Model based estimation of turmeric yield response to saline groundwater irrigation. Int. J. Sci. Res. Eng. Stud. 3, 8–12. https://doi.org/ISSN: 2349-8862

Knauer, K., Gessner, U., Fensholt, R., Forkuor, G., Kuenzer, C., 2017. Monitoring agricultural expansion in Burkina Faso over 14 years with 30 m resolution time series: The role of population growth and implications for the environment. Remote Sens. 9. https://doi.org/10.3390/rs9020132

Kogan, F.N., 1995. Application of vegetation index and brightness temperature for drought detection. Adv. Sp. Res. 15, 91–100. https://doi.org/10.1016/0273-1177(95)00079-T

Krishna Kumar, K., Rupa Kumar, K., Ashrit, R.G., Deshpande, N.R., Hansen, J.W., 2004. Climate impacts on Indian agriculture. Int. J. Climatol. 24, 1375–1393. https://doi.org/10.1002/joc.1081

Kuan, D.T., Sawchuk, A.A., Member, S., Strand, T.C., Chavel, P., 1985. Adaptive Noise Smoothing Filter for Images with Signal-Dependent Noise.

Kumar, M.D., Sivamohan, M.V.K., Narayanamoorthy, A., 2012. The food security challenge of the food-land-water nexus in India. Food Secur. 4, 539–556. https://doi.org/10.1007/s12571-012-0204-1

Kumar, V., Kumari, M., Saha, S.K., 2016. Discrimination of basmati and non-basmati rice types using polarimetric target decomposition of temporal SAR data. Curr. Sci. 110, 2166–2169. https://doi.org/10.18520/cs/v110/i11/2166-2169

Kumar, V., McNairn, H., Bhattacharya, A., Rao, Y.S., 2017. Temporal response of scattering from crops for transmitted ellipticity variation in simulated compact-pol SAR data. IEEE J. Sel. Top. Appl. Earth Obs. Remote Sens. 10, 5163–5174. https://doi.org/10.1109/JSTARS.2017.2757041

Kummu, M., Guillaume, J.H.A., Moel, H. De, Eisner, S., Flörke, M., Porkka, M., 2016. The world ' s road to water scarcity : shortage and stress in the 20th century and pathways towards sustainability. Nat. Publ. Gr. 1–16. https://doi.org/10.1038/srep38495

Kussul, N., Lemoine, G., Gallego, F.J., Skakun, S. V., Lavreniuk, M., Shelestov, A.Y., 2016. Parcel-Based Crop Classification in Ukraine Using Landsat-8 Data and Sentinel-1A Data. IEEE J. Sel. Top. Appl. Earth Obs. Remote Sens. 9, 2500–2508. https://doi.org/10.1109/JSTARS.2016.2560141

Lambin, E.F., Meyfroidt, P., 2011. Global land use change, economic globalization, and the looming land scarcity. Proc. Natl. Acad. Sci. 108, 3465–3472. https://doi.org/10.1073/pnas.1100480108

Lardeux, C., Frison, P.L., Tison, C., Souyris, J.C., Stoll, B., Fruneau, B., Rudant, J.P., 2009. Support vector machine for multifrequency SAR polarimetric data classification. IEEE Trans. Geosci. Remote Sens. 47, 4143–4152. https://doi.org/10.1109/TGRS.2009.2023908

Lee, E., Jayakumar, R., Shrestha, S., Han, Z., 2018. Assessment of transboundary aquifer resources in Asia: Status and progress towards sustainable groundwater management. J. Hydrol. Reg. Stud. 1–13. https://doi.org/10.1016/j.ejrh.2018.01.004

Lee, J.-S., Pottier, E., 2009. Polarimetric Radar Imaging: From Basics to Applications. Polarim. Radar Imaging From Basics to Appl. 440. https://doi.org/10.1201/9781420054989.fmatt

Lee, J.S., Jurkevich, I., Dewaele, P., Wambacq, P., Oosterlinck, A., 1994. Speckle filtering of synthetic aperture radar images: a review. Remote Sens. Rev. 8, 313–340. https://doi.org/10.1080/02757259409532206

Lee, J. Sen, 1983. Digital image smoothing and the sigma filter. Comput. Vision, Graph. Image Process. 24, 255–269. https://doi.org/10.1016/0734-189X(83)90047-6

Lee, J. Sen, Ainsworth, T.L., Wang, Y., Chen, K.S., 2015. Polarimetric SAR speckle filtering and the extended sigma filter. IEEE Trans. Geosci. Remote Sens. 53, 1150–1160. https://doi.org/10.1109/TGRS.2014.2335114

Lee, J. Sen, Grunes, M.R., Schuler, D.L., Pottier, E., Ferro-Famil, L., 2006. Scattering-

model-based speckle filtering of polarimetric SAR data. IEEE Trans. Geosci. Remote Sens. 44, 176–187. https://doi.org/10.1109/TGRS.2005.859338

Lee, J. Sen, Wen, J.H., Ainsworth, T.L., Chen, K.S., Chen, A.J., 2009. Improved sigma filter for speckle filtering of SAR imagery. IEEE Trans. Geosci. Remote Sens. 47, 202–213. https://doi.org/10.1109/TGRS.2008.2002881

Li, L., Zhao, Y., Fu, Y., Pan, Y., Yu, L., Xin, Q., 2017. High resolution mapping of cropping cycles by fusion of landsat and MODIS data. Remote Sens. 9, 1–19. https://doi.org/10.3390/rs9121232

Li, Q., Jiao, L., Hao, Y., 2007. Adaptive simplification of solution for support vector machine. Pattern Recognit. 40, 972–980. https://doi.org/10.1016/j.patcog.2006.07.005

Li, Y., Lampropoulos, G., 2016. RADARSAT-2 and TerraSAR-X polarimetric data for crop growth stages estimation. Int. Geosci. Remote Sens. Symp. 2016-Novem, 4510–4513. https://doi.org/10.1109/IGARSS.2016.7730176

Liang, H., Hu, K., Batchelor, W.D., Qi, Z., Li, B., 2016. An integrated soil-crop system model for water and nitrogen management in North China. Sci. Rep. 6, 1–20. https://doi.org/10.1038/srep25755

Liesenberg, V., Gloaguen, R., 2012. Evaluating SAR polarization modes at L-band for forest classification purposes in eastern Amazon, Brazil. Int. J. Appl. Earth Obs. Geoinf. 21, 122–135. https://doi.org/10.1016/j.jag.2012.08.016

Lievens, H., De Lannoy, G.J.M., Al Bitar, A., Drusch, M., Dumedah, G., Hendricks Franssen, H.J., Kerr, Y.H., Tomer, S.K., Martens, B., Merlin, O., Pan, M., Roundy, J.K., Vereecken, H., Walker, J.P., Wood, E.F., Verhoest, N.E.C., Pauwels, V.R.N., 2016. Assimilation of SMOS soil moisture and brightness temperature products into a land surface model. Remote Sens. Environ. 180, 292–304. https://doi.org/10.1016/j.rse.2015.10.033

Lillesand, T.M., Kiefer, R.W., Chipman, J.W., 2015. Remote Sensing And Image Interpretation, Wiley.

Lipper, L., McCarthy, N., Zilberman, D., Asfaw, S., Branca, G., 2018. Climate Smart Agriculture Building Resilience to Climate Change, Natural Resource Management and Policy. https://doi.org/10.1007/978-3-319-61194-5

Liu, C., Liao, W., Member, S., Li, H., Member, S., 2018. Unsupervised Classification of Multilook Polarimetric SAR Data Using Spatially Variant Wishart Mixture Model with Double Constraints 1–14. https://doi.org/10.1109/TGRS.2018.2819995

Liu, C., Shang, J., Vachon, P.W., McNairn, H., 2013. Multiyear crop monitoring using polarimetric RADARSAT-2 data. IEEE Trans. Geosci. Remote Sens. 51, 2227–2240. https://doi.org/10.1109/TGRS.2012.2208649

Liu, J., Pattey, E., Jégo, G., 2012. Assessment of vegetation indices for regional crop green LAI estimation from Landsat images over multiple growing seasons. Remote Sens. Environ. 123, 347–358. https://doi.org/10.1016/j.rse.2012.04.002

Liu, L., Ji, M., Dong, Y., Zhang, R., Buchroithner, M., 2016. Quantitative retrieval of organic soil properties from visible near-infrared shortwave infrared (Vis-NIR-SWIR) spectroscopy using fractal-based feature extraction. Remote Sens. 8, 1–18. https://doi.org/10.3390/rs8121035

Liu, M.W., Ozdogan, M., Zhu, X., 2014. Crop type classification by simultaneous use of satellite images of different resolutions. IEEE Trans. Geosci. Remote Sens. 52, 3637–3649. https://doi.org/10.1109/TGRS.2013.2274431

Liu, Y., Gong, W., Hu, X., Gong, J., 2018. Forest type identification with random forest using Sentinel-1A, Sentinel-2A, multi-temporal Landsat-8 and DEM data. Remote Sens. 10, 1–25. https://doi.org/10.3390/rs10060946

Llamas, M., Martínez-Santos, P., 2005. Intensive groundwater use: silent revolution and potential source of social conflicts. J. Water Resour. ... 131, 337–341. https://doi.org/10.1061/(ASCE)0733-9496(2005)131:5(337)

Lobell, D.B., Asner, G.P., 2003. Comparison of earth observing-1 ALI and Landsat ETM+ for crop identification and yield prediction in Mexico. IEEE Trans. Geosci. Remote Sens. 41, 1277–1282. https://doi.org/10.1109/TGRS.2003.812909

Loosvelt, L., Peters, J., Skriver, H., De Baets, B., Verhoest, N.E.C., 2012. Impact of reducing polarimetric SAR input on the uncertainty of crop classifications based on the random forests algorithm. IEEE Trans. Geosci. Remote Sens. 50, 4185–4200. https://doi.org/10.1109/TGRS.2012.2189012

Lopez-Martinez, C., Poitter, E., 2015. Polarimetric Scattering Decomposition Theorems, Basic Principles of Polarimetry.

Loveland, T.R., Reed, B.C., Ohlen, D.O., Brown, J.F., Zhu, Z., Yang, L., Merchant, J.W., Ohlen, D.O., Zhu, Z., Yang, L., Merchant, J.W., 2000. Development of a global land cover characteristics database and IGBP DISCover from 1 km AVHRR data. Int. J. Remote Sens. 21, 1303–1330. https://doi.org/10.1080/014311600210191

Löw, F., Michel, U., Dech, S., Conrad, C., 2013. Impact of feature selection on the accuracy and spatial uncertainty of per-field crop classification using Support Vector Machines. ISPRS J. Photogramm. Remote Sens. 85, 102–119. https://doi.org/10.1016/j.isprsjprs.2013.08.007

Lück, W., van Niekerk, A., 2016. Evaluation of a rule-based compositing technique for Landsat-5 TM and Landsat-7 ETM+ images. Int. J. Appl. Earth Obs. Geoinf. 47, 1–14. https://doi.org/10.1016/j.jag.2015.11.019

Lunetta, R.S., Knight, J.F., Ediriwickrema, J., Lyon, J.G., Worthy, L.D., 2006. Land-

cover change detection using multi-temporal MODIS NDVI data. Remote Sens. Environ. https://doi.org/10.1016/j.rse.2006.06.018

Luscombe, A., 2009. Image quality and calibration of RADARSAT-2. Int. Geosci. Remote Sens. Symp. 2, 757–760. https://doi.org/10.1109/IGARSS.2009.5418201

Ma, L., Li, M., Ma, X., Cheng, L., Du, P., Liu, Y., 2017. A review of supervised object-based land-cover image classification. ISPRS J. Photogramm. Remote Sens. 130, 277–293. https://doi.org/10.1016/j.isprsjprs.2017.06.001

Ma, Q., 2013. Application of RADARSAT-2 polarimetric data for land use and land cover classification and crop monitoring in Southwestern Ontario. Thesis. Graduate Program in Geography. The University of Western Ontario 144.

MacDonald Dettwiler and Associates Ltd., 2014. RADARSAT-2 Product Description 1–39.

Maggiori, E., Tarabalka, Y., Charpiat, G., Alliez, P., 2017. Convolutional Neural Networks for Large-Scale Remote-Sensing Image Classification. IEEE Trans. Geosci. Remote Sens. 55, 645–657. https://doi.org/10.1109/TGRS.2016.2612821

Mall, R.K., Singh, R., Gupta, A., Srinivasan, G., Rathore, L.S., 2006. Impact of climate change on Indian agriculture: A review. Clim. Change 78, 445–478. https://doi.org/10.1007/s10584-005-9042-x

Mangiarotti, S., Sharma, A.K., Corgne, S., Hubert-Moy, L., Ruiz, L., Sekhar, M., Kerr, Y., 2018. Can the global modeling technique be used for crop classification? Chaos, Solitons and Fractals 106, 363–378. https://doi.org/10.1016/j.chaos.2017.12.003

Mangiarotti, S., Sharma, A.K., Sekhar, M., Corgne, S., Ruiz, L., Kerr, Y., 2016. Chaos modeling applied to crops classification (Berambadi basin , South of India). rencontre du non-lin ′eaire 2016 76801.

Maréchal, J.C., Vouillamoz, J.M., Mohan Kumar, M.S., Dewandel, B., 2010. Estimating aquifer thickness using multiple pumping tests. Hydrogeol. J. 18, 1787–1796. https://doi.org/10.1007/s10040-010-0664-3

Margat, J., 2008. Exploitations et utilisations des eaux souterraines dans le monde. Géoscience pour une terre durable 52.

Margat, J., Gun, J. van der, 2013. Groundwater around the world: A geographic synopsis. CRC Press.

Martinez-Agirre, A., Alvarez-Mozos, J., Lievens, H., Verhoest, N.E.C., 2017. Influence of Surface Roughness Measurement Scale on Radar Backscattering in Different Agricultural Soils. IEEE Trans. Geosci. Remote Sens. 55, 5925–5936. https://doi.org/10.1109/TGRS.2017.2717043

Maryam Salehi, Maghsoudi, Y., Mohammadzadeh, A., 2017. Assessment of the Potential of H/A/Alpha Decomposition for Polarimetric Interferometric SAR Data. IEEE Trans. Geosci. Remote Sens. 2, 499–507. https://doi.org/10.1038/s41893-019-0287-1

Mavroforakis, M.E., Theodoridis, S., 2006. A geometric approach to support vector machine (SVM) classification. IEEE Trans. Neural Netw. 17, 671–682. https://doi.org/10.1109/TNN.2006.873281

McNairn, H., Shang, J., Jiao, X., Champagne, C., 2009. The contribution of ALOS PALSAR multipolarization and polarimetric data to crop classification. IEEE Trans. Geosci. Remote Sens. 47, 3981–3992. https://doi.org/10.1109/TGRS.2009.2026052

Meier, J., Zabel, F., Mauser, W., 2018. A global approach to estimate irrigated areas - A comparison between different data and statistics. Hydrol. Earth Syst. Sci. 22, 1119–1133. https://doi.org/10.5194/hess-22-1119-2018

Melton, F.S., Johnson, L.F., Lund, C.P., Pierce, L.L., Michaelis, A.R., Hiatt, S.H., Guzman, A., Adhikari, D.D., Purdy, A.J., Rosevelt, C., Votava, P., Trout, T.J., Temesgen, B., Frame, K., Sheffner, E.J., Nemani, R.R., 2012. Satellite irrigation management support with the terrestrial observation and prediction system: A framework for integration of satellite and surface observations to support improvements in agricultural water resource management. IEEE J. Sel. Top. Appl. Earth Obs. Remote Sens. 5, 1709–1721. https://doi.org/10.1109/JSTARS.2012.2214474

Minh, D.H.T., Ienco, D., Gaetano, R., Lalande, N., Ndikumana, E., Osman, F., Maurel, P., 2017. Deep Recurrent Neural Networks for mapping winter vegetation quality coverage via multi-temporal SAR Sentinel-1. IEEE Geosci. Remote Sens. Lett. 1–5.

Mitas, L., Mitasova, H., 2005. Spatial interpolation, in: Geographic Information Systems. pp. 481–492. https://doi.org/10.1007/978-981-13-8664-0_2

Molle, F., Shah, T., Barker, R., 2003. The Groundswell of Pumps : Multilevel Impacts of a Silent Revolution 1–18.

Mondal, P., Jain, M., DeFries, R.S., Galford, G.L., Small, C., 2015. Sensitivity of crop cover to climate variability: Insights from two Indian agro-ecoregions. J. Environ. Manage. 148, 21–30. https://doi.org/10.1016/j.jenvman.2014.02.026

Mondal, P., Jain, M., Robertson, A.W., Galford, G.L., Small, C., DeFries, R.S., 2014. Winter crop sensitivity to inter-annual climate variability in central India. Clim. Change 126, 61–76. https://doi.org/10.1007/s10584-014-1216-y

Mondal, P., Jain, M., Zukowski, M., Galford, G., DeFries, R., 2016. Quantifying fluctuations in winter productive cropped area in the Central Indian Highlands. Reg. Environ. Chang. 16, 69–82. https://doi.org/10.1007/s10113-016-0946-y

Morio, J., 2007. Application of information theory measures to polarimetric and interferometric SAR images. PSIP, 5th Int. Conf. Phys. Signal Image Process.

Mountrakis, G., Im, J., Ogole, C., 2011. Support vector machines in remote sensing: A review. ISPRS J. Photogramm. Remote Sens. 66, 247–259. https://doi.org/10.1016/j.isprsjprs.2010.11.001

Muhammad, S., Zhan, Y., Wang, L., Hao, P., Niu, Z., 2016. Major crops classification using time series MODIS EVI with adjacent years of ground reference data in the US state of Kansas. Optik (Stuttg). 127, 1071–1077 Contents. https://doi.org/10.1016/j.ijleo.2015.10.107

Mulder, V.L., de Bruin, S., Schaepman, M.E., Mayr, T.R., 2011. The use of remote sensing in soil and terrain mapping - A review. Geoderma 162, 1–19. https://doi.org/10.1016/j.geoderma.2010.12.018

Mulla, D.J., 2013. Twenty five years of remote sensing in precision agriculture: Key advances and remaining knowledge gaps. Biosyst. Eng. 114, 358–371. https://doi.org/10.1016/j.biosystemseng.2012.08.009

Narayanamoorthy, A., 2011. Development and composition of irrigation in India: Temporal trends and regional patterns. Irrig. Drain. 60, 431–445. https://doi.org/10.1002/ird.593

Navarro, A., Rolim, J., Miguel, I., Catalao, J., Painho, J., Vekerdy, Z., 2016. Crop Monitoring Based on SPOT-5 Take-5 and Sentinel-1A Data for the Estimation of Crop Water Requirements. Remote Sens. 8, 1–20. https://doi.org/10.3390/rs8060525

Nayak, R.K., Patel, N.R., Dadhwal, V.K., 2010. Estimation and analysis of terrestrial net primary productivity over India by remote-sensing-driven terrestrial biosphere model. Environ. Monit. Assess. 170, 195–213. https://doi.org/10.1007/s10661-009-1226-9

Niu, X., Ban, Y., 2013. Multi-temporal RADARSAT-2 polarimetric SAR data for urban land-cover classification using an object-based support vector machine and a rule-based approach. Int. J. Remote Sens. 34, 1–26. https://doi.org/10.1080/01431161.2012.700133

Niu, X., Ban, Y., Dou, Y., 2016. RADARSAT-2 fine-beam polarimetric and ultra-fine-beam SAR data for urban mapping: comparison and synergy. Int. J. Remote Sens. 37, 2810–2830. https://doi.org/10.1080/01431161.2015.1054050

Oh, Y., Sarabandi, K., Ulaby, F.T., 1992. An empirical model and an inversion technique for radar scattering from bare soil surfaces. IEEE Trans. Geosci. Remote Sens. 30, 370–381. https://doi.org/10.1109/36.134086

Olofsson, P., Foody, G.M., Stehman, S. V., Woodcock, C.E., 2013. Making better use of accuracy data in land change studies: Estimating accuracy and area and

quantifying uncertainty using stratified estimation. Remote Sens. Environ. 129, 122–131. https://doi.org/10.1016/j.rse.2012.10.031

Omar, H., Misman, M.A., Kassim, A.R., 2017. Synergetic of PALSAR-2 and Sentinel-1A SAR Polarimetry for Retrieving Aboveground Biomass in Dipterocarp Forest of Malaysia. Appl. Sci. 7, 675. https://doi.org/10.3390/app7070675

Ouchi, K., 2013. Recent trend and advance of synthetic aperture radar with selected topics. Remote Sens. 5, 716–807. https://doi.org/10.3390/rs5020716

Ozdogan, M., Gutman, G., 2008. A new methodology to map irrigated areas using multi-temporal MODIS and ancillary data: An application example in the continental US. Remote Sens. Environ. 112, 3520–3537. https://doi.org/10.1016/j.rse.2008.04.010

Ozdogan, M., Woodcock, C.E., Salvucci, G.D., Demir, H., 2006. Changes in summer irrigated crop area and water use in Southeastern Turkey from 1993 to 2002: Implications for current and future water resources. Water Resour. Manag. 20, 467–488. https://doi.org/10.1007/s11269-006-3087-0

Ozdogan, M., Yang, Y., Allez, G., Cervantes, C., 2010. Remote sensing of irrigated agriculture: Opportunities and challenges. Remote Sens. 2, 2274–2304. https://doi.org/10.3390/rs2092274

Pal, M., Mather, P.M., 2005. Support vector machines for classification in remote sensing. Int. J. Remote Sens. 26, 1007–1011. https://doi.org/10.1080/01431160512331314083

Palchowdhuri, Y., Valcarce-Diñeiro, R., King, P., Sanabria-Soto, M., 2018. Classification of multi-temporal spectral indices for crop type mapping: A case study in Coalville, UK. J. Agric. Sci. 156, 24–36. https://doi.org/10.1017/S0021859617000879

Pandya, M.R., Singh, R.P., Chaudhari, K.N., Bairagi, G.D., Sharma, R., Dadhwal, V.K., Parihar, J.S., 2012. Leaf area index retrieval using IRS LISS-III sensor data and validation of the MODIS LAI product over central india Leaf Area Index Retrieval Using IRS LISS-III Sensor Data and Validation of the MODIS LAI Product Over Central India. IEEE Trans. Geosci. Remote Sens. 44, 1858–1865. https://doi.org/10.1109/TGRS.2006.876028

Parrens, M., Al Bitar, A., Mialon, A., Fernandez-Moran, R., Ferrazzoli, P., Kerr, Y., Wigneron, J.P., 2017. Estimation of the L-Band Effective Scattering Albedo of Tropical Forests Using SMOS Observations. IEEE Geosci. Remote Sens. Lett. 14, 1223–1227. https://doi.org/10.1109/LGRS.2017.2703637

Paul, S., Ghosh, S., Oglesby, R., Pathak, A., Chandrasekharan, A., Ramsankaran, R., 2016. Weakening of Indian Summer Monsoon Rainfall due to Changes in Land Use Land Cover. Sci. Rep. 6, 1–10. https://doi.org/10.1038/srep32177

Pavelic, P., Patankar, U., Acharya, S., Jella, K., Gumma, M.K., 2012. Role of groundwater in buffering irrigation production against climate variability at the basin scale in South-West India. Agric. Water Manag. 103, 78–87. https://doi.org/10.1016/j.agwat.2011.10.019

Peck, J.C., 2007. Groundwater management in the High Plains Aquifer in the USA: legal problems and innovations. Agric. Groundw. Revolut. Oppor. Threat. to Dev. 296–319. https://doi.org/10.1079/9781845931728.0393

Pedregosa, F., Weiss, R., Brucher, M., 2011. Scikit-learn : Machine Learning in Python. J. ofMachine Learn. Res. 12, 2825–2830.

Pellegrini, P., Fernández, R.J., 2018. efficiency during the worldwide spread of the green revolution. https://doi.org/10.1073/pnas.1717072115

Peña-Arancibia, J.L., Mainuddin, M., Kirby, J.M., Chiew, F.H.S., McVicar, T.R., Vaze, J., 2016. Assessing irrigated agriculture's surface water and groundwater consumption by combining satellite remote sensing and hydrologic modelling. Sci. Total Environ. https://doi.org/10.1016/j.scitotenv.2015.10.086

Peña-Arancibia, J.L., McVicar, T.R., Paydar, Z., Li, L., Guerschman, J.P., Donohue, R.J., Dutta, D., Podger, G.M., van Dijk, A.I.J.M., Chiew, F.H.S., 2014. Dynamic identification of summer cropping irrigated areas in a large basin experiencing extreme climatic variability. Remote Sens. Environ. 154, 139–152. https://doi.org/10.1016/j.rse.2014.08.016

Pettry, D.E., Powell, N.L., 1975. Use of remote sensing in agriculture.

Pichierri, M., Hajnsek, I., 2017. Comparing Performances of Crop Height Inversion Schemes from Multifrequency Pol-InSAR Data. IEEE J. Sel. Top. Appl. Earth Obs. Remote Sens. 10, 1727–1741. https://doi.org/10.1109/JSTARS.2017.2668358

Pinty, B., Verstraete, M.M., 1992. GEMI : A Non-Linear Index to Monitor Global Vegetation from Satellites. Vegetatio 101, 15–20.

Pottier, E., Marechal, C., Allain-Bailhache, S., Meric, S., Hubert-Moy, L., Corgne, S., 2012. On the use of fully polarimetric RADARSAT-2 time-series datasets for delineating and monitoring the seasonal dynamics of wetland ecosystem. Int. Geosci. Remote Sens. Symp. 107–110. https://doi.org/10.1109/IGARSS.2012.6351625

Prasad, R., 2009. Retrieval of crop variables with field-based X-band microwave remote sensing of ladyfinger. Adv. Sp. Res. 43, 1356–1363. https://doi.org/10.1016/j.asr.2008.12.017

Qi, Z., Yeh, A.G.O., Li, X., 2017. A crop phenology knowledge-based approach for monthly monitoring of construction land expansion using polarimetric synthetic aperture radar imagery. ISPRS J. Photogramm. Remote Sens. 133, 1–17. https://doi.org/10.1016/j.isprsjprs.2017.09.009

Qiu, B., Huang, Y., Chen, C., Tang, Z., Zou, F., 2018. Mapping spatiotemporal dynamics of maize in China from 2005 to 2017 through designing leaf moisture based indicator from Normalized Multi-band Drought Index. Comput. Electron. Agric. 153, 82–93. https://doi.org/10.1016/j.compag.2018.07.039

Quiring, S.M., Ganesh, S., 2010. Evaluating the utility of the Vegetation Condition Index (VCI) for monitoring meteorological drought in Texas. Agric. For. Meteorol. 150, 330–339. https://doi.org/10.1016/j.agrformet.2009.11.015

Ramachandiran, K., Pazhanivelan, S., 2016. Abiotic factors (nntrogen and water) in maize : A review. Agric. Rev. 37, 317–324. https://doi.org/10.18805/ag.v37i4.6462

Reddy, M.A., 2008. Remote Sensing and Geographical Information Systems. B S Publications.

Réfrégier, P., Morio, J., 2006. Shannon entropy of partially polarized and partially coherent light with Gaussian fluctuations. J. Opt. Soc. Am. 23, 3036–3044.

Renmin, Y., Feng, L.I.U., Ganlin, Z., Yuguo, Z., Decheng, L.I., Jinling, Y., Fei, Y., 2016. Mapping Soil Texture Based on Field Soil Moisture Observations at a High Temporal Resolution in an Oasis Agricultural Area. Pedosph. An Int. J. 26, 699–708. https://doi.org/10.1016/S1002-0160(15)60078-9

Richards, J.A., Jia, X., 2006. Remote Sensing Digital Image Analysis. Springer. https://doi.org/10.1007/3-540-29711-1

Ridao, E., Conde, J.R., Mínguez, M.I., 1998. Estimating fAPAR from nine vegetation indices for irrigated and nonirrigated faba bean and semileafless pea canopies. Remote Sens. Environ. 66, 87–100. https://doi.org/10.1016/S0034-4257(98)00050-9

Robert, M., 2017. Modeling adaptive decision-making of farmer: An integrated economic and management model, with an application to smallholders in India. PhD Thesis. https://doi.org/10.15713/ins.mmj.3

Robert, M., Bergez, J.E., Thomas, A., 2018. A stochastic dynamic programming approach to analyze adaptation to climate change – Application to groundwater irrigation in India. Eur. J. Oper. Res. 265, 1033–1045. https://doi.org/10.1016/j.ejor.2017.08.029

Robert, M., Thomas, A., Sekhar, M., Badiger, S., Ruiz, L., Raynal, H., Bergez, J.E., 2017a. Adaptive and dynamic decision-making processes: A conceptual model of production systems on Indian farms. Agric. Syst. 157, 279–291. https://doi.org/10.1016/j.agsy.2016.08.001

Robert, M., Thomas, A., Sekhar, M., Badiger, S., Ruiz, L., Willaume, M., Leenhardt, D., Bergez, J.E., 2017b. Farm typology in the Berambadi Watershed (India): Farming systems are determined by farm size and access to groundwater. Water (Switzerland) 9, 1–21. https://doi.org/10.3390/w9010051

Rodda, J.C., Ubertini, L., 2004. The Basis of Civilization - Water Science ? IAHS.

Rodell, M., Velicogna, I., Famiglietti, J.S., 2009. Satellite-based estimates of groundwater depletion in India. Nature 460, 999–1002. https://doi.org/10.1038/nature08238

Rogan, J., Chen, D., 2004. Remote sensing technology for mapping and monitoring land-cover and land-use change 61, 301–325. https://doi.org/10.1016/S0305-9006(03)00066-7

Rolim, J., Navarro Ferreira, A., Saraiva, C., Catalão, J., 2016. A synergistic approach using optical and SAR data to estimate crop's irrigation requirements. Remote Sens. Agric. Ecosyst. Hydrol. XVIII 9998, 99980W. https://doi.org/10.1117/12.2241054

Rondeaux, G., Steven, M., Baret, F., 1996. Optimization of soil-adjusted vegetation indices. Remote Sens. Environ. 55, 95–107. https://doi.org/10.1016/0034-4257(95)00186-7

Rosas, J., Houborg, R., McCabe, M.F., 2017. Sensitivity of Landsat 8 surface temperature estimates to atmospheric profile data: A study using MODTRAN in dryland irrigated systems. Remote Sens. 9, 1–27. https://doi.org/10.3390/rs9100988

Roy, A.D., Shah, T., 2002. Socio-ecology of groundwater irrigation in India. Pagina 307–336.

Roy, D.P., Wulder, M.A., Loveland, T.R., C.E., W., Allen, R.G., Anderson, M.C., Helder, D., Irons, J.R., Johnson, D.M., Kennedy, R., Scambos, T.A., Schaaf, C.B., Schott, J.R., Sheng, Y., Vermote, E.F., Belward, A.S., Bindschadler, R., Cohen, W.B., Gao, F., Hipple, J.D., Hostert, P., Huntington, J., Justice, C.O., Kilic, A., Kovalskyy, V., Lee, Z.P., Lymburner, L., Masek, J.G., McCorkel, J., Shuai, Y., Trezza, R., Vogelmann, J., Wynne, R.H., Zhu, Z., 2014. Landsat-8: Science and product vision for terrestrial global change research. Remote Sens. Environ. 145, 154–172. https://doi.org/10.1016/j.rse.2014.02.001

Roy, D.P.P., Kovalskyy, V., Zhang, H.K.K., Vermote, E.F.F., Yan, L., Kumar, S.S.S., Egorov, A., 2016. Characterization of Landsat-7 to Landsat-8 reflective wavelength and normalized difference vegetation index continuity. Remote Sens. Environ. 185, 57–70. https://doi.org/10.1016/j.rse.2015.12.024

Roy, P.S., Behera, M.D., Murthy, M.S.R.R., Roy, A., Singh, S., Kushwaha, S.P.S.S., Jha, C.S., Sudhakar, S., Joshi, P.K., Reddy, C.S., Gupta, S., Pujar, G., Dutt, C.B.S., Srivastava, V.K., Porwal, M.C., Tripathi, P., Singh, J.S., Chitale, V., Skidmore, A.K., Rajshekhar, G., Kushwaha, D., Karnatak, H., Saran, S., Giriraj, A., Padalia, H., Kale, M., Nandy, S., Jeganathan, C., Singh, C.P., Biradar, C.M., Pattanaik, C., Singh, D.K., Devagiri, G.M., Talukdar, G., Panigrahy, R.K., Singh, H., Sharma, J.R., Haridasan, K., Trivedi, S., Singh, K.P., Kannan, L., Daniel, M., Misra, M.K., Niphadkar, M., Nagabhatla, N., Prasad, N., Tripathi, O.P., Rama Chandra

Prasad, P., Dash, P., Qureshi, Q., Tripathi, S.K., Ramesh, B.R., Gowda, B., Tomar, S., Romshoo, S., Giriraj, S., Ravan, S.A., Behera, S.K., Paul, S., Das, A.K., Ranganath, B.K., Singh, T.P.E., Sahu, T.R.F., Shankar, U., Menon, A.R.R.R.H., Srivastava, G., Neeti, Sharma, S., Mohapatra, U.B.I., Peddi, A., Rashid, H., Salroo, I., Hari Krishna, P., Hajra, P.K.J., Vergheese, A.O.K., Matin, S., Chaudhary, S.A., Ghosh, S., Lakshmi, U., Rawat, D., Ambastha, K., Malik, A.H., Devi, B.S.S.S., Sharma, K.C.L., Mukharjee, P., Sharma, A., Davidar, P., Raju, R.R.V., Katewa, S.S., Kant, S., Raju, V.S., Uniyal, B.P., Debnath, B., Rout, D.K.S., Thapa, R., Joseph, S., Chhetri, P., Ramachandran, R.M., 2015a. New vegetation type map of India prepared using satellite remote sensing: Comparison with global vegetation maps and utilities. Int. J. Appl. Earth Obs. Geoinf. 39, 142–159. https://doi.org/10.1016/j.jag.2015.03.003

Roy, P.S., Roy, A., Joshi, P.K., Kale, M.P., Srivastava, V.K., Srivastava, S.K., Dwevidi, R.S., Joshi, C., Behera, M.D., Meiyappan, P., Sharma, Y., Jain, A.K., Singh, J.S., Palchowdhuri, Y., Ramachandran, R.M., Pinjarla, B., Chakravarthi, V., Babu, N., Gowsalya, M.S., Thiruvengadam, P., Kotteeswaran, M., Priya, V., Yelishetty, K.M.V.N., Maithani, S., Talukdar, G., Mondal, I., Rajan, K.S., Narendra, P.S., Biswal, S., Chakraborty, A., Padalia, H., Chavan, M., Pardeshi, S.N., Chaudhari, S.A., Anand, A., Vyas, A., Reddy, M.K., Ramalingam, M., Manonmani, R., Behera, P., Das, P., Tripathi, P., Matin, S., Khan, M.L., Tripathi, O.P., Deka, J., Kumar, P., Kushwaha, D., 2015b. Development of decadal (1985-1995-2005) land use and land cover database for India. Remote Sens. 7, 2401–2430. https://doi.org/10.3390/rs70302401

Roy, S. Sen, Mahmood, R., Niyogi, D., Lei, M., Foster, S.A., Hubbard, K.G., Douglas, E., Pielke, R., 2007. Impacts of the agricultural Green Revolution-induced land use changes on air temperatures in India. J. Geophys. Res. Atmos. 112, 1–13. https://doi.org/10.1029/2007JD008834

Ruiz, L., Sekhar, M., 2016. Accompanying The adaptation of irrigated agriculture to climate CHAnge Table of contents. ANR 1–30.

Ruiz, L., Sekhar, M., Thomas, A., Badiger, S., Bergez, J.E., Buis, S., Corgne, S., Riotte, J., Raynal, H., Bandhyopadhya, S., 2016. Adaptation of irrigated agriculture to climate change : trans- disciplinary modelling of a watershed in South India 137–138. https://doi.org/10.5194/piahs-366-137-2015

Saadi, S., Simonneaux, V., Boulet, G., Raimbault, B., Mougenot, B., Fanise, P., Ayari, H., Lili-Chabaane, Z., 2015. Monitoring irrigation consumption using high resolution NDVI image time series: Calibration and validation in the Kairouan plain (Tunisia). Remote Sens. 7, 13005–13028. https://doi.org/10.3390/rs71013005

Salehi, M., Mohammadzadeh, A., Maghsoudi, Y., 2017. Adaptive speckle filtering for time series of polarimetric SAR images. IEEE J. Sel. Top. Appl. Earth Obs. Remote Sens. 10, 2841–2848. https://doi.org/10.1109/JSTARS.2017.2698020

Salgado, H., Génova, L., Brisco, B., Bernie, M., 2001. Surface soil moisture estimation

in argentina using RADARSAT-1 imagery. Can. J. Remote Sens. 27, 685–690. https://doi.org/10.1080/07038992.2001.10854911

Salmon, J.M.M., Friedl, M.A., Frolking, S., Wisser, D., Douglas, E.M., 2015. Global rain-fed, irrigated, and paddy croplands: A new high resolution map derived from remote sensing, crop inventories and climate data. Int. J. Appl. Earth Obs. Geoinf. 38, 321–334. https://doi.org/10.1016/j.jag.2015.01.014

Schneibel, A., Stellmes, M., Röder, A., Frantz, D., Kowalski, B., Haß, E., Hill, J., 2017. Assessment of spatio-temporal changes of smallholder cultivation patterns in the Angolan Miombo belt using segmentation of Landsat time series. Remote Sens. Environ. 195, 118–129. https://doi.org/10.1016/j.rse.2017.04.012

Schultz, M., Clevers, J.G.P.W., Carter, S., Verbesselt, J., Avitabile, V., Quang, H.V., Herold, M., 2016. Performance of vegetation indices from Landsat time series in deforestation monitoring. Int. J. Appl. Earth Obs. Geoinf. 52, 318–327. https://doi.org/10.1016/j.jag.2016.06.020

Sekhar, M., Riotte, J., Ruiz, L., Jouquet, P., Braun, J.J., 2016. Influences of climate and agriculture on water and biogeochemical cycles: Kabini critical zone observatory. Proc. Indian Natl. Sci. Acad. 82, 833–846. https://doi.org/10.16943/ptinsa/2016/48488

Sekhar, M., Ruiz, L., 2010. IFCPAR/CEFIPRA PROJECT - Adaptation of Irrigated agriculture to climate CHAnge (AICHA): Project Proposal. IFCPAR/CEFIPRA Water reso, 1–108.

Sekhar, M., Tomer, S.K., 2018. Groundwater Level Dynamics in Bengaluru City , India. https://doi.org/10.3390/su10010026

Sekhar M, Javeed Y, Bandyopadhyay S, Mangiarotti, S., Mazzega, 2011. Groundwater management practices and emerging challenges: Lessons from a case study in the Karnataka State of South India. CRC Press 1–26.

Senay, G.B., Friedrichs, M., Singh, R.K., Velpuri, N.M., 2016. Evaluating Landsat 8 evapotranspiration for water use mapping in the Colorado River Basin. Remote Sens. Environ. 185, 171–185. https://doi.org/10.1016/j.rse.2015.12.043

Seyfried, M., Lohse, K., Marks, D., Pierson, F., Holbrook, W.S., 2018. Reynolds Creek Experimental Watershed and Critical Zone Observatory. https://doi.org/10.2136/vzj2018.07.0129

Shah, T., 2009. Climate change and groundwater : India ' s opportunities for mitigation and adaptation. Environ. Res. Lett. 4, 1–13. https://doi.org/10.1088/1748-9326/4/3/035005

Shah, T., 2007. Crop per Drop of Diesel? Energy Squeeze on India's Smallholder Irrigation. Econ. Polit. Wkly. 42, 4002–4009. https://doi.org/10.2307/40276478

Shah, T., Bhatt, S., Shah, R.K., Talati, J., 2008. Groundwater governance through electricity supply management: Assessing an innovative intervention in Gujarat, western India. Agric. Water Manag. 95, 1233–1242. https://doi.org/10.1016/j.agwat.2008.04.006

Shah, T., Singh, O.P., Mukherji, A., 2006. Some aspects of South Asia's groundwater irrigation economy: Analyses from a survey in India, Pakistan, Nepal Terai and Bangladesh. Hydrogeol. J. 14, 286–309. https://doi.org/10.1007/s10040-005-0004-1

Shah, T., Ul Hassan, M., Khattak, M.Z., Banerjee, P.S., Singh, O.P., Rehman, S.U., 2009. Is Irrigation Water Free? A Reality Check in the Indo-Gangetic Basin. World Dev. 37, 422–434. https://doi.org/10.1016/j.worlddev.2008.05.008

Shahriar Pervez, M., Budde, M., Rowland, J., 2014. Mapping irrigated areas in Afghanistan over the past decade using MODIS NDVI. Remote Sens. Environ. 149, 155–165. https://doi.org/10.1016/j.rse.2014.04.008

Shao, Z., Zhang, L., 2016. Estimating forest aboveground biomass by combining optical and SAR data: A case study in genhe, inner Mongolia, China. Sensors (Switzerland) 16. https://doi.org/10.3390/s16060834

Sharma, A.K., Hubert-moy, L., Buvaneshwari, S., Sriramulu, B., Sekhar, M., Ruiz, L., Bandyopadhyay, S., Mohan, S., Corgne, S., Buvaneshwari, S., 2019. Evaluation of Radarsat-2 quad-pol SAR time series images for monitoring groundwater irrigation. Int. J. Digit. Earth 12, 1–21. https://doi.org/10.1080/17538947.2019.1604834

Sharma, A K, Hubert-Moy, L., Sriramulu, B., Sekhar, M., Ruiz, L., Bandyopadhyay, S., Corgne, S., 2018. Irrigation history estimation using multitemporal landsat satellite images: Application to an intensive groundwater irrigated agricultural watershed in India. Remote Sens. 10. https://doi.org/10.3390/rs10060893

Sharma, A.K., Ruiz, L., Sriramulu, B., Sekhar, M., 2018. Irrigated area estimation using Landsat satellite images in the Berambadi watershed. EGU Gen. Assem. Conf. Abstr. 20, 17445.

Sharma, A.K.K., Hubert-Moy, L., Betbeder, J., Ruiz, L., Sekhar, M., Corgne, S., 2016. Crop identification using time series of landsat-8 and radarsat-2 images: application in a groundwater irrigated region, south India. ESA LPS 2016 1, 103. https://doi.org/ISBN: 978-92-9221-305-3

Shiklomanov, I.A., 2000. Appraisal and Assessment of World Water Resources. Online) J. Water Int. 25, 250–8060. https://doi.org/10.1080/02508060008686794

Siebert, S., 2005. Development and validation of the global map of irrigation areas 535–547.

Siebert, S, Burke, J., Faures, J.M., Frenken, K., Hoogeveen, J., 2010. Groundwater use

for irrigation – a global inventory 1863–1880. https://doi.org/10.5194/hess-14-1863-2010

Siebert, S., Hoogeveen, J., Faures, J., Frenken, K., Feick, S., 2005. Development and validation of the global map of irrigation areas Development and validation of the global map of irrigation areas. Hydrol. Earth Syst. Sci. 2, 1299–1327.

Siebert, Stefan, Portmann, F.T., Döll, P., 2010. Global patterns of cropland use intensity. Remote Sens. 2, 1625–1643. https://doi.org/10.3390/rs2071625

Siebert, S., Zhao, G., 2014. Mapping of rainfed and irrigated agriculture in India – data inventory and documentation. INRES Work. Pap. 17.

Signal, S., Giordano, S., 2016. Démélange d ' images radar polarimétrique par séparation thématique de sources To cite this version : HAL Id : tel-01304068 l ' Université Paris-Est Démélange d ' images radar polarimétrique par séparation thématique de sources.

Singh, D.K., Singh, A.K., 2002. Groundwater situation in India: Problems and perspective. Int. J. Water Resour. Dev. 18, 563–580. https://doi.org/10.1080/07900620220000017400

Singh, G., Venkataraman, G., Yamaguchi, Y., Park, S.E., 2014. Capability assessment of fully polarimetric alos-palsar data for discriminating wet snow from other scattering types in mountainous regions. IEEE Trans. Geosci. Remote Sens. 52, 1177–1196. https://doi.org/10.1109/TGRS.2013.2248369

Singh, Y., Singh, V.P., Singh, G., Yadav, D.S., Sinha, R.K.P., Johnson, D.E., Mortimer, A.M., 2011. The implications of land preparation, crop establishment method and weed management on rice yield variation in the rice-wheat system in the Indo-Gangetic plains. F. Crop. Res. 121, 64–74. https://doi.org/10.1016/j.fcr.2010.11.012

Sitokonstantinou, V., Papoutsis, I., Kontoes, C., Arnal, A.L., Andrés, A.P.A., Zurbano, J.A.G., 2018. Scalable parcel-based crop identification scheme using Sentinel-2 data time-series for the monitoring of the common agricultural policy. Remote Sens. 10, 2–5. https://doi.org/10.3390/rs10060911

Skakun, S., Franch, B., Vermote, E., Roger, J.C., Becker-Reshef, I., Justice, C., Kussul, N., 2017. Early season large-area winter crop mapping using MODIS NDVI data, growing degree days information and a Gaussian mixture model. Remote Sens. Environ. 195, 244–258. https://doi.org/10.1016/j.rse.2017.04.026

Skriver, H., Mattia, F., Satalino, G., Balenzano, A., Pauwels, V.R.N., Verhoest, N.E.C., Davidson, M., 2011. Crop classification using short-revisit multitemporal SAR data. IEEE J. Sel. Top. Appl. Earth Obs. Remote Sens. 4, 423–431. https://doi.org/10.1109/JSTARS.2011.2106198

Spalding, R.F., Exner, M.E., 1993. Occurrence of Nitrate in Groundwater—A Review.

J. Environ. Qual. 22, 392.
https://doi.org/10.2134/jeq1993.00472425002200030002x

Sreelash, K., Buis, S., Sekhar, M., Ruiz, L., Kumar Tomer, S., Guérif, M., 2017. Estimation of available water capacity components of two-layered soils using crop model inversion: Effect of crop type and water regime. J. Hydrol. 546, 166–178. https://doi.org/10.1016/j.jhydrol.2016.12.049

Sreelash, K., Sekhar, M., Ruiz, L., Buis, S., Bandyopadhyay, S., 2013. Improved modeling of groundwater recharge in agricultural watersheds using a combination of crop model and remote sensing. J. Indian Inst. Sci. 93, 189–207.

Sriramulu, B., Riotte, J., Ruiz, L., Sekhar, M., Mohan Kumar, M.S., Kumar Sharma, A., Louis Duprey, J., Audry, S., Praveen, Y., Hemanth, M., Durand, P., Jacques Braun, J., 2016. High spatial variability of nitrate in the hard rock aquifer of an irrigated catchment: Implications for water resource assessment and vulnerability. Geophys. Res. Abstr. EGU Gen. Assem. 18, 2016–5430.

Sriramulu, B., Riotte, J., Ruiz, L., Sekhar, M., Sharma, A.K., 2017a. Impacts of land-use and soil properties on groundwater quality in the hard rock aquifer of an irrigated catchment : the Berambadi (Southern India) 19, 18884.

Sriramulu, B., Riotte, J., Sekhar, M., Kumar, M.S.M., Kumar, A., Louis, J., Audry, S., Giriraja, P.R., Praveenkumarreddy, Y., Moger, H., Durand, P., Braun, J., Ruiz, L., 2017b. Groundwater resource vulnerability and spatial variability of nitrate contamination: Insights from high density tubewell monitoring in a hard rock aquifer. Sci. Total Environ. 579, 838–847.
https://doi.org/10.1016/j.scitotenv.2016.11.017

Srivastava, H.S., Patel, P., Sharma, Y., Navalgund, R.R., 2009. Large-area soil moisture estimation using multi-incidence-angle RADARSAT-1 SAR data. IEEE Trans. Geosci. Remote Sens. 47, 2528–2535.
https://doi.org/10.1109/TGRS.2009.2018448

Steele-Dunne, S.C., McNairn, H., Monsivais-Huertero, A., Judge, J., Liu, P.W., Papathanassiou, K., 2017. Radar Remote Sensing of Agricultural Canopies: A Review. IEEE J. Sel. Top. Appl. Earth Obs. Remote Sens. 10, 2249–2273.
https://doi.org/10.1109/JSTARS.2016.2639043

Stibig, H.J., Belward, A.S., Roy, P.S., Rosalina-Wasrin, U., Agrawal, S., Joshi, P.K., Hildanus, Beuchle, R., Fritz, S., Mubareka, S., Giri, C., 2007. A land-cover map for South and Southeast Asia derived from SPOT-VEGETATION data. J. Biogeogr. 34, 625–637. https://doi.org/10.1111/j.1365-2699.2006.01637.x

Susan Moran, M., Alonso, L., Moreno, J.F., Cendrero Mateo, M.P., Fernando De La Cruz, D., Montoro, A., 2012. A RADARSAT-2 quad-polarized time series for monitoring crop and soil conditions in Barrax, Spain. IEEE Trans. Geosci. Remote Sens. 50, 1057–1070. https://doi.org/10.1109/TGRS.2011.2166080

Szogs, S., Arneth, A., Anthoni, P., Doelman, J.C., Humpenöder, F., Popp, A., Pugh, T.A.M., Stehfest, E., 2017. Impact of LULCC on the emission of BVOCs during the 21st century. Atmos. Environ. 165, 73–87. https://doi.org/10.1016/j.atmosenv.2017.06.025

Tal, A., 2016. Rethinking the sustainability of Israel's irrigation practices in the Drylands. Water Res. 90, 387–394. https://doi.org/10.1016/j.watres.2015.12.016

Taylor, R., 2014. When wells run dry. Nature 12, 30–38. https://doi.org/10.1038/516179a

Teluguntla, P., Thenkabail, P.S., Xiong, J., Gumma, M.K., Congalton, R.G., Oliphant, A., Poehnelt, J., Yadav, K., Rao, M., Massey, R., 2017. Spectral matching techniques (SMTs) and automated cropland classification algorithms (ACCAs) for mapping croplands of Australia using MODIS 250-m time-series (2000–2015) data. Int. J. Digit. Earth 10, 944–977. https://doi.org/10.1080/17538947.2016.1267269

Thakkar, A., Desai, V., Patel, A., Potdar, M., 2014. Land Use / Land Cover Classification of Remote Sensing Data and Their Derived Products in a Heterogeneous Landscape of a Khan-Kali Watershed , Gujarat. Asian J. Geoinformatics 14, 1–12.

Thenkabail, P., Biradar, C.M., Noojipady, P., Dheeravath, V., Li, Y.J., Velpuri, M., Reddy, G.P.O., Cai, X.L., Gumma, M., Turral, H., Vithanage, J., Schull, M., Dutta, R., 2008. A Global Irrigated Area Map (GIAM) Using Remote Sensing at the End of the Last Millennium, Water Management. https://doi.org/10.13140/RG.2.1.4945.0087

Thenkabail, P.S., 2010. Global croplands and their importance for water and food security in the twenty-first century: Towards an ever green revolution that combines a second green revolution with a blue revolution. Remote Sens. 2, 2305–2312. https://doi.org/10.3390/rs2092305

Thenkabail, P.S., Biradar, C.M., Noojipady, P., Dheeravath, V., Li, Y., Velpuri, M., Gumma, M., Gangalakunta, O.R.P., Turral, H., Cai, X., Vithanage, J., Schull, M.A., Dutta, R., Dheeravath, V., Li, Y., Velpuri, M., Gumma, M., Reddy, O., Gangalakunta, O.R.P., Turral, H., Cai, X., Vithanage, J., Schull, M.A., Dutta, R., Dheeravath, V., Li, Y., Velpuri, M., Gumma, M., Reddy, O., 2009a. Global irrigated area map (GIAM), derived from remote sensing, for the end of the last millennium. Int. J. Remote Sens. 30, 3679–3733. https://doi.org/10.1080/01431160802698919

Thenkabail, P.S., Biradar, C.M., Turral, H., Noojipady, P., Li, Y.J., Vithanage, J., Dheeravath, V., Velpuri, M., Schull, M., Cai, X., Dutta, R., 2006. An Irrigated Area Map of the World (1999) Derived from Remote Sensing, Water Management. https://doi.org/http://dx.doi.org/10.3910/2009.105

Thenkabail, P.S., Dheeravath, V., Biradar, C.M., Gangalakunta, O.R.P., Noojipady, P.,

Gurappa, C., Velpuri, M., Gumma, M., Li, Y., 2009b. Irrigated area maps and statistics of India using remote sensing and national statistics. Remote Sens. 1, 50–67. https://doi.org/10.3390/rs1020050

Thenkabail, P.S., Hanjra, M.A., Dheeravath, V., Gumma, M.K., 2011. Global Croplands and Their Water Use from Remote Sensing and Nonremote Sensing Perspectives. https://doi.org/10.1201/b10599-20

Thenkabail, P.S., Schull, M., Turral, H., 2005. Ganges and Indus river basin land use/land cover (LULC) and irrigated area mapping using continuous streams of MODIS data. Remote Sens. Environ. 95, 317–341. https://doi.org/10.1016/j.rse.2004.12.018

Thiruvengadachari, S., 1981. Satellite sensing of irrigation patterns in semiarid areas: an Indian study. Photogramm. Eng. Remote Sens. 47, 1493–1499.

Thomas, C., Ranchin, T., Wald, L., Chanussot, J., 2008. Synthesis of multispectral images to high spatial resolution: A critical review of fusion methods based on remote sensing physics. IEEE Trans. Geosci. Remote Sens. 46, 1301–1312. https://doi.org/10.1109/TGRS.2007.912448

Tobler, W.R., 1970. A Computer Movie Simulating Urban Growth in the Detroit Region, University of Michigan. https://doi.org/10.1017/CBO9781107415324.004

Tomer, S.K., Al Bitar, A., Sekhar, M., Zribi, M., Bandyopadhyay, S., Sreelash, K., Sharma, A.K., Corgne, S., Kerr, Y., 2015. Retrieval and multi-scale validation of Soil Moisture from multi-temporal SAR Data in a semi-arid tropical region. Remote Sens. 7, 8128–8153. https://doi.org/10.3390/rs70608128

Tucker, C.J., 1979. Red and photographic infrared linear combinations for monitoring vegetation. Remote Sens. Environ. 8, 127–150. https://doi.org/10.1016/0034-4257(79)90013-0

Turner, B.L., Eric F. Lambin, Reenberg, A., 2007. The emergence ofland change science for global environmental change and sustainability. PNAS 105, 20690–20695.

Turner, D.P., Cohen, W.B., Kennedy, R.E., Fassnacht, K.S., Briggs, J.M., 1999. Relationships between leaf area index and Landsat TM spectral vegetation indices across three temperate zone sites. Remote Sens. Environ. 70, 52–68. https://doi.org/10.1016/S0034-4257(99)00057-7

Ulaby, F.T., 1975. Radar Response to Vegetation. IEEE Trans. Antennas Propag. 23, 36–45. https://doi.org/10.1109/TAP.1975.1140999

Ulaby, F.T., Dobson, M.C., Brunfeldt, D.R., 1983. Improvement of Moisture Estimation Accuracy of Vegetation-Covered Soil by Combined Active Passive Microwave Remote-Sensing. Ieee Trans. Geosci. Remote Sens. 21, 300–307. https://doi.org/10.1109/TGRS.1983.350557

USGS, U.S. Geological Survery, 2016. Product Guide. Prod. Guid. Provisional Landsat 8 Surf. Reflectance Code Prod. 4.3, 1–40. https://doi.org/10.1080/1073161X.1994.10467258

Velpuri, N.M.M., Thenkabail, P.S.S., Gumma, M.K.K., Biradar, C., Dheeravath, V., Noojipady, P., Yuanjie, L., 2009. Influence of Resolution in Irrigated Area Mapping and Area Estimation. Photogramm. Eng. {&} Remote Sens. 75, 1383–1395. https://doi.org/10.14358/PERS.75.12.1383

Vermote, E.F., Tanré, D., Deuzé, J.L., Herman, M., Morcrette, J.J., 1997. Second simulation of the satellite signal in the solar spectrum, 6s: an overview. IEEE Trans. Geosci. Remote Sens. 35, 675–686. https://doi.org/10.1109/36.581987

Vittal, H., Ghosh, S., Karmakar, S., Pathak, A., Murtugudde, R., 2016. Lack of Dependence of Indian Summer Monsoon Rainfall Extremes on Temperature: An Observational Evidence. Sci. Rep. 6, 31039. https://doi.org/10.1038/srep31039

Vrieling, A., Skidmore, A.K., Wang, T., Meroni, M., Ens, B.J., Oosterbeek, K., O'Connor, B., Darvishzadeh, R., Heurich, M., Shepherd, A., Paganini, M., 2017. Spatially detailed retrievals of spring phenology from single-season high-resolution image time series. Int. J. Appl. Earth Obs. Geoinf. 59, 19–30. https://doi.org/10.1016/j.jag.2017.02.021

Vuolo, F., Neuwirth, M., Immitzer, M., Atzberger, C., Ng, W.-T., 2018. How much does multi-temporal Sentinel-2 data improve crop type classification? Int. J. Appl. Earth Obs. Geoinf. 72, 122–130. https://doi.org/10.1016/j.jag.2018.06.007

Wada, Y., Van Beek, L.P.H., Van Kempen, C.M., Reckman, J.W.T.M., Vasak, S., Bierkens, M.F.P., 2010. Global depletion of groundwater resources. Geophys. Res. Lett. 37, 1–5. https://doi.org/10.1029/2010GL044571

Wales, U. of N.S., 2002. Agriculture in india. India Nat. Environ- ment, Resour. Dev. 251–271.

Wang, H., Magagi, R., Goïta, K., 2018. Potential of a two-component polarimetric decomposition at C-band for soil moisture retrieval over agricultural fields. Remote Sens. Environ. 217, 38–51. https://doi.org/10.1016/j.rse.2018.08.003

Wang, H., Méric, S., Allain, S., Pottier, E., Wang, H., Méric, S., Allain, S., Sar, E.P.M., 2015. Multi-angular ground-based SAR system for soil surface roughness characterization To cite this version : HAL Id : hal-01169265. Electron. Lett.

Waske, B., Van Der Linden, S., 2008. Classifying multilevel imagery from SAR and optical sensors by decision fusion. IEEE Trans. Geosci. Remote Sens. 46, 1457–1466. https://doi.org/10.1109/TGRS.2008.916089

White, E. V., Roy, D.P., 2015. A contemporary decennial examination of changing agricultural field sizes using Landsat time series data. Geo Geogr. Environ. 2, 33–54. https://doi.org/10.1002/geo2.4

Wilken, F., Wagner, P.D., Narasimhan, B., Fiener, P., 2017. Spatio-temporal patterns of land use and cropping frequency in a tropical catchment of South India. Appl. Geogr. 89, 124–132. https://doi.org/10.1016/j.apgeog.2017.10.011

Wiseman, G., McNairn, H., Homayouni, S., Shang, J., 2014. RADARSAT-2 Polarimetric SAR response to crop biomass for agricultural production monitoring. IEEE J. Sel. Top. Appl. Earth Obs. Remote Sens. 7, 4461–4471. https://doi.org/10.1109/JSTARS.2014.2322311

Wood, S.A., Jina, A.S., Jain, M., Kristjanson, P., DeFries, R.S., 2014. Smallholder farmer cropping decisions related to climate variability across multiple regions. Glob. Environ. Chang. 25, 163–172. https://doi.org/10.1016/j.gloenvcha.2013.12.011

Xiao, X., Boles, S., Frolking, S., Li, C., Babu, J.Y., Salas, W., Moore, B., 2006. Mapping paddy rice agriculture in South and Southeast Asia using multi-temporal MODIS images. Remote Sens. Environ. 100, 95–113. https://doi.org/10.1016/j.rse.2005.10.004

Xie, Y., Shi, J., Ji, D., Zhong, J., Fan, S., 2017. A parameterized microwave emissivity model for bare soil surfaces. Remote Sens. 9, 1–16. https://doi.org/10.3390/rs9020155

Xiong, J., Thenkabail, P.S., Tilton, J.C., Gumma, M.K., Teluguntla, P., Oliphant, A., Congalton, R.G., Yadav, K., Gorelick, N., 2017. Nominal 30-m cropland extent map of continental Africa by integrating pixel-based and object-based algorithms using Sentinel-2 and Landsat-8 data on google earth engine. Remote Sens. 9, 1–27. https://doi.org/10.3390/rs9101065

Xu, L., Li, B., Yuan, Y., Gao, X., Zhang, T., 2015. A temporal-spatial iteration method to reconstruct NDVI time series datasets. Remote Sens. 7, 8906–8924. https://doi.org/10.3390/rs70708906

Yamaguchi, Y., Moriyama, T., Ishido, M., Yamada, H., 2005. Four-component scattering model for polarimetric SAR image decomposition. IEEE Trans. Geosci. Remote Sens. 43, 1699–1706. https://doi.org/10.1109/TGRS.2005.852084

Yan, L., Roy, D.P., 2016. Conterminous United States crop field size quantification from multi-temporal Landsat data. Remote Sens. Environ. 172, 67–86. https://doi.org/10.1016/j.rse.2015.10.034

Yan, L., Roy, D.P., 2014. Automated crop field extraction from multi-temporal Web Enabled Landsat Data. Remote Sens. Environ. 144, 42–64. https://doi.org/10.1016/j.rse.2014.01.006

Yang, Z., Shao, Y., Li, K., Liu, Q., Liu, L., Brisco, B., 2017. An improved scheme for rice phenology estimation based on time-series multispectral HJ-1A/B and polarimetric RADARSAT-2 data. Remote Sens. Environ. 195, 184–201. https://doi.org/10.1016/j.rse.2017.04.016

Yonezawa, C., Negishi, M., Azuma, K., Watanabe, M., Ishitsuka, N., Ogawa, S., Saito, G., 2012. Growth monitoring and classification of rice fields using multitemporal RADARSAT-2 full-polarimetric data. Int. J. Remote Sens. 33, 5696–5711. https://doi.org/10.1080/01431161.2012.665194

Yusoff, N.M., Muharam, F.M., Takeuchi, W., Darmawan, S., Abd Razak, M.H., 2017. Phenology and classification of abandoned agricultural land based on ALOS-1 and 2 PALSAR multi-temporal measurements. Int. J. Digit. Earth 10, 155–174. https://doi.org/10.1080/17538947.2016.1216615

Yuzugullu, O., Erten, E., Hajnsek, I., 2015. Rice Growth Monitoring by Means of X-Band Co-polar SAR: Feature Clustering and BBCH Scale. IEEE Geosci. Remote Sens. Lett. 12, 1218–1222. https://doi.org/10.1109/LGRS.2015.2388953

Zarcheshm, M., 2018. Delineation of Surface Water Features Using RADARSAT-2 Imagery and a TOPAZ Masking Approach over the Prairie Pothole Region in Canada. University of Saskatchewan Saskatoon, Saskatchewan, Canada.

Zhang, J., Yang, C., Zhao, B., Song, H., Hoffmann, W.C., Shi, Y., Zhang, D., Zhang, G., 2017. Crop classification and LAI estimation using original and resolution-reduced images from two consumer-grade cameras. Remote Sens. 9. https://doi.org/10.3390/rs9101054

Zhang, Y., Yang, B., Liu, X., Wang, C., 2017. Estimation of rice grain yield from dual-polarization Radarsat-2 SAR data by integrating a rice canopy scattering model and a genetic algorithm. Int. J. Appl. Earth Obs. Geoinf. 57, 75–85. https://doi.org/10.1016/j.jag.2016.12.014

Zhao, L., Yang, J., Li, P., Zhang, L., 2014. Characteristics analysis and classification of crop harvest patterns by exploiting high-frequency multipolarization SAR data. IEEE J. Sel. Top. Appl. Earth Obs. Remote Sens. 7, 3773–3783. https://doi.org/10.1109/JSTARS.2014.2308273

Zheng, B., Myint, S.W., Thenkabail, P.S., Aggarwal, R.M., 2015. International Journal of Applied Earth Observation and Geoinformation A support vector machine to identify irrigated crop types using time-series Landsat NDVI data. Int. J. Appl. Earth Obs. Geoinf. 34, 103–112 Contents. https://doi.org/10.1016/j.jag.2014.07.002

Zheng, Y., Zhang, M., Wu, B., 2016. Using high spatial and temporal resolution data blended from SPOT-5 and MODIS to map biomass of summer maize. 5th Int. Conf. Agro-Geoinformatics, Agro-Geoinformatics 2016. https://doi.org/10.1109/Agro-Geoinformatics.2016.7577683

Zhu, Z., 2017. Change detection using landsat time series: A review of frequencies, preprocessing, algorithms, and applications. ISPRS J. Photogramm. Remote Sens. 130, 370–384. https://doi.org/10.1016/j.isprsjprs.2017.06.013

Zribi, M., Gorrab, A., Baghdadi, N., Lili-Chabaane, Z., Mougenot, B., 2014. Influence of radar frequency on the relationship between bare surface soil moisture

vertical profile and radar backscatter. IEEE Geosci. Remote Sens. Lett. 11, 848–852. https://doi.org/10.1109/LGRS.2013.2279893

Zribi, M., Gorrab, A., Baghdadi, N., Lili-Chabaane, Z., Mougenot, B., Boulet, G., 2013. Radar frequency effect on the relationship between surface soil moisture vertical profile and radar backscatter. Geophys. Res. Abstr. EGU Gen. Assem. 15, 2013–11104.

Zribi, M., Muddu, S., Bousbih, S., Bitar, A. Al, Tomer, S.K., Baghdadi, N., Bandyopadhyay, S., 2019. Analysis of L-Band SAR Data for Soil Moisture Estimations over Agricultural Areas in the Tropics. Remote Sens.

Zwart, S.J., Bastiaanssen, W.G.M., de Fraiture, C., Molden, D.J., 2010. A global benchmark map of water productivity for rainfed and irrigated wheat. Agric. Water Manag. 97, 1617–1627. https://doi.org/10.1016/j.agwat.2010.05.018

References

List of publications

Publications

Sharma A. K., Hubert-Moy L., Buvaneshwari S., Sekhar M., Ruiz L., Bandyopadhyay S., Mohan, S., Corgne, S. Evaluation of Radarsat-2 quad-pol SAR time series images for monitoring irrigated cropland. *Int. J. of Digital Earth., 2019.* (https://doi.org/ 10.1080/17538947.2019.1604834).

Sharma A.K., Hubert-Moy L., Buvaneshwari S., Sekhar M., Ruiz L., Bandyopadhyay S., Corgne S. Irrigation History Estimation Using Multitemporal Landsat Satellite Images: Application to an Intensive Groundwater Irrigated Agricultural Watershed in India. *Remote Sens. 2018, 10,* 893. (https://doi.org/10.3390/rs10060893).

Mangiarotti, S., **Sharma, A. K.,** Corgne, S., Hubert-Moy, L., Ruiz, L., Sekhar, M., Kerr, Y. Can the global modelling technique be used for crop classification? *Chaos, Solitons and Fractals,* 2018, 106, pp. 363-378. (https://doi.org/10.1016/j.chaos.2017.12.003).

Subash, Y., Sekhar, M., Tomer, S.K., **Sharma, A.K.** (2017) A framework for assessment of climate change impacts on the groundwater system. (In: Sustainable Water Resources Management, Editors: C. S. P. Ojha, S. Rao, T. Zhang and A. Bardossy). Chapter 14, *ASCE Book Chapter.* https://doi.org/10.1061/9780784414767.ch14.

Buvaneshwari S., Riotte, J., Sekhar, M., Mohan Kumar, M. S., **Sharma, A. K.,** Duprey, J. L., Audry, S., Giriraj, P.R., Praveen, Y., Hemanth, M., Durand, P., Braun, J.J., Ruiz., L. (2017). Groundwater resource vulnerability and spatial variability of nitrate contamination: insights from high density tubewell monitoring in a hard rock aquifer. Science of Total Environment, 579, pp.838-847. (http://dx.doi.org/10.1016/j.scitotenv.2016.11.017).

Tomer, S.K., Al Bitar, A., Sekhar, M., Corgne, S., Bandyopadhyay, S., Sreelash, K., **Sharma, A.K.,** Zribi, M., and Kerr, Y. (2015). Retrieval and multi-scale validation of soil moisture from multi-temporal SAR data in a tropical region. Remote Sensing, Vol. 7(6), 8128-8153. (http://dx.doi.org/10.3390/rs70608128).

Manuscripts in-preparation

Sharma A. K., Hubert-Moy L., Buvaneshwari S., Sekhar M., Moger H., Corgne, S. Irrigated cropland identification for multiple cropping seasons in the Berambadi watershed of southern peninsular India.

Sharma A. K., Hubert-Moy L., Sekhar M., Betbeder J., Bandyopadhyay S., Mohan, S., Pottier E., Corgne, S. Turmeric crop monitoring using Radarsat-2 quad pol SAR and Landsat-8 time series images. *ISPRS Journal of Photogrammetry and Remote Sensing.*

Sharma A. K., Hubert-Moy L., Buvaneshwari S., Sekhar M., Corgne, S. Sensitivity analysis of Radarsat-2 ultrafine SAR images to the crop height detection in an intensive agricultural watershed of south India. *Remote Sens. Letters.*

Sharma A. K., Sekhar M., Buvaneshwari S., Hubert-Moy L., Moger H., Giriraj P., Ruiz L., Riotte J., Corgne, S. Assessing impact of intensive irrigation on groundwater resources in the Berambadi watershed, southern peninsular India. *Journal of Hydrology (VSI: Water Security).*

Sharma A. K., Hubert-Moy L., Betbeder J., Sekhar M., Bandyopadhyay S., Mohan, S., Pottier E., Corgne, S. Crop type classification using polarimetric decomposition of Radarsat-2 quad pol timeseries images. *IEEE TGRS.*

Sharma A. K., Hubert-Moy L., Sekhar M., Corgne, S. Land use and land cover studies using optical and SAR time-series dataset. *Book Chapter.*

Conferences, Proceedings, Oral and Poster

Sharma A. K., Ruiz L., Buvaneshwari, S., Sekhar M., Hubert-Moy L., Corgne S., 2018. Irrigated area estimation using Landsat satellite images in the Berambadi watershed. European Geophysical Union (EGU) General Assembly 2018, HS 6.5, PICO-presentation.

Sharma A. K., Hubert-Moy L., Betbeder J., Ruiz L., Sekhar M., Corgne S., 2016. Crop Identification using time series of Landsat-8 and Radarsat-2 images: Application in a groundwater irrigated region, South India. In Living Planet Symposium, Vol. 740, p. 103-106.

Buvaneshwari, S., Riotte, J., Ruiz, L., Sekhar, M., **Sharma, A K.,** Duprey, J.L., Audry, S., Braun, J.J., Mohan Kumar, M.S. Impacts of land-use and soil properties on groundwater quality in the hard rock aquifer of an irrigated catchment: the Berambadi (Southern India), Vol. 19 EGU General Assembly 2017-18884, Vienna

Mangiarotti S., **Sharma, A. K.,** Sekhar M., Corgne S., Ruiz L., Hubert-Moy L.& Kerr Y., Chaos theory applied to crops detection in South India, 14th Experimental Chaos and Complexity Conference, Banff, Canada, 113-115 (2016).

Mangiarotti S., **Sharma, A. K.,** Sekhar M., Corgne S., Ruiz L., Hubert-Moy L., Kerr Y., 2016. La modélisation du chaos appliquée à la classification des couverts agricoles (bassin versant de Berambadi, Inde du Sud). Comptes-Rendus de la 19e Rencontre du Non Linéaire, Paris, France, pp.73-78.

Buvaneshwari, S., Riotte, J., Ruiz, L., Sekhar, M., Mohan Kumar, M.S., **Sharma, A K.,** Duprey, J.L., Audry, S., Praveen, Y., Hemanth, M., Durand, P., Braun, J.J. High spatial variability of nitrate in hard-rock aquifer of irrigated catchment: Implications for water resource assessment and vulnerability, HS 2.3.8 EGU General Assembly 2016, April 18-22, 2016, Vienna.

Muddu S., Mangiarotti S., **Sharma, A. K.,** Corgne S., Ruiz L., Hubert-Moy L., 2015. Crop identification for the delineation of irrigated regions under scarce data conditions: a new approach based on chaos theory, AGU Fall meeting, 14-18 Dec. 2015, https://agu.confex.com/agu/fm15/meetingapp.cgi/Paper/78863.

Evaluation of high spatial and temporal resolution satellite images for land use monitoring in irrigated agricultural areas: application to the Berambadi watershed in India

Abstract: Agriculture is the backbone of India's economy and India uses a significant proportion of the fresh water available for irrigation. After the Green Revolution in the 1960s, India's agricultural sector grew exponentially, resulting in the overexploitation of fresh water for irrigation purposes. The main objective of this thesis is to monitor irrigated crops and cropland in the experimental Berambadi watershed using optical and radar satellite image time-series. The evolution of irrigated cropland in the watershed over three decades was studied using indices derived from optical images and the identification and characterization of irrigated land were carried out using optical and radar time-series. The results show the relevance of using several optical satellite products in cloudy weather for seasonal monitoring of irrigated cropland. They also highlight the potential of synergy between SAR Radarsat-2 polarimetric and optical image time-series for monitoring crop growth. This research shows that the intensive increase in irrigation in the Berambadi watershed over the decades has caused surface water in the downstream areas to disappear. Intensive irrigation of crops with groundwater for three seasons per year results in the cessation of surface runoff in the catchment area, with groundwater being depleted to 50 m from the surface.

Keywords : Agriculture, Irrigation, Remote sensing, Optical images, SAR images, Leaf Area Index, time-series analysis, SVM, ANCOVA, Image classification.

Evaluation d'images satellitaires à haute résolution spatiale et temporelle pour le suivi de l'utilisation des sols dans les zones agricoles irriguées: Application au bassin versant de Berambadi en Inde

Résumé : L'agriculture est l'épine dorsale de l'économie indienne et l'Inde utilise une part importante de l'eau douce disponible pour l'irrigation. Après la révolution verte qui a eu lieu dans les années 1960, le secteur agricole indien a connu une croissance exponentielle qui a entraîné une surexploitation de l'eau douce à des fins d'irrigation. L'objectif principal de cette thèse est d'effectuer un suivi des cultures et des terres cultivées irriguées dans le bassin hydrographique expérimental du Berambadi à l'aide de séries temporelles d'images satellite optiques et radar. L'évolution des terres cultivées irriguées dans le bassin versant au cours de trois décennies a été étudiée à l'aide d'indices dérivés des images optiques et l'identification et la caractérisation des terres irriguées ont été effectuées avec des séries temporelles optiques et radar. Les résultats montrent la pertinence de l'utilisation de plusieurs produits satellitaires optiques par temps nuageux pour la surveillance saisonnière des terres cultivées irriguées. Ils soulignent également le potentiel de la synergie entre les séries d'images polarimétrique SAR Radarsat-2 et les séries d'images optiques pour le suivi de la croissance des cultures. Cette recherche démontre que l'augmentation intensive de l'irrigation dans le bassin versant de Berambadi au fil des décennies a fait disparaître les eaux de surface dans les parties avales. L'irrigation intensive des cultures par les eaux souterraines pendant trois saisons par an entraîne l'arrêt de l'écoulement de surface dans le bassin versant, les eaux souterraines étant épuisées jusqu'à 50 m de la surface.

Mots-clés : Agriculture, Irrigation, Télédétection, Images optiques, Images SAR, Indice de surface foliaire, Analyse de séries temporale, SVM, ANCOVA, Classification des images.